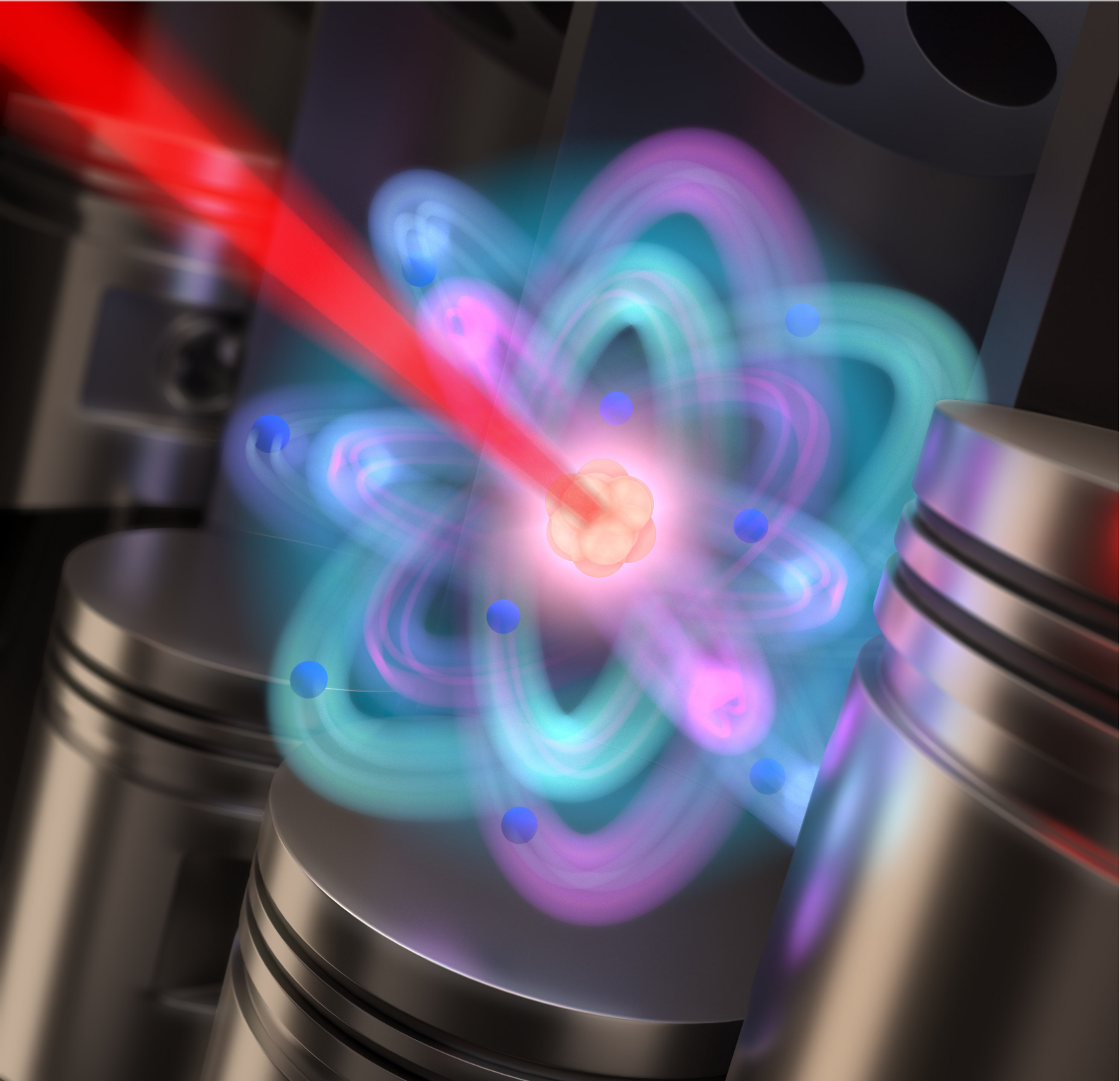


Johannes Roßnagel

# A Single-Atom Heat Engine

*Dissertation*



Fachbereich Physik, Mathematik und Informatik  
Johannes Gutenberg-Universität Mainz  
November 2016

# A Single-Atom Heat Engine

## Dissertation

Zur Erlangung des akademischen Grades

„Doktor der Naturwissenschaften“

am Fachbereich Physik, Mathematik und Informatik  
der Johannes Gutenberg-Universität in Mainz

vorgelegt von

**Johannes Roßnagel**

geboren in Heidelberg



JOHANNES GUTENBERG  
UNIVERSITÄT MAINZ

Mainz, November 2016



# Abstract

Heat engines convert thermal energy into mechanical work, typically involving a large number of atoms or molecules. In this thesis, I demonstrate that the working medium of thermal machines can be reduced to the ultimate limit of one single atom. This is the first experimental realization of a heat engine, where a single atom converts thermal excitations into mechanical work. As the working agent I used a single  $^{40}\text{Ca}^+$  ion, confined in a linear Paul trap with a special funnel-shaped geometry.

As a preparation for the experiments, I performed extensive numerical Monte-Carlo simulations of our system with realistic parameters in order to demonstrate its feasibility, to optimize the trap geometry, and to determine the expected range of the individual parameters. In collaboration with the group of Prof. Dr. E. Lutz, we established an analytical framework of the heat engine dynamics for a harmonic oscillator. We extended this model as well as the simulations to non-thermal reservoirs to demonstrate the corresponding capability for an increase of the engines performance.

For the experimental realization, I have driven the ion in a thermodynamic Stirling cycle by coupling it alternately to a hot and a cold reservoir. Thereby, the ion generates work from thermal excitations, which is extracted and stored in a designated degree of freedom. I have mapped and fully characterized the thermodynamic cycles of the engine for various temperature differences of the reservoirs by a direct and time resolved measurement of the ion's trajectory. However, this was only possible due to a novel temperature measurement technique, that allows for determining temperatures in a range between 0.1 and 100 mK. This technique is based on the spectroscopy of narrow dark two-photon resonances in the fluorescence spectrum of the ion and allows for time resolved measurements of the ion's thermal dynamics with a resolution of up to  $5\text{ }\mu\text{s}$ . From the measured thermodynamic cycles, I evaluated the output power  $P$  and the efficiency  $\eta$  of the engine, which reach up to  $P = 3.4 \times 10^{-22}\text{ J/s}$  and  $\eta = 0.28\%$  at a temperature difference of  $\Delta T = 66(8)\text{ mK}$  between the hot and the cold reservoir. These results are consistent with the predictions from an analytical model. The ability not only to generate work, but also to store it and to make it available to other oscillatory systems is a crucial step towards the implementation of more complex thermodynamic systems.

The model character of the trapped ions as harmonic oscillators allows one to transfer the findings from this thesis to other oscillatory systems. Furthermore, the versatility of trapped ion systems will allow one to analyze fluctuations of the engines parameters, which dominate on short timescales. With trapped ions initialized in the motional ground state, future heat engines may operate at the boarder of the classical and the quantum regime. Therefore, the presented work may inspire and initiate future thermodynamic experiments and more fundamental engine systems.





# Zusammenfassung

Eine Wärmekraftmaschine wandelt thermische Energie in mechanische Arbeit um, wobei das Arbeitsgas in der Regel eine große Anzahl von Atomen oder Molekülen umfasst. In der vorliegenden Arbeit zeige ich erstmals, dass das Arbeitsmedium einer Wärmekraftmaschine bis zur Grenze eines einzelnen Atoms reduziert werden kann. Dabei verwende ich ein einzelnes  $^{40}\text{Ca}^+$  Ion, welches in einer trichterförmigen Paul-Falle gefangen wird.

Zunächst habe ich umfassende numerische Monte-Carlo Simulationen durchgeführt, die auf realistischen Parametern beruhen und die Realisierbarkeit des Experimentes demonstrieren. Die Geometrie der Falle wurde auf Grundlage der Simulationen optimiert und der zu erwartende Bereich der einzelnen Parameter der Maschine bestimmt. Zusammen mit der Arbeitsgruppe von Prof. Dr. Eric Lutz haben wir einen analytischen Rahmen aufgestellt, in dem die Dynamik eines harmonischen Oszillators als Wärmekraftmaschine beschrieben werden kann. Unser analytisches und numerisches Modell haben wir auf nicht-thermische Bäder erweitert und gezeigt, dass sich so die Leistungsfähigkeit der Maschine deutlich erhöhen lässt.

Um die Wärmekraftmaschine experimentell zu realisieren, habe ich ein einzelnes gefangenes Ion abwechselnd an ein warmes und ein kaltes Bad gekoppelt, wodurch es einen Stirling-Kreisprozess durchläuft. Das Ion wandelt thermische Energie in mechanische Arbeit um, die in Bewegungsenergie gespeichert wird. Durch eine zeitaufgelöste Messung der Bewegung konnte ich thermodynamische Kreisprozesse für verschiedene Temperaturen der Bäder charakterisieren. Dies wurde erst durch eine neuartige Temperatur-Messmethode möglich, bei der Dunkelresonanzen im Fluoreszenz-Spektrum untersucht werden. Sie erlaubt eine Bestimmung der Temperatur des Ions im Bereich zwischen 0.1 mK und 100 mK und ermöglicht erstmals eine zeitliche Auflösung von Thermalisierungsprozessen. Aus den Kreisprozessen konnte ich die Leistung  $P$  der Maschine sowie deren Effizienz  $\eta$  ermitteln. Diese reichen bis zu  $P = 3.4 \cdot 10^{-22}$  J/s und  $\eta = 0.28\%$ , und stimmen mit den Vorhersagen eines analytischen Modells überein. Die Möglichkeit mechanische Arbeit nicht nur zu erzeugen, sondern auch zu speichern und für andere Systeme nutzbar zu machen, ist ein wichtiger Schritt für eine Integration in komplexere thermodynamische Systeme.

Durch die Modelleigenschaften von gefangenen Ionen als harmonische Oszillatoren können die Erkenntnisse meiner Arbeit auf verschiedene Oszillator-Systeme übertragen werden. In zukünftigen Experimenten soll die Maschine mit grundzustandsgekühlten Ionen an der Grenze zwischen Quantenmechanik und klassischer Mechanik betrieben werden. Das hohe Maß an Kontrolle ermöglicht eine Untersuchung der Fluktuationen der gemessenen Parameter, die auf kurzen Zeitskalen dominieren. Die vorliegende Arbeit wird die Entwicklung von zukünftigen Maschinen im Nanomaßstab inspirieren und weitere Experimente mit thermodynamischen Systemen motivieren.



# Contents

<b>1. Introduction</b>	<b>1</b>
1.1. From steam engines to single atoms . . . . .	2
1.2. Experimental thermodynamics on the nanoscale . . . . .	4
1.3. Microscopic and nanoscopic heat engines . . . . .	5
1.4. Non-classical and quantum reservoirs . . . . .	7
1.5. Quantum thermodynamics and quantum heat engines . . . . .	8
1.6. Trapped ions as a model system . . . . .	9
1.7. Outline of the Thesis . . . . .	10
<b>2. General concept of the single-atom heat engine</b>	<b>13</b>
2.1. The laws of thermodynamics . . . . .	13
2.1.1. Zeroth law: thermal equilibrium . . . . .	13
2.1.2. First law: energy conservation . . . . .	14
2.1.3. Second law: entropy . . . . .	14
2.1.4. Third law: absolute zero . . . . .	15
2.2. Thermodynamic cycles of heat engines . . . . .	15
2.2.1. The Otto cycle . . . . .	15
2.2.2. The Stirling Cycle . . . . .	16
2.3. Power and efficiency . . . . .	17
2.3.1. Carnot efficiency . . . . .	17
2.3.2. Efficiency at maximum power . . . . .	18
2.4. A funnel-shaped ion trap . . . . .	19
2.4.1. The harmonic trapping potential . . . . .	19
2.4.2. The tapered potential . . . . .	20
2.4.3. Origin and reduction of micromotion . . . . .	21
2.5. Working cycle of the single-atom heat engine . . . . .	22
2.6. Laser cooling . . . . .	24
2.7. The calcium ion . . . . .	26
<b>3. Results of analytical and numerical investigations</b>	<b>27</b>
3.1. The quantum harmonic oscillator as heat engine . . . . .	28
3.1.1. Thermal state of a quantum harmonic oscillator . . . . .	28
3.1.2. Otto cycle for a harmonic oscillator . . . . .	29
3.1.3. Work and efficiency . . . . .	31
3.2. Proof of concept - a single ion as working fluid . . . . .	33
3.2.1. Concepts of numerical simulations . . . . .	34
3.2.2. Monte Carlo simulations . . . . .	35

3.3.	Employing non-thermal reservoirs . . . . .	38
3.3.1.	Otto cycle with a squeezed thermal reservoir . . . . .	41
3.3.2.	Numerical simulations . . . . .	43
3.3.3.	Generation of squeezing . . . . .	45
3.3.4.	Remarks on the generation of work and the notion of efficiency . .	46
3.4.	Conclusion and Outlook . . . . .	47
<b>4.</b>	<b>Setup of the experiment</b>	<b>49</b>
4.1.	The funnel-shaped ion trap . . . . .	49
4.1.1.	The radio-frequency supply . . . . .	50
4.1.2.	The constant voltage supply . . . . .	53
4.1.3.	Electric field noise . . . . .	54
4.1.4.	Loading ions into the trap . . . . .	55
4.1.5.	Detection of fluorescence light . . . . .	55
4.1.6.	Generation of a magnetic quantization field . . . . .	58
4.2.	The vacuum setup . . . . .	58
4.3.	The laser system . . . . .	58
4.3.1.	Laser system for ionizing neutral Ca-atoms . . . . .	59
4.3.2.	Laser systems for cooling and detecting the ions . . . . .	60
4.3.3.	Scanning and switching of the beams . . . . .	61
4.3.4.	Frequency stabilization . . . . .	62
<b>5.</b>	<b>Coherent excitation of motion</b>	<b>65</b>
5.1.	Characterization of the ion trap . . . . .	65
5.1.1.	Measurement of trap frequencies . . . . .	65
5.1.2.	Trap frequencies in a tapered potential . . . . .	68
5.2.	Demonstration of the elements of the heat engine working principle . . .	69
5.3.	Determination of the damping coefficient . . . . .	70
5.3.1.	Step response to coherent drive . . . . .	70
5.3.2.	Broadening of the resonance . . . . .	74
5.4.	Addressing of single atoms and controlled interaction . . . . .	76
<b>6.</b>	<b>Incoherent thermal excitation</b>	<b>79</b>
6.1.	Temperature of a single trapped ion . . . . .	80
6.1.1.	The notion of temperature . . . . .	80
6.1.2.	Generation of thermal states at various temperatures . . . . .	82
6.2.	Principles of dark resonance thermometry . . . . .	85
6.2.1.	Calculation of dark resonance spectra . . . . .	86
6.2.2.	Dark resonances and thermal motion . . . . .	87
6.2.3.	Shaping the laser cooling by exploiting dark resonances . . . . .	90
6.3.	Determination of the laser linewidth . . . . .	91
6.4.	Temperature measurements in thermal equilibrium . . . . .	93
6.4.1.	Experimental parameters and characteristics . . . . .	93
6.4.2.	Experimental procedure . . . . .	93
6.4.3.	Measurement of steady-state temperatures . . . . .	94
6.5.	Investigation of thermal dynamics . . . . .	95
6.6.	Engineering thermal states by exploiting dark resonances . . . . .	96
6.7.	Spatial thermometry technique . . . . .	98

6.8. Outlook and applications . . . . .	100
<b>7. Experimental implementation of the single-atom heat engine</b>	<b>101</b>
7.1. Specific experimental parameters . . . . .	102
7.2. Electronic control of the experiment . . . . .	103
7.3. Resolved measurement of the ion's oscillation . . . . .	103
7.4. The thermodynamic cycles . . . . .	105
7.4.1. Measurement of the thermodynamic cycles . . . . .	105
7.4.2. Analytical derivation of the thermodynamic cycles . . . . .	108
7.4.3. A Stirling-like engine type . . . . .	110
7.5. Output power of the engine . . . . .	111
7.5.1. Stationary output power . . . . .	111
7.5.2. Start of the engine . . . . .	114
7.6. Efficiency of the engine . . . . .	116
7.7. Exclusion of non-thermal excitation of the ion . . . . .	118
7.8. Summary . . . . .	119
<b>8. Future perspectives of the single-atom heat engine device</b>	<b>121</b>
8.1. Single-atom heat pump . . . . .	121
8.1.1. Single-ion operation . . . . .	122
8.1.2. The three-ion heat pump . . . . .	123
8.2. Autonomous, self-contained engine . . . . .	124
8.3. Towards a quantum heat engine . . . . .	125
8.3.1. A heat engine at the ground state of motion . . . . .	126
8.3.2. The two-level system as heat engine . . . . .	126
8.4. The tapered ion trap as a tool for quantum information . . . . .	127
<b>Appendices</b>	<b>129</b>
<b>A. Appendix</b>	<b>129</b>
A.1. Treatment of trap electrodes . . . . .	129
A.2. Processing of PMT pulses . . . . .	130
A.3. Stroboscopic recording of the ions motion . . . . .	130
A.4. Radio-frequency signal generator for AOM driving . . . . .	131
A.5. Power stabilization during AOM scans . . . . .	132
A.6. Switching between lasers with two VCOs . . . . .	133
A.7. Design of a next generation funnel-shaped ion trap . . . . .	135
<b>B. List of publications</b>	<b>139</b>
<b>Bibliography</b>	<b>141</b>
<b>Acknowledgments</b>	<b>155</b>
<b>Curriculum Vitae</b>	<b>157</b>





# List of Figures

1.1. Schematic diagram of a heat engine . . . . .	2
1.2. Comparison of different experimental heat engine systems . . . . .	6
1.3. Probability distribution of motional states in phase space . . . . .	10
2.1. Thermodynamic cycles: the Otto and the Stirling cycle . . . . .	16
2.2. The linear Paul trap . . . . .	19
2.3. Geometry of the funnel-shaped ion trap . . . . .	20
2.4. The linear and the tapered trapping potential . . . . .	21
2.5. Fundamental mechanism converting thermal energy into motion . . . . .	23
2.6. Working principle of the single ion heat engine . . . . .	24
2.7. Mechanical analog of the single-atom heat engine . . . . .	25
2.8. Energetic level scheme of $^{40}\text{Ca}^+$ . . . . .	26
3.1. Otto cycle for a harmonic oscillator in the $\{n, \omega\}$ -representation . . . . .	29
3.2. Analytic analysis of work and efficiency of the Otto cycle . . . . .	32
3.3. Simulated energy-frequency diagram of the Otto cycle . . . . .	36
3.4. Simulated evolution of the radial energy during heat engine operation . . . . .	37
3.5. Ensemble average of the ion trajectories during heat engine operation . . . . .	37
3.6. Phase space distribution at different phases during an engine cycle . . . . .	38
3.7. Efficiency of the Otto engine as a function of the temperature ratio . . . . .	39
3.8. Efficiency at maximum power . . . . .	42
3.9. Simulated Otto cycle with a squeezed thermal reservoir . . . . .	44
3.10. Simulated efficiency at maximum power for different squeezing parameters . . . . .	45
3.11. Widths of pure thermal and squeezed thermal states . . . . .	46
4.1. Images of the funnel-shaped ion trap. . . . .	50
4.2. Exploded-view CAD-drawing of the ion trap setup . . . . .	51
4.3. Drawing of the helical resonator . . . . .	52
4.4. Radio frequency signal on the output lines of the helical resonator . . . . .	53
4.5. Electronic setup of the inversion circuit for electric noise . . . . .	54
4.6. Recorded voltage noise signal . . . . .	55
4.7. Camera image of a linear 5-ion crystal . . . . .	56
4.8. Acquisition process of the ICCD camera . . . . .	57
4.9. Technical scheme of the laser setup . . . . .	60
4.10. Orientation of the individual laser beams with respect to the ion trap . . . . .	61
4.11. Setup of the laser frequency stabilization to a reference cavity . . . . .	62

5.1. Amplitude of a harmonic oscillator as a function of the driving frequency	66
5.2. Measurement of the trap frequency by a modulated laser beam . . . . .	67
5.3. Measured radial trap frequencies as a function of the axial position . . . .	68
5.4. Demonstration of the fundamental working mechanism of the heat engine	69
5.5. Deliberate dissipation and step response to a coherent drive . . . . .	71
5.6. Determination of the damping coefficient . . . . .	72
5.7. Analysis of the damping coefficient by step response measurements . . . .	73
5.8. Broadening of the spectral resonances for different damping coefficients .	74
5.9. Characterization of the damping coefficient as a function of the parameters of the dissipation laser . . . . .	75
5.10. Addressability of single ions within a lon ion crystal . . . . .	77
5.11. Addressing of single ions in a 3-ion and a 4-ion crystal . . . . .	77
6.1. Spatial intensity distribution of a single ion at different temperatures . . .	82
6.2. Characterization of the voltage noise signal . . . . .	83
6.3. Emergence of dark resonances due to coherent population trapping . . . .	86
6.4. Emergence of four dark resonances in the fluorescence spectrum of $^{40}\text{Ca}^+$	88
6.5. 3D-surface plot of the calculates thermal broadening of dark resonances .	89
6.6. Determination of the linewidth of the laser sources . . . . .	92
6.7. Measured dark resonances at different temperatures . . . . .	94
6.8. Scan of a dark resonance in pulsed acquisition mode . . . . .	95
6.9. Time resolved thermal dynamics of trapped ions . . . . .	96
6.10. Influence of the dark resonance on the temperature of the ion . . . . .	97
6.11. Determination of the point spread function of the imaging optics . . . . .	98
6.12. Temperature measurement using the spatial thermometry technique . . .	99
7.1. Condensed sketch of the setup of the heat-engine experiment . . . . .	102
7.2. TTL circuit and timing of the heat-engine drive . . . . .	103
7.3. Time resolved measurement of the ion's oscillation . . . . .	104
7.4. Temperature dynamics of the ion in contact with the thermal reservoirs . .	106
7.5. Simulated temperature dynamics of the heat engine . . . . .	107
7.6. Measured thermodynamic Stirling cycle . . . . .	109
7.7. Output power of the engine . . . . .	112
7.8. Start of the engine from rest . . . . .	115
7.9. Efficiency of the engine . . . . .	116
7.10. Exclusion of non-thermal excitation of the ion . . . . .	118
8.1. Thermodynamic cycle of a heat pump for a harmonic oscillator . . . . .	122
8.2. Three ion heat pump configuration . . . . .	123
8.3. Segmented trap design . . . . .	124
8.4. Design for an autonomous operation of the single-ion heat engine . . . .	125
8.5. Approaches to realize a quantum heat engine with a trapped-ion system .	126
8.6. Bow-tie trap for quantum computation . . . . .	127
A.1. Electron-microscope images of the trap electrodes . . . . .	130
A.2. Circuit diagram for stretching the single photon pulses from the PMT . . .	131
A.3. Stroboscopic record of the breathing mode of a two ion crystal . . . . .	131
A.4. Block diagram of the controllable rf-signal generator . . . . .	132

A.5. Characteristics of the VCO module . . . . .	133
A.6. Step-response of an AOM as electro-optical shutter . . . . .	133
A.7. Stabilization of the defraction efficiency of an AOM . . . . .	134
A.8. Switching between two drive frequencies which for the AOM . . . . .	134
A.9. New design of the funnel-shaped ion trap . . . . .	135
A.10.Details and geometry of the new trap . . . . .	136



*"What are the possibilities of small but movable machines? They may or may not be useful, but they surely would be fun to make."*

— Richard Feynman, 1959

# 1 Introduction

The laws of thermodynamics impact our daily life like almost no other physical law. They describe the conservation of energy, its transformation from one form to another, and govern the exchange of heat and the generation of work. Their obvious effects on our everyday perception are as diverse as the process of cooking, the daily weather or the means of transport. Our modern society is entirely based on the existence of machines and engines, while the technological miniaturization has led to the development of increasingly smaller devices. One of the most intriguing questions of nanotechnology is whether the concept of motors may be reduced to the nanoscopic level. Nature shows us the way: muscles are outstanding molecular engines, with efficiencies far above any machine created by humans so far. To devise nano engines, a thermodynamic understanding of processes in small scale systems is essential. Statistical mechanics allows one to reduce the thermodynamic behavior of large systems to processes on the single particle level, and finally connects thermodynamics to quantum mechanics. However, when treating single particles, the thermodynamic framework changes. While classical systems are always in thermal contact with their surrounding, this interaction has to be treated explicitly for nanoscopic systems, and a limited particle number leads to fluctuating thermodynamic quantities. Even the physics of information processing and computation has a thermodynamic contribution. For instance, information may be converted into mechanical work and the erasure of information requires a minimum amount of heat.

In the early days, the understanding of thermodynamics was based on phenomenological findings. But by the time of the industrial revolution in 19th century it developed into a scientific discipline. Since then, thermodynamics has spread into many fields of research, such as engineering, biology, chemistry or nanotechnology. In this thesis we implement a single-atom heat engine, which combines the engineering approach and thermodynamics of nanoscopic systems. In order to introduce to these two disciplines, we will sketch their historical evolution in the following. This introduction, however, is intended to place the present work into its scientific context, but makes no claim to historical completeness. Subsequently, we will summarize the state of the art of nano-thermodynamic experiments and recent realizations of micro-sized heat engines. Finally, we will give brief insights in the field of quantum thermodynamics, with a focus on a variety of proposals for quantum heat engines, as well as on the technological progress of ion traps and their role as model systems. We close the introduction with an outline of this thesis.



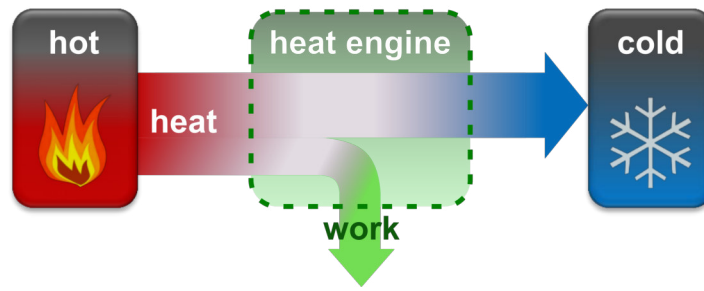


**Figure 1.1.** – A heat engine is a cyclically working device, that converts a difference in thermal energy between a hot reservoir and a cold reservoir to some degree into mechanical energy. Thereby, it converts non-directed, thermal motion of atoms into directed and coherent motion or, in other words, heat into work.

### 1.1. From steam engines to single atoms

The early scientists and philosophers, from the era of Greeks and Romans to the industrial revolution, tried to describe their daily perceptions on intuitive quantities, such as temperature and pressure, and the relations between them. But with the invention of thermal machines, there was a growing interest to understand the underlying processes. The first industrial piston-based steam engine, invented by Newcomen in 1712 and refined by Watt in 1765, gave rise a diversity of useful machines and engines [Ros10]. This encouraged scientists of the time to study the conversion of heat into work, in search of devices with higher efficiencies, dreaming of perpetual motion machines. Based on the conservation of thermal energy and the first ideas of entropy, called *moment of activity* at the time, Carnot derived the maximum efficiency of any cyclically working machine between two thermal reservoirs. He was the first to analyze the underlying physical principles of heat engines [Car24], stating in 1824:

*"The thermal agency by which mechanical effect may be obtained is the transference of heat from one body to another at a lower temperature",*

see Fig. 1.1. The understanding of heat being an individual form of energy was established by von Mayer and Joule independently in 1842 and 1843. Joule formulated the mechanical equivalent of heat [Rey92] as:

*"Wherever mechanical force is expended, an exact equivalent of heat is always obtained",* an early expression of the first law of thermodynamics.

However, scientists realized soon that no real machine is able to reach the maximum efficiency predicted by Carnot. The statements of Carnot and Joule failed to recognize that transformations of energy in the real world don't occur in isolated systems. The second law is the logical consequence, taking the increase of entropy into account. It breaks the temporal symmetry of the universe as it defines a specific direction of its evolution in time. It was Clausius who formulated the second law in a modern form in 1850 [Cla50]:

*"Heat can never pass from a colder to a warmer body without some other change, connected therewith, occurring at the same time".*

He also coined the term of *entropy*, based on Carnots *moment of activity*, and ends his work *"The mechanical Theory of Heat"* [Cla67] with a famous summary of the first and the second law:

*"The energy of the universe is constant. The entropy of the universe tends to a maximum".*

The evolution of industrial engines took their next step in 1816, when Stirling invented a closed cycle engine with external combustion, which was the first hot gas engine put to practical work [Fin01]. As an alternative to the common steam engines of those times, the Stirling engine is the prototype that most modern motors are based on. The simple setup, the closed air cycle as well as a successful down scaling led to a revival of Stirling engines in the mid of the 20th century as *domestic motors*, powered by a simple candle flame. The most efficient hot air engine was created by Otto in 1876. As a further development of a gas engine invented by Lenoir, this was the first internal combustion engine which used a compression of the gas mixture prior to ignition in order to increase the efficiency. The Otto engine started a veritable success story, which continues today with modern car engines. Both hot air engine types find their continuation in modern science: while the working principle of our single-atom engine builds on an Otto cycle, the experimental realization resembles a Stirling cycle for technical reasons.

The microscopic interpretation of thermodynamics started with Bernoulli in 1738 [Ber68], who described the origin of pressure as collisions of atoms with the walls. His ideas were successfully pursued by Clausius [Cla57] and Maxwell [Max71]. In 1867, Maxwell conceived a thought experiment to question the second law on the scale of single atoms. He invented an intelligent *being*, later called *demon*, that is able to separate hot and cold atoms in a closed system, and therefore decreases entropy [Max71]. Thereupon, Boltzmann tried to derive an analytical framework which reduces thermodynamic properties entirely to the kinetic behavior of individual atoms [Cal85]. He put the entropy on a statistical footing and derived its relation to the number of accessible microstates  $\Omega$  with his famous formula  $S = k_B \ln \Omega$ . His work encouraged scientists of the time to investigate the consequences of microscopic processes on thermodynamic quantities. Since at least 1905, when Einstein determined the Brownian motion to be a result of random interactions with water molecules, the postulate that *heat is a disordered movement of atoms* is an established result [Fli06]. Since then, stochastic thermodynamics has successfully derived all macroscopic thermodynamic quantities from statistical properties of the microscopic structure of matter [Sei12]. In 1961, Landauer fundamentally connected the expanding field of information theory with thermodynamic processes. He stated that the erasure of information is a dissipative process and requires a minimum amount of heat, equal to the entropy of one bit of information with two microstates,  $Q_L = k_B \ln 2$  [Lan61]. The Landauer principle states by implication that the entropy of a memory increases when information is stored, and therefore ensures that any intelligent demon acts in accordance with the second law.

The question of how to apply thermodynamics to single, isolated atoms arose with the discovery of nucleation reactions in the 1930s [Vol26, Fes87]. In the past decades, there is an ongoing size reduction of technical devices from the macroscale to the nanoscale, which is nowadays approaching the ultimate limit of single atoms. This process of miniaturization thus puts thermodynamics of single particles and nanosystems into the focus of research [Cer09]. Amongst others, Jarzynski and Crooks propelled the investigation of statistical processes on the nanoscale and for small particle numbers [Jar97, Cro99]. Their investigations demonstrate that there are substantial differences between thermodynamic processes for macrosystems and nanosystems. They showed that, as a consequence of the statistical nature of single particle processes, the thermodynamic quantities and state variables are subjected to fluctuations. These fluctuations can even lead to statistical short term violations of the laws of thermodynamics, as predicted by

Evans *et al.* [Eva93]. However, the laws hold, of course, for long time averages of the systems dynamics [Jar11].

In his 1959 talk *"There is plenty of room at the bottom"*, Feynman already envisioned tiny motors working at the single-atom level [Fey60]. He challenged physicists of the time to follow the visionary way of miniaturization, which had just begun, and to make a start towards engineering machines at the ultimate limit of single atoms. The start of the theoretical investigations of nanoscopic machines and devices is commonly accredited to Hill and his work on *"Thermodynamics of Small Systems"* by 1963 [Hil63]. The pioneering work of Scovil and Schulz-DuBois on maser heat engines in 1959 [Sco59] also triggered an intense and continuous effort in theoretical studies of heat engines and refrigerators on the nanoscale including their quantum properties [Ali79, Kos84, Gev92a, Lin03, Hen07]. In the 1970s and 1980s, Taniguchi and Drexler popularized the potential of nanotechnology, which boosted the development of numerous technical inventions on the nanoscale [Tan74, Dre86]. In the 1990s, a new series of molecular synthesis techniques allowed for the creation of various mechanical machines based mechanically linked molecules. On this basis, dramatic experimental progress in the last decade has lead to the diverse micro- and nanosized heat engines, which will be discussed in Sec. 1.3 in detail. The achievements in the miniaturization of machines, as well as its potential for future nanotechnological devices, has been acknowledged with the 2016 Nobel prize in chemistry for Sauvage, Stoddard and Feringa.

In this thesis, we follow a different approach and employ one single atom as working agent of an engine, thus fulfilling Feynman's dream [Roß16]. However, our engine was not conceived to complete the process of miniaturization, but rather to inspire and to motivate subsequent experiments in the field of single-atom and quantum thermodynamics.

## 1.2. Experimental thermodynamics on the nanoscale

On the nanoscale, the classical framework of thermodynamics has to be expanded. The classical description of the laws of thermodynamics has been formulated for mean values of state variables in the thermodynamic limit, thus for ensembles with a large number of particles on the order of  $10^{23}$  [Cen15]. The progress in stochastic thermodynamics has led to a transfer of the definitions of thermodynamic parameters to the level of single trajectories of microscopic systems [Sei12, Alo16b]. The increasing level of control of micro- and nanosystems in the past decade has allowed for a new generation of thermodynamic experiments. The high precision in preparation and readout allows to target former thought experiments, such as a Maxwell's demon or the Landauer principle.

A Maxwell's demon could be realized recently in various nanosystems. In cold atom systems a one-way barrier has been realized in search of effective cooling techniques, which acts as a Maxwell's demon sorting atoms according to their direction of motion [Tho08]. In the form of a Feynman ratchet, it permits the extraction of work from a single heat bath. A spatial asymmetry in dissipation has been used to obtain a directed motion from undirected Brownian motion and thus to perform work [Rou94, Par02]. In photonic systems a Maxwell's demon could be realized by electric feedback operations, which sort photons of a thermal light source to extract work into an electric circuit [Vid16]. A similar approach has been pursued by Koski *et al.* with a single electron system, where a Maxwell's demon uses information about a thermal electron to generate work from

its Brownian motion [Kos14a]. This process has even been inverted to use the demons information to reduce the entropy of the system [Kos15].

The Maxwell's demon experiments are closely linked to Landauer's erasure theorem. The relation between information and heat has been first demonstrated experimentally in a classical system using a micro-particle in an optical dipole trap [Bér12]. Koski *et al.* showed that the Landauer principle can be inverted and the amount of heat  $Q_L = k_B \ln 2$  can be extracted from one bit of information [Kos14a]. Recently, the Landauer principle has even been proven in the quantum regime employing a nuclear magnetic resonance setup [Pet16].

The emerging variety of single particle systems has allowed for the investigation of the statistical nature of the nano-thermodynamics in detail, as predicted by Jarzynski, Crooks and Evans. Short term fluctuations of thermodynamic parameters have been experimentally observed in different systems, as diverse as molecular systems [Col05, Ale12], levitated nanospheres [Gie14], nuclear spin systems [Bat14] and single trapped ions [An15]. The fact that on short timescales these fluctuations can even lead to a violation of the laws of thermodynamics has been demonstrated with nanoparticles [Wan02, Ver14a, Mar16]. However, the laws of thermodynamics hold, of course, for long time averages of the systems [Jar11]. A profound review of the field of fluctuation theorems for small scale thermodynamics has been composed by Seifert [Sei12], and more recently by Dinis *et al.* [Din16].

The above examples illustrate the variety of possibilities which open up on the basis of micro- and nano-sized system. However, most of the above cited experiments are still in the classical regime of thermodynamics. If we decrease the temperature of the system to the quantum regime, where the discreteness of energy levels becomes important, we are able to test the laws of thermodynamics in the realm of quantum mechanics experimentally. The use of quantum states instead of classical states for thermodynamical experiments is an exciting technological challenge and will provide important insights in the thermodynamics of quantum information processing. The increasing fidelity of preparation, control and readout of quantum states promises a rise of thermodynamic experiments in various quantum systems in the near future.

### 1.3. Microscopic and nanoscopic heat engines

The process of miniaturization has led to a growing interest in small scale engines, while the technical achievements in increasing precision of modern experiments has provided the necessary tools. The combination of both gave birth to several heat engines on the micro- and nanoscale in the past couple of years, as summarized in the following and sketched in Fig. 1.2.

Inspired by nature and by the biological motors in muscle cells, the creation of nano-sized engines started with the synthesis of appropriate molecular structures. In 1994, Sauvage *et al.* and Stoddard *et al.* both realized a mechanically moving device based on linked molecules [Liv94, Bis94], today seen as the "embryo of a non-biological molecular machine" [Fer16]. In 1999, Feringa *et al.* constructed the first notable molecular motor, where two parts of a macro-molecule rotate against each other when exposed to UV-light [Kou99]. This concept was refined and reduced to a single molecule in 2002 by Hugel *et al.* [Hug02]. They drove an optical transition between different structural configurations of a single polymer molecule cyclically, whereby the molecule is length-

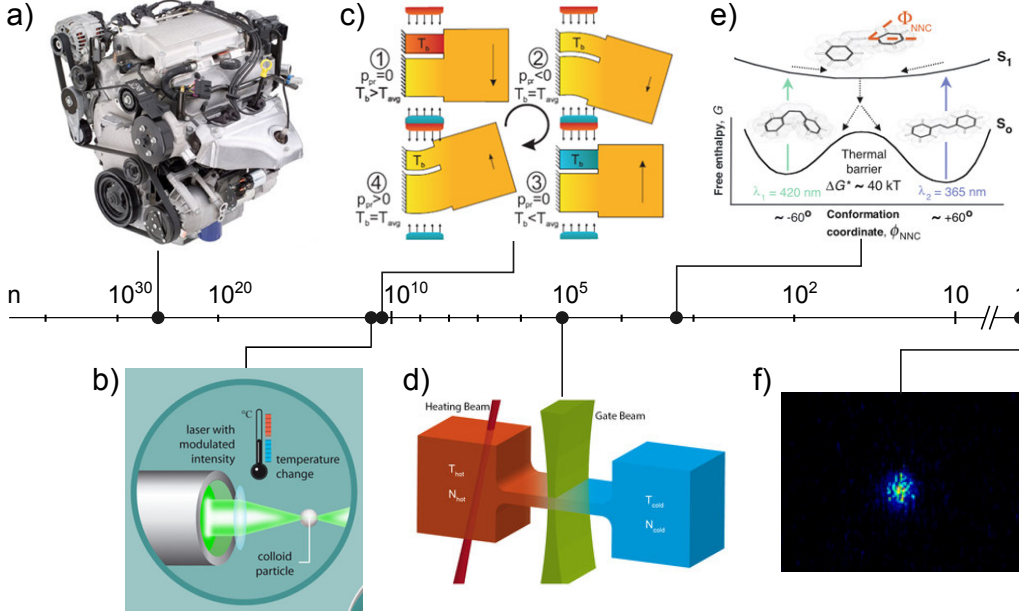


**Figure 1.2.** – Number of atoms  $n$  of the working agent of different heat engine systems. (a) Common car engine [car]. (b) Micro-sphere suspended in water and confined in an optical tweezer [Bli12]. (c) Solid state engine system: a silicon beam drives a micro-mechanical oscillator [Ste11]. (d) Two clouds of cold atoms at different temperature, connected by a small channel [Bra13a]. (e) A single azobenzene molecule works in an opto-mechanical cycle [Hug02]. (f) A single ion serves as working agent of the heat engine, this work [Roß16].

ened and contracted against an external force and thus performs work. This device, as well as Feringas engine, demonstrates the opto-mechanical energy conversion and hence are not heat engines in the proper sense. However, it demonstrated the possibility for a deliberate generation of mechanical work on the nanoscale.

The conversion of thermal energy into electrical power was demonstrated in a micro-electromechanical system in 2003 by Wahlen *et al.* [Wha03]. They used a small vapor bubble between two piezoelectric membranes and converted the expansion and contraction of the bubble into voltage differences in the membranes. But with a bubble size of  $1000 \mu\text{m}$  in diameter and  $60 \mu\text{m}$  high, this was still far away from targeting new regimes of thermodynamics. This approach, however, was pursued by Steeneken *et al.*, who demonstrated in 2011 a fully functional micro heat engine with a solid state working agent [Ste11]. They employed the resistive heating and thermal expansion of a micro-sized silicon beam to drive a mechanical oscillator at resonance. Interestingly, this engine runs with a continuous current and amplifies the oscillation of the load autonomously due to the piezoresistive effect of the silicon beam.

A major milestone was reached in 2012 with the stochastic heat engine of Blickle and Bechinger [Bli12]. They used a single melamine bead with  $3 \mu\text{m}$  in diameter, suspended in water and confined in the harmonic potential of an optical dipole trap. They analyzed the Brownian motion of this particle while driving a Stirling cycle by a periodic variation of the water temperature and the strength of the optical potential. Work and efficiency of the engine are derived from the time dependent spread of the Brownian motion. Since this system is working in the overdamped regime, both heat and work are dominated by

fluctuations due to the stochastic nature of the interactions. This experiment is widely acknowledged as the first micro-sized heat engine and has drawn much attention in the community. Recently, this experiment has been refined by Martinez *et al.* [Mar16]: in 2016 they published an outstanding work, where they could demonstrate that stochastic micro heat engines, although working in the classical regime, may exceed the Carnot efficiency on short timescales with a finite probability, as a consequence of fluctuating parameters. As mentioned above, on a long term basis the fluctuations balance out and the system obeys the classical expectations.

A single-cycle engine, based on the thermoelectric effect, has been demonstrated with cold atom clouds. Brantut *et al.* showed in 2013 that a directed atom current against a chemical potential is generated during the exchange of heat between two clouds of atoms at different temperature [Bra13a]. In 2015, an energy harvester has been realized experimentally by Thierschmann *et al.* using a three terminal quantum dot, where thermal fluctuations are directly converted into an electric current [Thi15].

All the above mentioned engine systems are working in the classical regime with thermal heat baths and still employ a large number of atoms. In this thesis, we demonstrate a heat engine reduced to a single atom, which represents the first thermal machine operating at the single-atom level. We employ a trapped ion in a linear Paul trap as model system. Trapped ions are a popular platform for experiments in the quantum regime, such as for quantum information processing. Although our engine is operated at high temperatures where a classical description is appropriate, it has the potential to enter a temperature range where the quantization of energy levels has to be taken into account. Likewise, the engine could be driven by or drive quantum states. Further specific proposals for future micro-sized heat engines have been published for different optomechanical setups [Zha14a, Dec15], microwave cavities [Ber14], and quantum dots [Hum02], which all have the potential to enter the quantum regime as well. However, an experimental demonstration of a quantum heat engine is still lacking.

## 1.4. Non-classical and quantum reservoirs

A reservoir is ideally an infinite pool of energy in equilibrium and with constant state variables, such as its temperature. When a system is in contact with a reservoir both exchange energy and the systems state variables, which are free to change, converge towards equilibrium with the reservoir. The heat capacity of the reservoirs is supposed to be much larger than the one of the system, and thus the state of the reservoir is not changed during interaction.

Standard heat engines run cyclically between two classical thermal reservoirs at different temperatures. The engine reaches thermal equilibrium alternately with both of the two reservoirs, resulting in a thermal state at the reservoir temperature. But not all engines operate in such a thermal equilibrium regime.

For macroscopic systems the reservoirs are treated by their mean values. For micro- and nanoscopic systems, however, the substructure of the reservoirs has to be taken into account and leads to fluctuating interactions. The constructive role of thermal fluctuations is exploited, e.g., by molecular Brownian motors such as ratchets [Par02, Bro06, Hän09, Sei12]. Also engines operating with nanospheres have shown such fluctuations, as mentioned above [Mar16].

Furthermore, on the microscale there are diverse non-thermal energy sources available.



There are, for instance, biological motors such as myosin proteins, which are based on completely different mechanisms. They operate in contact with a single isothermal reservoir and are driven far from equilibrium by external energy input, such mechanical, photonic or chemical energy [Bro06, Hän09, Sei12]. Also synthetic molecular motors are usually driven by electrochemical processes or concentration gradients. Recently, a Stirling engine has been realized, operating between two bacterial reservoirs at the same temperature but with different concentrations of bacterias, achieving high efficiencies [Kri16]. Such engines are not bound anymore to limits which are based on the assumption of thermal reservoirs, such as the classical Carnot limit [Scu03, Dil09]. Even the efficiency at maximum power can reach unity for strong driving [Sei11, Bro12]. However, the condition of positive entropy production still limits the thermodynamic performance of non-thermal reservoirs.

For single trapped ions and other quantum systems, like cold atoms, nanomechanical oscillators and optomechanical systems, there is variety a different artificial and non-thermal reservoirs available [Poy96, Lüt98, Rab04, Tom12, Woo14]. In this context, it is convenient to regard the non-thermal reservoirs as perturbed thermal reservoirs, characterized by their temperature and additional properties, which characterize their deviation from equilibrium [Aba14]. Theoretical studies have indicated that the efficiency of an engine may be increased beyond the classical limits by coupling it to engineered non-classical or nonequilibrium reservoirs, such as quantum coherent [Scu03] or quantum correlated [Dil09] reservoirs. Recent experimental advances in reservoir engineering techniques provide the necessary tools to realize a bath-like environment for a trapped ion with a relaxation towards a non-thermal state [Mya00, Tur00b, Wan13b, Kie15].

### 1.5. Quantum thermodynamics and quantum heat engines

For small thermodynamic systems at the nanoscale and at low temperatures, quantum effects become important and have to be fully taken into account, for the systems as well as for the reservoirs [Mil16]. Consequently, the reservoirs provide quantum properties and transfer them to the system, if an appropriate coupling between both is established.

The emerging field of quantum thermodynamics is, on the one hand, an important notion for all quantum systems and the basis to understand their thermal interactions, such as equilibration and thermalization [Kos13, Vin15]. On the other hand, quantum systems can be used to perform thermodynamic experiments in order to study, e.g., quantum phase transitions or thermal energy transport [Ber13, Eis15]. Recently, tremendous progress was achieved in engineering reservoir interactions for quantum states [Mya00, Tur00b, Wan13b, Kie15]. However, the notion of thermodynamic limitations has to be altered for quantum systems. In certain settings the second law splits into a whole family of second laws in order to meet the various possible transformations [Bra15a].

If we push thermodynamics towards the quantum regime, new questions arise immediately: what impact do quantum effects have on the performance of heat engines? In the last few decades, an intense theoretical effort has been devoted to the investigation of the potential and the limitations of engines in the quantum regime, e.g. for spin systems [Gev92b] or for three level systems [Ali79, Gev96]. More concrete proposals for

quantum engines employ cold atoms [Fia12], opto-mechanical devices [Zha14a] or electronic quantum circuits [Esp10, Pek15]. In particular, theoretical studies have indicated that quantum engines may outperform their classical analogs and provide efficiencies beyond the limits of classical engines, thereby employing engineered quantum coherences [Scu03, Scu10, Hor13, Dor13, Los15], as well as entanglement and quantum correlations [Dil09, Hov13, Gal14] to fuel the engine. Specifically, the aspect of quantum refrigerators for cooling quantum systems efficiently has attracted great interest [Lin10b, Lev12b]. The existence of quantized energy states can be exploited to tailor the energetics of the cooling mechanisms [Kol12, Lev12a]. Even hot energy sources can be used to cool quantum system, similar to an absorption refrigerator [Mar12, Cle12, Lev12b]. Furthermore, the thermodynamic aspect of information processing becomes important for the operation of small-scale quantum engines [Par15, Goo16].

Despite the multitude of proposals and theoretical investigations, there is no experimental demonstration of a quantum heat engine. This fact is mainly due to the limitations of the individual experimental systems, or on account of technical difficulties in reaching the quantum regime. Recent progress in the degree of control has enabled first steps being taken now [Thi15, Bra13a], but still it is unclear what quantum effects should be probed. However, at the quantum limit we will meet severe challenges: a key issue is the reservoir interactions with the quantum system. On the one hand there is a hot bath, which should not heat the system beyond the limit of resolved quantum states. On the other hand there is a cold bath, whose temperature is strictly limited by the third law [Gem04]. These tight limits can be circumvented when using quantum states other than thermal states and neatly engineered reservoirs. However, the interaction of quantum states with any form of environment is challenging, since those states are extremely sensitive to disturbances and fluctuations and tend to lose their coherence [Fri15].

Preparing the way towards the first experimental realization of a heat engine which operates in the quantum regime and exploits non-classical energy sources is one of the major motivations of this thesis. With a single trapped ion we have a system at hand which is intrinsically a quantum system and which has a model character for other harmonic oscillator systems. Therefore, it represents a good starting point for further study of quantum engines.

## 1.6. Trapped ions as a model system

The trapping potential in a common Paul trap provides a quadrupolar spatial shape. Hence the motion of a trapped ion can be described by a harmonic oscillator to very good approximation [Lei03]. Therefore, trapped ions provide an ideal and general model for other oscillatory system, such as micro- and nano-mechanical oscillators [Kar09, O'C10, Lin10a, Fau12], offering a broad spectrum of potential applications. Further, trapped ions provide an exceptional degree of control in their preparation and manipulation, great precision in the measurement of their parameters [Lei03], and the capability of coupling to engineered reservoirs [Poy96, Mya00, Kie15]. They permit cooling to the ground state of motion and versatile state preparation by interaction with laser radiation. For these reasons, they have played a prominent role in the experimental study of quantum simulations [Bla12], as well as quantum computation and information processing applications [Häf08, Bla08, Mon13]. In the past years, they also became invaluable tools for the investigation of quantum thermodynamics [Haz12, Ulm13, Pyk13, Ram14, An15].

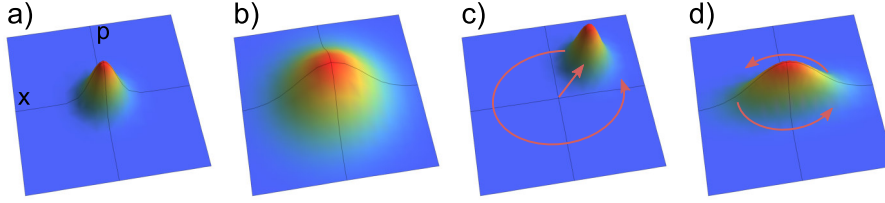


**Figure 1.3.** – Probability distribution of the relevant motional states of a single trapped ion in phase space (momentum – position) representation. (a) Cold thermal state of an ion at rest. The probability is distributed normally and centered at  $\{x = 0, p = 0\}$ . (b) Hot thermal state. The extent of the normal distribution increases with increasing temperature. (c) Coherent state. The distribution of the cold ion is displaced from the origin and rotates with elapsing time around it. In position space this corresponds to a sinusoidal oscillation. (d) Squeezed thermal state. The probability distribution is asymmetric and can be decomposed in two normal distributions with different widths along the two main axes in phase space. The state rotates with elapsing time, which corresponds to a breathing motion in position space.

The harmonic oscillator for a quantum system exhibits different states of motion, which represent the basis of our engine dynamics. Fig. 1.3 presents and compares the characteristics of different states of motion of the harmonic oscillator in phase space, which are relevant for the investigations throughout the present thesis: thermal states, coherent states and squeezed thermal states. When in contact with a thermal reservoir, the oscillator equilibrates towards a thermal state. It provides a thermal Boltzmann distribution for the individual phonon states, leading to a normal probability distribution in space and does not show any coherences or correlations. With higher temperature, the spatial extent increases. A coherent state corresponds to a harmonic oscillation of the ion in trapping potential and most closely resembles to a classical oscillation. A squeezed state provides a non-uniform distribution of its phase space quadratures,  $\Delta x \neq \Delta p$ . A squeezed thermal state is a thermal state whose circular phase-space distribution is *squeezed* to some degree to an elliptical shape with the same area.

## 1.7. Outline of the Thesis

This thesis is organized as follows: first, in Ch. 2, we give a short introduction to the general concept of the single-atom heat engine. We explain the fundamental coupling mechanism of individual degrees of freedom, which lead to the conversion of thermal energy into mechanical work. The fundamental considerations are accomplished by analytical and numerical investigations of the proposed engine system in Ch. 3. These studies demonstrate the feasibility of our engine system and define framework conditions for the following experiments. Thereby, we show how the engine may run at maximum output power and how non-thermal properties may be exploited to increase the conversion efficiency between input energy and output power. The experimental part starts with Ch. 4 and a detailed description of the experimental setup. This is followed by a characterization of the coherent motion and the effect of thermal excitation of the single trapped ion in Ch. 5 and Ch. 6, respectively. The first comprises a characterization of the ion trap and an analysis of the artificial dissipation in our system, while the latter treats heating and cooling processes of the ion, as well as the description of a specially developed thermometry technique. Finally, in Ch. 7, we present the realization of a

single-atom heat engine. We derive the working cycles of the engine from measured data and characterize the output power as well as the efficiency as a function of the temperatures of the individual heat baths. We end this thesis with Ch. 8 and an overview of future perspectives and possible applications of our engine system.



# 2

## General concept of the single-atom heat engine

This chapter gives a general overview of the fundamental principles of the single-ion heat engine. We first take a closer look at the laws of thermodynamics, focusing on their implications on the single-atom heat engine. In the following we present two of the most prominent types of engine cycles: the Otto cycle and the Stirling cycle. Both will be used to characterize our numerical and experimental findings in the course of this thesis. We introduce relevant characteristics of heat engines, namely power and efficiency, and discuss their limitations. In a second part we focus on the trapped ion system and present the central element of our engine, the funnel-shaped trapping potential. With this at hand, we give a short overview of the concrete working procedure of the single-ion heat engine. Finally, we end this chapter with a discussion of the reduced level scheme of  $\text{Ca}^+$  ions, which we use as working agent in our engine.

### 2.1. The laws of thermodynamics

The four laws of thermodynamics provide a framework, within which thermodynamic processes take place. They are defined as axioms, based on phenomenological findings. Their formulation uses terms like *system* and *environment*, where the latter usually acts as a thermal reservoir to the system. However, in realistic situations the dividing-lines between system, environment and the surrounding universe are blurred. In general, the reservoirs are assumed to be large enough such that the thermodynamic laws are fulfilled, but strictly speaking the entire universe accounts for thermodynamic balances. The framework of thermodynamics is a self-consistent and independent physical theory, only based on the assumptions of the following four laws.

#### 2.1.1. Zeroth law: thermal equilibrium

If two thermodynamic systems  $A$  and  $B$  are each in thermal equilibrium with a third system  $C$ , then  $A$  and  $B$  are in thermal equilibrium with each other [Max71]. This equivalence relation implies the foundation of the universal temperature  $T$  and does explicitly not depend on the specifications of the bodies  $A$ ,  $B$  and  $C$  or any other parameters. The temperature is defined as the intensive variable of state which is equal for two systems, if they are in thermal equilibrium [Cal85, Atk10].



### 2.1.2. First law: energy conservation

Energy can only be transformed from one form to another form, it cannot be created or destroyed. The internal energy  $U$  is the extensive variable of state which accounts for the total energy available for thermodynamic transformations. In this context, the first law says that the internal energy is changed by the balance of heat  $Q$  and work  $W$  contributions,

$$\Delta U = \delta Q + \delta W, \quad (2.1)$$

and is constant for any isolated system. This law establishes  $Q$  and  $W$  as different, but equivalent modes of energy transfer, and implies the conversion of one into the other. Note, that  $Q$  and  $W$  are no state variables but describe a flow of energy, they denote processes not objects. The added heat  $\delta Q = m c \Delta T$  is the amount of thermal energy that changes the temperature of a body with mass  $m$  and heat capacity  $c$  by  $\Delta T$ . The work  $\delta W = -F \Delta s$  is the mechanical energy input that moves a body by  $\Delta s$  against an external force  $F$ . The conversion of one into the other is the basis of all thermal machines.

Furthermore, the conservation of energy implies the non-existence of perpetual motion machines, which generate more energy than they consume.

### 2.1.3. Second law: entropy

Clausius expressed the second law in terms of a defined direction of heat flow [Cla67], saying that

*"Heat never passes spontaneously from a cold to a hot reservoir, without work being done on the system".*

Thereby, this statement introduces irreversibility as a fundamental asymmetry in nature. The state variable entropy  $S$  is changed by a heat flow and formally expressed in the Clausius inequality,

$$\Delta S \geq \frac{\delta Q}{T}, \quad (2.2)$$

where the equality applies to fictive reversible processes. Including the entropy, the Clausius statement says that all spontaneous processes in isolated systems lead to an increase of its entropy.

Regarding the operation of thermal machines, this statement claims that the heat sink is as important as the heat source. According to Eq. (2.2), the entropy of the heat source is reduced when heat flows out. As a consequence, a cold reservoir is required, where a part of the heat must flow in to increase the entropy to at least the same amount. This finding has led to the formulation of the second law by Kelvin and Planck [Wer66]:

*"It is impossible to devise a cyclically operating device, the sole effect of which is to absorb energy in the form of heat from a single thermal reservoir and to deliver an equivalent amount of work".*

Thus the positivity of entropy production limits the performance of heat engines, as it is impossible for any engine to convert heat into work entirely. The limits of validity of the second law of thermodynamics, especially in terms of information theory, have been pointed out by Maxwell [Max71], Szilard [Szi29], Landauer [Lan61] and others early on, but are subject to intensive discussions until today [Par15, Goo16].

Note, that the given definitions apply to purely thermal, classical and macroscopic systems, based on state variables such as temperature, energy or entropy, which are defined as mean values of large atomic ensembles.

#### 2.1.4. Third law: absolute zero

The temperature provides a lower limit, its absolute zero  $T \rightarrow 0$  K, a state with the minimum possible energy. However, this state is not attainable by a finite number of cyclic processes, as recognized by Nernst in 1905 [Ner69]. The third law defines an absolute reference for the temperature scale as well as for the entropy, since the absolute zero of temperature equals the zero point of entropy,  $S \rightarrow 0$ . To be more precise, for quantum systems with degenerate ground states with multiplicity  $q$ , the lowest entropy equals  $S_0 = k_B \ln q$ .

For more than a century the quest for absolute zero fascinated many researchers. In recent years this topic has seen a revival in the context of quantum thermodynamics [Rez09, Rai11, Kol12, Tor13]. Indeed, having temperatures of physical systems approaching absolute zero is crucial to modern quantum experiments. To identify the optimal cooling rates close to absolute zero, quantum machines and, in particular, quantum refrigerators play an important role [Lev12a].

## 2.2. Thermodynamic cycles of heat engines

Heat engines are cyclic operating systems, which convert a temperature difference between two thermal reservoirs to some amount into mechanical work. Thereby a working agent passes a thermodynamic cycle, where thermalization with reservoirs and free evolution processes alternate. During such cycles, the agent exchanges heat and work with the environment. The system acts as a heat engine if the work output dominates the work consumption, powered by a net heat absorption. It acts as a heat pump if a net amount of work is consumed in order to generate a heat output larger than the heat input.

The internal energy of a system is expressed as a product of a conjugate pair of an intensive and an extensive state variable, like for a classical macroscopic system pressure and volume (mechanical quantities) or temperature and entropy (thermal quantities) [Cal85, Atk10]. Using such pairs for a representation of a thermodynamic cycle leads to a clear formal description, where the area of the cycle equals the net mechanical work produced. From the relevant pairs of conjugate variables, all thermodynamic properties can be derived.

In view of the large number of different combinations of thermodynamic processes, we can define different idealized cycles, usually named after their inventor. For a clear description of the idealized processes, the cycles usually are defined such that one state variable is kept constant during this process. For real engines, the thermodynamic cycles may deviate significantly from their idealized counterparts. In the course of this thesis the Otto cycle and the Stirling cycle will play a major role.

### 2.2.1. The Otto cycle

The idealized Otto cycle consists of four individual processes [Cen15]. Heating and cooling processes are much faster than the dynamics of the piston and the system is isolated from the environment during the free evolution processes. These assumptions lead to a clear separation of the individual strokes. The Otto cycle describes most spark-ignition internal-combustion engines, such as car engines. It consists of two isochoric temperature changes, where heat is transferred between the agent and the reservoirs at

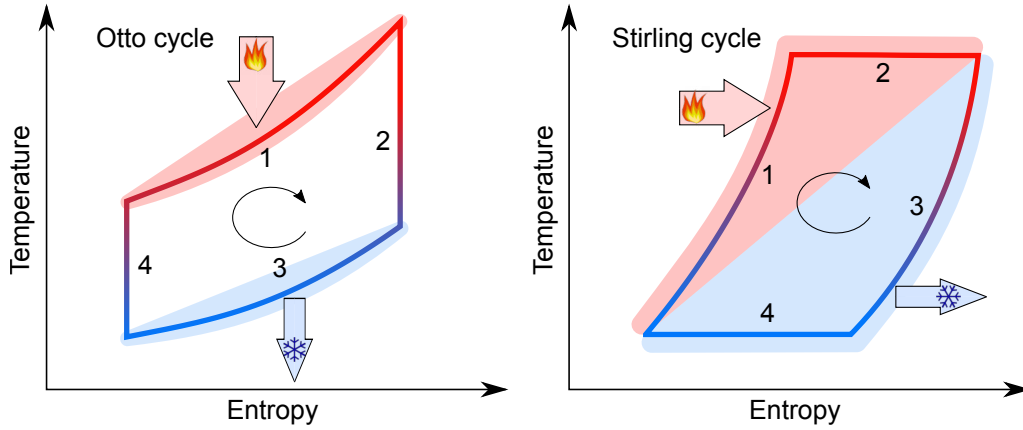


**Figure 2.1.** – Temperature – entropy diagrams for thermodynamic cycles. *Otto cycle:* (1) The hot reservoir (red shaded) supplies heat to the working agent, temperature and entropy increase at constant volume. (2) The system is isolated from the environment and expands freely at constant entropy, increasing its volume. The engine performs work. (3) The remaining heat is dumped in the cold reservoir (blue shaded) at constant volume, temperature and entropy decrease. (4) The working agent is compressed at constant entropy, work is performed on the system. *Stirling cycle:* (1) see Otto cycle. (2) The system expands while in thermal equilibrium with the hot bath, increasing volume and entropy. The engine performs work. (3) see Otto cycle. (4) The system is compressed while in contact with the cold bath, work is performed on the system. The area of the cycles correspond to the net amount of work produced during each cycle.

constant volume, and two isentropic processes, where the system is isolated from the environment and changes its volume at constant entropy. The latter are supposed to be adiabatic and reversible processes. During the expansion phase the agent moves a piston and thus performs work, while during the compression phase work is consumed to compress the agent by a displacement of the piston. Since the expansion occurs at higher pressure and temperature than the compression, the amount of generated work exceeds the work consumed. For details see Fig. 2.1 (a).

A main characteristic of the Otto cycle is the clear separation of defined reservoir interactions and free evolution processes, which applies well to the situation of a single trapped ion. The ion is suspended in vacuum and generally isolated from external influences, allowing for adiabatic processes. Thermal interactions occur deliberately through controlled interactions with laser beams and electric field noise. Therefore, theoretical and analytical investigations of our system concentrate on the Otto cycle.

### 2.2.2. The Stirling Cycle

The experimental realization of the single-atom heat engine will be described by a Stirling cycle [Fin01]. The Stirling engine is an idealized model for external combustion engines. As compared the Otto cycle, in a Stirling cycle the working agent is coupled permanently to one of the heat baths. Therefore, the isentropic processes are replaced by isothermal processes. During the expansion stroke, heat is absorbed and work is generated simultaneously. The compression stroke is the inverted process, where the agent consumes work and dispenses heat. Fig. 2.1 compares the Stirling cycle to the Otto cycle. As we will show in Sec. 7.4, the ion will be permanently coupled to one of the heat baths for technical reasons, and thus a description by a Stirling cycle is appropriate.

## 2.3. Power and efficiency

For a practical application of heat engines, the key characteristics are power and efficiency. Power is the net work of the engine per cycle, divided by the duration for one revolution,  $P = W / \tau_c$ . The work is the amount of mechanically usable energy, which is able to drive a mechanical load. The ability of extracting the generated work from the engine system and transferring it to a load is a crucial issue for nano-sized heat engines. In contrast to most of the nano-engine systems, we will show that our single-ion setup provides the intrinsic feature to transfer the work produced to a separate mode of oscillation and to store the energy in its amplitude. However, in this thesis we demonstrate the working principles of a single-ion engine without using the stored work in a mechanical sense, but dissipating it in order to measure and to characterize it.

The efficiency of an engine is the relative amount of thermal energy which is absorbed from the hot reservoir and converted into mechanical work,  $\eta = -W / Q_h$ ; the remaining heat is dumped in the cold reservoir. Note, in this respect, that positive signs for heat and work imply an energy flow from the environment to the engine system, while negative signs signify that energy flows from the system to the environment.

One of the basic and important assumptions in thermodynamic balances is that the reservoirs are given and the energetic costs for preparing them are not taken into account [Cal85, Cen15]. If these costs would be included, for instance in the calculation of efficiencies of heat engines, the energy conservation in the entire universe would lead to a vanishing efficiency for any engine: a reservoir can't provide more energy than it costs to prepare the reservoir. This is similar for car engines, where the energetic costs for generation, pumping and refinement of oil are not taken into account.

### 2.3.1. Carnot efficiency

Sadi Carnot showed already in 1824 that the efficiency of any cyclic operating engine is limited and that the maximum efficiency solely depends on the temperatures of the hot and the cold reservoir, not on working fluid nor the characteristics of the cycle [Car24]:

*"The motive power of heat is independent of the agents employed to realize it; its quantity is fixed solely by the temperatures of the bodies between which is effected, finally, the transfer of caloric<sup>1</sup>"*

The Carnot principle is a direct result from the second law of thermodynamics,  $\Delta S \geq Q/T$ . If we neglect internal losses, the generated work is the difference between the heat absorbed and the heat emitted,  $-W = Q_h + Q_c$ , and the efficiency reads

$$\eta = \frac{-W}{Q_h} = \frac{Q_h + Q_c}{Q_h}. \quad (2.3)$$

After one passage of the cyclic process, the total entropy of the environment, namely of the two reservoirs, must increase, which restricts the amount of heat exchanged with the reservoirs,

$$\oint dS = \Delta S_h + \Delta S_c = -\frac{Q_h}{T_h} - \frac{Q_c}{T_c} \geq 0 \quad \Rightarrow \quad Q_c \leq -Q_h \frac{T_c}{T_h}, \quad (2.4)$$

<sup>1</sup> Nowadays, we call the *motive power of heat* the maximum efficiency of a cyclic and reversible engine, and the notion of *caloric* corresponds to the exchange of heat.

## 2. General concept of the single-atom heat engine

---

where the equal sign corresponds to reversible processes. Inserting Eq. (2.4) in Eq. (2.3), we obtain the range of possible efficiencies

$$\eta \leq 1 - \frac{T_c}{T_h}, \quad (2.5)$$

where the Carnot efficiency  $\eta_C = 1 - T_c/T_h$  represents the upper bound.

### 2.3.2. Efficiency at maximum power

For theoretical investigations,  $\eta_C$  is an interesting characteristic of any engine system. However, for the Carnot cycle the total entropy of the system and its environment remains constant after one revolution,  $\oint dS = 0$ . The cycle then has to be an entirely reversible and quasistatic process. This means that the heat baths have to be infinitely large and the thermalization processes infinitely slow, resulting in a vanishing power output of the engine. For real engines, the thermalization processes are irreversible and the cycles are optimized for maximum power output. As a consequence, to maximize the power of an engine, efficiency is sacrificed; the power, not the efficiency, is optimized for practical purposes.

The endoreversible model is a minimal extension of the Carnot cycle where the internal dynamics of the engine are supposed to be reversible but the heat transfer is irreversible [DV95]. Formally, we introduce a thermal conductor which is in contact with the hot bath at  $T_h$ . Due to its finite heat capacity  $g$ , the other end of the conductor, which is in contact with the engine, provides a lower temperature  $T'_h < T_h$ . The heat flux through the conductor then is

$$Q_g = g(T_h - T'_h). \quad (2.6)$$

This heat is provided to the engine,  $Q_g = Q_h$ . The engine converts  $Q_h$  into work generates a work output according to Eq. (2.3) and using Eq. (2.5)

$$-W = \eta Q_h = g \left( 1 - \frac{T_c}{T'_h} \right) (T_h - T'_h). \quad (2.7)$$

We optimize the output power with respect to the variable temperature  $T'_h$  and find the optimality condition

$$\frac{dW}{dT'_h} = 0 \quad \Rightarrow \quad T'_h = \sqrt{T_h T_c}. \quad (2.8)$$

Supposing a reversible engine,  $\eta = 1 - T_c/T'_h$ , the condition Eq. (2.8) results in the efficiency at maximum power [Lef87]

$$\eta^* = 1 - \sqrt{\frac{T_c}{T_h}}, \quad (2.9)$$

with a maximum work output of  $-W_{max} = g(\sqrt{T_h} - \sqrt{T_c})^2$ . The expression Eq. (2.9) is commonly attributed to Curzon and Ahlborn, who derived it in 1975 [Cur75], although it has been calculated by Yvon [Yvo55], Novikov [Nov58] and Chambadal [Cha58] independently twenty years before. However, throughout this thesis we will follow the majority and refer Eq. (2.9) to as Curzon-Ahlborn efficiency. It is interesting to note that this efficiency relation is independent of the kind of thermodynamic cycle or the nature of the working agent, but only depends on the temperatures of the heat baths.

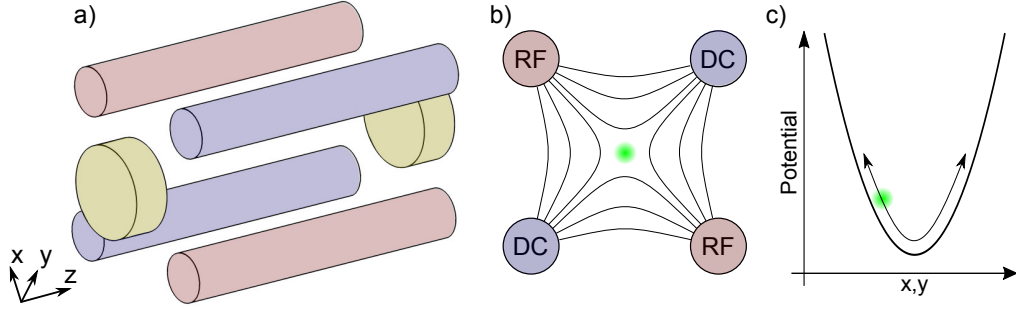


**Figure 2.2.** – The linear Paul trap. (a) Geometry comprising two endcaps and four elongated rod-electrodes. The endcaps (yellow) are grounded or biased with DC voltages. Usually, two opposing radial electrodes (red) provide an oscillating voltage, while the other two electrodes (blue) are grounded. (b) Electric field lines in the  $(x,y)$ -plane. The oscillating quadrupole field is confining the ion in the center of the trap. (c) The mean potential, arising from the oscillating fields, provides a harmonic confinement in the  $(x,y)$ -plane. The ion oscillates with  $x,y(t) \propto \sin(\omega_{x,y}t)$ , where the trap frequencies  $\omega_{x,y}$  depends on the strength of the trapping potential.

## 2.4. A funnel-shaped ion trap

### 2.4.1. The harmonic trapping potential

In Paul traps the ions are spatially confined by a combination of static and oscillating electric fields [Pau90, Lei03]. The most widespread kind of an ion trap is a linear Paul trap, where the trapping potential is rotationally symmetric and the equipotential planes provide ellipsoidal shapes. A simple design of a linear Paul trap is shown in Fig. 2.2 (a). It consists of two endcaps and four elongated electrodes in a parallel and symmetrical arrangement. To fulfill the Laplace equation  $\Delta\Phi = 0$  for the trapping potential  $\Phi$  inside the trap, a combination of static and oscillating electric fields is mandatory [Lei03]. A constant voltage is applied to the endcaps and provides a static confinement in  $z$ -direction (hereinafter referred to as *axial*). In the  $x,y$ -plane (referred to as *radial*) the symmetrical arrangement of the electrodes leads to an electric quadrupole field, see Fig. 2.2 (b). Applying an oscillating voltage with an amplitude  $U_{\text{rf}}$  at a radio-frequency  $\Omega_{\text{rf}}$  to two opposing electrodes leads to an oscillating saddle potential

$$V_{\text{rf}}(t) \propto \frac{U_{\text{rf}}}{r_0^2} \sin(\Omega_{\text{rf}} t) \cdot (x^2 - y^2), \quad (2.10)$$

where  $r_0$  is the distance of the electrodes to the trap axis. Due to the parabolic shape of the potential, the focusing force which drives the ions towards the minimum of the potential is always stronger than the defocusing force, similar to the *strong focusing* effect [Cou53]. Averaging over the fast oscillations of  $V_{\text{rf}}(t)$  leads to a linear ponderomotive restoring force

$$\vec{F}(t) = m \frac{d^2 \vec{x}(t)}{dt^2} = -\alpha \vec{x}(t), \quad (2.11)$$

proportional to the displacement  $\vec{x}$  from the coordinate origin and where  $m$  is the mass of the particle and  $k$  a constant relative to the potential strength [Lei03]. As a consequence of  $\vec{F} = -\nabla\Phi$ , the ion behaves like being trapped in a static harmonic potential in all

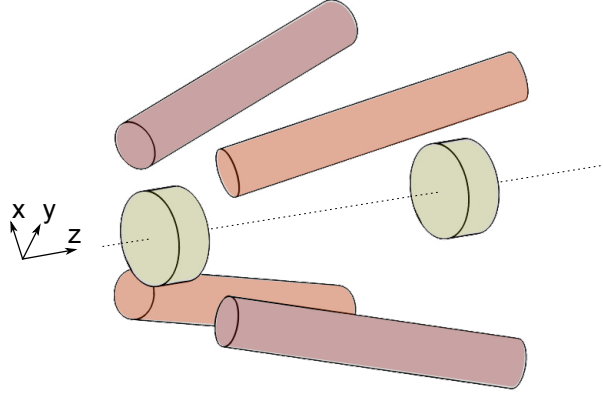


**Figure 2.3.** – Geometry of the funnel-shaped Paul trap. It provides an angle  $\theta$  between the rod electrodes and the trap axis  $z$ . To avoid massive axial micromotion resulting from the tapered geometry, we apply the same oscillating voltage signal to each pair of opposing electrodes (red and orange) but with inverted sign, see text. The endcaps (yellow) are biased with individual DC voltages.

three dimensions

$$\Phi_p = \frac{1}{2} \left( \alpha_x x^2 + \alpha_y y^2 + \alpha_z z^2 \right), \quad (2.12)$$

see Fig. 2.2 (c). Since  $\Phi_p$  is not a solution of the Laplace equation, it is often referred to as pseudo-potential. The solution of the equation of motion,

$$m \frac{d^2 \vec{x}(t)}{dt^2} = -\vec{\nabla} \Phi_p, \quad (2.13)$$

is a three dimensional harmonic oscillation  $x_i(t) = \sum_i A_i \cos(\omega_i t + \phi_i)$ , with independent oscillating frequencies  $\omega_i^2 = \alpha_i / m$  in all dimensions  $i \in \{x, y, z\}$ . If we introduce artificial friction to the system, the equation of motion is expanded by a term which takes into account the velocity dependent loss of energy. Additionally the system may be driven by an external and time dependent force  $F_d(t)$ , resulting in an inhomogeneous differential equation,

$$\frac{d^2 x}{dt^2} + 2\gamma \frac{dx}{dt} + \omega^2 x = F_d(t), \quad (2.14)$$

with damping coefficient  $\gamma$ . For a weakly damped harmonic oscillator ( $\gamma \ll \omega_z$ ) the dynamics of the ion are described by a modified oscillation frequency  $\omega_d^2 = \omega^2 - \gamma^2$ .

#### 2.4.2. The tapered potential

In this work we employ a specially designed linear Paul trap with a tapered geometry. In this design, the radial trap electrodes provide an angle  $\theta$  with respect to the trap axis  $z$ , resulting in a funnel-shaped geometry which is sketched in Fig. 2.3. While in axial direction the static confinement stays unchanged, we reach a dynamic confinement of the ion in the radial directions through a modified oscillating parabolic saddle potential of the form

$$V_{\text{rf}}(x, y, z, t) \propto \frac{U_{\text{rf}} \sin(\Omega_{\text{rf}} t)}{(r_0 + z \tan \theta)^2} \cdot (x^2 - y^2) + \frac{U_{\text{dc}}}{z_0^2} \cdot z^2. \quad (2.15)$$

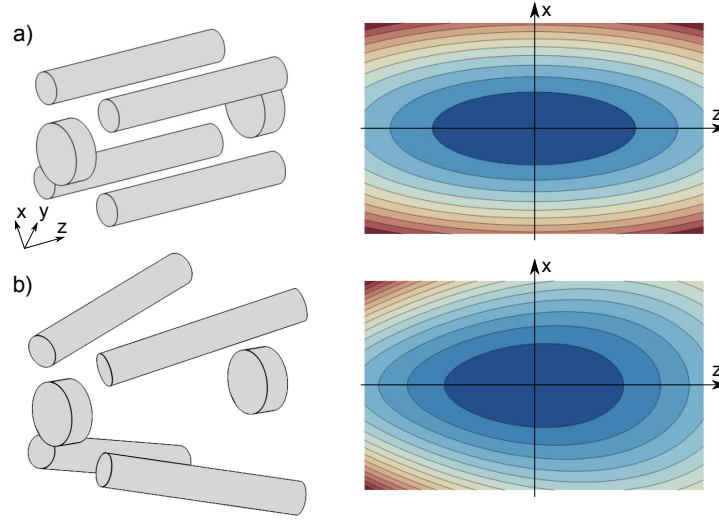


**Figure 2.4.** – Cross sections of the trapping potential  $(x,z)$ -plane. (a) Trapping potential in a linear Paul trap. The radial confinement ( $x$ -direction) results from fast oscillating voltages. The axial confinement ( $z$ -direction) stems from a combination of the oscillating potential and static fields. A harmonic confinement in all directions is achieved. (b) The funnel-shaped trap geometry results in a tapered trapping potential. The equipotential planes provide an "egg" shape. Such a trapping potential leads to a radial trap frequency which depends on the axial position, and hence to a coupling between the radial and axial degree of freedom.

This oscillating potential has a tapered shape and depends on the angle  $\theta$ .  $U_{\text{rf}}$  and  $U_{\text{dc}}$  are the oscillating and static voltages on the trap electrodes, respectively, while  $r_0$  and  $z_0$  are the distances of the electrodes from the center of the trap. The funnel-shaped geometry of the trap design leads to a ponderomotive potential of the form

$$\Phi_p(x,y,z) = \frac{m}{2} \frac{(\omega_{0x}^2 x^2 + \omega_{0y}^2 y^2) r_0^4}{(r_0 + z \tan \theta)^4} + \frac{m}{2} \omega_{0z}^2 z^2, \quad (2.16)$$

which is compared with the potential of linear trap in Fig. 2.4. As compared to a linear trap, the modified trap design leads to a conical structure of the equipotential planes and creates an effective coupling between the axial and radial degree of freedom. Comparing Eq. (2.16) to Eq. (2.12), it results in radial trap frequencies  $\omega_r(z)$  that depend on the axial position  $z$  according to

$$\omega_r(z) = \omega_0 \left[ 1 + (z - z_0) \frac{\tan \theta}{r_0} \right]^{-2}. \quad (2.17)$$

In the heat engine experiments, this dependance is essential to implement compression and expansion phases in the radial direction, while the ion moves back and forth along the trap axis.

### 2.4.3. Origin and reduction of micromotion

Superimposed to the harmonic secular motion, an ion confined in a Paul trap may exhibit a so-called micromotion [Lei03]. This is a fast oscillation which originates from the time-dependent oscillating saddle potential in Eq. (2.10). Consequently, the micromotion shows a frequency of  $\Omega_{\text{rf}}$ , which is generally much faster than the secular motion. The



amplitude of this micromotion depends on the distance  $r$  of the ion from the trap axis and vanishes for  $r = 0$ . However, due to inaccuracies in the trap geometry or external electric stray fields, the node of the effective trapping potential can deviate from the node of the oscillating electric quadrupole field, resulting in a non-vanishing amplitude of the micromotion. This excess motion can be compensated by applying additional static electric fields in the radial directions.

Linear Paul-traps are usually operated in a configuration, where the electric rf-signal is fed to two opposing trap electrodes, while the two remaining electrodes are connected to ground or biased with a constant voltage, see Fig. 2.2. If the ion is not perfectly centered with respect to the field lines, this leads to an additional micromotion in axial direction. The reference voltage of the ion at the node of the trapping potential is oscillating with the frequency of the rf-signal and half of its amplitude. As a consequence, the ion experiences an effective rf-signal originating from the static voltage of the end-caps, leading to an additional confinement in axial direction, as well as to micromotion in this degree of freedom. Usually, for linear Paul-traps, this axial micromotion vanishes if the ion is kept in the node of the oscillating saddle potential [Ber98]. However, in our case, due to the tapered geometry, there is a strong component of the oscillating field in axial direction, which leads to a macroscopic micromotion on the order of  $10 \mu\text{m}$  for low trap frequencies, see [Tol14]. Such a strong micromotion could conceal the expected heat engine dynamics. In order to mitigate the axial micromotion, we apply an rf-signal to all of the four electrodes: each pair of opposing electrodes is supplied with the same voltage signal,  $V(t) = \pm V_0 \sin(\Omega_{\text{rf}} t)$ , while the sign is reversed between both pairs as sketched in Fig. 2.3. This results in a static reference voltage of the ion at the node of the trapping potential, which is equal to the reference level of the static and oscillating voltages. As a consequence, the axial micromotion vanishes completely if the ion is centered at the node of the oscillating quadrupole field.

### 2.5. Working cycle of the single-atom heat engine

The fundamental principle can be described by analyzing the forces acting on the ion. In our case, the thermal energy during the operation of the engine is high compared to the energy spacing of the quantized harmonic oscillator states ( $k_B T \gg \hbar\omega_r$ , weak binding regime), thus a classical description of the dynamics is appropriate. We assume the ion to have minimized its potential energy in the trap, and thus all external forces are in equilibrium. Heating and cooling processes lead to thermal states with different temperatures  $T$ , providing a time-averaged spatial distribution described by

$$\zeta_r(r, T) = \frac{1}{2\pi\sigma_r^2(T)} \exp\left[\frac{-(r - r_0)^2}{2\sigma_r^2(T)}\right]. \quad (2.18)$$

The time-averaged width  $\sigma(T)$  of this two-dimensional Gaussian probability distribution depends on the temperature  $T$  according to

$$\sigma_r(T) = \sqrt{\frac{k_B T}{m\omega_r^2}}. \quad (2.19)$$

The heat engine is driven by alternately heating and cooling the ion in radial direction. We assume to have heat baths at hand to change the temperature of the radial thermal

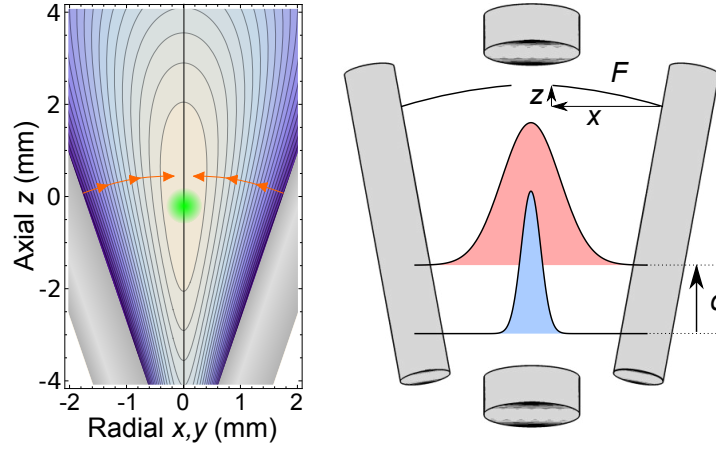


**Figure 2.5.** – Conversion of heat into work. (a) The ponderomotive potential in between the tapered trap electrodes (gray). The thermal probability distribution of the ion (green, not to scale) provides a finite and temperature dependent extent in radial direction. The radial restoring force (orange arrows), which originates from the ponderomotive potential, has an axial component for a non-zero radial distance from the trap axis, see text. (b) When a cold ion (blue) is heated, the radial extent of the thermal distribution increases and therefore the axial component of the radial restoring force rises. This leads to a shifted equilibrium position for a hot ion (red) as compared to a cold ion (blue).

state of the ion in a controlled way. Later, in the experimental part in Sec. 6.1, we will prove that this is achieved by exposing the ion to a combination of laser cooling and electric field noise [Tur00a]. Heating and cooling changes the spatial width  $\sigma_r(T)$  of the radial thermal state  $\xi_r(r, T)$ . Owing to the geometry of the trap, the gradient of the funnel-shaped pseudo-potential  $\Phi_p$  has a component in the axial direction  $z$ , that depends on the radial position  $r$ , see Fig. 2.5 (a).

Due to the tapered ponderomotive potential the restoring force  $F$  for an ion at a non-zero radial distance  $r$  from the trap axis has a component in axial direction, which rises with increasing  $r$ . It is obtained as the derivative of the ponderomotive potential  $\Phi_p$ ,

$$F_z(r > 0) = -\frac{d\Phi_p(r, z)}{dz} \neq 0. \quad (2.20)$$

As a consequence of the width of the radial thermal state  $\xi_r(r, T)$ , an ion centered at the trap axis is exposed to an additional force in axial direction. Consequently, the equilibrium position of the ion is shifted along the trap axis, see Fig. 2.5 (b). By integrating over the radial spatial distribution we obtain the temperature dependent force

$$F_z(T) = -\int_0^{2\pi} \int_0^\infty \xi_r(r, T) \frac{d\Phi_p(r, z)}{dz} r dr d\phi = \frac{4k_B r_0^4 \tan \theta}{(r_0 + z \tan \theta)^5} T. \quad (2.21)$$

This axial force  $F_z(T)$  is the basis of the conversion of a temperature difference into mechanical motion.

In the following, we analyze the dynamics of the ion when driven in a four stroke thermodynamic cycle, as shown in Fig. 2.6. During the first part of the cycle the ion is heated and the width  $\sigma_r(T)$  increases. As a result, during the second step, the ion moves along the  $z$ -axis to a weaker radial confinement. The displacement within the axial potential increases the total potential energy of the ion and work is produced. During

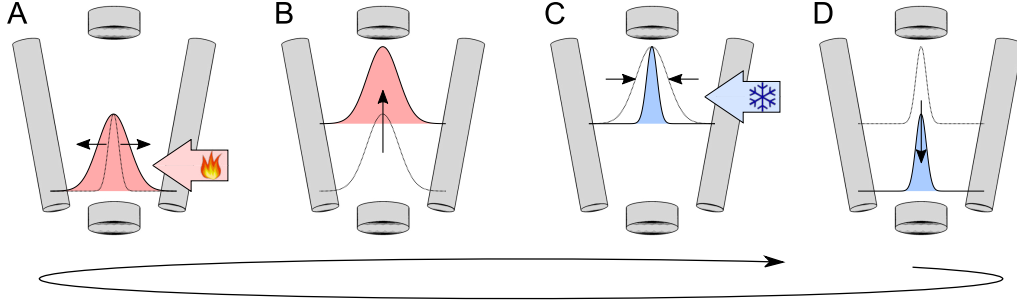


**Figure 2.6.** – Working principle of the single-ion heat engine driven in four consecutive strokes of an Otto cycle. (A) An initially cold ion is heated and the width of its probability distribution expands. (B) The increased spatial width in radial direction leads to a shift of the ion along the trap axis to the open end of the trap. (C) Cooling the ion reduces the radial width of its probability distribution. (D) Due to the restoring force of the axial potential, the ion moves back to its initial position. The thermodynamic cycle is closed and may be repeated.

the third step the ion is cooled to the initial temperature. The radial width  $\sigma_r(T)$  and the corresponding force  $F_z$  decreases. Owing to the restoring force of the axial potential the ion moves back to its initial position.

The combination of the heating and cooling processes give rise to a closed thermodynamic cycle, see Fig. 2.6. However, a typical heating and cooling of  $\Delta T = 10^{-2}$  K leads to a force in axial direction of the order of  $F_z = 10^{-22}$  N, with a corresponding static displacement of the order of  $z = F_z / (m \omega_z^2) = 10^{-8}$  m. However, it is desirable to increase the displacement  $z$  of the ion, in order to achieve stronger compression and expansion of the radial mode, as well as to facilitate the detection of the axial motion. To this end, we switch between heating and cooling periods with precise timing, such that the cycle repeats itself at a rate equal to the axial trap frequency  $\omega_z$ . Due to Eq. (2.21), the resulting modulation of the temperature  $T(t)$  leads to a periodic force  $F_z(t)$  in the axial direction. The engine therefore effectively drives a harmonic oscillation in the axial direction. The work produced in each cycle is thus resonantly transferred to the axial degree of freedom and the energy is stored in the amplitude of the  $z$ -oscillation.

However, the essentially frictionless nature of the system leads to an ever increasing oscillation. In order to contain this oscillation, we provide adjustable damping to the axial mode. A steady state operation is reached when the work generated by the engine is balanced by the energy dissipated by the controlled damping.

For future applications and more complex engine systems, the storage of the generated work in an independent degree of freedom is very important. This storage mode can be seen as a flywheel, as sketched in Fig. 2.7, where other oscillatory systems may be coupled to, in order to be driven by the engine [Aba12].

## 2.6. Laser cooling

One of the most fundamental processes within this work is laser cooling and the interaction of a trapped ion with coherent radiation. Photons with an energy  $E_\gamma = \hbar\omega$  can drive transition of the electrons between individual energy eigenstates of the atomic shell, if  $E_\gamma$  matches the transition energy  $\Delta E$ . If the ion is in motion with a velocity  $v$ , the Doppler effect shifts the resonance frequency  $\omega_0$  by  $\Delta\omega = \omega_0 v/c$ , with  $c$  being

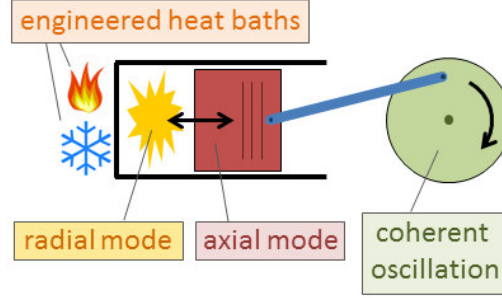


**Figure 2.7.** – Sketch of the mechanical analog of the single atom heat engine: a cylinder with a piston and a flywheel. The working agent is the radial mode of the ion (corresponding to the gas mixture), interacting with engineered reservoirs (ignition and thermalization). The expansion of the radial mode leads to a displacement of the ion in axial direction (piston). The work produced is stored in the energy of the coherent axial oscillation (flywheel).

the speed of light. By detuning  $E_\gamma$ , only the ions with the appropriate velocity class are resonant to  $E_\gamma$ . We can tune the frequency of the laser such that photons are only absorbed, if the ions are moving towards the laser source. Thereby, each absorption process reduces the momentum  $p$  of the ion by the photon momentum,  $p' = p - \hbar k$ . The subsequent spontaneous emission is isotropic, and thus the momentum transfer averages out after many scattering events. The result is a reduced kinetic energy of the ion. Since this cooling process is based on Doppler-shifted resonances, it is often referred to as Doppler cooling. For more details of the fundamental processes of Doppler cooling, refer to [Ste86a] and [Met99].

As the ion is trapped in a harmonic potential, it performs oscillations and thus a single laser beam is sufficient to cool all degrees of freedom [Lei03]. To cool an ion from room temperature to rest, on the order of  $10^4$  photon scattering events are needed. This number reveals the need for short lived cycling transitions for laser cooling thermal ions efficiently. However, a short lifetime  $\tau$  causes a broad resonance of the electronic transition,  $\Gamma = 1/(2\pi\tau)$ . This limits the effective cooling for ions with low temperatures, since ions moving in the same direction as the photons provide a finite absorption probability and therefore are accelerated. For a two level system, and neglecting the linewidth of the lasers as well as micromotion, the highest cooling rate is obtained for a detuning of the laser frequency from resonance of  $\Delta\omega/2\pi = -\Gamma/2$ , and the resulting minimum temperature, the Doppler cooling limit, is [Ste86a]

$$T_D = \frac{\hbar \Gamma}{2 k_B}, \quad (2.22)$$

where  $k_B$  is the Boltzmann constant. However, in most experiments, the atomic level structure is more complex than a two level atom, the laser linewidth is not negligible and micromotion generates sidebands of the resonances. As a consequence, the theoretical limit  $T_D$  is usually not reached [Cir94a].

In order to cool trapped ions further down towards the ground state of motion, resolved sideband cooling or electromagnetically induced transparency cooling may be employed [Die89, Roo00, Lei03].

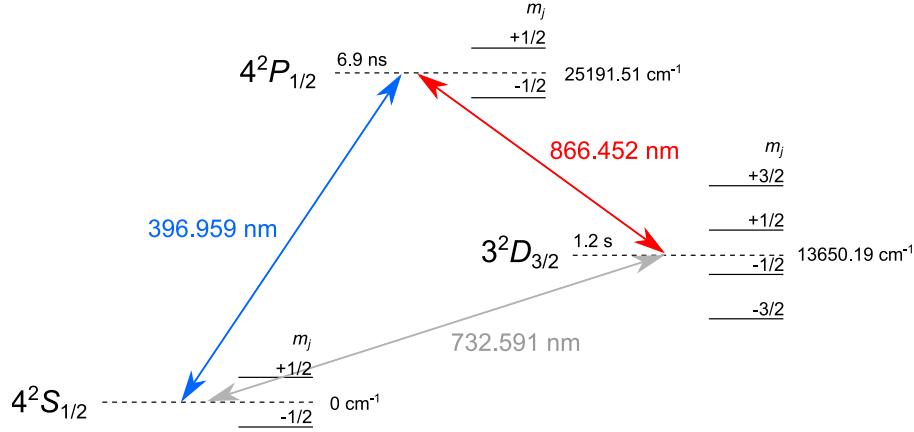


**Figure 2.8.** – The relevant part of the energetic level scheme of  $^{40}\text{Ca}^+$  reduces to a three level system. The individual levels are shown together with their radiation lifetime and their total energy in terms of their wavenumber. The transitions between the indicated levels are shown as well. The colored transitions are driven by light fields. The spacing of the energy levels is not drawn to scale.

## 2.7. The calcium ion

In order to reduce the experimental complexity and to achieve good conditions for laser cooling, earth-alkali ions are usually used in Paul-trap experiments. Their level scheme is similar to alkali-atoms, having one single valence electron in an S-state above a closed shell. Additionally, atoms without nuclear spin and thus without hyper-fine structure are favorable. In our experiments we use  $^{40}\text{Ca}^+$  ions, which have an electronic ground-state configuration of the closed electron shell of Argon with one additional S electron,  $[\text{Ar}] 4s^2 S_{1/2}$ . The relevant part of the energetic level structure can be reduced to a three-level system with fine structure levels  $4s^2 S_{1/2}$ ,  $3d^2 D_{3/2}$  and  $4p^2 P_{1/2}$ , see Fig. 2.8. The short lived  $S_{1/2} \leftrightarrow P_{1/2}$  dipole transition with a lifetime of  $\tau_P = 6.9 \text{ ns}$  [Het15] is used for laser cooling and is driven by a light field near 397 nm. The short lifetime  $\tau_P$  results in a natural linewidth of  $\Gamma_{SP} = [2\pi\tau_P]^{-1} = 22.1 \text{ MHz}$ . However, the ion decays from the  $P_{1/2}$  state with a probability of  $p = 0.064$  to the metastable state  $D_{3/2}$  [Ram13]. The  $S_{1/2} \leftrightarrow D_{3/2}$  transition is a quadrupole transition, and thus provides a long lifetime of 1.18 s [Kre05]. In order to reach a closed cycling transition for laser cooling all the population which decays into  $D_{3/2}$  is pumped back to the  $P_{1/2}$  state by a light field near 866 nm. If a magnetic field is applied, the individual magnetic sub-levels  $m_j$  split according to the Zeeman effect. Individual transitions between the  $m_j$  levels are addressed separately by choosing the appropriate polarization of the laser beams with respect to the quantization axis of the magnetic field.

# 3

## Results of analytical and numerical investigations

In this chapter we present analytical and numerical investigations of the single-ion heat engine dynamics. Due to its conceptual simplicity, we consider a quantum Otto cycle where the bath interactions and the expansion and compression phases are strictly separated. Therefore, we simulate a single trapped ion confined in a tapered potential and coupling it alternately to two engineered thermal reservoirs. We use realistic experimental parameters, to be as close to a real experimental environment as possible. As for all realistic machines, the thermodynamic Otto cycle runs in finite time and therefore the engine has non-zero output power [And84]. We will show that our device converts incoherent thermal motion into coherent regular motion, thus fulfilling the fundamental definition of heat engines.

In the first part, starting with Sec. 3.1, we will present analytical derivations of the key parameters of the Otto cycle, based on the framework of the quantum harmonic oscillator. The latter plays an important role in theoretical investigations of thermodynamic quantum devices, e.g. [Lin03, Rez06, Qua07]. We will show how to determine the output power and the efficiency at maximum power in the limit of adiabatic processes. A detailed analysis for non-adiabatic processes can be found in [Aba15]. The analytical derivations are fully valid for the quantum regime, where the discreteness of the energy spectrum plays an important role. However, it can be applied to classical mechanics in the hot temperature limit without loss of generality, following the Ehrenfest theorem [Ehr27]. We further present semi-classical Monte Carlo simulations in Sec. 3.2, that demonstrate the experimental feasibility of the single-ion heat engine and allows us to identify experimental constraints. In general, all of the parameters of our engine system are tunable over a wide range, in particular the temperatures of the heat baths and the trap frequencies. In this idealized system the maximum efficiency can be achieved over a large span of temperatures. This first part is based on our publication

### **Single-ion heat engine at maximum power,**

O. Abah, J. Roßnagel, G. Jacob, S. Deffner, F. Schmidt-Kaler, K. Singer and E. Lutz,  
Phys. Rev. Lett. **109**, 203006 (2012).

In the second part of this chapter, starting with Sec. 3.3, we will extend our findings to non-thermal heat baths. Again, we will present both, analytical investigations and Monte-Carlo simulations of the system. We will demonstrate by the example of squeezed thermal reservoirs that the efficiency at maximum power can be increased beyond the

standard Carnot-limit, which is based on purely thermal reservoirs. These findings manifest the potential of non-thermal heat baths in the context of nano heat engines and show how different energy sources can be used simultaneously to drive nanoscopic engines and to increase their output power. In order to consider the constraints of the second law of thermodynamics we will deduce a generalized Carnot bound, which limits engine systems with non-thermal reservoirs and takes the increased total energy of the reservoirs into account. This second part is completed by an extended paragraph about the interpretation of our findings on heat engines with non-thermal reservoirs, Sec. 3.3.4. The results in this part are based on our publication

**Nanoscale Heat Engine Beyond the Carnot Limit,**

J. Roßnagel, O. Abah, F. Schmidt-Kaler, K. Singer and E. Lutz,  
Phys. Rev. Lett. **112**, 030602 (2014).

### 3.1. The quantum harmonic oscillator as heat engine

We start with an analytical formalism to fully describe the key parameters of an Otto engine based on a quantum harmonic oscillator. This formalism starts from the mean energies of the harmonic oscillator after each of the four strokes. These energy states fully characterize the dynamics of the engine and allow to calculate all relevant parameters, in particular the efficiency at maximum output power.

#### 3.1.1. Thermal state of a quantum harmonic oscillator

We assume a one dimensional harmonic oscillator with the mean number of phonons  $n$ . The classical and quantum representations of the Hamiltonian of this system are

$$\hat{H}_c = \frac{1}{2m}\hat{p}^2 + \frac{m\omega^2}{2}\hat{x}^2 \quad \text{and} \quad \hat{H}_q = \hbar\omega \left( \hat{a}^\dagger \hat{a} + \frac{1}{2} \right), \quad (3.1)$$

respectively, with  $n = \langle n | \hat{a}^\dagger \hat{a} | n \rangle$ . The Schrödinger equation  $\hat{H} |\Psi\rangle = E |\Psi\rangle$  reveals the energy of the phonon states

$$E_n = \hbar\omega(n + 1/2). \quad (3.2)$$

The harmonic oscillator is in a thermal state if the phonon state  $|n\rangle$  is occupied with a probability proportional to the Boltzmann factor

$$P_n = \frac{1}{Z} e^{-\beta E_n} \quad (3.3)$$

with the inverse temperature  $\beta = 1/(k_B T)$  and a normalization factor  $Z$  [Sch01, Ger05]. When measuring  $n$  of the quantum system in thermal equilibrium many times, the mean phonon number results to [Mee96, Lei03]

$$\langle n(\beta, \omega) \rangle = \frac{1}{\exp[\beta \hbar \omega] - 1}, \quad (3.4)$$

also known as the Planck distribution [Sch01]. The temperature  $T$  of the system is then defined as

$$T(\langle n \rangle, \omega) = \frac{\hbar\omega}{k_B \ln \left( \frac{\langle n \rangle + 1}{\langle n \rangle} \right)}. \quad (3.5)$$

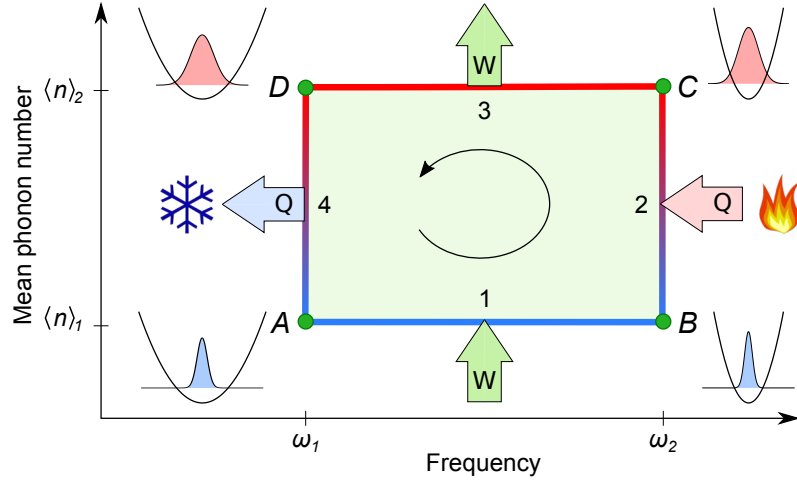


**Figure 3.1.** – Otto cycle for a harmonic oscillator in the  $\{n, \omega\}$ -representation. During the isentropic strokes 1 and 3, the frequency of the oscillator is varied between  $\omega_1$  and  $\omega_2$  at constant phonon number distribution. During the isochoric strokes 2 and 4, the temperature of the oscillator is changed at constant frequency between  $\beta_1$  and  $\beta_2$  and the mean phonon number is changed between  $\langle n \rangle_1$  and  $\langle n \rangle_2$ . The individual states of the ion in the harmonic potential are sketched. While the engine consumes work during stroke 1, it produces work during stroke 3. Due to the higher total energy of stroke 3 the net work of the cycle is positive and equals its area.

Using the mean phonon number Eq. (3.4) and the energy of the harmonic oscillator Eq. (3.2), we obtain the mean energy for a thermal state

$$\langle H \rangle = \frac{\hbar\omega}{2} \coth\left(\frac{\beta\hbar\omega}{2}\right), \quad (3.6)$$

where we have used the trigonometric replacement  $\coth(x) = 1 + 2[\exp(2x) - 1]^{-1}$ .

### 3.1.2. Otto cycle for a harmonic oscillator

In order to drive the quantum harmonic oscillator in a thermodynamic cycle, the parameters  $\beta$  and  $\omega$  become functions of time. Compared to macroscopic engines, the trap frequency corresponds to the volume of the system, while the thermal energy is related to its pressure. The engine is now coupled alternately to two heat baths at inverse temperatures  $\beta_i = 1/(k_B T_i)$  with  $(i = 1, 2)$ . The Otto cycle for the harmonic oscillator consists of four consecutive steps, which are analogue to the strokes of a classical Otto engine:

1. *Isentropic compression:*  $A(\omega_1, \beta_1) \rightarrow B(\omega_2, \beta_1)$ : the frequency is varied during time  $\tau_1$  while the system is isolated. The evolution is unitary and quasistatic. The phonon number distribution and the von Neumann entropy of the oscillator are constant.
2. *Hot isochore:*  $B(\omega_2, \beta_1) \rightarrow C(\omega_2, \beta_2)$ : the oscillator is weakly coupled to a reservoir at inverse temperature  $\beta_2$  at fixed frequency and allowed to relax during time  $\tau_2$  to the thermal state C.
3. *Isentropic expansion:*  $C(\omega_2, \beta_2) \rightarrow D(\omega_1, \beta_2)$ : the frequency is changed back to its



### 3. Results of analytical and numerical investigations

initial value during time  $\tau_3$ . The isolated oscillator evolves unitarily and quasistatically at constant entropy and constant phonon numbers into state  $D$ .

4. *Cold isochore*:  $D(\omega_1, \beta_2) \rightarrow A(\omega_1, \beta_1)$ : the system is weakly coupled to a reservoir at inverse temperature  $\beta_1 > \beta_2$  and relaxes to the initial thermal state  $A$  during  $\tau_4$ . The frequency is again kept constant.

The mean energies  $\langle H \rangle$  of the oscillator at the four stages of the cycle are [Aba15]

$$\langle H \rangle_A = \frac{\hbar\omega_1}{2} \coth\left(\frac{\beta_1\hbar\omega_1}{2}\right), \quad (3.7a)$$

$$\langle H \rangle_B = \frac{\hbar\omega_2}{2} \coth\left(\frac{\beta_1\hbar\omega_1}{2}\right), \quad (3.7b)$$

$$\langle H \rangle_C = \frac{\hbar\omega_2}{2} \coth\left(\frac{\beta_2\hbar\omega_2}{2}\right), \quad (3.7c)$$

$$\langle H \rangle_D = \frac{\hbar\omega_1}{2} \coth\left(\frac{\beta_2\hbar\omega_2}{2}\right), \quad (3.7d)$$

This set of equations is valid for systems in the quantum regime,  $\beta\hbar\omega \gg 1$ , as well as in the classical limit,  $\beta\hbar\omega \ll 1$ . In the latter the expressions simplify according to  $\coth(x) \approx 1/x$ .

The single-ion system represents a harmonic oscillator which is in general thermally isolated from its environment. In the limit of adiabatic processes, the probability distribution for phonon states, Eq. (3.3), remains unchanged, while the frequency  $\omega$  and thus the energy level spacing is changed [Sch01]. Note that adiabatic in the quantum thermodynamic context means that the individual transitions occur isolated from their environment and quasistatically. Consequently, there is no heat exchange or thermalization and the transitions are much slower than the timescales of the internal dynamics, which are on the order of  $1/\omega$ . As we will show later, in the experimental realization the timescale of the thermodynamic transitions is set by the axial trap frequency  $1/\omega_z$ , while the timescale of the internal thermalization processes is on the order of the radial trap frequency  $1/\omega_r$ . The assumption of quasistatic processes holds as long as  $\omega_z \ll \omega_r$ . After thermalization with the heat baths, the system is in thermal equilibrium at stages  $A$  and  $C$ .

However, as a result of the adiabatic and isentropic processes, at stages  $B$  and  $D$  the system is still distributed thermally with respect to  $A$  and  $C$ , respectively, while the level spacing has changed. As a consequence, the states  $B$  and  $D$  are non-thermal states and, in contrast to macroscopic systems, the engine operates far from equilibrium [Def13].

Now, we want to find a well suited and meaningful representation of the Otto cycle. In the case of an isolated harmonic oscillator, the relevant pair of conjugate variables is the frequency  $\omega$  (intensive) and the mean phonon number  $\langle n \rangle$  (extensive), whose product equals its internal energy [Lin03]. The Otto cycle of the harmonic oscillator is sketched in Fig. 3.1 in the  $\{n, \omega\}$ -representation. The total internal energy changes during the each of the transitions, either by changing the probability distribution Eq. (3.3) and thus  $\langle n \rangle$ , or by changing the frequency  $\omega$ ; always keeping the other variable constant,

$$dE = \hbar\langle n \rangle \cdot d\omega + \hbar\omega \cdot d\langle n \rangle. \quad (3.8)$$

As shown in [Lin03], the change of the internal energy can be compared directly to the differential form of the second law of thermodynamics

$$dE = dW + dQ. \quad (3.9)$$

By comparing Eq. (3.8) and Eq. (3.9), we identify the work produced  $dW$  and the heat exchanged  $dQ$  as

$$dW = \hbar \langle n \rangle \cdot d\omega \quad \text{and} \quad dQ = \hbar \omega \cdot d\langle n \rangle. \quad (3.10)$$

As a consequence, Eq. (3.8) is a representation of the second law of thermodynamics for a harmonic oscillator, and the area of the  $\{n, \omega\}$ -diagram reveals directly the work produced during each cycle.

However, often it is more convenient for practical reasons to choose a different representation basis for the thermodynamic cycles. It is widespread to use an energy-frequency representation  $\{H, \omega\}$ , since  $\langle H \rangle$  is actively changed during the strokes and contains all information about the thermal and the mechanical properties. The same applies here. In the following we will show how to calculate all relevant thermodynamic quantities, such as heat, work and efficiency, from the total energy  $\langle H \rangle$  of the four states of the system, Eqs. (3.7a-3.7d).

### 3.1.3. Work and efficiency

In order to determine the efficiency of the quantum Otto cycle, we need to evaluate work and heat for each of the above steps. During stroke 2 and 4, the frequency is constant, and thus only heat is exchanged with the reservoirs. On the other hand, during stroke 1 and 3, the system is isolated and only work is performed by modulating the frequency.

Let us now derive the mean values for heat and work during the individual steps. The mean work during the first stroke is

$$\langle W_1 \rangle = \langle H \rangle_B - \langle H \rangle_A = \left( \frac{\hbar \omega_2}{2} - \frac{\hbar \omega_1}{2} \right) \coth \left( \frac{\beta_1 \hbar \omega_1}{2} \right). \quad (3.11)$$

The mean heat exchanged with the hot reservoir during the second stroke reads

$$\langle Q_2 \rangle = \langle H \rangle_C - \langle H \rangle_B = \frac{\hbar \omega_2}{2} \left[ \coth \left( \frac{\beta_2 \hbar \omega_2}{2} \right) - \coth \left( \frac{\beta_1 \hbar \omega_1}{2} \right) \right]. \quad (3.12)$$

In a similar way, the average work and heat for the third and fourth stroke are given by

$$\langle W_3 \rangle = \langle H \rangle_D - \langle H \rangle_C = \left( \frac{\hbar \omega_1}{2} - \frac{\hbar \omega_2}{2} \right) \coth \left( \frac{\beta_2 \hbar \omega_2}{2} \right) \quad (3.13)$$

and

$$\langle Q_4 \rangle = \langle H \rangle_A - \langle H \rangle_D = \frac{\hbar \omega_1}{2} \left[ \coth \left( \frac{\beta_1 \hbar \omega_1}{2} \right) - \coth \left( \frac{\beta_2 \hbar \omega_2}{2} \right) \right]. \quad (3.14)$$

For a heat engine operation, heat is absorbed from the hot reservoir  $\langle Q_2 \rangle \geq 0$  and flows into the cold reservoir  $\langle Q_4 \rangle \leq 0$ . Regarding the mechanical energy of the engine, work is consumed by the system during the first stroke  $\langle W_1 \rangle \geq 0$ , while it produces work during the third stroke  $\langle W_3 \rangle \leq 0$ . The net work of the system is negative,

### 3. Results of analytical and numerical investigations

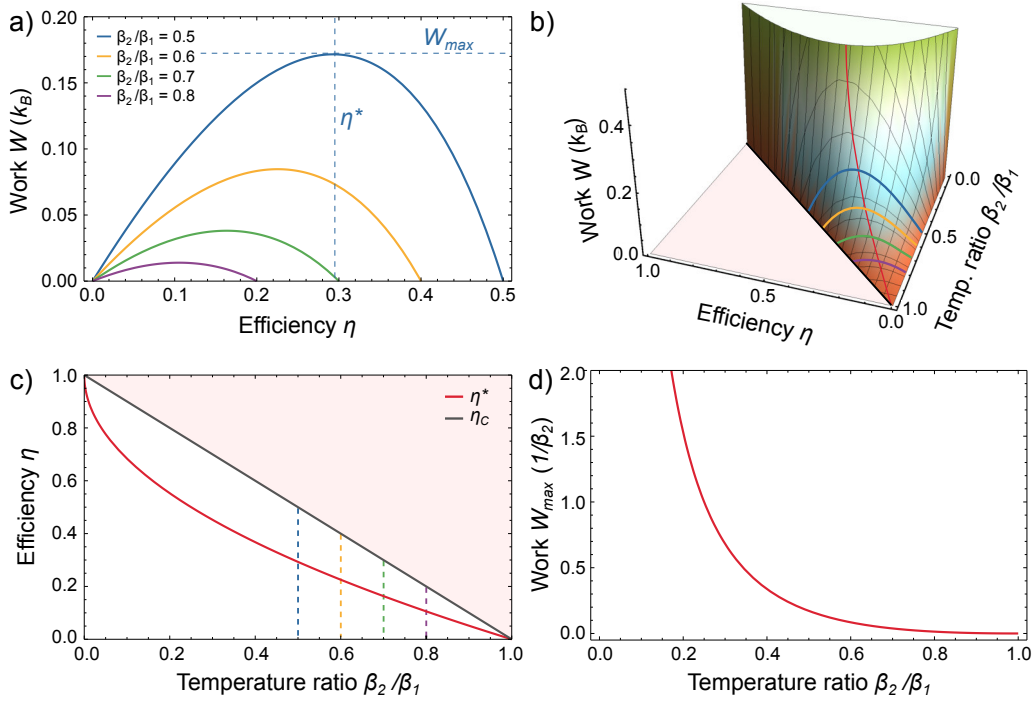


**Figure 3.2.** – Analysis of work and efficiency of the Otto cycle in the high temperature limit for different ratios of the bath temperatures  $\beta_2/\beta_1$ . (a) Mean work  $\langle W \rangle_{\text{ht}}(\eta)$  in terms of  $k_B$  as a function of the efficiency  $\eta$  for different constant values  $\beta_2/\beta_1$ . For  $\eta^*$  the generated work reaches its maximum,  $\langle W \rangle_{\text{max}}$ . (b) 3D representation of the mean work  $\langle W \rangle_{\text{ht}}(\eta)$  for continuous values of  $\beta_2/\beta_1$ . The curves in (a) correspond to vertical intersections along the colored lines. Efficiencies above the Carnot limit  $\eta_C = 1 - \beta_2/\beta_1$  (red shaded area) are excluded by the second law of thermodynamics. (c) Efficiency  $\eta^*$  as a function of  $\beta_2/\beta_1$ , which corresponds to the ridge of the work surface, red line in b). The curves from a) are indicated by dashed lines. The Carnot efficiency for thermal machines  $\eta_C$  serves as comparison. (d) Maximum mean work  $\langle W \rangle_{\text{max}}$  corresponding to  $\eta^*$ , normalized to  $1/\beta_2$ , as a function of  $\beta_2/\beta_1$ , cf. red line in b). For  $\beta_2/\beta_1 \rightarrow 0$  the temperature difference diverges and so  $\langle W \rangle_{\text{max}}$  does.

$\langle W \rangle = \langle W_1 \rangle + \langle W_3 \rangle \leq 0$ , and thus the system generates more work than it consumes, as expected for heat engines.

The efficiency of the harmonic oscillator engine, defined as the ratio of the total work per cycle and the heat received from the hot reservoir, then follows as

$$\eta = -\frac{\langle W_1 \rangle + \langle W_3 \rangle}{\langle Q_2 \rangle} = 1 - \frac{\omega_1}{\omega_2}. \quad (3.15)$$

For practical purposes, we search for the maximum output power for given bath temperatures, and for the corresponding efficiency at maximum power. In the high temperature limit, where  $\beta\hbar\omega \rightarrow 0$  and  $\coth(x) \approx 1/x$ , the net work reads

$$\begin{aligned} \langle W \rangle_{\text{ht}} = \langle W_1 \rangle + \langle W_3 \rangle &= \frac{1}{\beta_1} \left( \frac{\omega_2}{\omega_1} - 1 \right) + \frac{1}{\beta_2} \left( \frac{\omega_1}{\omega_2} - 1 \right) \\ &= \frac{1}{\beta_1} \left( \eta - \frac{\beta_1}{\beta_2} \frac{\eta}{1 - \eta} \right). \end{aligned} \quad (3.16)$$

In Fig. 3.2 (a) we plot  $\langle W \rangle_{\text{ht}}$  as a function of the efficiency  $\eta$ , for different constant tem-

perature ratios  $\beta_2/\beta_1$ . Analytically, we find the maximum of these curves by optimizing  $\langle W \rangle_{\text{ht}}$  with respect to  $\Delta\omega = \omega_2 - \omega_1$ , while keeping all parameters but  $\omega_2$  constant,

$$\frac{d\langle W \rangle_{\text{ht}}}{d\omega_2} = 0 \quad \Rightarrow \quad \frac{\omega_2}{\omega_1} = \sqrt{\frac{\beta_1}{\beta_2}}. \quad (3.17)$$

Applying this condition to the expression for the efficiency Eq. (3.15), we find the efficiency at maximum power output

$$\eta^* = 1 - \sqrt{\frac{\beta_2}{\beta_1}}, \quad (3.18)$$

which corresponds to the well known Curzon-Ahlborn efficiency for classical systems, Eq. (2.9), see also [Aba12]. We have thus shown that the quantum energy representation of the four states of the heat engine agrees well with the classical expectations in the high temperature limit. Fig. 3.2 illustrates the behavior of  $\eta^*$  and of the corresponding work output  $\langle W \rangle_{\text{max}}$  as a function of  $\beta_2/\beta_1$ .

Eq. (3.18) indicates that maximum efficiency of 1 may be attained when  $\beta_1 \rightarrow \infty$ . In this low-temperature limit for the cold bath, quantum effects become crucial. Repeating the above optimization in the regime  $\beta_1 \hbar \omega_1 \rightarrow \infty$  with  $\coth(\infty) = 1$ , we find for the efficiency at maximum power

$$\eta_q^* = 1 - \sqrt{\frac{\hbar \omega_1 \beta_2}{2}} \quad (3.19)$$

for  $\omega_2 = \sqrt{2\omega_1/\hbar\beta_2}$ . Here, the classical thermal energy  $k_B T_1$  is replaced by the ground state energy of the oscillator  $\hbar \omega_1/2$ . The above expression is the quantum extension of the Curzon-Ahlborn efficiency.

Note, that a single particle engine exhibits statistical fluctuations in all of the thermodynamic variables from cycle to cycle, in contrast to thermodynamic systems based on large ensembles of particles. Therefore, in the following, we employ the mean values of the thermodynamic variables. The features of fluctuations are extensively discussed in [Din16].

### 3.2. Proof of concept - a single ion as working fluid

In this section, we demonstrate the feasibility of the implementation of the thermodynamic cycle of a heat engine for a single trapped ion, as introduced in Sec. 2.5. Therefore, we present numerical results of semiclassical Monte-Carlo simulations of the trapped ion system driven in an Otto cycle. We employ realistic experimental parameters and the tapered trap geometry, which has been presented in Sec. 2.4.2. Later in Sec. 6.1.2, we will prove experimentally that the interaction with thermal reservoirs can be mimicked by either laser cooling (cold reservoir) or a combination of electric field noise and laser cooling (hot reservoir) [Tur00b]. Both interactions are modeled by Monte-Carlo simulations.

Since we aim to achieve realistic experimental conditions, we model the bath coupling by simulating the interaction with laser photons and electric field noise in a realistic fashion, instead of changing the temperature of the ion by an interaction with a virtual perfect heat bath or by a direct adjustment of the phase-space variables. In this way, we will demonstrate the functionality of our experimental approach. Furthermore, we will investigate how the maximum work  $\langle W \rangle_{\text{max}}$  of the engine may be achieved.

### 3.2.1. Concepts of numerical simulations

In order to solve the equations of motion of the trapped ion under realistic conditions, we first have to model the geometry of the trapping potential inside the trap, as explained in detail in [Sin10]. To obtain the time variable electric fields inside the trap volume the Laplace equation  $\Delta\Phi(\vec{x}) = 0$  has to be solved for each point in space with Dirichlet boundary conditions  $\Phi(\vec{x}) = U_i$  on the surface of the  $i$ th electrode. To reduce the computational requirements we employ the *Boundary Element Method* (BEM) [Poz02]: we discretize the surface of the electrodes into small rectangular-shaped elements and calculate the electric potential at any point in space as a superposition of the contributions of all elements with surface charge  $Q_i$ , using Coulomb's law  $\Phi(\vec{x}) = \sum_i Q_i / (4\pi\epsilon_0 |\vec{x} - \vec{x}_i|)$ .

To simulate the dynamics of the ion, we model radio-frequency oscillations of the electrode voltages and thus a time dependent potential  $\Phi(\vec{x}, t)$ . For a fast numerical propagation of the ion trajectory we approximate the numerical solution of the potential  $\Phi(\vec{x}, t)$  by an analytical and time dependent description  $\Phi'(\vec{x}, t)$ , similar to Eq. (2.15). This leads to a modified force on the ion  $\vec{F}(\vec{x}, t) = -(q/m)\vec{\nabla}\Phi'(\vec{x}, t)$  after each time step  $h$ . This equation of motion allows us to propagate the ion trajectory in phase-space. To solve the equation of motion we use the Störmer-Verlet method, which is based on a partitioned Runge-Kutta propagator [Gre06]. It is time invariant, energy and phase space conservative and popular in molecular dynamics simulations [Ver67]. Thereby, position  $\vec{x}_n$  and velocity  $\vec{v}_n$  are propagated jointly, starting from  $\vec{x}(t_0) = \vec{x}_0$  and  $d\vec{x}(t_0)/dt = \vec{v}_0$ , following the recursion [Sin10]

$$\vec{v}_{n+1/2} = \vec{v}_n + \frac{h}{2} \cdot \vec{F}_n(\vec{x}_n) \quad (3.20)$$

$$\vec{x}_{n+1} = \vec{x}_n + h \cdot \vec{v}_{n+1/2} \quad (3.21)$$

$$\vec{v}_{n+1} = \vec{v}_{n+1/2} + \frac{h}{2} \cdot \vec{F}_{n+1}(\vec{x}_{n+1}), \quad (3.22)$$

where the notion  $x_n$  is a short form of  $x(t_n)$ , with  $t_n = n \cdot h$ .

The interaction of the ion with the laser beams is modeled by realistic Monte-Carlo simulations. Therefore we modify the velocity  $\vec{v}_{n+1/2}$  after Eq. (3.21) by the total momentum transfer of the photon absorption and emission process. First, a photon at the frequency of the laser  $\nu_L$  is absorbed with momentum  $p_L = \hbar\vec{k}_L$ . During the subsequent spontaneous decay, a photon is emitted at the frequency of the atomic resonance  $\nu_L$  with momentum  $p_{sp} = \hbar\vec{k}_{sp}$ . Thus,  $\vec{v}$  is modified by

$$\vec{v}'_{n+1/2} = \vec{v}_{n+1/2} + P_{sp} \cdot \left( \frac{\hbar|k_L|}{m} \vec{u}_L - \frac{\hbar|k_{sp}|}{m} \vec{u}_{sp} \right). \quad (3.23)$$

Here,  $\vec{u}_L$  is the direction vector of the laser beam and  $\vec{u}_{sp}$  is a random direction vector accounting for the isotropic spontaneous emission. The scattering probability  $P_{sp}$  is non-zero during periods where the lasers are on, and is calculated by [Cas88]

$$P_{sp} = \Gamma \cdot h \cdot \frac{S}{1 + 2S}, \quad (3.24)$$

with the saturation parameter

$$S = I \cdot \frac{\Gamma^2}{\left( \Delta\nu - \vec{k}_L \cdot \vec{v}_{n+1/2} \right)^2 + \Gamma^2}, \quad (3.25)$$

where  $\Gamma = 1/(2\pi\tau) = 23.1$  MHz is the natural linewidth,  $I$  the relative laser intensity with respect to the saturation limit and  $\Delta\nu$  the spectral detuning of the laser. In each time step  $h$  a photon scattering event takes place if a random number is larger than  $P_{\text{sp}}$ , while  $h$  should be smaller than the lifetime  $\tau$  of the excited atomic level ( $\tau = 6.9$  ns for  $\text{Ca}^+$ ). Here, we have done several approximations: we reduce the level scheme to a two level system, we ignore the linewidth of the laser and we neglect the time delay between the absorption and emission event. For the heat engine dynamics with a high absolute temperature of the ion,  $k_B T \gg \hbar k$ , these approximations have a marginal effect and the Monte-Carlo simulation of laser cooling leads to realistic results.

To heat the motional state of the ion we expose the ion to electric field noise. This effect is simulated by adding a static electric field  $\vec{E}$  in the radial  $(x,y)$ -plane to trapping potential  $\Phi'(\vec{x},t)$ . Amplitude and direction of  $\vec{E}$  are randomly changed for each time step, following a normally distributed probability for the amplitude with a variable expectation value  $\mathcal{N}$ .

According to the Monte-Carlo method, the probabilistic nature of a thermal state of the ion is reproduced by a repeated sampling of several thousand classical trajectories of the ion under randomized interactions [Cas88]: the initial parameters for each trajectory are chosen randomly according to a Boltzmann distribution. The thermal probability distribution during the experimental runs are realized through photon scattering and electric noise interaction [Sre94]. The ensemble of all trajectories reveals a normally distributed probability for position and velocity coordinates of the ion. In the following this technique will be discussed in more detail.

### 3.2.2. Monte Carlo simulations

We reach a dynamic confinement of the ion in the trap volume through the oscillating parabolic and tapered saddle potential Eq. (2.15) with a trap drive frequency  $\Omega_{\text{rf}} = 60$  MHz. We assume a funnel-shaped trap geometry, as sketched in Fig. 2.3, with an angle of the rf-electrodes of  $\theta = 20^\circ$  with respect to the trap axis. The length of the trap is 5 mm and the radial distance of the rf-electrodes to the trap axis is  $r_0 = 1$  mm at the position of the ion. The axial and radial trap frequencies of the ion are  $\omega_{0,z}/(2\pi) \simeq 35$  kHz and  $\omega_{0,x}/(2\pi) \simeq \omega_{0,y}/(2\pi) \simeq 6.0$  MHz. A small offset field in the  $x$ -direction lifts the degeneracy of both radial oscillations. The time steps  $h$  of the numerical integration are chosen much shorter than the oscillation period of the trapping field,  $h \ll 1/\Omega_{\text{rf}}$ , in order to resolve the micromotion of the ion.

The trapped ion is initially prepared in a thermal state at low temperature by randomized initialization of position and velocity with Gaussian probability distribution and consecutive laser cooling to the cooling limit in all spatial directions. The engine is then driven by alternately heating and cooling the radial modes of the ion. As discussed above, thereby we mimic the interaction with a hot and a cold reservoir. Both interactions are oriented in radial direction, parallel to the  $(x,y)$ -plane. Therefore, only the radial components of  $\vec{x}$  and  $\vec{v}$  are addressed by the thermal reservoirs. The axial degree of freedom experiences a residual heating due to spontaneously emitted photons during laser cooling of the radial modes. The coupling to the heat reservoirs is switched on and off with a given period. A change in temperature  $T$  of the radial thermal state of the ion leads to a modification in the axial component of the restoring force of the trap, which changes the equilibrium position  $z_0(T)$  (see Sec. 2.5). Heating and cooling the radial state hence moves the ion back and forth along the trap axis, resulting in the closed Otto

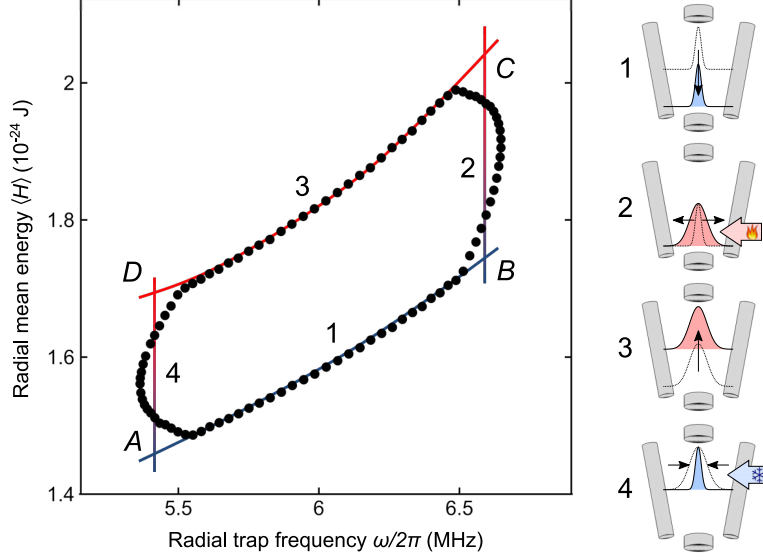


**Figure 3.3.** – Simulated energy-frequency diagram of the Otto cycle driven in the radial mode of the ion. The continuous line represents the ideal process, while the dots show the results of the Monte Carlo simulations. Here we have plotted the mean of  $10^5$  individual runs of the simulation. Remaining fluctuations due to the micromotion are eliminated by averaging each point in time over one oscillation period of the trap drive  $1/\Omega_{rf}$ . The curved shape of the latter is due to the harmonic oscillation of the ion and the finite interaction time with the heat baths. The pictograms illustrate the four individual strokes of the cycle.

cycle. A numerically simulated cycle is shown in Fig. 3.3. The energy gained by each cycle in the radial degrees of freedom is stored in the axial motion. The energy transfer is maximized, if the coupling of the ion to the thermal reservoirs is resonant with the axial trap frequency. Therefore, the switching of the heating and cooling is adjusted to match  $\omega_z$ . Each interaction is acting on the ion for 20% of an axial trap period. The ensemble of driven oscillators is thus excited coherently in axial direction, such that heating and cooling takes place at the turning points of the trajectory. In such a way, the cyclic temperature change of the radial thermal state is directly converted into an increasing coherent axial oscillation. By a variation of the noise amplitude  $\mathcal{N}$ , radial temperatures in the range of 20 to 200 mK were achieved, corresponding to  $0.1 < \beta_2/\beta_1 < 1$  and respective radial phonons numbers of about 400 and 4000. For a stable maximum axial amplitude of about 1 mm, the relative variation of the radial frequency at 6.0 MHz is in our setup about 50%.

To get a better understanding of the dynamics, we focus on the individual parameters of the thermodynamic cycle in Fig. 3.3, the radial energy and the radial frequency in terms of the axial position. Fig. 3.4 investigates the evolution of the total energy of the radial degrees of freedom,  $E_r = m/2 (v_r^2 + \omega_r^2 x_r^2)$ . It shows how the system evolves towards a steady state between heating and cooling. A detailed analysis of the energy changes allows to identify heating and cooling processes, as well as the change of the total energy due to the variation in the trap frequency. During the latter periods work is performed by the engine. The motion of the ion in all spatial directions is analyzed in Fig. 3.5. The undirected, statistical and thermal motion in radial direction is converted into a regular and coherent motion of the ion in axial direction, which is the central

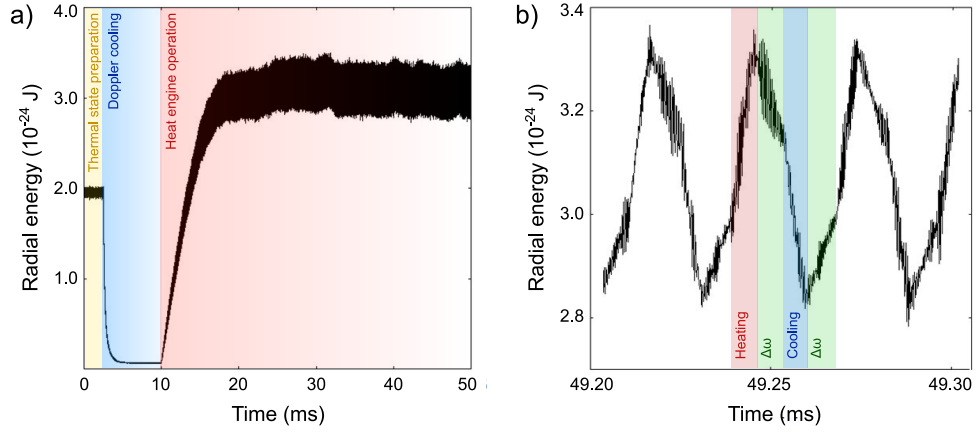


**Figure 3.4.** – Simulated evolution of the radial energy during heat engine operation. (a) First, the ensemble is randomly initialized at an average energy of  $\langle H_r \rangle = 2 \times 10^{-24}$  J. Subsequent laser cooling reduces the energy to a steady state between photon absorption and emission processes. When starting the engine, first the cooling process is less effective than heating due to the small velocities. This changes with increasing energy in favor of the cooling efficiency. At  $\langle H_r \rangle \approx 3 \times 10^{-24}$  J, a steady state is set up between heating and cooling. (b) A detailed analysis of the energy evolution in steady state allows to identify heating and cooling periods as well as isentropic compression and expansion phases.

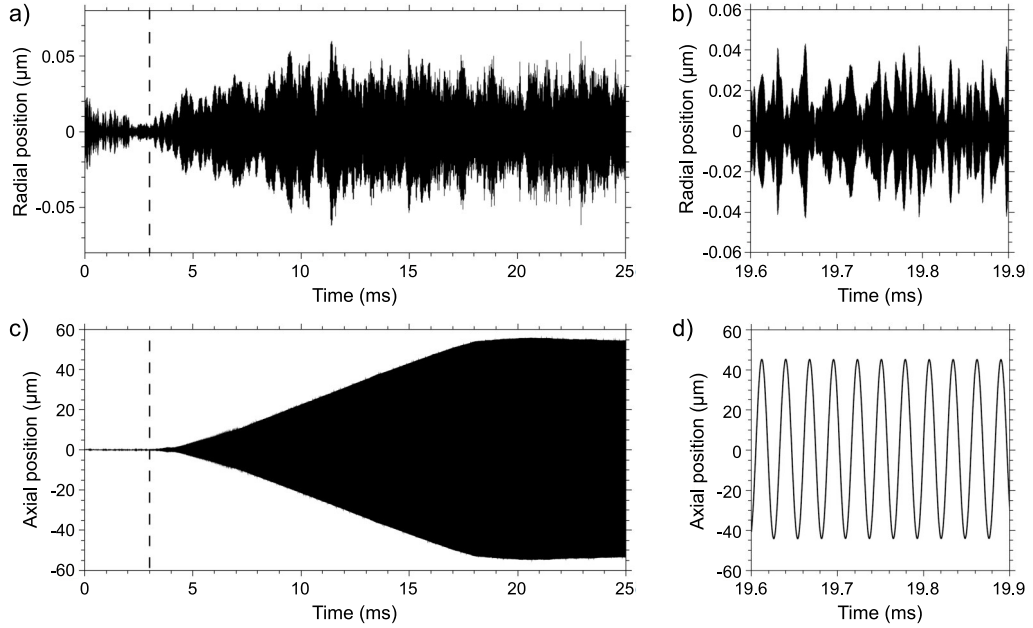


**Figure 3.5.** – Ensemble average of several thousand ion trajectories during heat engine operation. The engine is started at  $t = 3$  ms; at  $t = 18$  ms the axial dissipation confines the amplitude in a steady state. (a) Radial component. After the start of the engine an increase in the total variance of the ensemble average is observed, while statistical fluctuations are dominant. (b) On a scale of the oscillation period  $1/\omega_z$  the statistical fluctuations are still dominant. (c) Axial component. The ensemble average reveals a phase coherent superposition of regular oscillations with increasing amplitude. The artificial dissipation limits the amplitudes to some tens of micrometers. (d) A magnification of the trajectory reveals the regular oscillation. The resolved trajectories (b) and (d) illustrate the conversion from incoherent into coherent motion.



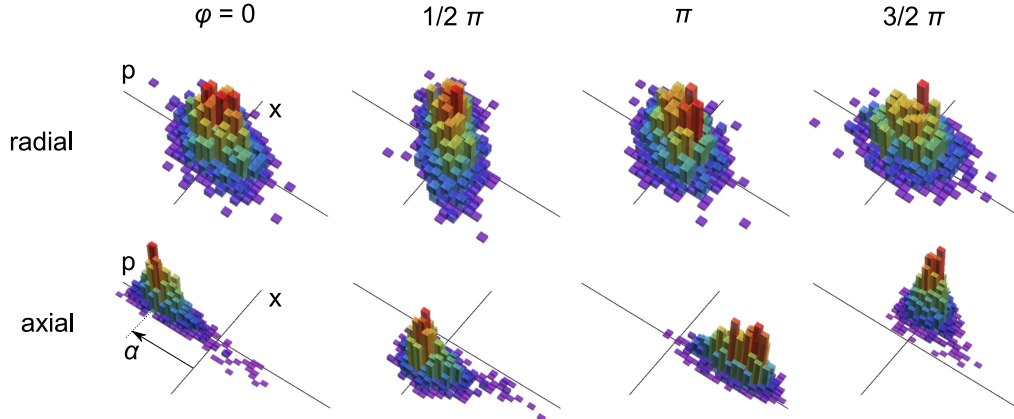


**Figure 3.6.** – Phase space distribution of the motional state at different phases during an engine cycle: the radial mode is changing from thermal to non-thermal states, always centered at the origin of the coordinates. In axial direction, a coherent oscillation with typical displacement of  $\alpha = 10^3$  ground state wave packet sizes displays the functional performance of the engine.

working principle of any heat engine.

An analysis of the ensemble average in phase space illustrates this working principle. Due to the isentropic compression and expansion phases the phase space distribution of the radial components changes between thermal and nonthermal states, but, as shown in Fig. 3.6, it is always centered at the origin of the coordinates. Due to the mode coupling a change in the variance of this centered distribution is converted into a displacement of the distribution of the axial mode, which then performs a phase synchronized oscillation. The increasing axial oscillation is only limited by the trap geometry. However, to reach a steady state of the oscillation, a red-detuned low intensity dissipation laser is applied in axial direction that damps the coherent movement and removes the excess heating from spontaneous emission events.

In our setup, the oscillation amplitude in steady state as well as the trap frequencies of the ion can be changed by virtue of the laser and trap parameters precisely. This unique flexibility of the device can be exploited to satisfy the optimality condition for maximum output power derived previously. Fig. 3.7 shows that by properly adjusting the parameters our simulated Otto engine is able to run at maximum efficiency at maximum power in an interval  $0.5 < \beta_2/\beta_1 < 1$ . The maximum efficiency, determined through Eq. (3.15) with values taken from simulated cycles as shown in Fig. 3.3, is about  $\eta^* \approx 30\%$ . This maximum efficiency is significantly larger than those obtained to date experimentally [Ste11, Bli12]. The expected net power of the engine is of the order of  $P \simeq 10^{-20}$  J/s. We will show in the experimental part of this thesis, that in real experiments this idealized efficiency is not reached yet due to significant technical limitations. However, these limitation are of technical nature rather than physical restrictions.

### 3.3. Employing non-thermal reservoirs

Among the different kind of thermodynamic machines, we find two major classes. First we have the well known combustion engines, which operate between two heat baths at different temperatures  $T_1 < T_2$  and convert the temperature difference into mechan-

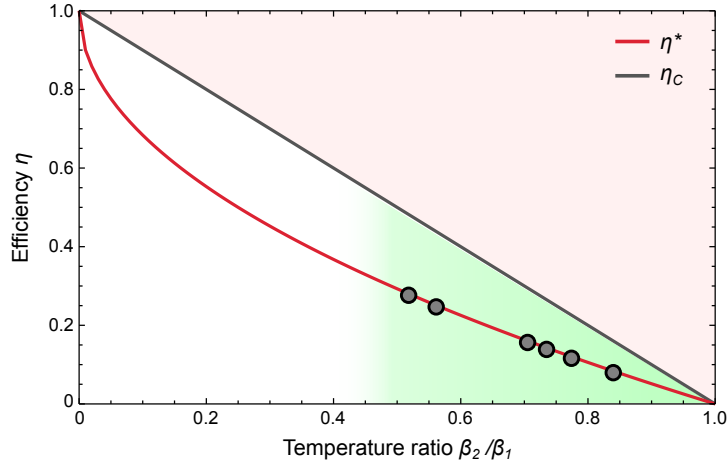


**Figure 3.7.** – Efficiency  $\eta$  of the Otto engine as a function of the temperature ratio  $\beta_2/\beta_1$ . The black line the Carnot efficiency  $\eta_C$  with highest possible  $\eta$  but zero output power. The red line corresponds to the theoretical adiabatic process with maximum output power and the efficiency  $\eta^*$ , Eq. (3.18). The black points are the results of the numerical simulations and demonstrate that the engine runs at maximum power. The green shaded area indicates the accessible parameter range for realistic conditions, including the limited dimensions of the trap, the laser beams and the detection devices, with an upper bound at  $\omega_2 \approx 1.5\omega_1$ .

ical work [Cal85, Cen15]. Then there are molecular motors, which operate with one single heat bath, the ambient temperature [Jül97, How01, Rei02a]. They are driven by a variation of some external parameters. We find those kind of engines in biological motor proteins as well as in artificial nano machines [Scu03, Kay07, Hän09, Leg15]. The efficiency of thermally driven classical combustion heat engines is generally bound to the Carnot efficiency  $\eta_C$  [Cen15]. The Carnot formalism is a direct consequence of the second law of thermodynamics and is based on purely thermal and equilibrium reservoirs. However, when transferring this formalism to non-thermal or non-equilibrium systems, the fundamental assumptions of Carnot do no longer hold and deviations are expected. For molecular motors, an extreme form of non-thermal machines, the efficiency may in principle reach unity  $\eta \simeq 1$  [Par99, Ast07, Toy10, Toy11], and even the efficiency at maximum power may reach  $\eta^* \simeq 1$  for strong driving [Sei11, Bro12]. Different theoretical studies have already shown that heat engines may exceed the Carnot bound when coupled to engineered non-equilibrium resources, such as quantum coherent [All00, Scu03], quantum correlated [Dil09] or non-Markovian reservoirs [Zha14b]. Other examples of quantum heat engines are masers or photocells, which are classically limited by the Carnot efficiency as a consequence of the detailed balance between absorption and emission. Here as well, different approaches show that this classical limit can be overcome by exploiting their quantum properties [Mil03, Scu10, Nal13, Dor13]. All of these systems are characterized by a temperature as well as additional parameters that quantify the degree of deviation from pure thermal states. However, they all are consistent with the physics behind the second law of thermodynamics, since the total entropy change of the system is still positive,  $\Delta S \geq 0$ , as shown in [Bou13]. In order to respect the additional information included in non-classical reservoirs, the second law of thermodynamics has to be revised for those system, leading to a generalized Carnot bound [Aba14, Woo15, Gar15]. For micro- and nanoscopic engines the thermodynamic observables are no longer deter-

mined by their mean values, but become highly fluctuating quantities, even in thermal equilibrium. Thermal fluctuations of energy fluxes can lead to statistical violations of the Carnot bound on short timescales, while the second law of thermodynamics holds for the long time average of the system. Those statistical short term violations of the second law have been predicted theoretically [Kie04, Ver14a, Ver14b, Cam15] and demonstrated experimentally [Wan02, Mar16].

In this section, we extend the general theory of a thermal (quantum) heat engine from Sec. 3.1.2 to the case where it is coupled to a non-thermal reservoir. The fundamental motivation of our studies is to demonstrate that non-thermal reservoirs provide certain features that are not accessible with classical engine systems. Our investigations were motivated by the recent advances in experimental reservoir engineering techniques, such as in ion traps [Poy96, Mya00, Lin13, Kie15], in optical lattices [Die08, Ver09], in circuit QED [Mur12, Sha13b] and in microwave cavities [Pie07, Sar11]. We evaluate both the efficiency and the efficiency at maximum power of the single-ion engine. We show that the efficiency at maximum power can be increased beyond  $\eta_C$  by exploiting the non-thermal properties of the reservoir, without questioning the universality of the general framework of thermodynamics. However, by exceeding  $\eta_C$  we demonstrate that non-thermal reservoirs can achieve efficiencies, even for maximum work output, which are not accessible for engines operating in thermal equilibrium.

Explicitly, we investigate the influence of non-thermal reservoirs on heat engines on the example of a squeezed thermal reservoir. The reason for this choice is the experimental realizability and the simplicity in the theoretical description of its dynamics. Squeezing is a general concept in quantum optics [Scu97]. It may be characterized by a parameter  $\kappa$  such that the phase-space quadratures of a state are, respectively, multiplied by  $e^\kappa$  and  $e^{-\kappa}$  [Tei89], see Fig. 1.3 (d). Squeezed ground states of the harmonic oscillator were first observed in photonic systems [Slu85] and extensively studied in [Bre97]. Additionally, phononic [Mee96], number state [Orz01] and spin state [Est08] squeezing were observed in ion systems and Bose-Einstein condensates. The properties of squeezed thermal states are subject to theoretical studies since a long time [Fea88, Kim89, OV91, Wan93, Mar93a, Mar93b]. Squeezed thermal noise has first been experimentally realized in a Josephson parametric amplifier [Yur88]. However, while interactions of quantum systems with squeezed thermal reservoirs have been analyzed theoretically [Kal06, Ban08, Dod11, Sha13a], we only find a small number of applications to quantum optics [Kie15, Lo15], while their use in quantum thermodynamics and their effect on the performance of thermodynamic machines is largely unexplored to date.

In the following, we continue our investigations on the harmonic oscillator Otto cycle. To analyze the effect of squeezing, we couple the engine to a high-temperature squeezed thermal reservoir, while the low-temperature reservoir is still purely thermal. We find that the efficiency at maximum power rises exponentially with the squeezing parameter  $\kappa$ , surpassing the standard Carnot limit and converging towards unity exponentially. We further present an experimental scheme to mimic the interaction with a squeezed thermal reservoir for the single trapped ion system by combining reservoir and state engineering techniques [Lei03]. Again, we demonstrate the experimental realizability of such a scheme by Monte-Carlo simulations with realistic trap parameters and laser interaction. We show that the single-ion engine may run at maximum power up to an efficiency which is four times larger than the efficiency obtained with two thermal reservoirs and a factor of two above the standard Carnot bound. In order to fulfill the

constraints of the second law, we deduce a generalized Carnot bound, which limits the efficiency of an engine operating between squeezed thermal reservoirs.

### 3.3.1. Otto cycle with a squeezed thermal reservoir

We start with an analytical investigation of the system. Therefore, we consider a quantum Otto cycle for a harmonic oscillator similar to Sec. 3.1.2, which is shown schematically in the inset of Fig. 3.8 (a). The hot reservoir is replaced by a squeezed thermal reservoir with a hot inverse temperature  $\beta_2$  and squeezing parameter  $\kappa$ . During interaction, the harmonic oscillator relaxes to a non-displaced squeezed thermal state with mean phonon number [Mar93a]

$$\langle n^*(\beta, \omega, \kappa) \rangle = \langle n \rangle + (2 \langle n \rangle + 1) \cdot \sinh^2(\kappa), \quad (3.26)$$

where  $\langle n \rangle = \langle n(\beta_2, \omega_2) \rangle$  is the mean thermal occupation number, see Eq. (3.4). We assume the duration of this interaction to be much shorter than the duration of the isentropic process, and thus it is assumed to take place at constant frequency  $\omega_2$ . Consequently, it corresponds to an isochoric process. The mean energy after equilibration with a squeezed thermal reservoir is given by [Mar93a],

$$\langle H \rangle_s = \hbar \omega \langle n^*(\beta, \omega, \kappa) \rangle = \frac{\hbar \omega}{2} \coth \left( \frac{\beta \hbar \omega}{2} \right) \left[ 1 + \left( 2 + \frac{1}{\langle n \rangle} \right) \cdot \sinh^2 \kappa \right]. \quad (3.27)$$

In the following, we will keep the inverse temperature  $\beta_2$  constant and vary the amount of squeezing  $\kappa$ , increasing the energy of the state C in the cycle. The additional energy is still present at D, after the isentropic and adiabatic compression. The cycle is closed by coupling the system to the cold thermal bath. Because of the stochastic nature of this process, it erases any phase relation and thus thermalizes the squeezed thermal state, resulting a pure thermal state with cold temperature  $\beta_1$  at point A. The mean energy of the four stages of the Otto cycle now reads [Aba15]

$$\langle H \rangle_A = \frac{\hbar \omega_1}{2} \coth \left( \frac{\beta_1 \hbar \omega_1}{2} \right), \quad (3.28a)$$

$$\langle H \rangle_B = \frac{\hbar \omega_2}{2} \coth \left( \frac{\beta_1 \hbar \omega_1}{2} \right), \quad (3.28b)$$

$$\langle H \rangle_C = \frac{\hbar \omega_2}{2} \coth \left( \frac{\beta_2 \hbar \omega_2}{2} \right) \Delta H(\kappa), \quad (3.28c)$$

$$\langle H \rangle_D = \frac{\hbar \omega_1}{2} \coth \left( \frac{\beta_2 \hbar \omega_2}{2} \right) \Delta H(\kappa), \quad (3.28d)$$

with the non-thermal energy addition  $\Delta H(\kappa) = 1 + (2 + 1/\langle n \rangle) \sinh^2 \kappa$ .

Work is exchanged by the oscillator during the compression and expansion phases, whereas heat and non-thermal energy are exchanged during the relaxation with the reservoirs. Similar to the procedure in Sec. 3.1.2 we find the efficiency as ratio between the net work of the engine and the total (non-)thermal energy supplied to the system,

$$\eta = - \frac{\langle W_1 \rangle + \langle W_3 \rangle}{\langle Q_2 \rangle} = 1 - \frac{\omega_1}{\omega_2}, \quad (3.29)$$

which is unaffected by the squeezing (it cancels out) and equal to Eq. (3.15). This is an important statement, since it shows that by employing squeezed thermal reservoirs, we

### 3. Results of analytical and numerical investigations

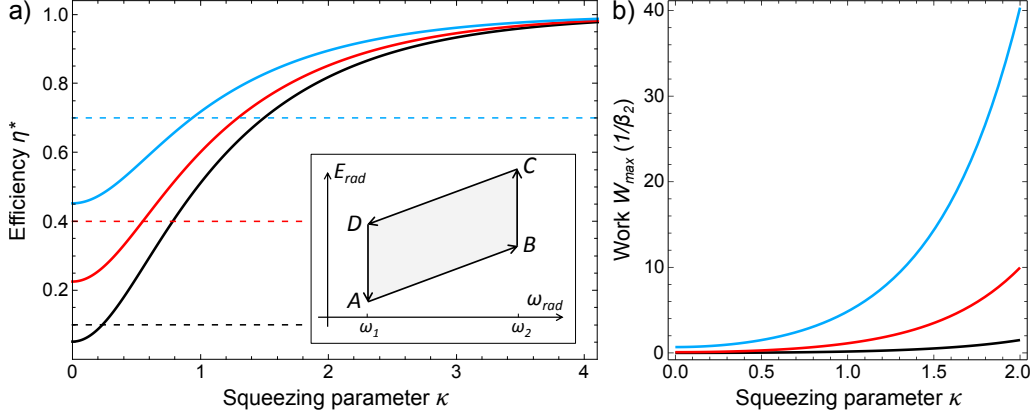


**Figure 3.8.** – (a) Efficiency at maximum power  $\eta^*$  of the Otto engine, Eq. (3.18), plotted as a function of the squeezing parameter  $r$ . Black, red and blue lines correspond to the temperature ratios  $\beta_2/\beta_1 = 0.9, 0.6$ , and  $0.3$ , respectively. The dashed lines in the corresponding color denote the standard Carnot efficiency for each temperature ratio. The inset shows the energy-frequency diagram of an idealized Otto cycle. Squeezing is applied during the hot bath interaction between points B and C, leading to an increase of  $\eta^*$  with  $\kappa$ , approaching unity exponentially. (b) The corresponding maximum mean work  $\langle W \rangle_{max}$  normalized to  $1/\beta_2$  and using a frequency ratio  $\omega_2/\omega_1$  according to the optimality condition Eq. (3.31).

do not influence the intrinsic energy conversion process of the heat engine. However, the squeezing provides additional energy to the system. Because of the constant  $\eta$ , the mean work of the engine increases with increasing input energy,

$$\langle W \rangle_{ht}(\kappa) = \langle W_1 \rangle + \langle W_3 \rangle = \frac{1}{\beta_1} \left( \frac{\omega_2}{\omega_1} - 1 \right) + \frac{1}{\beta_2} \left( \frac{\omega_1}{\omega_2} - 1 \right) \cdot (1 + 2 \sinh^2 \kappa), \quad (3.30)$$

where we used again the high temperature approximation. As a consequence of the enhanced output power, the efficiency at maximum power  $\eta^*(\kappa)$  rises. To calculate  $\eta^*(\kappa)$ , we follow the procedure as above and maximize the mean work Eq. (3.30) with respect to the frequency difference  $\Delta\omega = \omega_2 - \omega_1$ , while we keep all parameters but  $\omega_2$  constant. In the high-temperature limit,  $\hbar\beta_i\omega_i \ll 1$ , we find that the power is maximum when the frequencies satisfy the condition

$$\frac{\omega_2}{\omega_1} = \sqrt{\frac{\beta_1(1 + 2 \sinh^2 \kappa)}{\beta_2}}. \quad (3.31)$$

As a result, the efficiency at maximum power is given by

$$\eta^*(\kappa) = 1 - \sqrt{\frac{\beta_2}{\beta_1(1 + 2 \sinh^2 \kappa)}}, \quad (3.32)$$

an expression which depends explicitly on the degree of squeezing  $\kappa$ . For thermal reservoirs ( $\kappa = 0$ ), this equation is equivalent to  $\eta^*$  in Eq. (3.18). Remarkably,  $\eta^*(\kappa)$  rises with increasing  $\kappa$  and approaches unity exponentially for large  $\kappa$ ,

$$\eta^*(\kappa \gg 1) \simeq 1 - \sqrt{2 \frac{\beta_2}{\beta_1} \exp(-2\kappa)}. \quad (3.33)$$

Fig. 3.8 shows the increasing  $\eta^*(\kappa)$  and the corresponding maximum work output  $\langle W \rangle_{\max}(\kappa)$  for different temperature ratios. While the Curzon-Ahlborn efficiency for thermal systems is by definition smaller than the standard Carnot efficiency, which is indicated by dashed lines in Fig. 3.8 (a), we observe that  $\eta^*(\kappa)$  may surpass this classical limit even at moderate squeezing parameters. Thereby it demonstrates how non-thermal reservoir interactions may be employed to reach a regime which is inaccessible for pure thermal systems. However, following from the second law for this non-equilibrium situation, the efficiency is bound by a generalized Carnot efficiency [Hua12, Aba14],

$$\eta_C^{gen} = 1 - \frac{\beta_2}{\beta_1(1 + 2 \sinh^2(\kappa))}. \quad (3.34)$$

Note that the standard Carnot efficiency is an expression of the second law for one particular configuration: two thermal reservoirs at two different temperatures. Eq. (3.34) extends this result to a more general non-equilibrium setting that involves one thermal and one non-thermal reservoir. Comparing Eq. (3.34) to the standard Carnot efficiency,  $\eta_C = 1 - \beta_2/\beta_1$ , indicates that non-thermal reservoirs may be characterized by an effective temperature  $T^{\text{eff}}$  in order to obtain the familiar form of the laws of thermodynamics [Rei02a, Aba14]. For a squeezed thermal reservoir we find

$$T_2^{\text{eff}} = T_2 \left( 1 + 2 \sinh^2(\kappa) \right). \quad (3.35)$$

Consequently, squeezing a thermal reservoir can be seen as an amplification of its thermal energy, increasing its total energy depending on its temperature. When coupled to an engine, the increase of the output power strongly depends on the initial temperature of the reservoir,  $T_2 = 1/(k_B \beta_2)$ , see Fig. 3.8 (b).

### 3.3.2. Numerical simulations

To support our analytical findings, we consider again the realistic proposal for an Otto heat engine presented in the section above. We have performed semiclassical Monte-Carlo simulations of the Otto cycle using the same methods as before. We assume trap frequencies of  $\omega_r/2\pi = 3$  MHz and  $\omega_z/2\pi = 36$  kHz at the position of the ion. The angle of the electrodes is  $\theta = 20^\circ$  and the distance of the ion to the radial electrodes is  $r_0 = 1$  mm.

The coupling to the reservoirs is mimicked as before by a combination of the velocity dependent scattering forces of a laser beam and electric field noise on the trapping field, both acting on the radial degrees of freedom. In the presence of a hot squeezed thermal reservoir, the radial state of the ion equilibrates to the temperature of the reservoir, but is additionally squeezed during the interaction [OV91]. We mimic the coupling to such a squeezed thermal reservoir by combining reservoir engineering (for the thermal component) and state engineering (for the squeezed component) techniques. Squeezing of the *radial* state of the ion is implemented by modulating the radial confining potential at double the trap frequency [Jan92, Gal09]. In order to make sure that no work is done on the *axial* degree of freedom, the squeezing operation is implemented in such a way that the mean value of the potential energy is not changed after the operation. To this aim, the radial trap frequency  $\omega_r$  is first increased to  $\omega_r' = \omega_r + \Delta\omega$  for a quarter of a radial oscillation period,  $t' = 2\pi/(4\omega_r')$ . Then the frequency is lowered to  $\omega_r'' = \omega_r - \Delta\omega$  for another quarter of a radial oscillation period,  $t'' = 2\pi/(4\omega_r'')$ , before it is returned to its

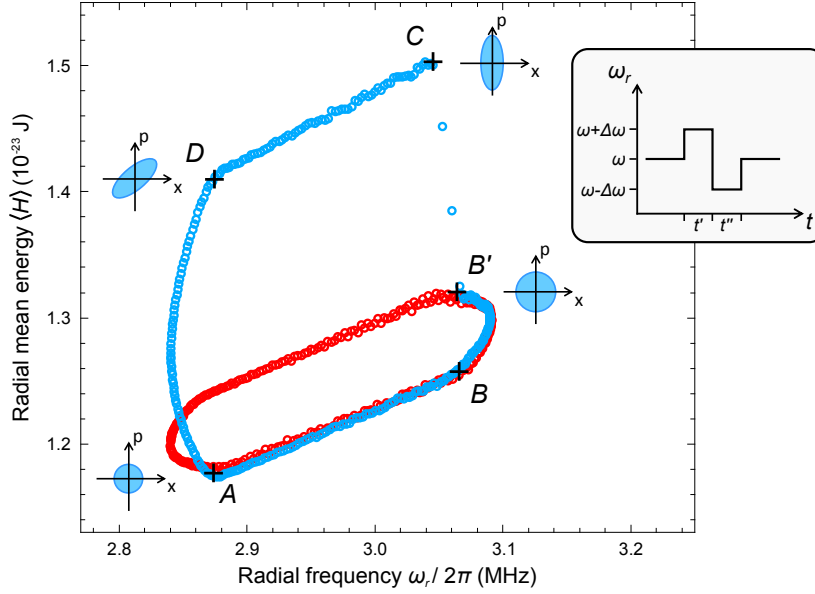


**Figure 3.9.** – Comparison of simulated Otto cycles of the single-ion heat engine, with two thermal reservoirs (red) and with a hot squeezed thermal reservoir (blue). The corresponding phase-space distributions of the states are sketched next to points A, B', C and D, showing the change in temperature of a thermal state (rotational symmetric Gaussian distribution) and the squeezing of those states (ellipses). The interactions with the hot thermal bath (B'B) and the squeezing operation (B'C) are performed sequentially to discriminate both effects in their dynamics. The squeezing leads to a significant increase of the produced work. In order to suppress effects of micromotion, a 5 MHz Fourier low pass filter has been applied. Inset: Squeezing operation applied between points B' and C. The radial trap frequency  $\omega_r$  is parametrically switched to higher and lower values.

initial value  $\omega_r$  (see inset in Fig. 3.9). The implications of this squeezing operation, as well as alternative techniques, are discussed in Secs. 3.3.3 and 3.3.4.

We numerically simulate engine cycles with different  $\Delta\omega$  to achieve different squeezing parameters  $\kappa$ . The thermodynamic Otto cycle of the engine is shown in Fig. 3.9, where a cycle including a squeezed thermal bath (blue points) is compared to that employing pure thermal reservoirs with the same temperature ratio (red points). The difference in the area of the cycles corresponds to the increase in energy due to the squeezing operation. The phase space distribution  $(x, p)$  is sketched for each of the states. In order to analyze the influence of the thermal and the non-thermal part of the reservoir interaction separately, we simulate the coupling to the squeezed thermal bath in two consecutive steps: first by heating the radial state of the ion, followed by a squeezing operation. Since the reservoir interaction is assumed to be negligibly short and thus to occur at constant radial frequency, the order and the separation of the two processes has no influence on the dynamics of the engine, but is chosen for a better understanding. Regarding the performance of the engine, not the relaxation process itself, but only the relaxed state matters [Aba15].

The resulting efficiencies  $\eta^*$  are shown in Fig. 3.10, where we matched the frequency ratios to the optimality condition Eq. (3.31). At a fixed ratio of the bath temperatures of  $\beta_2/\beta_1 = 0.88$  we attain good agreement with the theoretical prediction for  $\eta^*(\kappa)$ , Eq. (3.32), for different squeezing parameters in the range  $0 < \kappa < 0.4$ . The maximum

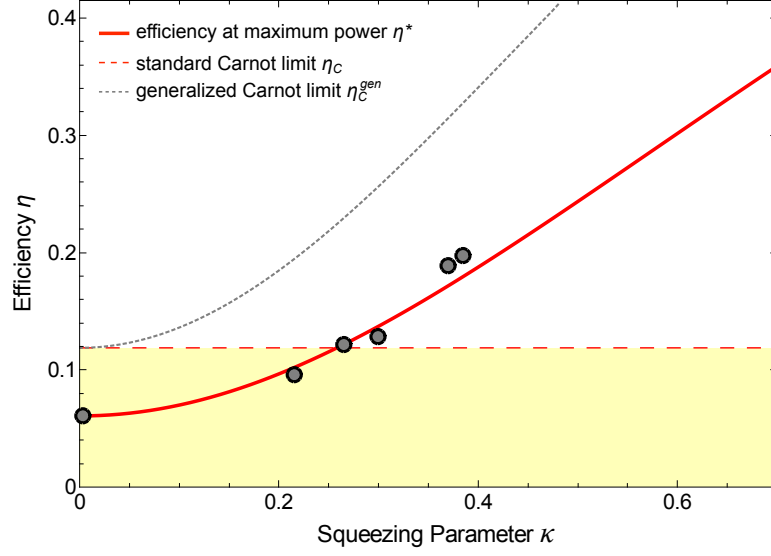


**Figure 3.10.** – Numerical simulation of the efficiency at maximum power  $\eta^*(\kappa)$ , given by the generalized Curzon-Ahlborn efficiency (3.32), as a function of the squeezing parameter  $\kappa$  (solid red line), at a fixed temperature ratio of  $\beta_2/\beta_1 = 0.88$ . The region below the red dashed line (yellow shaded) corresponds to possible efficiencies with purely thermal bath interactions, bounded by the standard Carnot limit. The results of the Monte-Carlo simulations (black dots) demonstrate with the given trap geometry that by squeezing the thermal state with  $\kappa \sim 0.4$  the efficiency can be increased by a factor of four, which is two times higher than the corresponding standard Carnot bound. The black dotted line shows the generalized Carnot limit Eq. (3.34) for an engine interacting with a hot squeezed thermal bath.

ratio  $\omega_2/\omega_1$  is limited by the opening angle  $\theta$  of the funnel-shaped potential and by a maximum amplitude  $a$  for the axial coherent oscillation. Considering realistic trapping potentials, this amplitude is chosen to be smaller than  $a < 1$  mm [Vah09]. These constraints limit the achievable squeezing parameters to  $\kappa < 0.5$  at maximum power. We observe that for a squeezing parameter of  $\kappa \simeq 0.4$  the efficiency is quadrupled and two times higher than the standard Carnot limit. To achieve an comparable efficiency with pure thermal reservoirs, maintaining a maximized power output, an increase of the temperature ratio by 70 % would be needed, whereat the output power is still 35 % lower than for an engine which employs squeezing. These numbers underpin the power of non-thermal reservoirs in the context of nanoscopic engines.

### 3.3.3. Generation of squeezing

Let us now focus on an experimental realization of a squeezed thermal reservoir interaction for trapped ions. Thermal reservoirs at different temperatures are engineered via Doppler cooling and tailored electrical noise on the trap electrodes [Tur00a]. Squeezing of the ground-state wave function of a trapped ion was first demonstrated using resolved sideband excitation on the second motional sideband [Mee96]. However, this approach requires a system initially in the ground state and long interaction times. As described above, to realize squeezing for any initial temperature is to modulate the harmonic potential at double the trap frequency [Jan92, Gal09]. This leads to an elliptical deformation of the phase space distribution of the thermal state (see Fig. 3.9), which is the signature



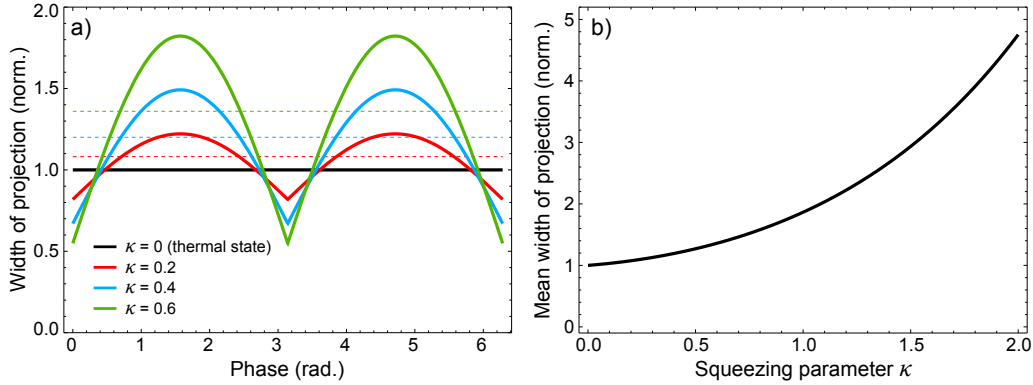


**Figure 3.11.** – Comparison of the width of pure thermal and squeezed thermal states. (a) Width of the projection of the phase space distribution for one full rotation in phase space, for a thermal state and squeezed states with different squeezing parameters  $\kappa$ , normalized to the width of a pure thermal distribution. Dashed lines give the according mean variance for one full rotation. (b) Normalized mean width of the projection as a function of  $\kappa$ .

of a squeezed thermal state. In combination with the randomized thermal interaction, this operation mimics a coupling to a squeezed thermal reservoir: the squeezed thermal state after interaction corresponds by all means to a state we would expect by relaxation to a fictitious squeezed thermal reservoir.

To our knowledge, such a scheme to generate squeezed states of motion has not yet been implemented experimentally due to the high demands on the control of the electrode voltages. However, in the recent years there has been huge technical progress on the precise and fast control of trapping potentials, allowing for demanding transport operations [Wal12b, Rus14] and the controlled compression of ion crystals [Ulm13]. An instantaneous *bang-bang* control of the trapping field has been demonstrated in 2016 with nanosecond switching, which should be appropriate for the generation of large squeezed states [Alo16a].

However, a more sophisticated approach for the implementation of squeezed reservoirs for trapped ions has been recently demonstrated experimentally, where a dissipative relaxation from a ground state into a squeezed state of motion is realized [Cir93, Kie15]. However, this requires the ions to be in the ground state of motion and the timescale of the relaxation process is not yet short enough to meet the demands for our heat engine system. But, certainly, this is the right path to follow.

For the characterization of the resulting squeezed states, an analysis by side-band spectroscopy would be the appropriate choice [Mee96, Zen95, Cir93], while the work output leads to an increasing amplitude of the oscillation in the axial direction, which may be analyzed on camera images or again by sideband spectroscopy [Wal12b].

#### 3.3.4. Remarks on the generation of work and the notion of efficiency

Now, we have closer look on the proposed generation of squeezed states. By modulating the confinement in radial direction, the second moment of its probability distribution (its variance) is accelerated, while the first moment (its center of gravity) stays unchanged. Therefore, an external energy source has to perform work on the distribution of the ion, and thereby increases its total energy. This is a unitary operation with no entropy change and thus no heat transfer. However, the external work is performed on the

radial mode only (agent), while the axial mode (piston) stays unaffected. The probability distribution of the axial degree of freedom and its higher moments are not changed. Consequently, no direct work is performed on the piston by the squeezing operation<sup>2</sup>, but only indirectly by the mode coupling mechanism of the engine. Note, that the coupling mechanism between agent and piston is designed such that it only senses the change in the mean variance between low and high energy states of the agent and translates it into mechanical work of the piston. It is not sensitive to any phase information of the squeezed state, since  $\omega_r \gg \omega_z$ . As the mean variance of a squeezed thermal state is higher than the one of a pure thermal state with same energy, see Fig. 3.11, it results in a higher output power.

We end this section with a short note on the energy sources of reservoirs in thermodynamics: as we have mentioned in Sec. 2.3, it is agreed that the energetic costs of preparing and providing the reservoirs are not included in the efficiency balance. As a consequence of this general agreement, only the energy of the state after relaxation with the reservoir enters, and, in our case, the dynamics of the relaxation process and the way of how the energy is provided does not enter the efficiency balance. Therefore, the work performed on the radial state may be seen as the work required to generate the reservoir.

### 3.4. Conclusion and Outlook

In this chapter we have presented an analytical framework to describe the dynamics of an Otto cycle for a harmonic oscillator, which is valid in the classical as well as in the quantum regime. We have derived and analyzed the work and the efficiency at maximum power. We have combined the analytical framework with a numerical study of our proposed single-ion heat engine setup, which represents, in our case, a classical harmonic oscillator in a very good approximation. We have demonstrated the experimental feasibility of our approach and have shown that, indeed, the efficiency at maximum power may be reached by our system for a wide range of parameters. Furthermore, we have pointed out how our system can be extended to engineered non-thermal reservoirs, and that the efficiency at maximum power can be enhanced dramatically. The use of non-thermal reservoirs offers additional degrees of control and manipulation, which may be exploited to increase the work generation.

Our system may operate as a heat pump by inverting the sense of the rotation of the thermodynamic cycle. In this way, a temperature difference can be generated between two reservoirs initially at the same temperature, transferring heat from a cold to a hot reservoir. Such a nano refrigerator may be useful to cool various kinds of oscillators by coupling it to their motional degrees of freedom. The transfer of our analytical framework to quantum refrigerators has been done for thermal heat baths by Abah and Lutz [Aba16], and for the squeezed thermal reservoir approach by Long and Liu [Lon15b], both in close cooperation with us.

The following part of this thesis is dedicated to the experimental realization of the single ion heat engine, operated in a classical regime with thermal reservoirs at temperatures which are high as compared to the quanta of the harmonic oscillator.

<sup>2</sup> The small radial frequency change seen in Fig. 3.9 is due to the axial motion  $z(t)$  of the ion during the squeezing, and not to the squeezing itself. A similar effect is observed during the interaction with the thermal bath BB'.



# 4

## Setup of the experiment

The experimental setup of the heat engine system consists of the funnel-shaped ion trap inside a vacuum chamber, an electronic supply system, as well as different laser systems for ionizing calcium atoms and for cooling and manipulating the trapped ions. The individual parts are presented and discussed in detail in following sections.

### 4.1. The funnel-shaped ion trap

The heart of this experiment is the funnel-shaped Paul-trap, see Sec. 2.4, which provides the tapered trapping potential where the heat engine mechanism is based on. Since our trap is the first of its kind, we decided to keep its geometry as simple as possible. We use a macroscopic rod trap design, composed of two flat end-cap electrodes, four cylindrical radio-frequency (rf) electrodes, as well as four cylindrical biasing electrodes. The trap assembly is shown in Fig. 4.1. We chose an angle of  $\phi = 10^\circ$  between the rf-electrodes and the trap axis. This angle provides a reasonable coupling between the radial and the axial degrees of freedom, while it still guarantees stable trapping conditions. In order to bring the rf-electrodes as close together as possible on the narrow side of the funnel, electrodes with a small diameter are required. We use commercial syringe needles<sup>3</sup> with an outer diameter of only 0.8 mm as electrodes. The needles are made of stainless steel, they provide a high manufacturing quality and are perfectly straight over a length of several centimeters. Further discussion about the installation of these electrodes is provided in App. A.1. At the narrow side of the funnel geometry, the electrodes are mounted with a distance of  $\sqrt{2}$  mm to trap axis.

As end-caps we use  $25 \times 25$  mm plates of machinable glass-ceramics<sup>4</sup> with a thickness of 4 mm. These plates also serve as mounts for the trap-electrodes and thus facilitate the construction of the trap, see Fig. 4.2. The inner faces of the ceramic plates are coated with a nickel-molybdenum bonding-layer (150 nm) and a top-layer of gold (100 nm)<sup>5</sup>. This coating provides an electrically conductive surface with little surface reactivity [Sch09]. The distance between the end-caps is chosen to be 8 mm, which is a compromise between a small geometry, a solid construction, and undisturbed electric field lines of the radial trapping field at the center of the trap. Additionally, the end-caps have a hole in their

<sup>3</sup> Sterican 21G cannula, Braun Melsungen AG.

<sup>4</sup> Machinable Glass Ceramic MACOR, Corning Inc.

<sup>5</sup> The bonding layer has been evaporated by the group of Prof. W. Heil. The gold layer has been applied by the group of Prof. M. Kläui. We thank both groups for their cooperation

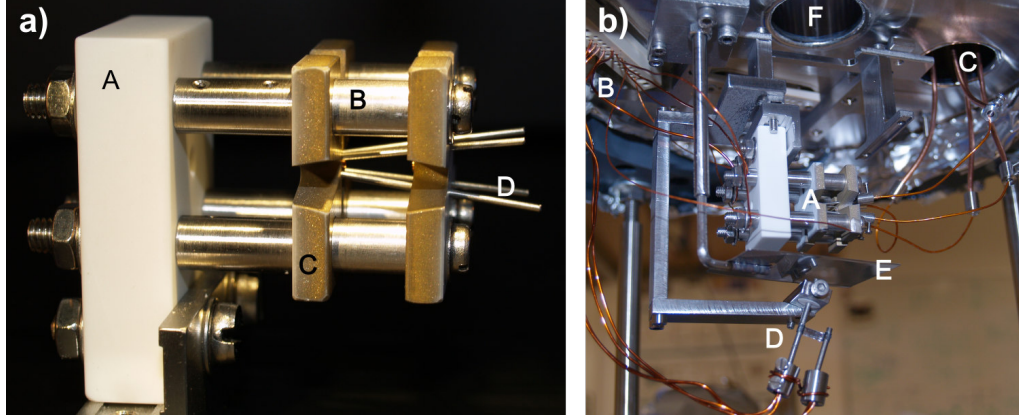


**Figure 4.1.** – Images of the funnel-shaped ion trap. a) Trap after assembling, composed of an isolating ceramic mount (A), four outer-electrodes (B), two gold-coated ceramic end-caps (C) and the four rf-electrodes in funnel geometry (D). b) Top flange of the vacuum chamber with mounted trap (A), multi-pin static voltage feed-through (B), the four rf-feed-throughs (C), the calcium oven in its holder (D), a mechanical shutter for the atom beam (E) and an optical access for the laser beam in vertical directions, which addresses the radial degrees of freedom of the ion (F).

center to give access to a laser beam propagating along the trap axis. The diameter of the holes is 1.0 mm, which allows for using a laser-beam with a homogenous intensity profile over the center region of the trap without causing stray light from the electrodes. Again, stray light of the laser beams may lead to charges on ceramic surfaces, which distort the trapping potential. To prevent charging processes, a small copper tube with a length of 2 mm is inserted to the center holes on the trap-side and electrically connected to the coating. The holes constrain the minimum distance of the rf-electrodes from the trap axis to be no smaller than 1 mm and thus restrict the geometry of the trap to the dimensions chosen for our design.

To compensate for external electric stray fields and thereby to minimize micromotion, an additional set of four cylindrical biasing electrodes complements the trap setup [Ber98]. The electrodes have a linear and parallel geometry and are placed behind the four rf-electrodes, as shown in Fig. 4.2. To provide a rigid geometry we chose a diameter of the outer-electrodes of 6 mm and a distance of 10 mm to the trap axis. Additionally, since the diameter of these electrodes is much larger than the one of the rf-electrodes, they provide a strong effect on the electric field at the center of the trap and only small voltages are needed to move the ion to the node of the rf-field. This feature becomes important when heating the ions with electrical noise via these outer electrodes, since low noise amplitudes are sufficient to heat the ion considerably. To assure an electrical isolation between the electrodes and the end-caps, the gold coating has been removed on a 0.1 mm band around the mounting holes of all electrodes.

##### 4.1.1. The radio-frequency supply

In order to trap ions at reasonable trap frequencies, rf-signals with several hundred Volts amplitude on the trap electrodes are needed. The rf-signal is generated by an analogue signal generator<sup>6</sup> and amplified by a 2 W amplifier<sup>7</sup>. A helical resonator is employed

<sup>6</sup> Signal Generator SMS2, Rohde & Schwarz GmbH & Co. KG.

<sup>7</sup> ZHL-1-2W, Mini-Circuits. Water cooled to reduce temperature fluctuations.

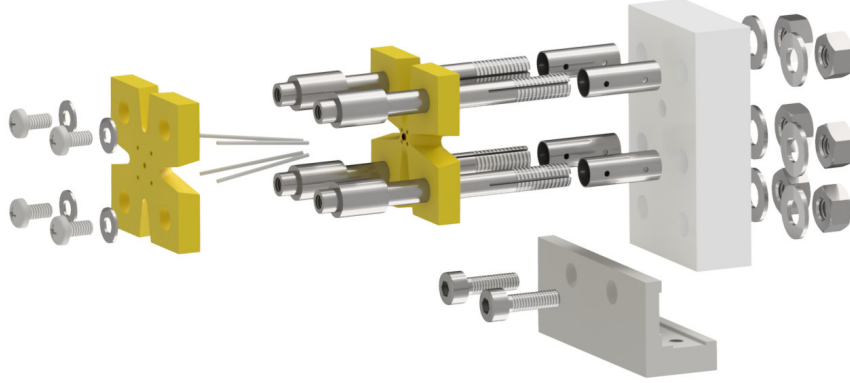


**Figure 4.2.** – Exploded-view drawing of the ion trap setup. The trap electrodes are mounted between the two gold-coated end-caps, which are held by the outer electrodes. The whole trap setup is mounted on a ceramic holder. The cutouts in the end-caps allow the optical access to the center of the trap for the individual laser beams along diagonal directions.

for impedance matching between the 50 Ohm rf-source and the high impedance ion-trap [Mac59, Tol14]. The helical resonator is essentially a shielded LC circuit. A copper coil, placed inside a metal cylinder, represents the inductance as well as a cylindrical capacitor. The impedance of the ion trap, the cables and the vacuum feed-throughs provide the load impedance and thus contribute to the resonance frequency of the entire system [Siv12]. The rf-electrodes dominate the load impedance and provide a capacitive load with  $C_t = 3.9$  pF for each of the electrodes, and with negligible resistance and inductance. The absolute value of the impedance for a purely capacitive load reads  $|Z_t| = [\Omega_{\text{rf}} C]^{-1}$ . Consequently, for typical drive frequencies of  $\Omega_{\text{rf}}/2\pi \approx 20$  MHz the trap impedance  $|Z_t| \approx 10^5$  Ohm is much larger than the impedance of the rf-source,  $|Z_s| = 50$  Ohm. For this reason, a variable impedance matching is indispensable.

As mentioned in Sec. 2.4.3, we use an anti-symmetric rf-drive signal fed to the four trap electrodes. Such a signal is obtained by employing a helical resonator in  $\lambda/2$ -geometry, where the coil has a ground connection at its center and the two open ends are connected to the trap electrodes. Fig. 4.3 (a) shows a cutaway-model of our helical resonator design. The rf-signal is coupled to the coil via a variable sliding-contact. The resulting oscillating voltage inside the resonator system has a node at the center and two anti-nodes at the open ends. Variable capacitors at the output of the resonator allow for a fine adjustment of the phase and the amplitude ratio of the output signal, see Fig. 4.3 (b). Additionally, two capacitive dividers on the resonator outputs allow to monitor an rf-signal with reduced amplitude. In our setup, we employ two pieces of BNC-cables with different lengths (RG-58 with a capacity of 68 pF/m) to realize a divider with a little total load capacity. The division factor is then defined by the length ratio of the two pieces and has been measured to be  $\kappa = 118$ . The recorded monitor signal is presented in Fig. 4.4, with a resulting resonance frequency of the entire oscillating circuit of  $\Omega_{\text{rf}}/2\pi = 21.41$  MHz. Since  $\Omega_{\text{rf}}$  is large compared to all trap frequencies, crosstalk and resonance effects are avoided. A high  $\Omega_{\text{rf}}$  reduces the amplitude of the residual micromotion, but requires higher amplitudes of the driving signal to achieve the desired trap frequency  $\omega$  [Lei03]. With this setup, we reach amplitudes of  $V_\Omega \approx 1$  kV

#### 4. Setup of the experiment

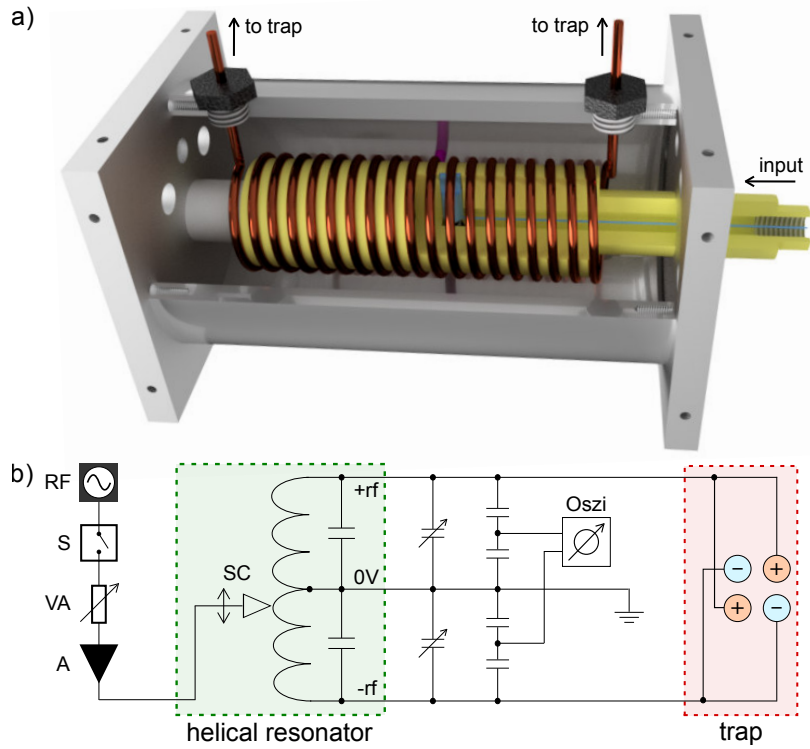


**Figure 4.3.** – The helical resonator in  $\lambda/2$  geometry. (a) Cutaway-drawing of the silver-coated housing and the helical resonator (HR) with mass contact (magenta) at the center of the copper coil. A threaded Teflon cylinder (yellow) is screwed inside the coil; it moves the sliding contact (blue) along the coil and allows for precise impedance matching. (b) Equivalent circuit diagram of the HR setup. The rf-signal at 21.41 MHz is provided by a signal generator (RF). A switch (S) and a variable attenuator (VA) allow to manipulate the trap potential. The rf-signal is amplified by a 2 W amplifier (A) and fed to the inductivity of the HR by the sliding contact (SC). The HR has additional variable capacities on both output channels to adjust for deviations of the rf-signal on the trap electrodes. Capacitive dividers allow to monitor the rf-signal on a 2-channel oscilloscope (Oszi). The two output signals with opposite sign drive the capacitive load of the 4 trap electrodes in a diagonal configuration.

peak-to-peak on the trap electrodes, resulting in secular frequencies of the trapped ion in the radial directions of  $\omega_{x,y}/2\pi \approx 500$  kHz. A switch<sup>8</sup> and a variable attenuator<sup>9</sup> allow for clearing the trap and for controlling the depth of the trapping potential precisely. While a perfect anti-symmetric trap drive prevents the ion from any micromotion in axial direction, a phase shift and an amplitude mismatch between the two signals causes residual micromotion. From the monitor signal in Fig. 4.4 (a) we deduce a phase shift between the two outputs of  $\Delta\phi = 179.74(6)^\circ$ , thus a resulting phase error of  $\delta\phi < 0.3^\circ$ . The relative amplitude difference is measured to be  $\Delta V_\Omega/V_\Omega = 4.8\%$ . Both effects add up to an excess axial micromotion, depending on the displacement  $d$  of the ion from the node of the rf-field. For the given parameters and an axial displacement of  $d = 50\ \mu\text{m}$ , the micromotion has been simulated to provide an amplitude of  $a < 50$  nm. Its relative amplitude of  $a/d < 0.1\%$  is negligible for all applications within this thesis. Note that not

<sup>8</sup> ZYSWA-2-50DR, Mini-Circuits.

<sup>9</sup> ZX73-2500-S+, Mini-Circuits.

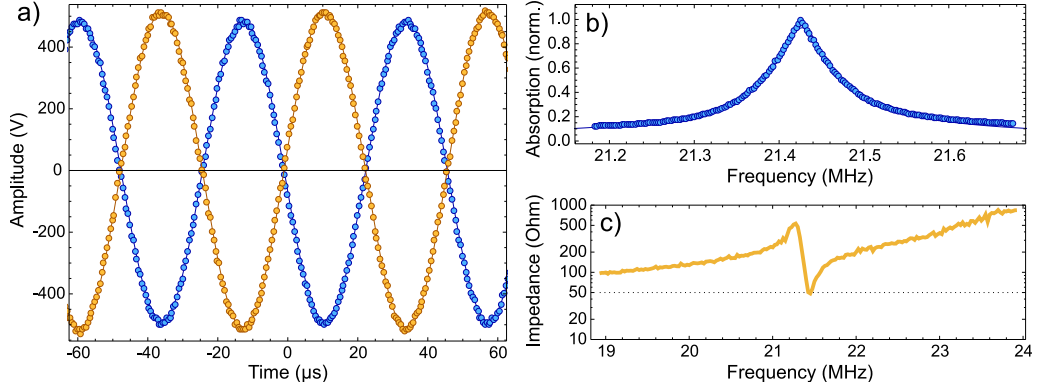


**Figure 4.4.** – (a) Opposing radio frequency signal on the two output lines of the helical resonator, measured via the capacitive dividers and multiplied by  $\kappa$ . Fitted sine-functions reveal a relative phase of  $\Delta\phi = 179.74(6)^\circ$  between the two signals and a relative amplitude difference of  $\Delta A / A = 0.05$ . (b) Spectrum of the normalized power absorption of the resonance circuit. The full width at half maximum  $\Delta\Omega = 92(1)$  kHz reveals a  $Q$ -factor  $Q = 237(3)$ . (c) Impedance of the resonance circuit as a function of the probe frequency. The resonator is tuned to match the 50 Ohm impedance of the input signal at resonance.

using an anti-symmetric trap drive would result in a relative micromotion of  $a/d = 6\%$  for a similar displacement, see [Tol14].

The measured spectrum of the power absorption of the helical resonator system is shown in Fig. 4.4 (b). The fit of a resonance curve reveals a quality factor of the entire resonator system of  $Q = \Omega_{\text{rf}} / \Delta\Omega_{\text{rf}} = 237(3)$  [Dem08]. Therefore, the resonator provides a good filtering of the input signal and suppresses electric noise as well as higher orders of the drive frequency efficiently, see [Tol14]. The quality factor corresponds to the amplification of the input signal by the resonator,  $V_\Omega = QV_{\text{in}}$ , and allows to provide rf-signals with high amplitudes  $V_\Omega$  to the trap electrodes. The effect of the helical resonator on the impedance of the entire resonator system is shown by a measured spectrum in Fig. 4.4 (c). At the resonance frequency, the impedance of the system matches 50 Ohm and thus the reflected part of the input signal is strongly reduced.

#### 4.1.2. The constant voltage supply

Ambitious experiments with trapped ions impose high demands on the constant voltages applied to the trap electrodes, since any electrical noise leads to artificial and undesirable heating-rates [Bro15]. In our experiment, the end-caps and the biasing-electrodes are supplied with constant voltages from a 12-channel low noise DAC (Digital-to-Analog Converter) unit, which has been developed in our group<sup>10</sup>, see [Zie12]. It provides an actively stabilized voltage in the range of -10 V to +10 V with 16-Bit resolution and a noise level below 20  $\mu\text{V}$ . Typical voltages on the end-caps are 7.0 V on the wide side of the taper and 9.0 V on the narrow side, leading to an axial trap frequency of  $\omega_z/2\pi = 170$  kHz. In order to reduce the excess micromotion, the outer-electrodes are biased with typical voltages between 0.9 V and 3.5 V. Furthermore, two opposing outer-electrodes have an additional offset of 1.5 V in order to break the symmetry of the radial trapping potential and to lift the degeneracy of  $\omega_x$  and  $\omega_y$ . The individual DAC channels are controlled by

<sup>10</sup> Op40 DC Segment Controller, H. Lenk, University of Mainz.



#### 4. Setup of the experiment

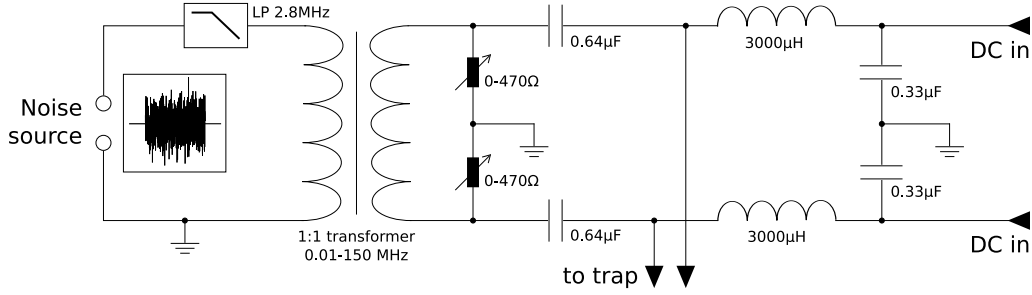


**Figure 4.5.** – Electronic setup of the noise inversion circuit. The noise signal is provided to a balance-unbalance transformer with an equal turns ratio and a low frequency cut-off far below the switching frequency. To eliminate high frequency terms, we use an additional low pass filter (LP). The resulting signals on both output lines of the secondary coil have the same amplitude but inverted sign. A bias-tee in both lines allows to superpose the noise signal with the static voltage (DC), which is used for compensating micromotion. Variable resistors allow to adjust for differences in the amplitudes on both lines.

a field-programmable gate array<sup>11</sup> (FPGA), allowing for fast and precise voltage changes at a clock frequency of 50 MHz. Additionally, the FPGA controls a 30-channel TTL-unit, which triggers all time-relevant components of the experiment.

##### 4.1.3. Electric field noise

As we will shown in Sec. 6.1.2, the most efficient way for controlled heating is to expose the trapped ion to a combination of white electric field-noise and laser cooling. A Gaussian probability distribution of the noise signal then guarantees the generation of hot thermal states of the ion. In our setup, electrical noise is provided to two opposing outer-electrodes, thus effecting the radial component of the trapping field.

However, by applying the electric field noise to the electrodes, we want to excite a thermal Brownian motion of the trapping potential without changing the external parameters like the trap frequencies. Therefore, we need to superpose the trapping potential with a position independent electric noise field. This is reached by applying the same noise signal with inverted sign on two opposing outer-electrodes. In the experimental setup, we achieve a differential noise signal by feeding the noise to a balun transformer<sup>12</sup>, as shown in Fig. 4.5. White and Gaussian voltage noise causes naturally a white and Gaussian current noise in the primary and secondary windings of the transformer. When identical loads are connected to each side of the secondary windings, the current in both loads has the same absolute value but inverted sign. As a result, the voltages on the two outer-electrodes, being capacitive loads, have the same amplitude but inverted sign as well. A measurement of the two noise signals is presented in Fig. 4.6, together with the sum of both. For the given exemplary voltage signals, the residual standard deviation of the summed signal increases by 0.014 V above the background signal when noise is applied. This increase leads to a fluctuation of the radial trap frequencies, but is negligible as compared to the standard deviation of the noise signals, 0.3 V, and even more as compared to the trapping fields  $V_{\Omega}$ . Consequently, applying the same noise signal with inverted sign to opposing outer electrodes results in

<sup>11</sup> Avnet Virtex-5 FXT Evaluation Kit, Avnet electronics marketing, Phoenix, USA.

<sup>12</sup> FTB-1-6\*A 15+, Mini-circuits.

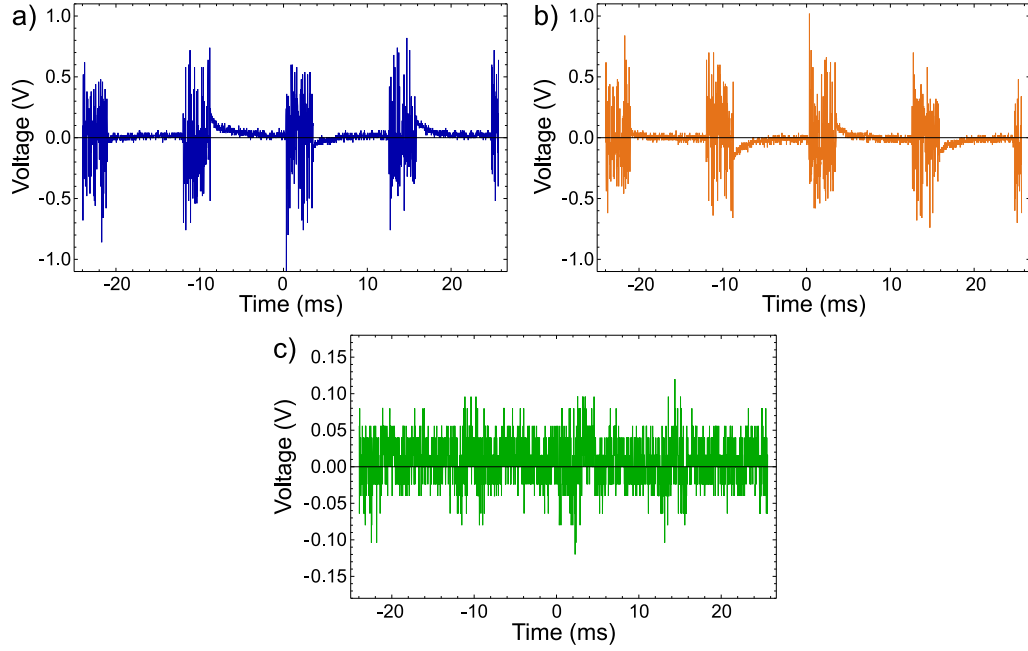


**Figure 4.6.** – Noise signal which is fed to the electrodes. (a) and (b) Original and inverted noise signal after the inversion circuit. As it is needed for the heat engine operation, the noise is switched on and off with a repetition rate of 82 kHz and a duty cycle of 0.3. (c) The sum of the original and the inverted noise signal. The two signals cancel each other to a remaining standard deviation by 0.014 V above the background signal.

a random movement of the trap potential with negligible effect on the trap frequencies.

#### 4.1.4. Loading ions into the trap

The  $^{40}\text{Ca}^+$ -ions are loaded into the trap by ionizing neutral calcium atoms within the trap volume. Therefore, we use a resonant two step photo-ionization process. The neutral atoms are thermally evaporated from a hot cavity. We resistively heat the rear part of a titanium tube, filled with granular calcium, with a typical current of 5.2 A. The effusing atoms are collimated and directed by the extended geometry of the oven tube in order to pass the volume of the trap. Inside the trap, the atoms are first resonantly excited and then non-resonantly ionized [Ebl11, Tol14]. As soon as the Ca-atoms are ionized, they are interacting with the (oscillating) electric fields and confined within the trapping potential, as long as their thermal energy is lower than the depth of the potential, typically  $E_{\text{kin}} \lesssim 5 \text{ eV}$ . Subsequently, the ions are Doppler cooled on the  $S_{1/2} \leftrightarrow P_{1/2}$  transition and form crystalline structures at the minimum of the trapping potential due to Coulomb interaction. The increasing Coulomb energy for each additional ion allows to reduce the number of ions deliberately by briefly lowering the potential depth below the corresponding threshold energy, such that, for instance, only one ion remains.

#### 4.1.5. Detection of fluorescence light

The fluorescence light of the trapped ions at 397 nm is collected by a lens system with a numerical aperture of 0.26, see [Ebl11]. The image of the ions is projected onto the photo-

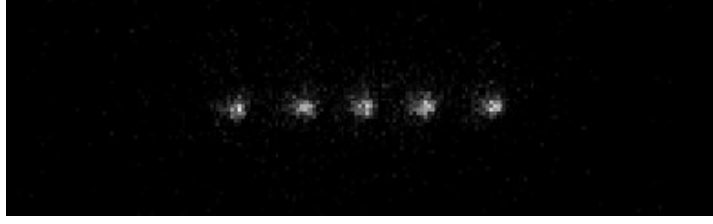


**Figure 4.7.** – Camera image of a linear 5-ion crystal, taken by the EMCCD camera with an exposure time of 100 ms. The corresponding trap frequencies are 170 kHz axial and 420 kHz radial. The distance of the ions is evaluated via the effective pixel size of  $0.667\ \mu\text{m}$  and results to  $18\ \mu\text{m}$  between the neighboring inner ions and  $20\ \mu\text{m}$  between the the outer ions and their neighbors. These values agree with the simulation of an ion crystal at the same trap frequencies.

sensitive chip of a detector. Within this thesis three different devices are employed to detect the fluorescence light of the ion: an EMCCD<sup>13</sup>-camera, an ICCD<sup>14</sup>-camera, as well as a photomultiplier tube<sup>15</sup> (PMT). For detecting the ions we operate the EMCCD-camera with a chip size of  $(8 \times 8)\ \text{mm}$  and  $(1002 \times 1004)$  pixels, providing a quantum-efficiency of 0.4 at 397 nm. For the imaging system, a magnification factor of 12.0(1) is obtained from a comparison of the measured ion distance on camera images and the calculated ion positions from simulations with the given trap frequencies. It leads to a spatial resolution of  $0.667(5)\ \mu\text{m-per-pixel}$  on the camera images, which is sufficient for a precise determination of the ion positions, see Fig. 4.7. An optical bandpass filter<sup>16</sup> reduces the background light at wavelengths different than 397 nm by  $10^{-4}$ . The exposure time of the camera is limited by internal electronic noise originating from thermal excitations within the potential wells of the individual pixels, as well as due to the shift operations during the readout process [Ise15]. These dark-counts compete with the fluorescence-signal of the ion, limited by its scattering rate, the numerical aperture of the objective, as well as the quantum-efficiency of the camera. Using this camera setup, an exposure time of 1 ms is necessary to detect an ion at all, while for a precise determination of the position of the ion the exposure time should exceed 50 ms. This time is long compared to the timescales of dynamic processes of the ion, such as secular frequencies or thermalization processes. In order to circumvent the issue of limited exposure time we have used the PMT and the ICCD-camera for time-critical measurements.

The PMT is well suited for all measurements where short exposure times are crucial, but where no spatial resolution is needed. It provides a quantum efficiency of 0.27 and almost no dark-counts. It records single photons and thus enables us to measure with exposure times of only some microseconds. The PMT is operated in parallel to the camera. A beam-splitter between the objective and the camera reflects 30 % of the fluorescence-light onto the photo-cathode of the PMT. An adjustable aperture in the focus of this beam path suppresses most of the background light. The single-photon events are counted and processed by a self-programmed 50 MHz micro-controller<sup>17</sup> (MC). For more details, see App. A.2. As we demonstrate in Sec. 6.6, we have successfully reduced the exposure time to  $5\ \mu\text{s}$ .

<sup>13</sup> Electron Multiplying Charge-Coupled Device, iXon 885, Andor Technologies Ltd.

<sup>14</sup> Intensified Charge-Coupled Device, PI-MAX4:1024EMB, Princeton-Instruments.

<sup>15</sup> P25PC, Electron Tubes Enterprises Ltd. (now being sold by Sens-Tech Ltd.)

<sup>16</sup> BP 394nm x 10nm OD4, Edmund Optics Ltd.

<sup>17</sup> 32 Bit and 50 MHz, PIC32MX250F128B, Microchip Technology Inc.

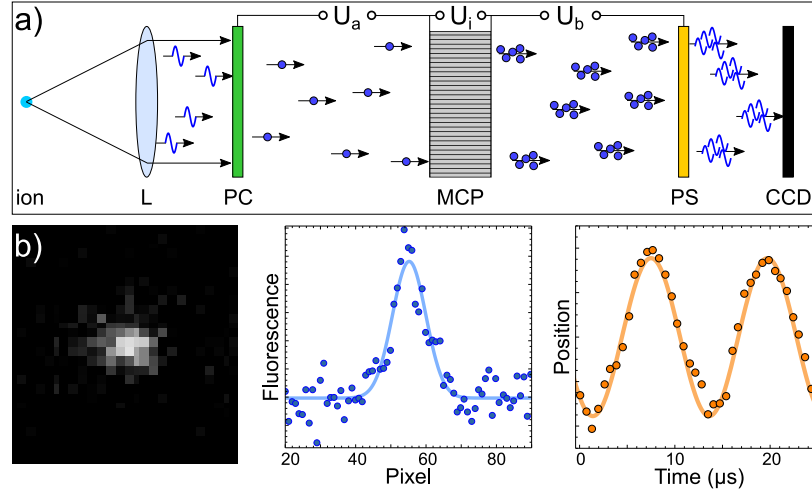


**Figure 4.8.** – Acquisition process of the ICCD camera. (a) Single fluorescence photons from the ion are collected by an objective lens (L) and converted into single electrons by a photo cathode (PC). The electrons are accelerated towards a multi channel plate (MCP) by a control voltage  $U_a$  and multiplied. The resulting electron bunches are accelerated by a constant voltage  $U_b$  onto a phosphorus screen (PS), where they are back converted into photon bunches and recorded by a CCD camera. The gain of the device is controlled by the MCP voltage  $U_i$ . (b) Reconstruction of the ion trajectory. The fluorescence distribution from images integrated on the CCD chip is projected on the trap axis (blue points) and fitted by a normal-distribution (blue line). This precisely reveals the center position of the thermal distribution of the ion. Taking those images at different phases of the oscillation allows to reconstruct the ion trajectory (orange points and line).

To resolve the oscillation of a trapped ion we need both, a time resolution in the microsecond range, as well as a spatial resolution on the micrometer scale. These requirements are complied by the ICCD camera, which combines the advantages of a PMT and a CCD camera. Fig. 4.8 illustrates the acquisition process: the fluorescence photons are converted to electrons by a photo-cathode and accelerated by a voltage difference towards a micro-channel-plate (MCP), where the electrons are multiplied. A subsequent phosphorus-screen converts the electrons back to photons which are detected by a CCD camera. Switching the photo-cathode voltage to a level higher than the MCP voltage, the photo-electrons are repelled by the MCP and detection is avoided. The camera chip provides  $(1024 \times 1024)$  pixels at a size of  $(13 \times 13) \mu\text{m}$ , leading to an effective pixel length of  $1.07(9) \mu\text{m}$  on recorded images. The camera system shows a total quantum efficiency of 0.1 at 397 nm. The gating mechanism allows for exposure times as short as 2 ns. However, to record a resolved oscillation of the ion, we use a typical exposure time of 700 ns. The internal gating is triggered externally and synchronized with the driven oscillation of the ion, and the fluorescence at a fixed phase  $\phi$  of the oscillation is integrated for typically  $10^5$  frames on the CCD-chip. The phase  $\phi$  is then scanned over a full oscillation period and an analysis of the ion position for each  $\phi$  allows to reconstruct the resolved oscillation of the ion [Näg98]. A sinusoidal fit of the data reveals precisely the amplitude of the oscillation and its phase relative to the driving signal. The ICCD camera was a loan from *Princeton-Instruments* and was to our disposal only for a three weeks period<sup>18</sup>.

<sup>18</sup> We thank Princeton-Instruments and especially Norbert Gulde for the collaboration.

##### 4.1.6. Generation of a magnetic quantization field

To apply a static magnetic field in order to provide a defined quantization axis and to lift the degeneracy of the fine structure levels of the Ca-ions, we have mounted two orthogonally oriented coil-pairs in the horizontal plane, as well as one coil for the vertical direction. The coils for the horizontal magnetic field components have each a diameter of 120 mm and 210 windings. They have a distance of 170 mm to the center of the trap and are mounted symmetrically on the flanges of the vacuum chamber. Each opposing coil pair is operated in a quasi-Helmholtz configuration, such that the magnetic field can be assumed to be homogenous over the length of the ion trap. The vertical magnetic field component is generated by a single coil with a diameter of 240 mm and 280 windings, which is placed on the top flange at a distance of 115 mm to the center of the trap, again leading to a nearly homogenous magnetic field inside the trap volume. The individual magnetic field strengths are tuned to compensate for external magnetic fields (mainly the earth magnetic field) and to provide a well defined quantization field of  $B = 4.7 \times 10^{-4}$  T in the horizontal plane. This results in a Zeeman-splitting of the atomic sub-states along the direction of  $\vec{B}$ . At the given magnetic field strength  $B$ , the ground state Zeeman-splitting equals  $\Delta\omega_Z/2\pi = 13.2$  MHz. By choosing the appropriate polarization of the laser beams we can address the sub-states individually. To facilitate the addressing of the individual spin-states of the ion, the direction of the magnetic quantization field is oriented along one of the optical axes of the vacuum-chamber and has an angle of  $45^\circ$  to the trap axis.

##### 4.2. The vacuum setup

In order to reduce the probability of collisions of the trapped ion with background gas particles, we operate the trap setup in an ultra high vacuum (UHV) environment. We use a stainless steel vacuum vessel with a volume of  $1.4 \times 10^{-2}$  m<sup>3</sup>, which is copper-sealed against the environment. Employing a titanium-sublimation pump<sup>19</sup> and an ion-getter pump<sup>20</sup> simultaneously, we reach a final pressure of  $P_{\text{UHV}} < 2 \times 10^{-11}$  mbar. With such a low pressure, the collision rate  $s_r$  of the trapped ion with background gas particles is reduced to  $s_r < 10^{-6}$  s<sup>-1</sup>.

The trap is mounted on the CF200 top flange of the vacuum vessel, as shown in Fig. 4.1. The optical access of laser beams in the horizontal plane, as well as the imaging of the trapped ions, is allowed by 8 CF60-viewports. For the camera objective, an inverted viewport is installed, which allows to place the objective at a distance of 61 mm to the trap center [Ebl11]. In order to provide a laser-cooling beam in the vertical direction, an additional viewport is installed on the top flange. On the bottom side we use a combination of an in-vacuum mirror with a viewport in the sidewall of the vessel, which becomes necessary by the position and geometry of the vacuum pumps.

##### 4.3. The laser system

For ion trap experiments laser light at different wavelengths is needed: for the ionization of Ca-atoms, and for cooling, manipulating, as well as for detecting the trapped Ca-ions.

---

<sup>19</sup> TSP, tectra GmbH.

<sup>20</sup> VacIon Plus 75 StarCell, Agilent Technologies.

As shown in Sec. 2.7, the relevant part of the energy level structure of  $^{40}\text{Ca}^+$ -ions can be reduced to a three-level system with fine-structure levels  $^2S_{1/2}$ ,  $^2D_{3/2}$  and  $^2P_{1/2}$ . The cooling transition  $S_{1/2} \leftrightarrow P_{1/2}$  is addressed by a lightfield near 397 nm. In order to reach a closed cycling transition for effective laser cooling, all the population which decays into the metastable state  $D_{3/2}$  is pumped back to the  $P_{1/2}$  state by a laser at 866 nm. A controlled and efficient excitation of internal states of the ion requires laser-light sources which are stable in frequency and intensity. We employ grating-stabilized diode laser systems, which meet all requirements for our experiments: they are available at the desired wavelengths, they run in single-mode operation with a typical spectral linewidth below 1 MHz (measured in Sec. 6.3), they provide an optical output power on the order of  $10^{-2}$  W, and show a long durability at low maintenance effort. To obtain the demanded frequency stability, the lasers are locked to an external cavity. Fine adjustment of frequency and power, as well as switching of the laser beams, is achieved by acousto-optic modulators (AOM). The wavelengths of all lasers are continuously measured by an 8-channel wavelength-meter<sup>21</sup> with an accuracy of 30 MHz. In the following we will discuss the individual elements of the laser setup.

#### 4.3.1. Laser system for ionizing neutral Ca-atoms

The ionization process of neutral  $^{40}\text{Ca}$ -atoms consists of two excitation steps: first, a resonant excitation from the ground-state  $[\text{Ar}] 4s^2 \ ^1S_0$  to the excited-state  $[\text{Ar}] 4s 4p \ ^1P_1$ , followed by a non-resonant ionization with a photon energy exceeding the ionization potential (IP). The resonant transition has a total width  $\Gamma_I = 35.0$  MHz at a transition energy of  $E_I = 23652.304 \text{ cm}^{-1}$ , corresponding to a wavelength of  $\lambda_I = 422.79230 \text{ nm}$ <sup>22</sup> [Kra15]. In order to drive this transition efficiently, we use a commercial extended-cavity diode laser<sup>23</sup> with a grating in Littrow-configuration, which provides a linewidth of about 1 MHz. An optical power of 2 mW is largely sufficient to saturate the resonant transition rate of  $A_I = 2.2 \times 10^8 \text{ s}^{-1}$  [Kra15]. The resonance wavelength has to account for the Doppler shift of the thermal atoms, depending on the relative direction between the atom beam and the laser beam.

For the non-resonant ionization step, the electron in the excited state absorbs a photon with an energy high enough to overcome the atomic binding energy. Therefore, the photon energy has to be larger than the difference between the excited  $P_1$ -state and the IP at  $49306.3 \text{ cm}^{-1}$  [Kra15]. The non-resonant ionization cross-section, typically of the order of  $10^{-17} \text{ cm}^2$  [Rae10], is low compared to resonant transitions and decreases with increasing photon energy. As a consequence, this process limits the efficiency of the ionization and thus requires a high photon flux density and an energy above, but close to the IP. Therefore, we use a free-running laser diode with a central wavelength at 375 nm and a total output power of 8 mW.

The two laser beams are superposed with a polarizing beam splitter and focused into the trap volume. We achieve typical rates for ionization and subsequent trapping of  $10 \text{ s}^{-1}$ , depending on the atom flux which is set by the temperature of the atom source. Mechanical shutters in both laser beam paths, built from modified loud-speakers [Sin02], allow for controlled loading of a desired number of ions.

<sup>21</sup> WS-U 30, HighFinesse GmbH.

<sup>22</sup> In this thesis, all optical wavelengths are given as vacuum wavelengths.

<sup>23</sup> DL 100, TOPTICA Photonics AG.

#### 4. Setup of the experiment

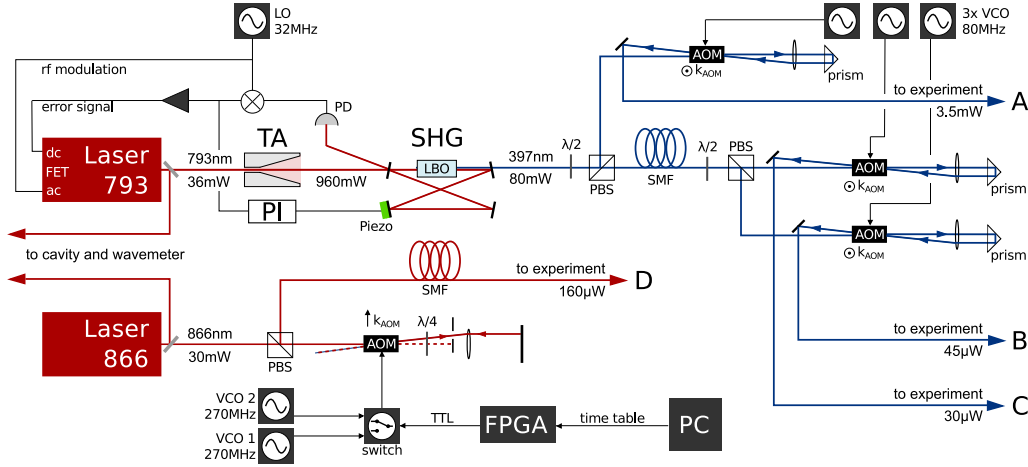


**Figure 4.9.** – Technical scheme of the laser setup for cooling and detecting the ions. The light emitted from the laser diode at 793 nm is amplified in a temperature stabilized tapered amplifier (TA). Subsequent second harmonic generation (SHG) in a Lithium-Triborate (LBO) crystal, placed in a ring cavity, generates a lightfield at 397 nm. Typical laser power on each step is noted. One of the mirrors of the SHG-cavity is mounted on a piezo, where a Pound-Drever-Hall (PDH) locking scheme regulates the cavity length and compensates for thermal drifts. To level out fast frequency fluctuations, the PDH-error-signal is fed to the field-effect transistor (FET) of the current modulation of the laser diode via the dc-input of an internal bias-tee. The 397 nm beam is distributed on different pathways via half-wave plates ( $\lambda/2$ ) and polarizing beams splitters (PBS). Each beam provides an acousto-optic modulator (AOM) in double pass configuration and is guided towards the experiment via single mode fibers (SMF). The second laser diode runs at 866 nm. Its beam passes through an AOM in double pass configuration, which allows for frequency scans in a range of 150 MHz without changing the beam pointing. Two different VCOs connected to the AOM allow for fast and precise frequency jumps, triggered by the field-programmable gate array (FPGA). Both lasers are locked to an external cavity, see Fig. 4.11.

#### 4.3.2. Laser systems for cooling and detecting the ions

The  $S_{1/2} \leftrightarrow P_{1/2}$  dipole transition of the  $\text{Ca}^+$ -ions is used for laser cooling and provides a scattering rate of  $1.4 \times 10^8 \text{ s}^{-1}$  [Kra15], resulting in a natural linewidth of  $\Gamma_{SP} = 22.1 \text{ MHz}$ , see Sec. 2.7. To drive this transition we use a grating-stabilized diode laser in Littrow-configuration<sup>24</sup> at 793.91845 nm. The laser beam is first amplified by a tapered amplifier (TA) and subsequently frequency-doubled in a resonant cavity (Second Harmonic Generation, SHG) to obtain photons at 396.95923 nm. The setup of this laser is shown in Fig. 4.9. In order to keep the output power and the frequency on a constant level, the wavelength of the laser diode and the length of the SHG-cavity are stabilized on each other, using the Pound-Drever-Hall (PDH) locking technique [Bla01], see Fig. 4.9. As re-pumping laser, driving the  $D_{3/2} \leftrightarrow P_{1/2}$  transition, we use a home built grating-stabilized diode laser in Littrow-configuration, running at 866.45090 nm.

In a standard configuration, the laser beams at 397 nm and 866 nm are oriented parallel to one another and perpendicular to the magnetic field, see Fig. 4.10. They have an angle of  $45^\circ$  to the trap axis and  $60^\circ$  to the radial directions, and thus all vibrational modes are addressed simultaneously. The polarization of both laser beams is adjusted to be linear and perpendicular to the magnetic field, leading to a superposition of  $\sigma^+$  and

<sup>24</sup> DL-SHG 100, TOPTICA Photonics AG.

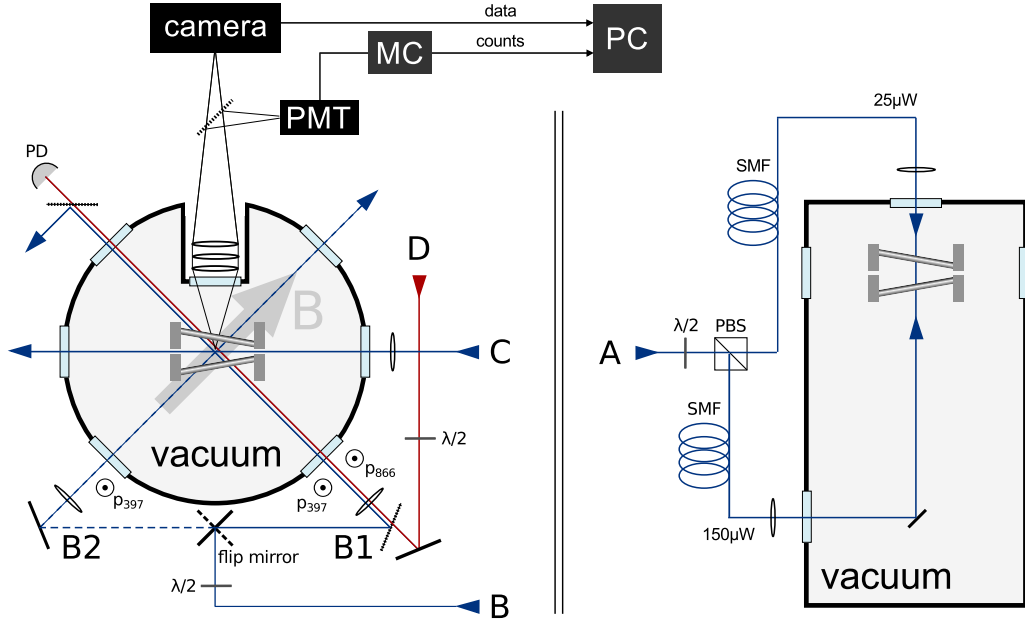


**Figure 4.10.** – Orientation of the individual laser beams with respect to the ion trap, in a top-view (left) and a side-view (right). The capital letters correspond to the output beams of Fig. 4.9. While the 866 nm beam is always used in a diagonal orientation, the 397 nm beam has different possible directions, to address and manipulate the states of the ions selectively. The fluorescence light is captured by an objective and projected on a camera (EMCCD or ICCD), as well as on the PMT. The data of both devices is read out and processed by the control computer (PC) and represents the main observable in our experiments.

$\sigma^-$  polarization with respect to the magnetic quantization axis. This configuration is advantageous for the resolution of dark resonances, see Sec. 6.2. The intensity and the size of both laser beams at the position of the ions are typically  $35 \mu\text{W}$  at a beam waist of  $160 \mu\text{m}$  for the 397 nm laser and  $80 \mu\text{W}$  at a beam waist of  $380 \mu\text{m}$  for the 866 nm laser, saturating the individual transitions. A flip-mirror permits to change the beam path of the 397 nm laser to propagate parallel to the direction of the magnetic field (beam path  $B'$ , dashed line in Fig. 4.10). The polarization of this beam path is again chosen to be linear, such that both  $\sigma^+$  and  $\sigma^-$  transitions are driven. An additional beam of the 397 nm laser is oriented along the axis of the trap and addresses the axial degree of freedom of the trapped ions only. Finally, a 397 nm beam crosses the trap volume in vertical direction and has an angle of  $45^\circ$  to both radial direction,  $x$  and  $y$ . It addresses the radial states of motion exclusively, and will be used to control and change the temperature of these degrees of freedom. In order to avoid a radiation pressure induced force on the ion in vertical direction, we apply two counter-propagating beams<sup>25</sup>, as shown in Fig. 4.10.

#### 4.3.3. Scanning and switching of the beams

Acousto-optical modulators<sup>26</sup> (AOM) are installed in all beam-paths of both lasers. Double pass configurations are used to control the intensity of the beams and to tune

<sup>25</sup> This doesn't lead to a standing light wave, since the beams are detuned by 2 MHz and sent through a 5 m single mode fiber each, whereby thermal fluctuations destroy the relative coherence between both beams.

<sup>26</sup> 397 nm setup: QZF-80-20, Brimrose Corp.; 866 nm setup: TEF-270-100, Brimrose Corp.



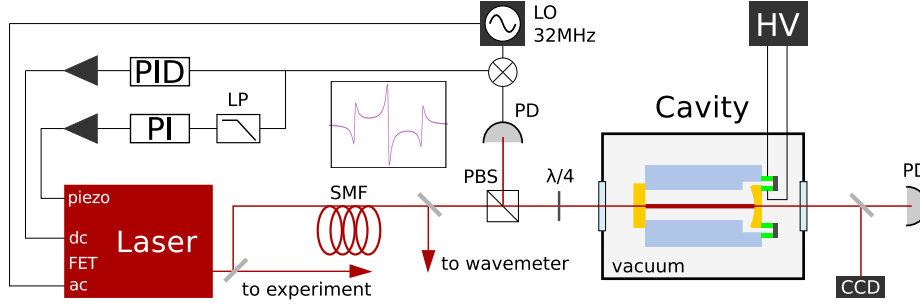


**Figure 4.11.** – The reference cavity is composed of two mirrors in hemispherical configuration (yellow), mounted on a spacer (blue) and is placed in a vacuum chamber to prevent fluctuations of its optical length. One of the mirrors is mounted on a stack of two counter-acting piezo-rings (green) to tune the length of the cavity by a variable high-voltage (HV) supply. A CCD-camera and a PD monitor the transmission signal of the cavity modes. The PDH-lock is composed of a local oscillator (LO), a PD and a frequency mixer. The errorsignal is fed in parallel to a PI and a PID circuit, which regulate the angle of the grating by a piezo and the current of the laser diode by a field-effect transistor (FET).

their frequency without changing the beam pointing [Don05]. Each AOM is controlled by an amplified signal of a home-built voltage controlled oscillator (VCO) system<sup>27</sup>, which is adjustable in frequency and intensity, see App. A.4. An rf-switch allows for alternating between two different VCO systems at different drive-frequencies on a timescale of 10 ns, and is connected to the AOM in the branch of the 866 nm laser, see Fig. 4.9 and [Tol14].

To perform frequency scans of the fluorescence spectrum a constant intensity of the AOM output over a range of 40 MHz is required. However, an AOM has an RLC resonance circuit for impedance matching, which shows a strongly frequency dependent absorption profile. Here, the beam intensity is kept constant using a gauge function for corrected driving power values as a function of the driving frequency, which was measured previously with a photo-diode (PD). The power thus remains constant with a stability  $> 99\%$  during frequency scans, see App. A.5 for details.

#### 4.3.4. Frequency stabilization

For cooling the trapped ions, the frequencies of both lasers are red-detuned with respect to the corresponding atomic transition  $\Delta_{397,866} < 0$ . The temperature of the ions during laser-cooling strongly depends on the detuning  $\Delta_{397}$  [Ste86a]. In order to achieve a constant and well defined temperature of the ions, the frequency fluctuation of the lasers should be reduced to a minimum. Furthermore, later in Sec. 6.4, we will exploit narrow band resonances within the fluorescence spectrum of the ions to determine their temperature, which may be washed out by frequency fluctuations of the lasers. As a consequence, these fluctuations should be small as compared to the linewidth of the corresponding atomic resonances. In order to reduce fluctuations and drifts, the frequency of the diode lasers is stabilized on an external reference cavity. The reference cavity, sketched in Fig. 4.11, is composed of two mirrors, mounted on a solid spacer. The latter is made of Zerodur<sup>28</sup>, which provides a low relative thermal expansion coefficient of  $0 \pm 1 \times 10^{-7}/\text{K}$ . The reference cavity is placed in a vacuum chamber to prevent

<sup>27</sup> Op5 AOM-Driver, H. Lenk, University of Mainz.

<sup>28</sup> ZERODUR, Schott AG.

fluctuations of its optical length due to air convection and temperature changes. To further reduce thermally induced fluctuations of the cavity length, the Zerodur-spacer is placed on two ceramic holders, which provide a decoupling from the environment with a thermal conductivity of  $< 1 \text{ J}/(\text{K m s})$ . The mirrors of the cavity are in a stable hemispherical configuration: one plane mirror and one concave mirror with a radius of curvature of 250 mm are mounted at a distance of 100 mm. Both of them provide a reflectivity of 99.0(5) % for the relevant wavelengths<sup>29</sup>. The cavity has a calculated finesse of  $\mathcal{F} \approx 350$  and a free spectral range of  $FSR = 1.5 \text{ GHz}$ . One mirror is mounted on a stack of two counter-acting piezo-rings, which compensate each other for thermal fluctuations. A high voltage control<sup>30</sup> of the piezo allows for tuning the length of the cavity in order to match a  $\text{TEM}_{00}$  mode to the desired wavelength close to the resonance frequency of the ion. We use a PDH locking scheme to stabilize the laser frequency to the resonance line of the cavity. A simple CCD camera<sup>31</sup>, as well as a photo diode are available to monitor the transmission signal of the cavity modes.

For the 397 nm laser, the error-signal from PDH lock on the reference cavity is low-pass filtered and fed to a digital PI-regulator<sup>32</sup>. The correction signal controls the piezo which adjusts the angle of the grating of the laser diode. This locking scheme compensates for slow drifts of  $< 10 \text{ kHz}$ . To level out fast frequency fluctuations, a second PID regulator<sup>33</sup> with a bandwidth of 100 MHz controls the JFET on the current modulation of the laser diode. However, the portion of the intensity coupled to the SHG-cavity, and thus its output power, depends on the relative frequency deviation between the resonance of the SHG-cavity and the frequency of the laser diode. To reduce these fluctuations, the fast PID controller of the laser diode uses the error signal from the SHG-cavity, instead of the one from the external cavity. Slow drifts are compensated by the piezo controlled length of the SHG-cavity, see Sec. 4.3.2. For the 866 nm laser we use the error-signal of the reference cavity as input for both, the slow PI regulator, controlling the piezo on the grating, as well as the fast PID-regulator to level the current in the diode.

---

<sup>29</sup> batch number D214K008, Layertec GmbH.

<sup>30</sup> EBS8030, iseg Spezialelektronik GmbH.

<sup>31</sup> USB-webcam VC2PMA, Conrad Electronic, lens removed.

<sup>32</sup> DigiLock 110, Toptica Photonics AG.

<sup>33</sup> PDD 110, Toptica Photonics AG.



# 5

## Coherent excitation of motion

The unique properties of the funnel-shaped ion trap are the basis for the operation of the heat engine experiments. Here, we provide a characterization of the effect of the tapered trapping potential on the motional behavior of the ion. Furthermore, we present preparatory measurements which are prerequisites for the characterization of the single-atom heat engine.

We start this chapter with a presentation of the measurement techniques for a precise determination of the trap frequencies of the ion in Sec. 5.1. These techniques are used to characterize the effect of the tapered potential by measuring the radial trap frequency of the ion as a function of its position along the trap axis. As direct consequence of the tapered potential, we demonstrate in Sec. 5.2 the fundamental elements where the heat engine functionality is based on: a change of the extent of the motional state of the ion in radial direction leads directly to a shift of its equilibrium position along the trap axis. We will demonstrate this effect using a coherent oscillation in radial direction, in combination with a precise determination of the ions position from camera images. During the heat engine operation, the ion is running in a steady state, where a controlled dissipation balances the engine's output power. Consequently, the dissipation confines the resulting oscillation of the ion and is indispensable for a continuous heat engine operation. In Sec.5.3 we show that laser cooling leads to a controlled dissipation and present a detailed study of two different approaches to determine the corresponding damping coefficient. Furthermore, we show in Sec.5.4 that, as a consequence of the tapered potential, each ion in a linear ion crystal provides an individual radial trap frequency. This feature allows us to address the vibrational modes of the ions locally.

Parts of this section, comprising the characterization of trap as well as the demonstration of the working principle of the heat engine, have been published in:

**Nano-Motor aus einem einzelnen Atom,**

J. Roßnagel, K.N. Tolazzi, O. Abah, E. Lutz, F. Schmidt-Kaler and K. Singer,  
GIT Labor-Fachzeitschrift 6, 51 (2014).

### 5.1. Characterization of the ion trap

#### 5.1.1. Measurement of trap frequencies

The fundamental tool for the characterization of the ion trap is the measurement of the trap frequencies of the ion. The underlying principle is to drive the harmonic oscillator

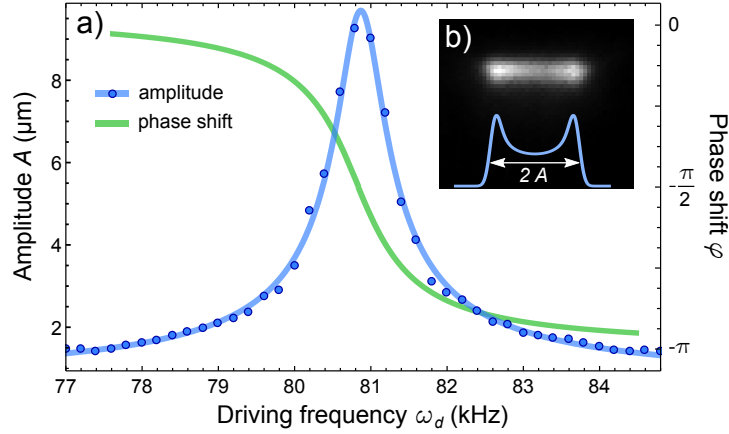


**Figure 5.1.** – Resonance of the harmonic oscillator. (a) Measured steady state amplitude  $\mathcal{D}$  of the oscillation in axial direction  $z$  as a function of the driving frequency  $\omega_d$ , measured with continuous damping by laser cooling with  $30 \mu\text{W}$ . The fit of Eq. (5.1) (blue line) to the data (blue dots) reveals a resonance frequency of  $\omega_z = 80.86(1) \text{ kHz}$ , a damping coefficient of  $\gamma = 1950(60) \text{ s}^{-1}$ , and an acceleration  $F_d/m = 17.1(4) \times 10^3 \text{ m s}^{-2}$ . The corresponding phase shift  $\phi$  (green) between the drive and the oscillation of the ion goes from  $\phi = 0$  for  $\omega_d \ll \omega_z$  to  $\phi = -\pi$  for  $\omega_d \gg \omega_z$ . (b) Camera image of an oscillating ion. The projection of the fluorescence distribution on the direction of oscillation shows the characteristic behavior from Eq. 5.4. Each point in a) corresponds to an individual camera image similar to b).

by an oscillating perturbing force with a variable driving frequency  $\omega_d$ , and to analyze the oscillation amplitude from camera images. For a weakly damped harmonic oscillator,  $\gamma \ll \omega_z$ , the steady state amplitude  $A$  of the oscillation is governed by the driving force  $F_d$  and the dissipation  $\gamma$ , and reads

$$A(\omega_d) = \frac{F_d/m}{\sqrt{(\omega_i^2 - \omega_d^2)^2 + (2\gamma\omega_d)^2}}, \quad (5.1)$$

with the oscillating mass  $m$ . The amplitude  $A$  peaks in a resonance if  $\omega_d = \omega_i$ , with  $\omega_i \in \{\omega_x, \omega_y, \omega_z\}$ . Here, we are only interested in the relative amplitude, whose maximum reveals the resonance frequency  $\omega_i$ , as shown in Fig. 5.1 (a). When scanning over the resonance, the phase shift between the driving signal and the oscillation of the ion changes according to

$$\phi(\omega_d) = \arctan\left(\frac{2\omega_d\gamma}{\omega_z^2 - \omega_d^2}\right). \quad (5.2)$$

Consequently, the resulting time resolved trajectory of the driven damped harmonic oscillator at steady state reads

$$x_i(t) = A(\omega_d) \cdot \sin(\omega_d t - \phi(\omega_d)). \quad (5.3)$$

We use two different techniques to drive a coherent oscillation of the ion:

i) We superpose the electromagnetic trapping potential with an oscillating electric field by connecting a signal generator to one of the trap electrodes. The amplitude of the oscillation is evaluated as a function of the driving frequency  $\omega_d$  by analyzing camera images. For exposure times longer than the oscillation period, we observe spatially smeared fluorescence images of an oscillating ion, as shown in Fig. 5.1 (b). The projection

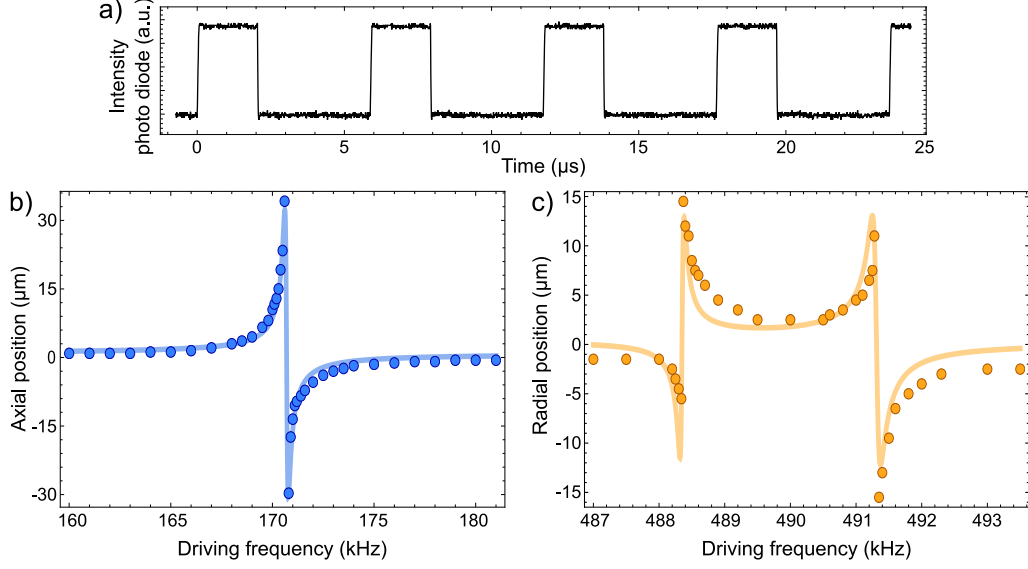


**Figure 5.2.** – Measurement of the eigenfrequencies of an ion by a modulated laser beam. (a) Modulation signal at 170 kHz on a photo diode. (b) Measurement and fit of the axial trap frequency resulting to  $\omega_z = 170.697(2)$  kHz. (c) Same for the radial eigenfrequencies revealing  $\omega_x = 488.350(5)$  and  $\omega_y = 491.31(1)$ .

of the fluorescence distribution  $\mathcal{F}_m$  on an axis parallel the direction of the oscillation is well described by a time-integrated and sinusoidally modulated Gaussian,

$$\mathcal{F}_m(x) \propto \int_{-\pi/2}^{\pi/2} \exp \left[ -\frac{(x - \mathcal{D} \sin \phi)^2}{\sigma^2} \right] d\phi. \quad (5.4)$$

Here, the modulation depth  $\mathcal{D}$  corresponds to the steady state amplitude  $A$  of the coherent oscillation. The width of the Gaussian  $\sigma$  is determined from the fluorescence distribution of an ion at rest. An exemplary measurement of the resonance of a trapped ion is shown in Fig 5.1. A fit of Eq (5.1) reveals the resonance frequency  $\omega_i$  of the ion.

ii) We excite an oscillation of the ion by a modulation of the intensity of the cooling laser. This leads to a modulation of the radiation pressure on the ion, and thus to an oscillating driving force [Dre04]. The intensity modulation is achieved by switching the AOM-driving on and off at a frequency  $\omega_d$ . When the cooling laser is pulsed, likewise the recorded intensity of the fluorescence signal is. If the pulses are short as compared to one oscillation period, the ion is illuminated only at one specific phase of its oscillation, which is measured and evaluated in Fig. 5.2. For the non-resonant case, the phase  $\phi$  between the oscillation and the driving signal is  $\phi = 0^\circ$  or  $\phi = 180^\circ$ . The laser pulses reach the ion at a turning point, but the amplitude of the oscillation vanishes. When approaching the resonance, the phase change is negligible but the amplitude of the oscillation increases, the turning points move outwards. When  $\omega_d$  is close to the resonance  $\omega_0$ ,  $\phi$  changes from  $0^\circ$  to  $180^\circ$  and consequently the fluorescence signal switches from the one turning point to the other. The center of gravity of the detected fluorescence distribution  $z_f$  is well modeled by the function

$$z_f(\omega_d) = \frac{\alpha_z(\omega_d - \omega_0)}{(\omega_d - \omega_0)^2 - \Gamma^2} + z_0, \quad (5.5)$$

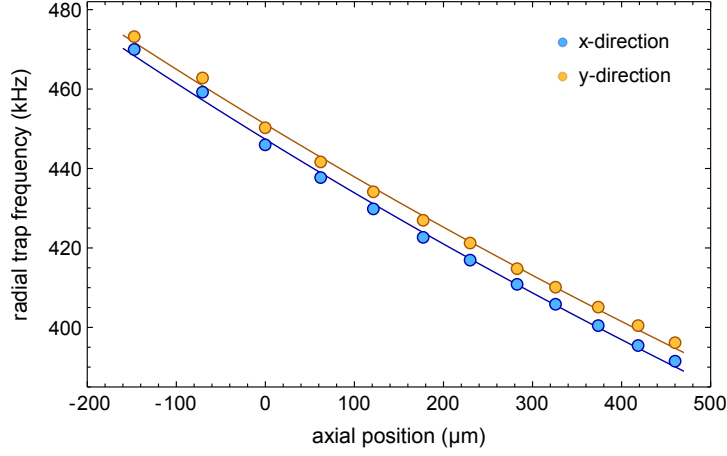


**Figure 5.3.** – Measured trap frequencies  $\omega_r$  in both radial directions as a function of the relative position along the  $z$ -axis, measured with technique i) (see text). A fit of Eq. (2.17) to the data reveals the absolute position of the ion inside the trap.

where the constant  $\alpha_z$  is related to the amplitude of the oscillation and  $\Gamma$  is the width of the resonance [Dre04]. Consequently, this technique provides a precise measurement of the resonance frequency of the ion.

There are two essential differences between the techniques i) and ii). One is the evaluation procedure: in i) broad and smeared out fluorescence distributions are fitted, resulting in an uncertainty of  $10^2$  Hz. In ii) we evaluate the shift of the turning points by fitting a localized fluorescence image, resulting in an improved uncertainty of  $10^1$  Hz. The second difference is in the driving operation: ii) is based on a modulation of the scattering rate of photons and may influence temperature and dissipation. In contrast, the modulation of the trapping potential in i) does not change the interaction of the ion with light fields.

### 5.1.2. Trap frequencies in a tapered potential

We measure the radial trap frequencies  $\omega_{x,y}(z)$  at different positions  $z$  along the trap axis to characterize the coupling between the radial and the axial modes of oscillation, Eq. (2.17), experimentally. The results are shown in Fig. 5.3, revealing the strong dependence of  $\omega_{x,y}$  on  $z$ , as well as its  $1/z^2$  behavior. From a fit of Eq. (2.17) to the measured data we obtain  $\omega_{x0}/2\pi = 447.4(5)$  kHz and  $\omega_{y0}/2\pi = 451.1(5)$  kHz. The lifted degeneracy of the two radial trap frequencies is achieved by an additional static electric field. This measurement allows to obtain the radial distance  $r_0$  of the ion to the trap electrodes at the position  $z = z_0$ . Averaged over both radial directions, the fit of Eq. (2.17) yields a geometry factor of

$$\frac{\tan \theta}{r_0} = 154(3) \frac{\text{rad}}{\text{m}} \quad \Rightarrow \quad r_0 = 1.19(2) \times 10^{-3} \text{ m}. \quad (5.6)$$

By taking the geometry of the trap into account (see Sec. 4.1),  $r_0$  reveals the absolute position of the ion at a distance of  $z_0 = 7.7(8) \times 10^{-4}$  m from the endcap at the narrow side of the trap. The position of the ion has been chosen on the narrow side, since the coupling of the modes scales with the distance of the ion to the electrodes, according to

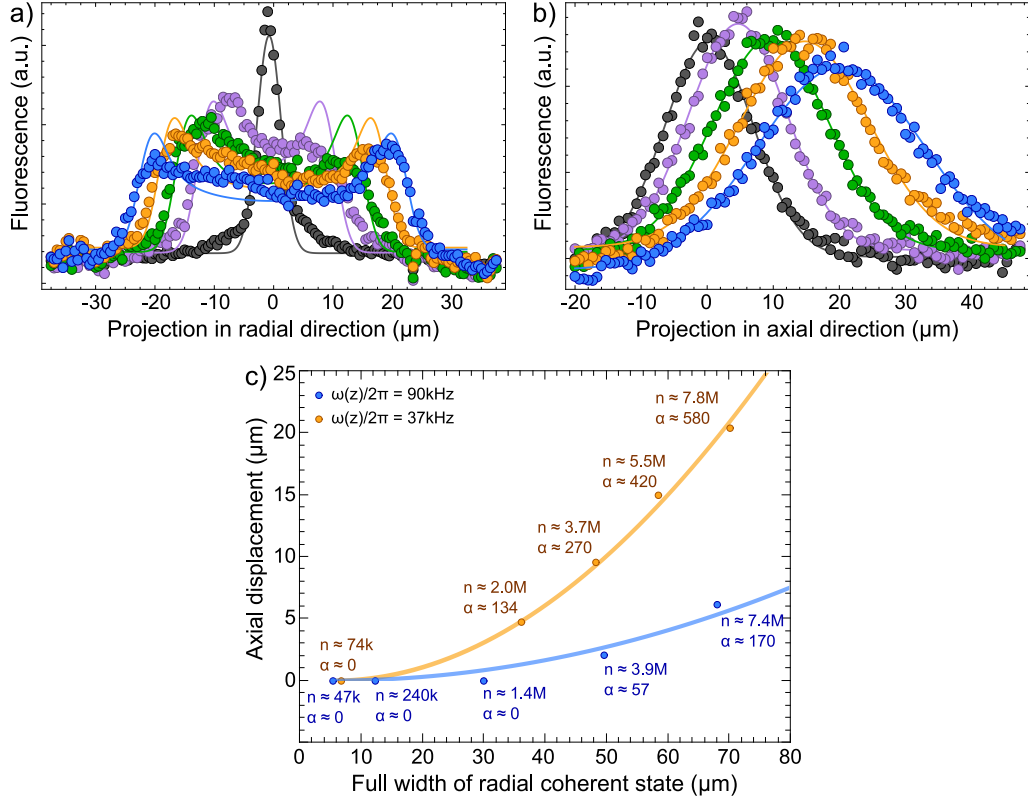


**Figure 5.4.** – Demonstration of the fundamental working mechanism of the heat engine. (a) Projection of the fluorescence distribution of the ion on the radial direction when driven harmonically. The increase of the amplitude of the oscillation with a radial trap frequency of  $\omega_r/2\pi = 468\text{ kHz}$  has been measured from 0 to  $22\text{ }\mu\text{m}$  by fits of the integrated probability distribution of coherent states. (b) Projection of the integrated fluorescence distribution on the axial direction, corresponding to the measurements in a), at an axial trap frequency of  $37\text{ kHz}$ . (c) Evaluation of the shift of the ion along the trap axis as a function of its extent in radial direction, using trap frequencies of  $\omega_z/2\pi = 90\text{ kHz}$  and  $\omega_z/2\pi = 37\text{ kHz}$ . For each point, the mean phonon number  $n$  of the radial coherent excitation is given, as well as the axial shift in multiples  $\alpha$  of its ground-state wave-packet size. A quadratic fit, resulting from the 3-dimensional harmonic potential shape, represents well the measured data.

Eq. (2.17). Knowing the precise position of the ion allows us to obtain precise numbers for the trapping potential and its higher momenta. These numbers are essential for the analytical calculation of the expected force, power and efficiency of the engine in Ch. 7.

## 5.2. Demonstration of the elements of the heat engine working principle

In order to demonstrate the elements of the working principle, we analyze the shift of the position of the ion along the trap axis as a function of the width of its radial distribution. The particular kind of the radial state does not matter, since the trapping potential is sensitive only on its variance in radial direction,  $(\langle x^2 \rangle + \langle y^2 \rangle)$ . Using a resonant modulation of the voltage on the outer electrodes, we induce a coherent oscillation of the ion in radial direction. Such a coherent oscillation allows to achieve large amplitudes of



some tens of micrometers with a high degree of control. As shown in Sec. 2.5, a change in the variance of the radial state leads to a shift of the equilibrium position of the ion along the trap axis.

In Fig. 5.4 we compare the projection of the fluorescence distribution of the coherent oscillation at different amplitudes with the corresponding static shift along the trap axis. At trap frequencies of  $\omega_z/2\pi = 37$  kHz and  $\omega_r/2\pi = 468$  kHz, an oscillation amplitude of  $\mathcal{D} = 38$   $\mu\text{m}$  in radial direction leads to a shift of  $\Delta z = 22$   $\mu\text{m}$ . To obtain a quantitative correlation, we have evaluated those measurements for different axial trap frequencies, which are shown in Fig. 5.4 (c). The expected quadratic behavior  $\Delta z \propto \mathcal{D}^2$ , see Sec. 2.5, is well reproduced. These measurements demonstrate the effects of the coupling of the radial and the axial mode of oscillation as a consequence of the tapered trapping potential. For the heat engine operation, this mechanism translates a change of the ions temperature (variance of the radial state) into mechanical work (shift in axial direction) [Tol14].

### 5.3. Determination of the damping coefficient

In order to provide damping to a coherent oscillation in the axial degree of freedom, we apply a cooling laser along the trap axis. The according damping coefficient  $\gamma$  is controlled by tuning the laser parameters. Knowing  $\gamma$  precisely allows to extract the driving power from the amplitude of a steady state oscillation. Additionally, a thermal excitation of the axial mode originates from spontaneous decay through laser cooling. During the heat engine operation, the incoherent, thermal excitation in axial direction may conceal the coherent oscillation of the ion, why a cooling process along this direction becomes necessary.

In order to provide efficient cooling whilst maintaining controlled but low damping of the oscillation, the axial cooling laser is applied only around the turning points of the axial motion, see Fig. 5.5 (a). At the turning points, the center of mass velocity of the ion vanishes and the laser is cooling the thermal excitation only [Met99]. Extending the cooling period results in an increasing damping of the coherent oscillation. The duty cycle of the pulsed dissipation laser is chosen to be 20 %, if not otherwise noted. This duty cycle provides a damping which contains the driven coherent oscillation typically within some 10  $\mu\text{m}$  during heat engine operation. Regarding the thermal excitation, it provides enough cooling to counteract the heating processes, while the power of the dissipation laser is not saturating the  $S_{1/2} - P_{1/2}$  transition. Note, that a saturation of the  $S_{1/2} - P_{1/2}$  transition by the dissipation laser would change the scattering rate of the cooling laser for the thermal bath interaction and would influence the resulting temperatures.

In the following we will present two independent ways to determine the damping and to characterize its behavior.

#### 5.3.1. Step response to coherent drive

The first method employs the step response of the ions motion in the axial direction to a coherent drive, under the influence of damping. At time  $t = 0$ , we start to drive a Doppler cooled ion in axial direction with a drive frequency  $\omega_d$  close to its resonance frequency  $\omega_z$ . A rectangular voltage modulation is applied to the end-caps, which is controlled by an rf-

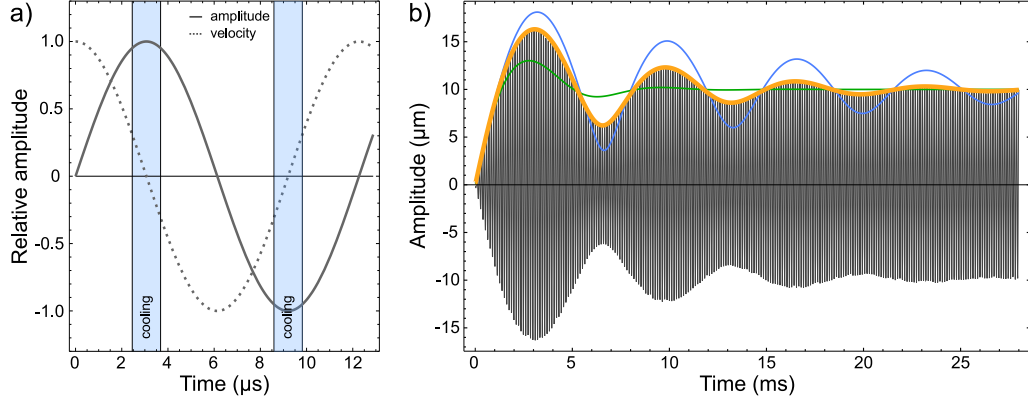


**Figure 5.5.** – (a) Laser cooling is applied around the turning points (blue) of the oscillation. The duty cycle of the cooling pulses over one oscillation period is 0.2. (b) Simulated step response of the ion's motion to a coherent drive. The gray line shows the time resolved oscillation of the ion. A detuning of the driving frequency  $\omega_d$  to the resonance frequency  $\omega_z$  of  $\Delta\omega = 1.5$  kHz leads to a beat signal, reflected by the envelope function (orange), which decays through dissipation and reaches a steady state with amplitude  $A$ . The effect of the damping coefficient  $\gamma$  is illustrated by three different envelope functions for  $\gamma = 700$  s $^{-1}$  (blue),  $\gamma = 1500$  s $^{-1}$  (orange) and  $\gamma = 3000$  s $^{-1}$  (green).

switch<sup>34</sup>. For  $t > 0$ , the displacement  $\mathcal{D}(t)$  of the coherent state increases until it reaches a steady state between drive and the dissipation with an amplitude  $A$ . Focusing on the trajectory of the ion,  $\mathcal{D}(t)$  represents the envelope function of the resolved oscillation of the ion. Using the EMCCD camera, the exposure time  $\tau_{\text{exp}}$  cannot be reduced below 1 ms and is thus much longer than the oscillation period of the ion,  $\tau_{\text{exp}} \gg 1/\omega_z$ . The acquisition process thus integrates over many oscillations and, as a consequence,  $\mathcal{D}(t)$  is the only accessible observable.

The time-resolved trajectory of the ion under step response reads [Dem08]

$$z(t) = A_0 \left[ \sin(\omega_z t) - \frac{\omega_z}{\omega_d} \sin(\omega_d t) e^{-\gamma t} \right], \quad (5.7)$$

and is illustrated in Fig. 5.5 (b). Right after starting the drive,  $t \gtrsim 0$ , the ion starts to oscillate with its resonance frequency  $\omega_z$ . To resolve the frequency of the driving signal, a time  $t \gg \omega_d^{-1}$  is needed. The interference between  $\omega_d$  and  $\omega_z$  leads to a beat note at  $\omega_b = \omega_z - \omega_d$ . Due to the dissipation, the initial oscillation with  $\omega_z$  decays in company of the beat, and for  $t \gg \omega_d^{-1}$  the ion oscillates with  $\omega_d$ . It reaches a steady state amplitude  $A(\omega_d, \gamma, F_d)$  according to Eq. (5.1), which is governed by the driving force  $F_d$  and the damping coefficient  $\gamma$ . The envelope function  $\mathcal{D}(t)$  of the ion's oscillation is obtained by a frequency decomposition of the beat signal into a fast and a slow oscillation [Dem08],

$$c = \frac{\omega_z + \omega_d}{2} \quad \text{and} \quad \omega_b = \omega_z - \omega_d.$$

The frequencies  $\omega_z$  and  $\omega_d$  can thus be rewritten as

$$\omega_z = c + \frac{\omega_b}{2} \quad \text{and} \quad \omega_d = c - \frac{\omega_b}{2}.$$

<sup>34</sup> ZYSWA-2-50DR, Mini-Circuits.

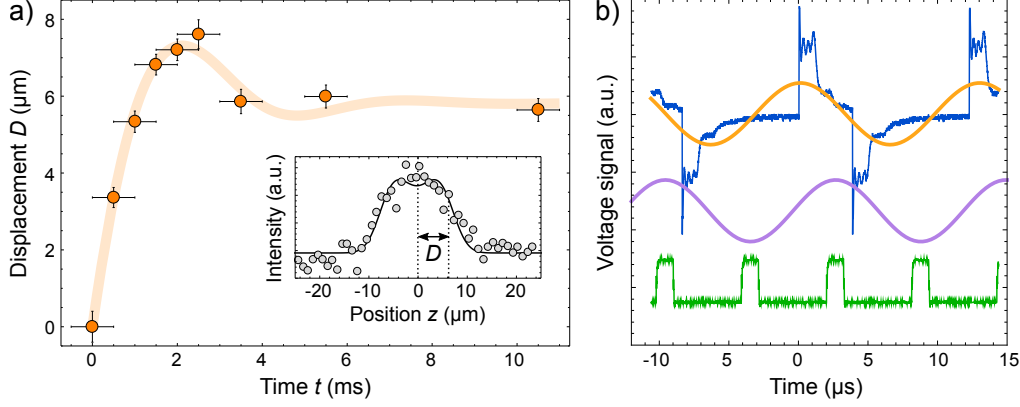


**Figure 5.6.** – (a) Determination of the damping coefficient  $\gamma$ . The step response is evaluated by determining the amplitude  $A$  of the ion's oscillation (orange circles) at time  $t$  after switching on the end-cap drive. A fit to the data (orange line) reveals  $\gamma_i = 520(100) \text{ s}^{-1}$  and a beat-note of  $\omega_b/2\pi = 190(10) \text{ Hz}$ . Inset: Determination of oscillation amplitude at 5.5 ms by fitting Eq. (5.4) (black line) to the projection of the corresponding camera images (gray circles). (b) Timing of the cooling pulses. The rectangular driving signal (blue), measured just at the vacuum feed-throughs, is deformed through the high pass filter properties of the transformer, cf. Fig. 4.5. To deduce the phase of the ion, this signal is fitted by a cosine (orange). On resonance, the harmonic oscillation of the ion follows with  $\delta\phi \approx -90^\circ$  phase shift (violet). The photo-diode signal of the dissipation laser (green) is tuned to the turning points by a delay of  $2.1 \mu\text{s}$  with respect to the driving signal.

Using Euler's formula  $e^{i\phi} = \cos \phi + i \sin \phi \rightarrow \sin \phi = \text{Im}[e^{i\phi}]$ , we can rewrite Eq. 5.7 as

$$z(t) = A_0 \text{Im} \left[ e^{i(c+\omega_b/2)t} - \frac{\omega_z}{\omega_d} e^{-\gamma t} e^{i(c-\omega_b/2)t} \right] = A_0 \text{Im} \left[ e^{ict} e^{i\omega_b t} - \frac{\omega_z}{\omega_d} e^{-\gamma t} e^{ict} \right],$$

which is in trigonometric representation

$$z(t) = A_0 \left[ \sin(ct) \left( \cos(\omega_b t) - \frac{\omega_z}{\omega_d} e^{-\gamma t} \right) + \cos(ct) \sin(\omega_b t) \right].$$

However, we are interested in an analytical description of the time depending amplitude  $\mathcal{D}(t)$  of the oscillation, not in the resolved motion of the ion  $z(t)$ . In phase-space, the fast oscillating components  $\sin(ct)$  and  $\cos(ct)$  are perpendicular. The amplitude  $\mathcal{D}(t)$  is then defined by the length of the phase-space vector, which is calculated according to the Pythagorean formula

$$\mathcal{D}(t) = A \sqrt{\left( \cos(\omega_b t) - \frac{\omega_z}{\omega_d} e^{-\gamma t} \right)^2 + \sin(\omega_b t)^2}. \quad (5.8)$$

The envelope function  $\mathcal{D}(t)$  is plotted in Fig. 5.5 (b) for different values for  $\gamma$  and is compared to the time resolved oscillation  $z(t)$ .

In order to determine  $\gamma$  in the experiment, the amplitude  $\mathcal{D}(t)$  can be extracted from the fluorescence distribution on camera images at different times  $t$  after switching on the coherent drive. We employ an exposure time  $\tau_{\text{exp}} = 1 \text{ ms}$ , which is much longer than the oscillation period of the ion,  $\tau_{\text{osc}} = 2\pi/\omega_z = 12.3 \mu\text{s}$ , but still short enough to resolve the dynamics of the step response. An example of a step response measurement is shown in Fig. 5.6 (a). Each point is determined by fitting  $\mathcal{F}_m$ , Eq. (5.4), to the projected intensity

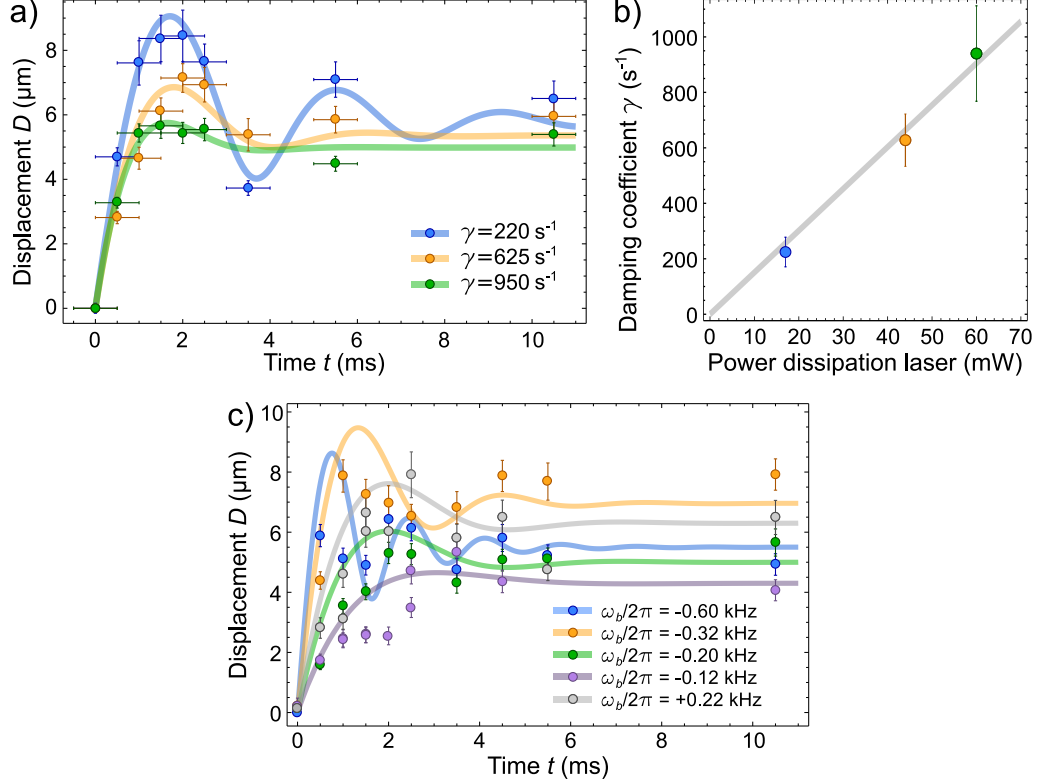


**Figure 5.7.** – Determination of the damping coefficient  $\gamma$  by a measurement of the displacement  $\mathcal{D}(t)$  as a function of time. (a)  $\mathcal{D}(t)$  for different power  $P_d$  of the pulsed dissipation laser at a duty cycle of  $d_d = 0.2$ :  $P_d = 17 \text{ mW}$  (blue),  $46 \text{ mW}$  (orange), and  $60 \text{ mW}$  (green) (power measured at  $d_d = 1$ ). The detuning of the driving signal has been set to  $\omega_b/2\pi = 0.25 \text{ kHz}$ . The uncertainty of  $\mathcal{D}$  is of statistical nature, while the error bars along the time axis represent the exposure time of  $1 \text{ ms}$ . A fit to the data reveals  $\gamma = 220(60) \text{ s}^{-1}$ ,  $650(100) \text{ s}^{-1}$ , and  $1000(250) \text{ s}^{-1}$ , respectively, where the uncertainty of  $\gamma$  stems from the fitting error. (b) Resulting  $\gamma$ -values from a), revealing a linear trend  $\gamma(P_d) = 15(1) \cdot P_d (\text{s} \cdot \mu\text{W})^{-1}$ . (c)  $\mathcal{D}(t)$  for different  $\omega_b$  at constant  $\gamma$ . The resonance frequency is measured to be  $\omega_z = 81.5 \text{ kHz}$  and the resulting damping coefficient stays in the range  $\gamma = 700 \pm 100 \text{ s}^{-1}$ . The driving power has been adjusted to achieve approximately the same steady-state amplitude for all  $\omega_b$ . For the sake of clarity we don't display the time error-bars.

distribution, as shown in the inset of Fig. 5.6 (a). The function  $\mathcal{D}(t)$ , Eq. (5.8), is fitted to the measured amplitudes and reveals the damping coefficient of the axial dissipation laser.

To calculate the right timing of the laser pulses, we approximate the effective driving signal by a cosine function, see Fig. 5.6 (b). The ion follows the corresponding oscillation of the electric field with a  $\pi/2$  phase shift [Dem08]. Additionally, the charging process of the capacitive load of the bias tees and the electrodes leads to a lag of the electric field oscillation inside the trap behind the driving signal, which is calculated in Sec. 7.3 and results to  $800 \text{ ns}$ .

In general, the strength of the dissipation can be adjusted by varying the detuning  $\Delta\nu_d$  and the power  $P_d$  of the axial laser, by changing the timing of its pulses with respect to the ion's oscillation, or by modifying its duty cycle. For practical reasons, we use the power of the axial dissipation laser  $P_d$  to tune  $\gamma$ , as shown in Fig. 5.7 (b). We observe a decrease

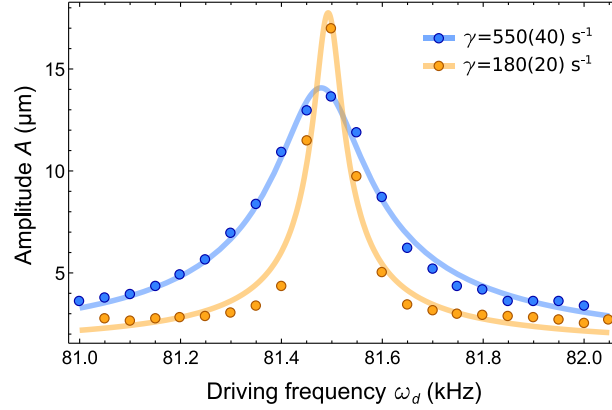


**Figure 5.8.** – Broadening of the spectral resonances of the oscillation of the ion for different damping coefficients. The steady-state amplitude  $A$  is recorded as a function of the driving frequency  $\omega_d$  for different strengths of the pulsed dissipation laser. The fit of Eq. (5.1) (solid line) to the data (dots) reveals damping coefficients of  $\gamma = 550(40) \text{ s}^{-1}$  and  $\gamma = 180(20) \text{ s}^{-1}$ .

of the decay-time of the beat signal when increasing  $P_d$  from 17 mW to 60 mW, where  $P_d$  is measured on a continuous beam instead of the pulsed beam<sup>35</sup>. The corresponding  $\gamma$  is thereby tuned from 200 to 1000  $\text{s}^{-1}$ .

To characterize the influence of the beat signal, we have varied the driving signal  $\omega_d$  stepwise between the measurements, see Fig. 5.7 (c). The best precision for an analysis of  $\gamma$  is achieved for  $\omega_b$  being small but non-vanishing. Then, not only the rise time of  $\mathcal{D}(t)$  but also the decay of the beat signal can be included to the fitting procedure for  $\gamma$ . However, if  $\omega_b \gg \gamma$  the laser pulses are not applied anymore in the turning points of the oscillation, because of the additional phase shift for a non-resonant drive, see Eq. (5.2). The effective detuning of the dissipation laser is then changed, since it interacts with the ion at higher velocities. This effect will be discussed in more detail in the following section.

Note, that the inverse decay of the oscillation can be used equally to evaluate  $\gamma$ , where the decaying amplitude is measured after stopping the drive. In this case we measure an exponential decay of  $\mathcal{D}(t)$ , again superposed with a beat between the driving frequency and the eigenfrequency of the harmonic oscillator. However, since the beat is then on low amplitudes, in contrast to step response presented before, the contributions of the decay and of the beat are hard to differentiate. Although the resulting values of  $\gamma$  are comparable, the precision of the results is strongly reduced.

### 5.3.2. Broadening of the resonance

A complementary method to determine  $\gamma$  is to observe the steady-state oscillation amplitude as a function of the driving frequency. As shown by Eq. (5.1), the width as well as the height of the spectral resonance profile is governed by  $\gamma$ . The amplitude of the oscillation is again determined from projections of the camera images. A measurement of the steady-state amplitude  $A(\omega_d)$  is shown in Fig. 5.8. Compared to the step-response, this technique is more robust against fluctuations and is less demanding on the camera image acquisition. It allows longer exposure times and thus enables us to characterize

<sup>35</sup> The reduced integrated power of the pulsed beam easily falls below the background threshold.

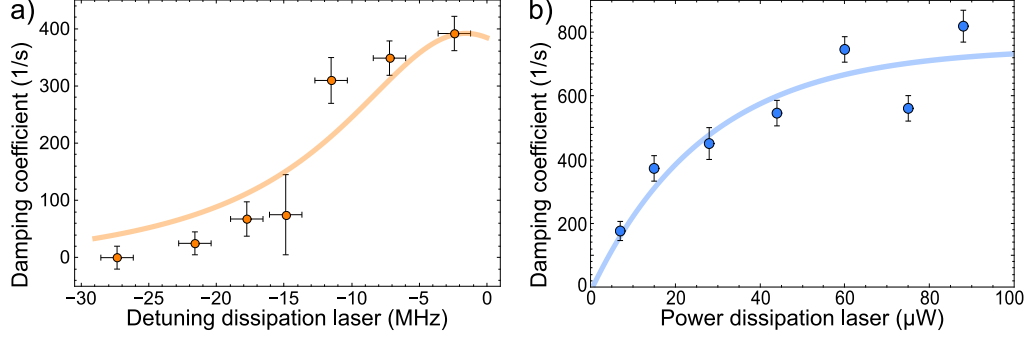


**Figure 5.9.** – Characterization of the damping coefficient  $\gamma$  as a function of the parameters of the dissipation laser. (a) Variation of the detuning  $\Delta\nu$  from the atomic resonance at a laser power of  $P_d = 23 \mu\text{W}$ . Eq. (5.9) has been fitted to the data, and we obtain a maximum damping coefficient at resonance  $\gamma(\Delta\nu = 0) = 390(80) \text{ s}^{-1}$ . (b) Variation of the laser power  $P_d$ , at a detuning  $\Delta\nu = -9(3) \text{ MHz}$ . The fit of Eq. (5.10) approximates well the measured data and reveals a saturation power of  $P_0 = 27(9) \mu\text{W}$ . Both data sets have been measured by the evaluation of the broadening of the resonances.

the dependencies of  $\gamma$  on external parameters with a reasonable investment of time. However, when scanning the driving frequency while using a pulsed dissipation laser, the phase shift  $\phi(\omega_d)$ , Eq. (5.2), becomes important. It leads to a deviation of the cooling pulses from the turning points of the ion's trajectory. As a consequence, the ion has a higher velocity when interacting with the laser beam and thus the effective  $\gamma$  is changed. For small  $\gamma$  and thus steep phase changes, we observe a reduced amplitude on the flanks of the resonance signal, see Fig. 5.8, which may stem from the phase mismatch. However, it seems that these deviations are small and Eq. (5.1) is still a good approximation for the measured resonances.

We investigate the spectral broadening of the resonances to characterize  $\gamma$  in more detail. We therefore record the resonances as a function of the detuning  $\Delta\nu_d$  and the power  $P_d$  of the dissipation laser.

In a simplified model, we expect  $\gamma$  to be proportional to the scattering rate of photons,  $\gamma \propto s_{sc}(\Delta\nu)$ , since laser cooling is the origin of dissipation.  $s_{sc}(\Delta\nu)$  corresponds to the spectral lineshape of the  $S_{1/2} - P_{1/2}$  resonance [Ste86a],

$$s_{sc}(\Delta\nu, t) = s_{0\nu} \frac{(\Gamma_P/2)^2}{(\Delta\nu + \Delta\nu_D(t))^2 + (\Gamma_P/2)^2}. \quad (5.9)$$

with the natural linewidth  $\Gamma_P = 23.1 \text{ MHz}$ , see Sec. 2.7. Due to the oscillation of the ion the line is Doppler shifted by  $\Delta\nu_D(t) = \Delta\nu_{D0} \sin(\omega_z t)$ . The maximum Doppler-shift for an amplitude of  $10 \mu\text{m}$  results to  $\Delta\nu_{D0} = \pm 13 \text{ MHz}$ , at a trap frequency of  $\omega_z = 81 \text{ kHz}$ . However, the damping laser is applied around the turning points and within this period the according Doppler shift ranges between  $-4$  and  $4 \text{ MHz}$ . It cancels, if we approximate the resonance line to be linear on this scale, since the velocity is symmetric around the turning points. Fig. 5.9 (a) shows the measured data  $\gamma(\Delta\nu)$  with a fit of Eq. (5.9), which reproduces well the general behavior of  $\gamma(\Delta\nu)$ . Here,  $\Delta\nu$  has been measured by the wavemeter, which is subject to strong fluctuations on the MHz scale. As a consequence, and because of the scattering of the measured  $\gamma$  values, Fig. 5.9 (a) gives a rough idea of the influence of  $\Delta\nu$  on  $\gamma$ , but does not allow to confirm or disprove the validity of our simplified model.

Regarding the dependance on the laser power  $P_d$ , we expect by our model an increasing  $\gamma$  for increasing  $P_d$ . However, for high laser power, the  $S_{1/2} - P_{1/2}$  transition is saturated and  $\gamma$  may reach a plateau. The analytical description therefore follows the exponential approach

$$s_{sc}(P_d) = s_{0p} \left( 1 - e^{-\frac{P_d}{P_0}} \right). \quad (5.10)$$

Fig. 5.9 (b) shows  $s_{sc}(P_d)$  fitted to the measured data  $\gamma(P_d)$ . Again, Eq. (5.10) reproduces well the general behavior of  $\gamma(P_d)$ , without allowing for substantiated statements about the model.

This qualitative analysis of  $\gamma$  gives a good idea of its behavior, but it can't be complemented by quantitative statements, since  $\gamma(\Delta\nu, P_d)$  is a function of both, power and detuning of the laser. For a complete analysis a 2-dimensional scan of  $\gamma$  in the  $(\Delta\nu, P_d)$  plane should be recorded, which would exceed the scope of our study. Nonetheless, the presented techniques are adequate to determine  $\gamma$  for the specific situation during the heat engine experiments, which are presented in Ch. 7.

#### 5.4. Addressing of single atoms and controlled interaction

Finally, we present another feature of the tapered trapping potential: due to the asymmetry in the trapping potential each ion in a linear chain of ions provides an individual radial trap frequency. Consequently, the oscillation of each ion can be addressed separately by an external drive. If the driving frequency is resonant to one of the ions, the other ions still couple through Coulomb-interaction to the oscillating ion, but do not experience a resonant excitation. Fig. 5.10 shows this effect qualitatively in a linear 7 ion crystal, where the oscillation amplitude decays with  $1/d^2$  with the distance  $d$  to the driven ion. If the inter-ion distance is large and the spectral dissipation-broadening of the resonances is reduced to a minimum, the excitation of common modes is suppressed completely and only the ion which is resonant to the external drive oscillates. The addressing of single ions, as well as the decoupling of the common modes of oscillation, has been demonstrated in a three and in a four ion crystal in Figs. 5.11 (a) and (b), where the axial trap frequency has been set to 40 kHz and 30 kHz, respectively.

The fact that in a tapered trapping potential the coupling between the modes of neighboring ions can be tuned deliberately through the ion distance and their dissipation promises advantages when studying, for instance, the transport of heat or energy along ion chains [Lin11, Ber13, Ram14]. A study of such phenomena has failed so far because of technical difficulties and fast thermalization of the modes of oscillation. A strongly reduced interaction facilitates such investigations. Furthermore, the addressing of single ions may provide strong advantages for quantum computation with ion strings, as we discuss in Sec. 8.4.

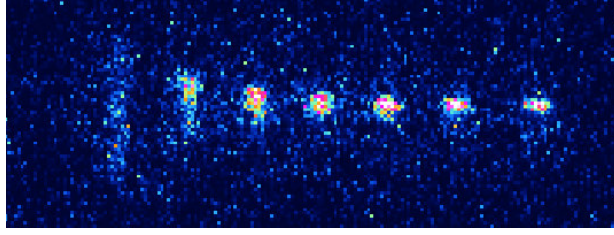


**Figure 5.10.** – Camera image of a linear ion crystal of 7 ions. The excitation frequency is set to the resonance frequency of the left ion. The Coulomb-interaction, together with a high dissipation broadening of the resonances, leads to an oscillation of the neighboring ions, but with an amplitude proportional to the interaction range  $1/d^2$ , with  $d$  being their distance from the oscillating ion.

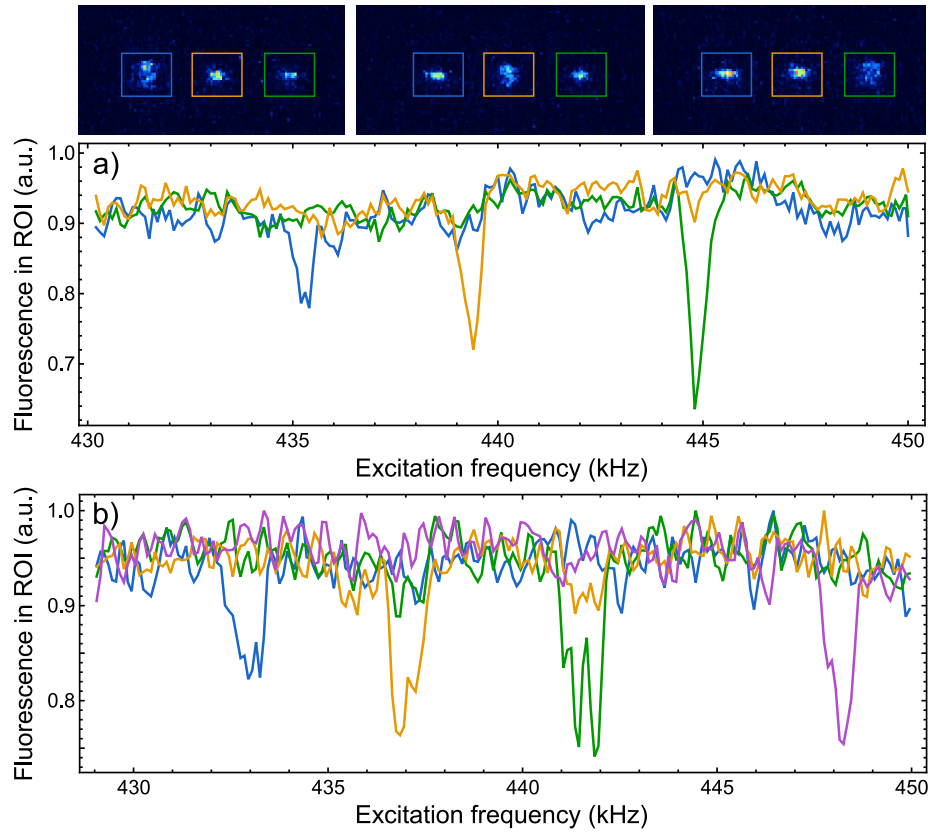


**Figure 5.11.** – (a) Individual addressing in a linear chain of 3 ions. The driving frequency has been scanned over a range of 20 kHz, addressing the resonance of only one ion at once. Each of the curves corresponds to the integrated fluorescence signal of one of the regions of interest (ROI), indicated on the camera images. The fluorescence signal for an oscillating ion is slightly reduced due to the additional Doppler shift. The difference in the distance of the individual resonance frequencies is a result of the  $1/z^2$  dependence of the trap frequency as discussed in Sec. 5.1.1. (b) The same measurement with a linear crystal of 4 ions. The contrast of the signal is reduced, but the ions are still addressed individually.





# 6

## Incoherent thermal excitation

This chapter is dedicated to the questions: "*What is temperature, how can we control it, and how can we measure it?*" The notion of *temperature* is clear for macroscopic systems, but becomes more complex on the nanoscopic scale. Here, we first want to focus in Sec. 6.1 on the identification and characterization of thermal states, before we discuss how to control and tune the temperature of single trapped ions deliberately. Controlling and measuring the temperature of single particles is essential for many different applications. Especially for the measurements of the single-ion heat engine in the next chapter a fast, precise and non-invasive thermometry technique is mandatory in order to analyze thermodynamic cycles. Furthermore, there is growing interest in the field of quantum thermodynamics and techniques like reservoir engineering or dissipative state preparation have moved into focus of ion trap experiments [Bér12, Toy13, Kie15]. In this chapter we experimentally demonstrate a method for a rapid determination of the temperature of trapped ions which is suitable for monitoring fast thermalization processes. The method is based on the multi-level electronic structure and the occurrence of dark resonances in the fluorescence signal of trapped ions. Narrow dark resonances originate from coherent population trapping in a three level system [Alz76, Ari76, Ari96] and provide a high velocity sensitivity of their fluorescence signal.

This new method complements the thermometry toolbox for trapped ions at an intermediate range between  $10^{-1}$  and  $10^{+2}$  mK, the typical temperatures of Doppler cooled and moderately heated ions. For highly excited thermal states there are already well established techniques, such as Doppler recoiling or spectral thermometry. The Doppler recoiling technique is appropriate for a temperatures range  $10^{-1} - 10^{+1}$  meV ( $10^3 - 10^5$  mK) [Eps07, Wes07]. For lower temperatures spectral thermometry and spatial thermometry have proved to be useful techniques. Spectral thermometry uses the line shape of the fluorescence signal to extract the temperature of the ion [Nag83], but is accompanied by rather large uncertainties [Has98, Her09]. Extracting the temperature from the spatial distribution of a thermal atom is limited by the resolution of the imaging system [Nor11]. By a precise calibration of the imaging optics and its magnification, temperatures down to the Doppler limit can be measured [Knü12].

In this chapter we demonstrate that spatial thermometry supplements the dark resonance technique perfectly for higher temperatures. For experiments in the strong-binding regime  $\omega \gg \Gamma$  (trap frequency  $\omega$  much larger than transition linewidth  $\Gamma$ ) and close to the ground state of motion, precise temperature measurements can be achieved by spectroscopy of the sidebands of an optical transition  $\nu$ , which originate from the oscillation

of the ion. The mean phonon number of the vibrational state of the ion is then deduced from the relation of the excitation probabilities on the red and blue sidebands  $\nu - \omega$  and  $\nu + \omega$ , respectively [Tur00a, Eps07, Bro15]. Dark resonance thermometry, however, can be applied in the weak-binding regime  $\omega \ll \Gamma$ , where sidebands are not resolved due to low trap frequencies, and for thermal states between a few and up to some hundreds of phonons.

We start the discussion of dark resonance thermometry with a derivation of the appearance of dark resonances in a multi-level system from the steady-state solution of the optical Bloch equations in Sec. 6.2. This analytical model is used to obtain temperature values from measured resonances. We show in a semi-classical picture how dark resonances can be used to tune the temperature of the ions. The laser linewidth is a crucial parameter for dark resonance thermometry. For both lasers which are used for spectroscopy, the linewidth is on the same order of magnitude as the broadened resonances are. As a consequence, any uncertainty of the laser linewidth affects the precision of the resulting temperatures. In Sec. 6.3 we deduce the laser linewidth from the error-signal of the PDH locking scheme. While we show in Sec. 6.4 the results of steady state temperature measurements, Sec. 6.5 focuses on measurements of the dynamics of heating and cooling processes, and demonstrates the limits and effects of the temporal resolution of the measurement. Furthermore, in Sec. 6.6, we show how the ion temperature can be controlled between 0.7 mK and more than 10 mK by tuning the cooling laser to selected features of the dark resonances. Finally, in Sec. 6.7 we compare our method to the spatial thermometry technique. Sec. 6.8 summarizes the results of the dark resonance thermometry technique and proposes possible applications.

The key features and basic demonstrations of the dark resonance thermometry technique have been published in:

**Fast thermometry for trapped ions using dark resonances,**  
J. Roßnagel, K.N. Tolazzi, F. Schmidt-Kaler and K. Singer,  
New J. Phys. 17, 045004 (2015).

## 6.1. Temperature of a single trapped ion

### 6.1.1. The notion of temperature

For a classical, macroscopic and ideal gas system in the thermodynamic limit (large number of particles), the individual particles are interacting and exchange their kinetic energy. Each of the particles is experiencing a Brownian motion under random kicks from the other particles [Uhl30]. Since we observe the system as a whole, not the individual trajectories but the mean values of the observables are of interest. Through the interaction of the particles, the distribution of kinetic energy tends towards an equilibrium. The temperature  $T$  is then defined as the mean kinetic energy  $\langle E_{\text{kin}} \rangle$  in each degree of freedom  $f$ ,

$$\langle E_{\text{kin}} \rangle = \frac{f}{2} k_B T. \quad (6.1)$$

When heat is added to the system, it is distributed over all particles and all degrees of freedom and the system reaches again a thermal equilibrium.

On the other hand, for quantum systems there is clear definition of the temperature as well. In Sec. 3.1.1 we have presented the phonon distribution for a quantum harmonic

oscillator in thermal equilibrium. We have shown that its temperature can be derived from the mean value  $\langle n \rangle$  of many measurements of its phonon number according to

$$T(\langle n \rangle, \omega) = \frac{\hbar\omega}{k_B \ln \left( \frac{\langle n \rangle + 1}{\langle n \rangle} \right)} \quad (6.2)$$

Now we want to compare this to microscopic and nanoscopic systems in the classical weak binding regime,  $k_B T \ll \hbar\omega$ , and thus to the situation in our experiment. In those systems, a classical trajectory of single particle is observed as a function of time. However, the temperature is a statistical quantity and thus it is impossible to assign a temperature to a single particle for a particular moment. The ergodic hypothesis states that for thermodynamic systems the ensemble average of a large system equals the time average of a single particle. Thereby, the statistical definition of temperature is translated to single-atom systems. In contact with a thermal bath, the single particle experiences fluctuating disturbances of its trajectory and therefore exhibits Brownian motion. As a consequence of the equipartition theorem, the temperature  $T$  of a single atom can be defined as the mean energy of this thermal Brownian motion, and therefore corresponds to the mean squared displacement  $\sigma$

$$\sigma^2 = \frac{k_B T}{\rho} t \quad \text{with} \quad \sigma^2 = \frac{1}{\tau} \int_0^\tau \mathcal{R}(t)^2 dt, \quad (6.3)$$

where  $\mathcal{R}$  is the displacement of the Brownian trajectory from its starting point,  $\rho$  is a constant and proportional to the friction and  $\tau$  is the observation time [Uhl30, Mar15]. This definition of temperature becomes intuitively clear for the situation of colloidal microparticles immersed in water, as used in many thermodynamic experiments [Bli12, Bér12, Mar16]. These particles are in permanent contact with the surrounding water molecules. Observing the microparticle therefore equals the observation of one single particle of a large ensemble in thermal equilibrium. Considering the equipartition theorem and the ergodic hypotheses, there is no doubt that the Brownian motion of this particle reflects the temperature of the system.

For isolated systems, such as a single trapped ion or a levitated microparticle in vacuum [Mil14], the situation is more complex. In such systems, there is no physical contact with a thermal heat bath. To define and control the temperature for such systems, we have to mimic the bath interaction by external means. How would the particle behave, if it would be in contact with a thermal heat bath? It would exhibit a Brownian motion, as the microparticle in water does. In our case, the ion is confined in a harmonic potential, which leads to a normal distribution of the time averaged displacement and velocity of the ion [Bla86, Mee96]. Consequently,  $\sigma$  is the width of the thermal probability distribution  $p$  of the ions displacement  $x$ ,

$$p(x) = \sqrt{\frac{1}{2\pi\sigma^2}} \exp \left[ -\frac{(x - x_0)^2}{2\sigma^2} \right], \quad (6.4)$$

and the temperature of the ion in the weak reads

$$T = \frac{m\omega^2\sigma^2}{k_B}. \quad (6.5)$$

Fig. 6.1 shows the measured probability distribution of the recorded fluorescence of a trapped ion at different temperatures. A fit of  $p(x) \propto \exp[-x^2/\sigma^2]$  to the data and the

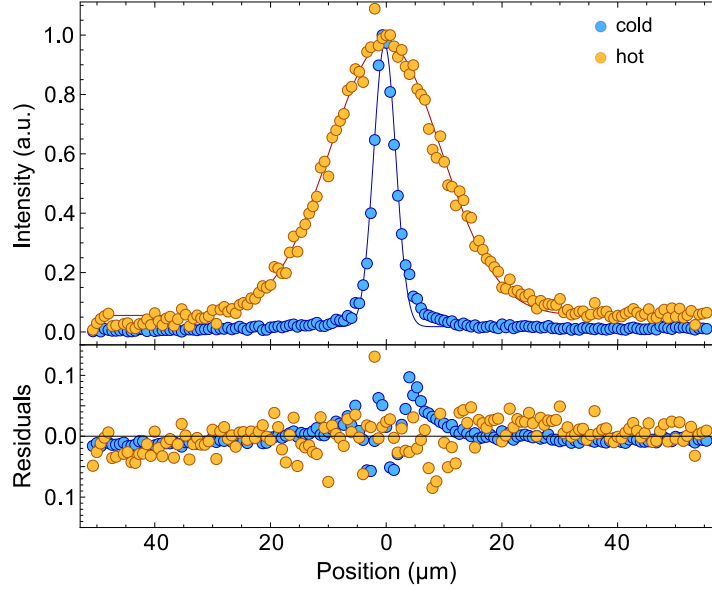


**Figure 6.1.** – Spatial intensity distribution of the fluorescence signal of the ion, while in contact with thermal baths at different temperatures, together with fitted Gaussian distributions. The residuals demonstrate the agreement of the data with the fitted function. We observe little deviations at the lower edges which are seen on all ion images and result from halo-like aberrations of the camera objective. These effects don't scale with the extent of the fluorescence distribution and thus disappear for larger distributions.

corresponding residuals demonstrate the Gaussianity of the fluorescence distribution. However, the Gaussian distribution is a necessary, but no sufficient condition for proofing a thermal state. There might be other states, e.g. squeezed states, whose time-averaged projection has a Gaussian shape as well. But, at least, a Gaussian distribution excludes a variety of different motional states, most important coherent states which are likely to be excited. To guarantee a purely thermal state of the ion we need to know the nature of the applied excitation. If this excitation is completely incoherent, provides a Gaussian probability distribution and is irreversible, a non-thermal state of the ion can be excluded. Consequently, such an environment mimics an effective thermal heat bath for the trapped ion [Cir94b, Poy96].

### 6.1.2. Generation of thermal states at various temperatures

We initialize our experiment by laser cooling the ion. The interaction of a harmonically bound two-level atom with a laser field is well-understood [Cir92]. In a classical description, a laser-cooled atom experiences random recoils from photon absorption and emission events [Ste86a]. The isotropic emission of photons leads to a random Brownian motion. By the nature of the incoherent spontaneous emission process, all prerequisites for the generation of a thermal state are met. In a more sophisticated analysis, the master equation describing the dynamics of a harmonically bound two-level atom with a laser field is identical to that of a damped harmonic oscillator coupled to a thermal bath [Cir94b, Poy96]. The corresponding stationary state is hence thermal. In the following experiments we will employ laser cooling for generating cold thermal states or to decrease the temperature of hot thermal states in a controlled way.

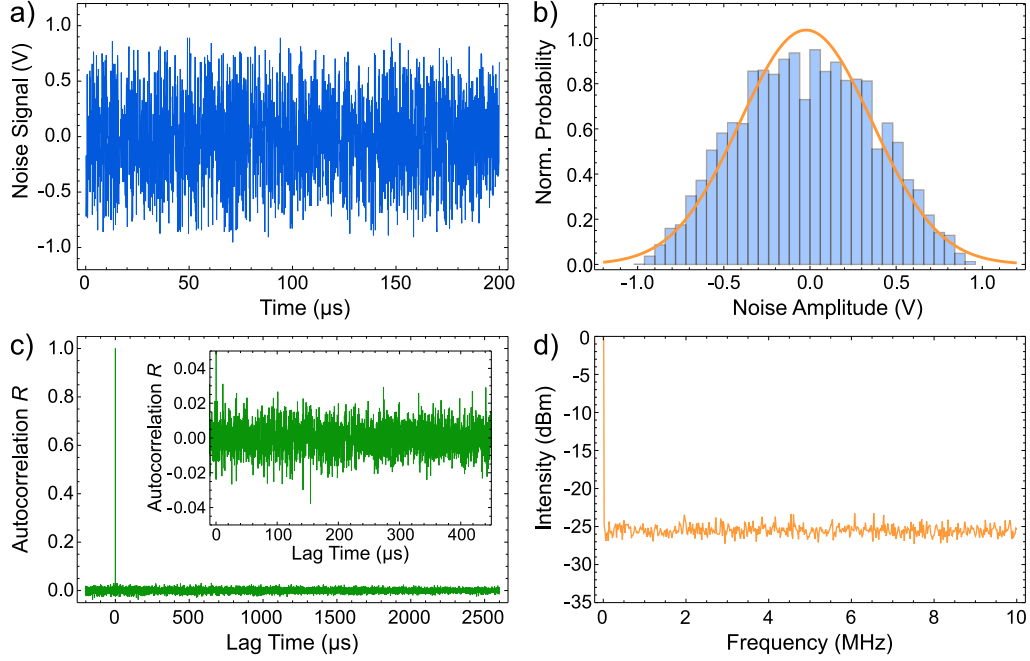


**Figure 6.2.** – (a) Noise signal as a function of time, with  $\mathcal{N} = 0.5 V_{rms}$  and 2000 samples. (b) Histogram of the noise signal including 13 k samples. A fit of a normal probability distribution shows the Gaussianity of the noise. (c) Auto-correlation-function of the noise signal. The finite correlation is due to limited samples size. The auto-correlation demonstrates the high quality of the quasi-random distribution of the digital signal. (d) Frequency spectrum of the white noise, showing an equal probability distribution in a frequency range of up to 10 MHz.

Unfortunately, the interaction with a laser beam alone is unsuitable for increasing the thermal energy. For a blue detuned laser beam, the absorption provides an energy gain as compared to the emission process and dominates the dynamics by increasing the kinetic energy of the ion. However, the absorption process is velocity dependent and will amplify any coherent oscillation of the ion parametrically. This results in regular oscillation of the ion rather than a thermal excitation.

In order to generate thermal states at higher temperatures in a defined way, we expose the ion to white, Gaussian electric field noise, as it has been shown in other experiments [Tur00a, Mar15]. In the classical picture, the kicks due to the Gaussian noise result in a Brownian motion and thus leave the ion in a thermal state at higher temperature. In particular, the Maxwellian velocity distribution of the ion remains Maxwellian during the noise interaction. The width of the velocity distribution increases during the heating process, but the distribution remains thermal. The master equation for an ion subjected to Gaussian noise is also of the form of that of a harmonic oscillator coupled to a thermal bath [Fey63]. The linearity of these two master equations ensures that the Gaussian shape of the phase space distribution is preserved.

However, in principle one could record the noise pattern of the generator and, after some time, run the same pattern backwards. If we have started with an ion at rest, we should end up with an ion at rest after the interaction with the noise signal and with its inverse signal, since a trapped ion is a perfectly isolated system. Additionally, the electric field noise leads to an ever increasing amplitude. To counteract these problems

we combine the noise interaction with a simultaneous laser cooling. The velocity dependent cooling rate limits the increasing temperature and the system tends towards an equilibrium between heating and cooling rate. Furthermore, the additional spontaneous emission events scramble the defined Brownian motion of the noise generator, and an inversion of the trajectory is thus impossible. As a consequence, due to the white noise spectrum and the Gaussian probability distribution of the electric noise, and in combination with laser cooling, it acts as a thermal heat bath on the trapped ion.

To guarantee a heating in radial direction only, without affecting the axial degree of freedom, we need to shuffle the position of the potential minimum randomly around in the radial plane, without changing the strength of the trapping potential. As discussed in Sec. 4.1.3 this is achieved by applying the same noise signal with inverted sign on two opposing outer-electrodes. As a noise source we use an arbitrary function generator<sup>36</sup> which provides noise signals of up to  $\mathcal{N} = 10 V_{\text{rms}}$ . Fig. 6.2 (a) and (b) show a recorded noise signal together with its histogram. A fit to the data reveals a Gaussian-like distribution. A slight drop for small amplitudes may result from the limited resolution during the record of the signal. Since the noise generator is running digitally, the output signal is a pseudo-random-noise with a bandwidth of 20 MHz. The corresponding normalized auto-correlation function

$$R_{\mathcal{N}}(\tau) = \frac{1}{T} \int_0^T \mathcal{N}(t + \tau) \mathcal{N}(t) dt \quad (6.6)$$

is presented in Fig. 6.2 (c). The resulting delta-function like auto-correlation  $R_{\mathcal{N}}(\tau) = \delta(\tau)$  demonstrates that the generator is not repeating a fixed noise pattern but continuously generates random output voltages. This is important when applying electric noise to a trapped ion, since any signal repetition with a rate close to one of the trap frequencies would excite coherent oscillations of the ion. The residual correlation of  $|R_{\mathcal{N}}| \leq 0.02$  is due to the finite size of the recorded sample. Fig. 6.2 (d) shows the frequency spectrum of the noise. It provides an equal distribution in range of up to 10 MHz and thus can be regarded as white.

We have now shown that laser cooling, as well as the electric field noise, are engineered thermal environments for the trapped ion. During interaction, the temperature of the ion is changed and approaches a steady-state temperature, while its motional state stays thermal. We show in Sec. 6.5 that, indeed, the dynamics of the temperature changes behave like thermalization processes. As a consequence, these environments mimic thermal heat baths where the ion is coupled to, while the steady-state temperatures correspond to the effective bath temperatures [Cir94b, Poy96].

In the experiment we apply the noise in such a way that the trapping potential is not squeezed but shifted according to the noise signal. As described in Sec. 4.1.3, the noise signal is fed with opposing signs to two opposing electrodes, and thus shuffles the potential around, while the trap frequency stays constant. The force  $F$ ,

$$\vec{F}(r, t) = m \vec{a}(r, t) = e \vec{E}(r, t), \quad (6.7)$$

corresponding to the electric field

$$\vec{E}(r, t) = \vec{\nabla} \Phi(r) \cdot \mathcal{N}(t), \quad (6.8)$$

<sup>36</sup> 50 MHz Arbitrary Waveform/Function Generator 3390, Keithley Instruments GmbH.

exerts kicks on the ion and leads to the Brownian motion. Here, we have decomposed the potential of the trapping field  $\vec{E}$  into a static part  $\Phi$  and the superimposed noise signal  $\mathcal{N}(t)$ . The thermal energy corresponds to the time-average of the kinetic energy

$$E_{th} = \langle E_{kin}(t) \rangle = \frac{1}{2}m \langle v^2(t) \rangle = \frac{1}{2}k_B T. \quad (6.9)$$

In the harmonic potential of the trap we find  $\langle v^2(t) \rangle = \omega \langle a^2(t) \rangle$ , which relates  $T$  to  $\mathcal{N}(t)$  according to

$$T = \frac{m\omega}{k_B} \langle a^2(t) \rangle = \frac{e\omega}{k_B} \langle E^2(t) \rangle = \frac{e\omega}{k_B} (\vec{\nabla} \Phi(x))^2 \langle \mathcal{N}^2(t) \rangle. \quad (6.10)$$

Thus the temperature of the ion scales quadratically with the root-mean-square amplitude of the noise signal  $\mathcal{N}_{rms}(t)$ , which we refer to as  $\mathcal{N}$  in the following,

$$T \propto \mathcal{N}^2. \quad (6.11)$$

## 6.2. Principles of dark resonance thermometry

So far dark resonances have been shown to provide a useful tool for compensating micromotion in ion traps or tuning the cooling rate for single ions [Rei02b, Esc03, Lis05]. Recently they have been used to determine the temperature of laser cooled neutral atom clouds in the sub-millikelvin regime [Pet12]. We have adopted this technique for the first time for trapped ion systems. Observing and analyzing the lineshape of those dark resonances provides a temperature measurement which is accurate over a large dynamic range and which is well-suited for applications in systems with low trap frequencies. It can be applied to large ion crystals and to observe fast thermal processes, which typically occur in the range of  $10^{-4}$  s. While dark resonance thermometry can be employed within a wide range of temperatures it is convenient to use and does not require any additional lasers or technical components as compared to Doppler laser-cooling.

We first need to derive a theoretical model for the line shape of the dark resonances depending on the temperature in order to analyze the measured spectra. As described in Sec. 2.7, in our case the spectrum of the  $^{40}\text{Ca}^+$ -ion can be approximated by a three-level system with fine structure levels  $^2S_{1/2} = |1\rangle$ ,  $^2D_{3/2} = |3\rangle$  and  $^2P_{1/2} = |2\rangle$ , while the magnetic field lifts the degeneracy of the electronic states leading to an 8-level system [Sch95, Obe99]. However, to qualitatively describe coherent population trapping (CPT) and the appearance of dark resonances we start with the idealized case of a general three-level system. Later, this model is expanded to an 8-level system with a quantitative analysis corresponding the experimental parameters.

CPT first was observed as a drop of the fluorescence signal from Na atoms in a vapor cell [Alz76]. It has been described as a pumping of atoms into a dark non-absorbing state, created by destructive interference of excitation pathways from two stable levels to a common excited level [Kha15]. The effect of CPT should not be confused with the occurrence of electromagnetically induced transparency (EIT), where a strong light-field induces dressed states of the excited level due to the AC-Stark effect [Fle05]. Both effects have similar physical principles, based on interferences in a three-level-system, but differ in many essential points: while CPT uses the interference of both optically driven transitions to generate a dark state, for EIT only one laser is needed. The interference



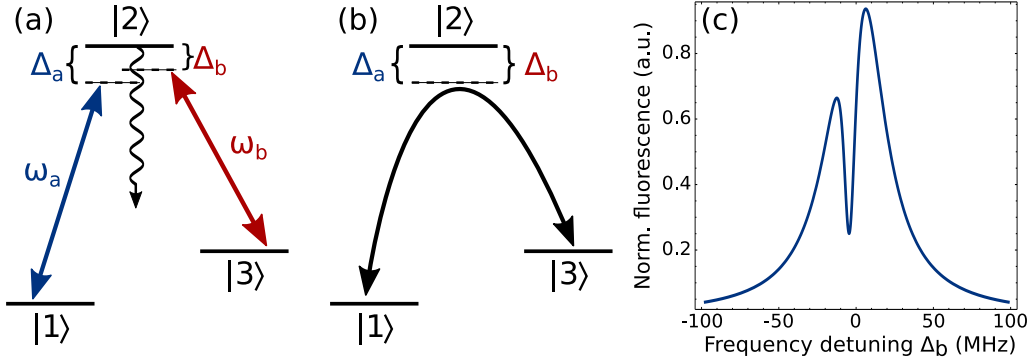


**Figure 6.3.** – Emergence of dark resonances due to coherent population trapping. (a) Three-level system with atomic states  $|1\rangle$ ,  $|2\rangle$  and  $|3\rangle$ , and two near-resonant light fields with frequencies  $\omega_a$  and  $\omega_b$  in  $\Lambda$ -configuration. For  $\Delta_a \neq \Delta_b$  the fluorescence from  $|2\rangle$  are observed. (b) If  $\Delta_a = \Delta_b$  the population is trapped in a coherent superposition of  $|1\rangle$  and  $|3\rangle$ . This state is not coupled to  $|2\rangle$  and consequently no fluorescence is observed. (c) To obtain a spectrum of resonance fluorescence the detuning  $\Delta_a$  is scanned. If both detunings are equal  $\Delta_a = \Delta_b$  the fluorescence shows a drop, the dark resonance.

arises between the doublet of the dressed states. A second probe laser is used to probe this effect, not to generate it [Kha15].

We now consider three states  $|1\rangle$ ,  $|2\rangle$ ,  $|3\rangle$  in  $\Lambda$ -configuration, where two near-resonant light fields with frequencies  $\omega_a$  and  $\omega_b$  drive the atomic transitions  $\omega_{12}$  and  $\omega_{23}$ , respectively (see Fig. 6.3 (a)). As long as the detunings  $\Delta_i$  of both light fields are different  $\Delta_a \neq \Delta_b$  the excited state  $|2\rangle$  is populated, and fluorescence from spontaneous decay is observed. In the case that  $\Delta_a = \Delta_b$  a coherent superposition of the states  $|1\rangle$  and  $|3\rangle$  is generated. If the radiation lifetime of  $|1\rangle$  and  $|3\rangle$  is much longer than the lifetime of  $|2\rangle$ , a significant part of the population is transferred into this superposition state and coherent population trapping is achieved. Since this state is decoupled from the individual driving fields, no spontaneous decay from  $|2\rangle$  is observed, resulting in a "dark" resonance [CT11]. When scanning the frequency of one of the two fields while keeping the other constant, a drop in the fluorescence spectrum of  $|2\rangle \rightarrow |1\rangle$  is observed (see Fig. 6.3 (b)). Note that the steady state of the internal dynamics is generally reached much faster than any relevant external timescales, in particular thermalization processes [Tol14].

For an ion in motion, this dark resonance line is shifted due to the Doppler effect. Because a thermal state of an ion consists of many different velocity classes, it leads to a broadening of the dark resonance. Additional broadening is caused by the phase fluctuations of the laser fields, denoted by a spectral linewidth  $\Gamma$ . However, if the spectral linewidth of the lasers is known, the measured broadening of the dark resonance feature allows to determine the temperature of the ion by comparing with calculated spectra.

### 6.2.1. Calculation of dark resonance spectra

For a quantitative determination of the ion temperature from the measured fluorescence spectra, a model for the theoretical lineshape is required. Therefore we describe the dynamics of a general  $N$ -level system by a Lindblad master equation, the time evolution of the density matrix. We consider the Hamiltonian of the system

$$\mathcal{H} = \mathcal{H}_{dip} + \mathcal{H}_{ion} \quad (6.12)$$

which is composed of  $\mathcal{H}_{dip}$ , the ion-light dipole interaction and  $\mathcal{H}_{ion}$ , describing internal states of the ion including the detuning of the two light fields  $\Delta_a$  and  $\Delta_b$  [Fle05, CT11]. The motional state of the ion, not included in the Hamiltonian, will be introduced later as a spectral Doppler shift of the detunings  $\Delta_{a,b}$ .

The Lindblad master equation for the density matrix  $\hat{\rho}$  reads [Cir92]

$$\frac{d\hat{\rho}}{dt} = -\frac{i}{\hbar} [\mathcal{H}, \hat{\rho}] + \mathcal{L}(\hat{\rho}). \quad (6.13)$$

The spontaneous decay of the population of the excited levels is introduced by the dissipative Lindblad operator

$$\mathcal{L}(\hat{\rho}) = \sum_i \left[ \mathcal{C}_i \hat{\rho} \mathcal{C}_i^\dagger - \frac{1}{2} \left( \mathcal{C}_i^\dagger \mathcal{C}_i \hat{\rho} + \hat{\rho} \mathcal{C}_i^\dagger \mathcal{C}_i \right) \right]. \quad (6.14)$$

where the transition operators  $\mathcal{C}_i = \sqrt{\Gamma_{pq}} |q\rangle \langle p|$  describe the dissipation along the dipole transitions  $p \rightarrow q$ . They depend on the decay rates according to Fermi's golden rule [CT77, Scu97]

$$\Gamma_{pq} = \frac{8\pi^2}{3\epsilon_0 \hbar \lambda_{pq}} \left| \langle p | \vec{D} | q \rangle \right|^2 \quad (6.15)$$

with the atomic dipole operator  $\vec{D}$  and the transition wavelength  $\lambda_{pq}$ .

The spectral widths of the light fields  $\Gamma_a$  and  $\Gamma_b$  are included as an additional broadening of the corresponding atomic level  $|q\rangle$ , see [Obe99] and [Tol14]. Phase fluctuations between the atomic state and the light field lead to a decay of the dark state and are modeled by transition operators  $\mathcal{C}_{a,b} = \sqrt{\Gamma_{a,b}} |q\rangle \langle q|$  [CT77, CT11].

To obtain the resulting spectrum of the fluorescence light, the steady state solution  $d\hat{\rho}/dt = 0$  is required. In the following we will solve this equation numerically. We transform Eq. (6.13) into a matrix equation, in which the density matrix  $\hat{\rho}$  with dimension  $N \times N$  is represented by a vector with  $N^2$  entries, where  $N$  is the number of atomic levels involved. Consequently, the master equation with the Lindblad operator  $L_{ik}$  in matrix form is described by

$$\frac{d\vec{\rho}_i}{dt} = \sum_{k=1}^{N^2} L_{ik} \vec{\rho}_k = 0 \quad \text{with} \quad i \in \{1, \dots, N^2\}. \quad (6.16)$$

One of these equations (for simplicity  $i = 1$ ) is replaced by the normalization condition  $\text{Tr}(\hat{\rho}) = 1$ . Finally, to obtain the steady state solution  $\hat{\rho}^0$  we solve the homogeneous equation (6.16) with  $d\vec{\rho}/dt = 0$  by numerical matrix inversion. The fluorescence rate  $\mathcal{F}$  is then proportional to the population in the excited state(s)  $j$

$$\mathcal{F} \propto \hat{\rho}_{jj}^0. \quad (6.17)$$

To get a fluorescence spectrum including the dark resonances, as shown in Fig. 6.3 (b) for a three-level system,  $\mathcal{F}$  has to be calculated for every detuning  $\Delta_i$  of the corresponding light field within the range of interest.

### 6.2.2. Dark resonances and thermal motion

Now, we take the finite temperature of the ion into account, assuming a thermal state at temperature  $T$ . For conditions with phonon numbers  $n \gg 1$ , the motional state of the

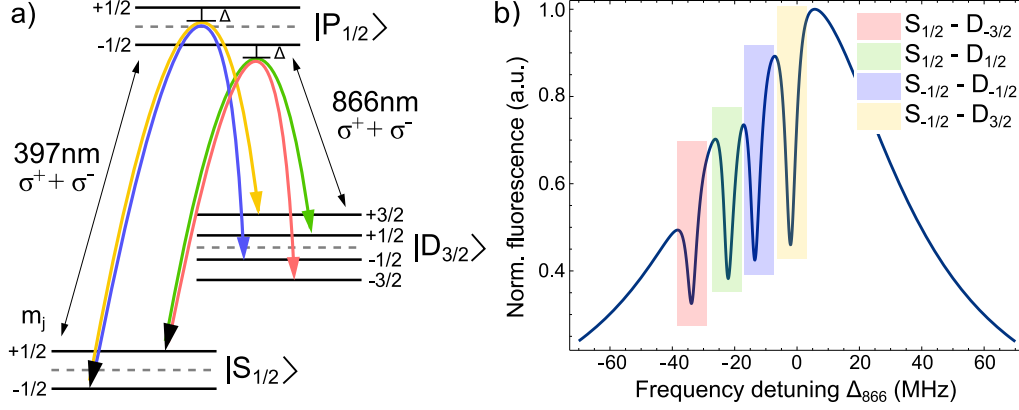


**Figure 6.4.** – (a) Zeeman splitting lifts the degeneracy of the three-level system (dashed lines), leading to a 8-level system, not drawn to scale. The polarization of the two light fields leads to 4 possible coherent transitions from the ground states  $S_{1/2}$  into the metastable states  $D_{3/2}$ . (b) Calculated spectrum of the 8-level system under respect of the given polarizations, leading to 4 dark resonances. The background colors indicate the corresponding transitions.

ion can be introduced in a semi-classical way. We consider the two light fields to have an angle  $\alpha$  with respect to each other. A velocity  $\vec{v}$  of the ion results in a Doppler shift of the two frequencies  $\omega_a$  and  $\omega_b$  and thus modifies their detuning by the vector product

$$\delta\Delta_i(v, \alpha) = \vec{k}_i \cdot \vec{v}, \quad (6.18)$$

where  $\vec{k}_i$  are the corresponding wave-vectors. Through the inclusion of the Doppler shifted detunings in the calculation of the spectrum we get a fluorescence rate  $\mathcal{F}(\alpha, \vec{v})$  depending on  $\alpha$  and  $\vec{v}$ . We obtain a temperature-dependent fluorescence rate  $\tilde{\mathcal{F}}(T)$

$$\tilde{\mathcal{F}}(T) = \int P_T(\vec{v}) \cdot \mathcal{F}_\alpha(\vec{v}) d\vec{v}, \quad (6.19)$$

by integrating over all velocity classes in the Maxwell-Boltzmann distribution

$$P_T(\vec{v}) = \left( \frac{m}{2\pi k_B T} \right)^{3/2} e^{(-m\vec{v}^2/2k_B T)} \quad (6.20)$$

with atomic mass  $m$  and Boltzmann-constant  $k_B$ .

For a numerical solution of Eq. (6.19) we discretize  $\vec{v}$  into distinct velocity classes along the directions of the laser beams. To obtain a fluorescence spectrum, scattered photons near 397 nm are recorded as a function of the detuning  $\Delta_{866}$ , while  $\Delta_{397}$  is kept constant. Note, that scanning  $\Delta_{397}$  is unfavorable for thermometry, as its detuning has a strong influence on the cooling rate. As a magnetic field is applied to define the quantization axis, the degeneracy of the electronic states is lifted, resulting in an 8-level system [Sch95, Obe99], see Fig. 6.4 (a). Depending on the polarizations of the laser beams up to 12 dark resonance lines can be observed. In our experiment the polarizations of both beams are chosen such that only  $\sigma^+$  and  $\sigma^-$  transitions are addressed, leading to the appearance of 4 dark resonances (Fig. 6.4). Regarding the  $P_{1/2} \leftrightarrow D_{3/2}$  transition, the  $\sigma^\pm$ -polarization avoids dark states in the  $D_{3/2}$  manifold, which would not be coupled to any  $P_{1/2}$  level. For the  $S_{1/2} \leftrightarrow P_{1/2}$  transition a  $\sigma^\pm$ -polarization is convenient as it leads to an excitation of transitions which are maximally apart and therefore most easily resolved.

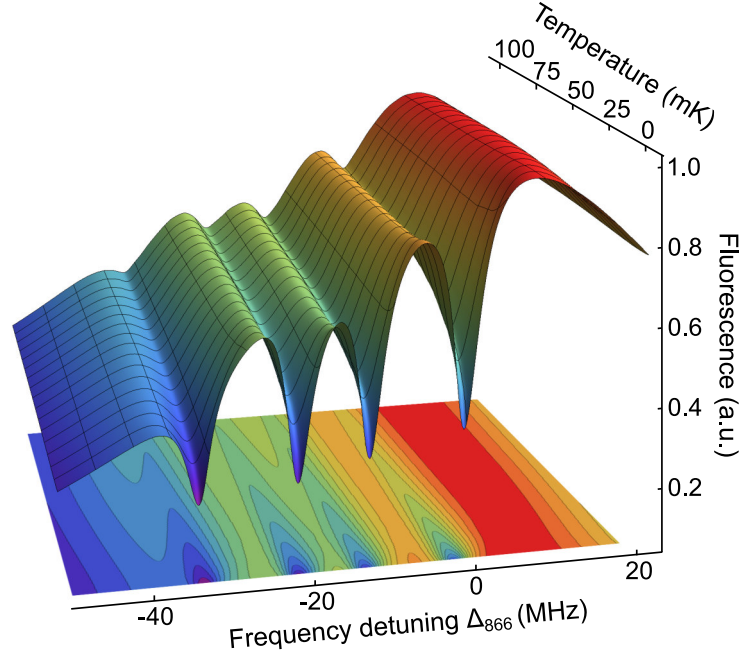


**Figure 6.5.** – 3D surface plot of the calculated fluorescence spectrum as a function of the frequency detuning  $\Delta_{866}$  and as a function of the temperature of the ions. The decreasing depths of the resonances for increasing temperatures is emphasized by the contour plot on the bottom, where blue (red) indicates low (high) fluorescence.

For the 8-level system, the matrix form of  $\mathcal{H}$  as well as the coupling operators  $\mathcal{C}_i$  are given explicitly in [Tol14]. The Zeeman-splitting leads to a 64-dimensional Lindblad operator  $L_{ik}$  in Eq. (6.16) and thus to a time consuming matrix decomposition. To reduce the computational complexity we approximate the effect of temperature on the dark resonances by a relative Doppler broadening  $\Gamma_D(T, \alpha)$ . It can be deduced from the variance of the relative Doppler shift  $\delta\Delta = \delta\Delta_{397} - \delta\Delta_{866}$  and reads

$$\Gamma_D(T, \alpha) = |\vec{k}_{397} - \vec{k}_{866}| \sqrt{\frac{k_B T}{2m}} = \sqrt{k_{397}^2 + k_{866}^2 - 2k_{397}k_{866} \cos(\alpha)} \sqrt{\frac{k_B T}{2m}}. \quad (6.21)$$

Regarding the shape of the dark resonances, the laser linewidths and the Doppler broadening act in a similar way. Therefore,  $\Gamma_D$  is treated as an additional contribution to the broadening due to the spectral widths of the lasers. During the following applications both methods, using Eq. (6.19) and Eq. (6.21), have been compared for different spectra and lead to consistent results for the temperatures within their uncertainties. The resulting line shape of the dark resonances as a function of the temperature  $T$  is shown in Fig. 6.5. To determine the ion temperature the measured fluorescence data is fitted by  $\tilde{\mathcal{F}}(T)$  using a Markov-chain Monte-Carlo parameter estimation [Pos14].

The thermal broadening  $\Gamma_D(T, \alpha)$  shows a strong dependence on the relative orientation  $\alpha$  of the  $k$ -vectors of the two lasers. The strongest influence of the temperature, and thus the highest sensitivity especially at low temperatures, is achieved for counter propagating laser beams ( $\alpha = \pi$ ), where  $\Delta_{397}$  and  $\Delta_{866}$  are Doppler shifted with opposite signs. However, already for moderate temperatures of a few millikelvin the contrast of the dark resonances becomes too small to assign a reliable temperature. In this range, the best

choice is a collinear beam configuration ( $\alpha = 0$ ), which shows a reduced sensitivity, but is well suited for a wide range of temperatures up to several tens of millikelvin, as shown in Fig. 6.5. As most of the measurements in this thesis are performed at relatively high temperatures, we will only use the collinear beam configuration here. A detailed analysis of the sensitivity as a function of  $\alpha$ , as well as measurements in the counter-propagating beam configuration, are presented in [Tol14].

### 6.2.3. Shaping the laser cooling by exploiting dark resonances

For temperature measurements in general, the interaction of any measurement device with the system under investigation changes the temperature of the system. Here, the non-linear modification of the photon scattering rate in vicinity of dark resonances affects the equilibrium temperature of the ion. However, this effect can be exploited to tune the temperature of the ion only by using the non-linear properties of dark resonances. In the following it is analyzed in a semi-classical picture, where the Doppler shift reduces the light scattering of selected velocity classes.

For Doppler cooling, during which the 866 nm laser may be far detuned from dark resonances, the cooling rate is limited by the spontaneous emission lifetime  $\tau_p = 6.9$  ns of the  $P_{1/2}$  level. We assume the weak binding regime, which means that the period of the secular motion is much larger than the lifetime,  $\omega \ll 1/\tau_p$ . The steady state of the internal dynamics is typically reached after  $10^{-7}$  s and therefore, at least in our case, much faster than any secular motion. The ion does not move considerably during the scattering process [Ste86b, Met99] and we can assume a constant velocity. In the vicinity of a dark resonance the velocity-dependent Doppler cooling force is affected by the modified scattering rate. To analyze its influence we introduce the effective Doppler shift  $\delta\Delta^{\text{DR}}$  of the relative detuning of the laser frequencies with respect to a dark resonance,  $\Delta^{\text{DR}} = \Delta_{866} - \Delta_{397}$ . In consideration of  $\delta\Delta^{\text{DR}}$ , the condition for a dark resonance reads

$$\Delta_{\delta}^{\text{DR}} = \Delta^{\text{DR}} - \delta\Delta^{\text{DR}} = \Delta_{866} - \Delta_{397} - (\nu_{866} - \nu_{397}) \frac{\vec{v} \cdot \vec{e}}{c} = 0, \quad (6.22)$$

where  $\nu_i$  are the absolute frequencies of the lasers,  $\vec{e}$  is their direction and  $\vec{v}$  the velocity vector of the ion. The relative Doppler shift  $\delta\Delta^{\text{DR}}$  has the opposite sign of the two individual Doppler shifts, because  $\nu_{866} < \nu_{397}$ . If the ion moves in the same direction as the laser beams,  $\vec{v} \uparrow \vec{k}_i$ , photon scattering leads to an amplification of the motion of the ion. This heating process limits the achievable temperature during Doppler cooling [Met99]. However, if the frequency of the 866 nm laser is red detuned with respect to the dark resonance ( $\Delta^{\text{DR}} < 0$ ), those velocity classes with  $\vec{v} \uparrow \vec{k}_i$  are Doppler shifted into resonance  $\Delta_{\delta}^{\text{DR}} \approx 0$ . Photon scattering then is suppressed and the resulting excitation of the ion motion is reduced. As a consequence, for  $\Delta^{\text{DR}} < 0$  a lower temperature can be achieved, similar to the velocity dependent coherent population trapping (VSCPT) schemes for samples of neutral atoms [Asp88].

In Sec. 6.6 we present the corresponding measurements which demonstrate how the non-linear features of the scattering rate of photons in the region of dark resonances are used to tune the temperature of the ions within a large range.

### 6.3. Determination of the laser linewidth

To obtain the temperature from measured dark resonances, a precise knowledge of the laser linewidths  $\delta\nu_i$  is crucial. There are several common methods to determine the linewidth of continuous-wave lasers. In general, the determination of an optical frequency requires a frequency reference, which provides a higher accuracy than the linewidth under investigation. A beat signal of both frequencies then allows to convert fluctuations from the optical regime to frequencies which can be evaluated with electronics. For broadband lasers (e.g.  $\Delta\nu > 1$  GHz, multimode operation) techniques of spatial spectroscopy are sufficient, such as diffraction patterns of optical gratings. For narrow bandwidth lasers ( $\Delta\nu < 100$  MHz, single-mode operation) a high-finesse optical resonator can be used as a frequency reference. However, to construct a resonator with such a narrow linewidth is a complex and costly affair. Less demanding is the common technique of a self-heterodyne linewidth measurement, where the spectral line of the laser under investigation is used as frequency reference at the same time [Oka80]. The beam therefore is superposed with a delayed portion of itself, and the spectral width of the beat note reveals the laser linewidth. However, for narrow bandwidth lasers the coherence length is on the order of  $10^4$  m, and the required delay lines are expensive and bulky.

Here we show that an external locking-cavity can be used to measure  $\Delta\nu$ , although the cavity linewidth is much broader than the laser linewidth. We exploit the error-signal, resulting from the Pound-Drever-Hall lock, to convert frequency fluctuations of the laser to voltage fluctuations, as illustrated in Fig. 6.6. The conversion coefficient is defined by the slope of the error-signal around its zero-crossing. The error-signal is obtained from a scan of the laser frequency over the resonance of the cavity, and, as a consequence, the recorded error-signal is a function of time. In order to determine the velocity of the scan in units of the laser frequency, we set the range of the scan to more than a full spectral range (FSR) of the cavity, as demonstrated in Fig. 6.6 (b). The resulting conversion coefficient allows us to derive the spectral linewidth of the laser from the variance of the locking signal, while the laser is locked to the cavity, see Fig. 6.6 (c). By this procedure, the  $\sigma$ -linewidths of the 866 nm laser and of the 397 nm laser result to

$$\delta\nu_{866} = 209(12) \text{ kHz} \quad (6.23)$$

$$\delta\nu_{397} = 173(8) \text{ kHz}. \quad (6.24)$$

Here we have subtracted the electrical background noise quadratically, which has been determined in a separate measurement. The linewidths are in the specified range of  $\delta\nu < 300$  kHz for the types of grating stabilized diodes which are used [DK14]. As expected, the emission spectrum of the 397 nm laser is narrower than the one of the 866 nm laser, which results from the additional frequency filtering by the SHG cavity.

The precise knowledge of the laser linewidths is the basis for the determination of an absolute temperature in the following sections, and, at the same time, limits the precision of the temperature measurements.

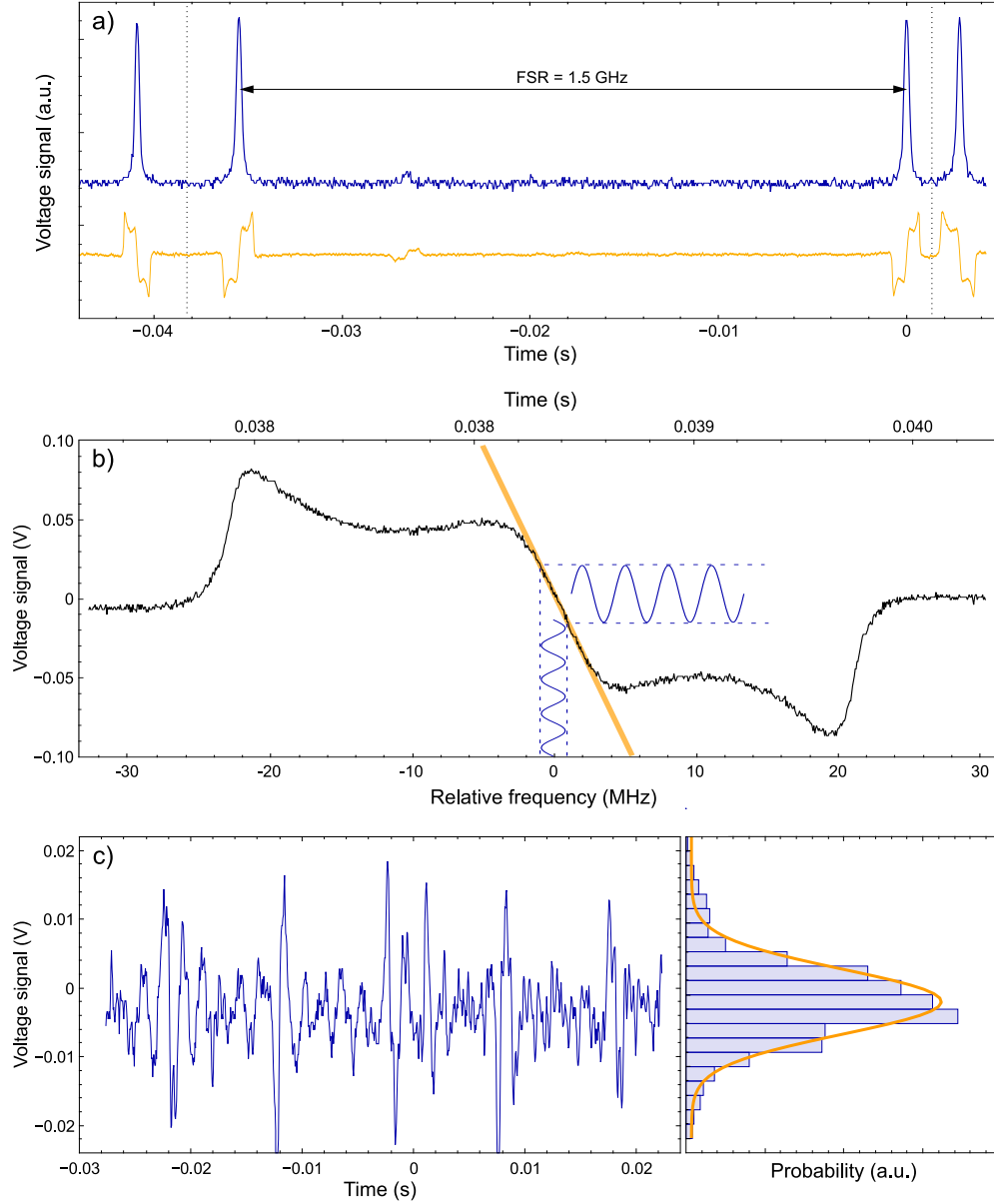


**Figure 6.6.** – Procedure to determine the linewidth of the laser sources. Here, as example, the linewidth of the 397 nm laser. (a) A scan of the full spectral range of the reference cavity is used to calibrate the scan velocity. The graph shows the transmission signal (blue) and the error signal of the cavity (orange). (b) Error signal from the PDH-lock (black). The slope of the linear control signal around the zero-crossing (orange) is measured to 22.2(2) mV/MHz. When locked to the zero crossing, a frequency oscillation (blue) is linearly translated to a voltage oscillation. (c) Resulting voltage fluctuations of the error signal of the locked laser (blue line). The  $\sigma$ -width of the distribution of the fluctuations (blue bars and orange fit) results to  $\sigma_{397} = 4.36$  mV and reveals a laser linewidth of  $\Delta\nu_{397} = 173$  kHz.

## 6.4. Temperature measurements in thermal equilibrium

### 6.4.1. Experimental parameters and characteristics

For the measurements in this section we drive the trap electrodes with a peak-to-peak voltage of about 890 V, leading to radial trap frequencies of  $\omega_x/2\pi = 468$  kHz and  $\omega_y/2\pi = 472$  kHz. Applying a constant voltage of 9 V to both end-caps results in an axial trap frequency of  $\omega_z/2\pi = 170$  kHz.

We use beam path *B1* from Fig. 4.10, where the two laser beams are oriented parallel to one another and perpendicular to the magnetic field. The laser beams address and cool all vibrational modes simultaneously. The polarization of both beams is chosen by waveplates to be perpendicular to the magnetic field, leading to a superposition of  $\sigma^+$  and  $\sigma^-$  polarization with respect to quantization axis. The intensity of the 397 nm beams is  $35 \mu\text{W}$  at a beam waist of  $160 \mu\text{m}$  and for the 866 nm laser  $80 \mu\text{W}$  at a beam waist of  $380 \mu\text{m}$ . To record the fluorescence spectra the PMT is employed, while the camera image is used for trapping, controlling and preparing the ions. The use of the PMT allows to count single photons, which enables us to perform measurements with exposure times of as short as some microseconds. For the spectral scans a constant intensity of the 866 nm laser beam over a range of 50 MHz is required. To avoid power fluctuations during frequency scans, we employ the stabilization technique presented in Sec. 4.3.3.

### 6.4.2. Experimental procedure

To record a spectrum, the frequency of the 866 nm beam is scanned via the drive frequency of the according AOM. We can chose two different modes of operation: First, a wide scan of the spectrum including all dark resonances is recorded, where the frequency is tuned continuously over the region of interest and the scattered photons are recorded. The corresponding spectrum is used to obtain most of the external parameters, which are assumed to stay constant subsequently. A fit of the data by the calculated fluorescence rate  $\mathcal{F}(\Delta_{866})$  allows to determine Rabi-frequencies  $\Omega_{397}$  and  $\Omega_{866}$ , detuning  $\Delta_{397}$ , and the magnetic field strength  $B$ .

The second mode of data acquisition is a pulsed operation, where we only scan over one of the resonances. The temperature is determined from the model fit as the only free parameter. As discussed before, scattering photons within dark resonances affects the temperature of the ion. In order to greatly reduce these processes, we perform scans as follows:

- i) For an equilibration time  $t_e \geq 2$  ms the frequency of the 866 nm laser is set at some fixed detuning  $\Delta_e$ , far from any dark resonance, resulting in a steady-state of the ion temperature.
- ii) Then, for a much shorter measurement time of typically  $t_m = 20 \mu\text{s}$ , the drive frequency of the AOM is switched to a detuning  $\Delta_m$  by switching between the two VCO drivers of the AOM, see Fig. 4.9 and App. A.6. Only during  $t_m$  the fluorescence photons are recorded on the PMT.

This procedure is repeated multiple times for detecting in total about  $10^4$  photons at the desired  $\Delta_m$ . Then,  $\Delta_m$  is stepped to the next value to obtain the full shape of one of the dark resonances. A fit with the analytical model reveals the temperature  $T$  of the ion.



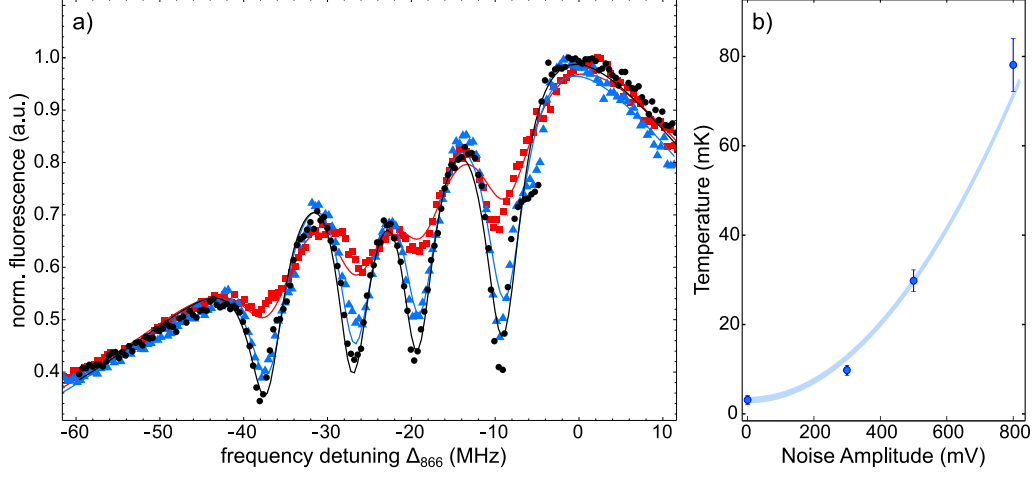


**Figure 6.7.** – (a) Dark resonances for different applied electronic noise amplitudes (0 V<sub>rms</sub> (black), 300 mV<sub>rms</sub> (blue), 800 mV<sub>rms</sub> (red)). A fit yields  $\Omega_{397}/2\pi = 12$  MHz,  $\Omega_{866}/2\pi = 8$  MHz,  $\Delta_{397}/2\pi = 14$  MHz and  $B = 4.7 \times 10^{-4}$  T. The effective temperatures result to 3.1(5) mK (black), 9(1) mK (blue) and 78(6) mK (red). (b) Measured temperature as a function of the noise amplitude, following  $T \propto \mathcal{N}^2$ .

### 6.4.3. Measurement of steady-state temperatures

We now demonstrate temperature measurements with a linear crystal of 5 ions. The number of ions increases the heat capacity of the crystal because of a larger number of vibrational modes, but the steady state temperature, being an intensive quantity, is the same as for a single ion. On the other hand, using more ions increases the rate of scattered photons and therefore reduces the required number of repetitions for each measurement.

Fig. 6.7 shows the recorded fluorescence spectra at different amplitudes of the electric field noise. The temperature is obtained by a fit of  $\mathcal{F}(\Delta_{866})$  to the data. In absence of any heating process we measure the experimental cooling limit to be  $T_0 = 3.1(5)$  mK. As compared to the theoretical limit of Doppler cooling for the  $^{40}\text{Ca}^+$ -ion, Eq. (2.22),  $T_D = 0.55$  mK is still a factor of 6 lower than  $T_0$ . However,  $T_D$  is based on calculations for a 2-level system and for perfect cooling conditions. The experimental value  $T_0$  depends on the laser parameters as well as the trap geometry. As a side remark we want to emphasize that our setup has not been optimized for reaching a small  $T_0$  but to guarantee stable trapping conditions even for high noise amplitudes. In order to generate higher temperatures of the ion we apply noise amplitudes of 300 mV<sub>rms</sub>, 500 mV<sub>rms</sub> and 800 mV<sub>rms</sub>. The fit to the data reveals temperatures of  $T = 9(1)$  mK, 30(3) mK and 78(6) mK, respectively. Thus, the temperature shows the expected quadratic dependence on the electric field noise amplitude  $T = T_0 + \alpha \mathcal{N}^2$ , with  $T_0 = 3.1$  mK, see Fig. 6.7 (b). A fit to the data reveals a temperature dependence of  $\alpha = 110$  mK/V<sup>2</sup>.

For the frequency scans presented in Fig. 6.7 we have used the continuous acquisition scheme only. Interestingly, at low temperatures, we observe deviations from the fit curve on the high energy side of the resonances, most pronounced close to  $\Delta_{866} = -6$  MHz. At the same time we observe that the dark resonances appear to be deeper than expected by the analytical model. These peculiarities are a result of the heating and cooling effect in vicinity of the dark resonances, as predicted in Sec.6.2.3. Later, in Sec. 6.6 we will exploit

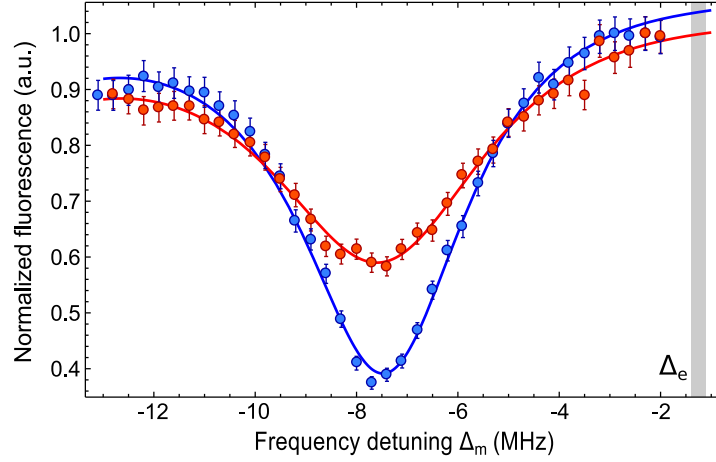


**Figure 6.8.** – Scan of the  $|S_{1/2}, -1/2\rangle - |D_{3/2}, 3/2\rangle$  dark resonance in the pulsed acquisition mode. The frequency of the 866 nm laser is set to  $\Delta_e$  for an equilibration time  $t_e \geq 2$  ms. Then, for  $t_m = 20 \mu\text{s}$ , the frequency is switched to  $\Delta_m$  and the fluorescence is recorded. By scanning  $\Delta_m$  the shape of the spectrum is obtained. A fit of  $\mathcal{F}(T)$ , with  $T$  being the only free parameter, reveals the temperature of the ion. Here, we find  $T = 3.1$  mK for the blue resonance and  $T = 9.4$  mK for the red resonance.

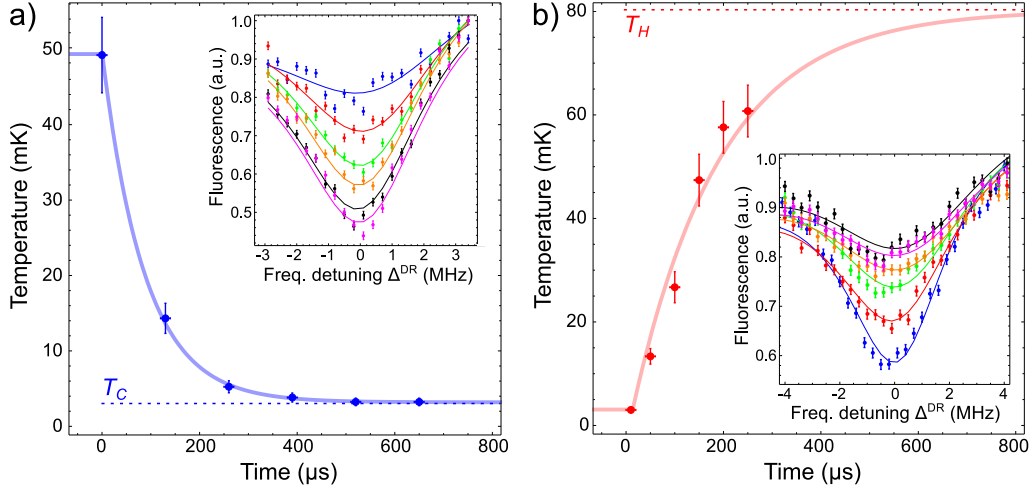
these effects to tune the temperature of the ions deliberately.

However, these artifacts in the recorded spectra are absent in the pulsed acquisition mode. Fig. 6.8 shows the spectrum of the most pronounced resonance, which corresponds to the  $|S_{1/2}, -1/2\rangle - |D_{3/2}, 3/2\rangle$  transition. The measurement time of  $t_m = 20 \mu\text{s}$  guarantees that the influence of the measurement itself on the temperature is negligible. All free parameters of  $\mathcal{F}(\Delta_{866})$  except the temperature have been determined by a scan of the full spectrum. Then, measuring a single resonance in the pulsed acquisition mode is sufficient to determine the temperature of the ion precisely.

## 6.5. Investigation of thermal dynamics

One of the major strengths of the dark resonance thermometry technique is the ability to capture the time evolution of the temperature of the ion during thermal equilibration processes. This feature is a mandatory prerequisite for the analysis of the reservoir interaction of thermodynamic machines and creates new possibilities for the investigation of thermal dynamics in general.

To demonstrate such an equilibration measurement, we start with a laser cooled ion. The laser cooling process mimics an interaction with a cold reservoir at  $T_C$ . In order to bring the system out of equilibrium we apply an electric noise pulse, corresponding to a sudden temperature change of the reservoir. Consequently, we observe an increase of the temperature  $T$  of the ion. We record fluorescence spectra with the pulsed measurement technique at different time delays between 50 and 650  $\mu\text{s}$  after the start of the noise pulse, see Fig. 6.9 (a). Fitting the measured temperatures with a thermalization function,  $\mathcal{T}_H(t) = T_H (1 - \exp(-\Delta t / \tau_H))$ , reveals a time constant of  $\tau_H = 257(40) \mu\text{s}$ . Similarly, we observe the inverse cooling process. Therefore we apply an electrical noise pulse of 2 ms, while laser cooling the ion with a fixed detuning  $\Delta_e$  to reach an initial steady state temperature  $T_H$ . Then, we switch the noise off and observe the re-cooling process, see



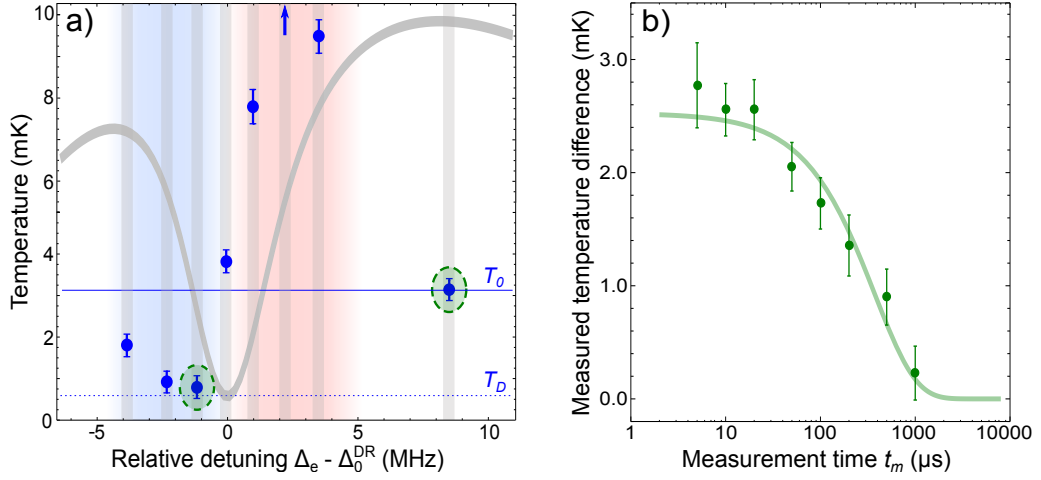
**Figure 6.9.** – Time resolved thermal dynamics of trapped ions. (a) Cooling of an ion crystal: Ions are first simultaneously excited by electrical noise and laser cooling ( $\Delta_e = 0$ ), resulting in a steady state temperature of  $T = 49(5)$  mK as measured from the shape of dark resonances, see inset. Once the electrical noise is switched off, the laser cooling reduces  $T$  with an exponential constant  $\tau_C = 87(2)$   $\mu$ s, reaching finally  $T_C = 3.0(5)$  mK. (b) Ion heating dynamics: Starting with a laser cooled crystal, we turn on the electric noise, which increases  $T$  with  $\tau_H = 257(40)$   $\mu$ s to a steady state at  $T_H = 81(7)$  mK. In both cases we use short exposure times of  $t_m = 20$   $\mu$ s.

Fig. 6.9 (b). An exponential fit of  $\mathcal{T}_C(t) = T_H \exp(-\Delta t / \tau_C) + T_C$  reveals  $\tau_C = 87(3)$   $\mu$ s. Here, the heating rate of the trap [Tol14, Bro15] is neglected as compared to the concurrent errors: at low temperatures the dominant error results from the systematic uncertainty of the spectral linewidth  $\Gamma$  of the laser sources. An uncertainty in the knowledge of the laser linewidth of 30 kHz results in a temperature uncertainty of 0.4 mK. For high temperatures, the statistical error of the fits dominates.

In the language of reservoir engineering [Cir94b, Poy96], such heating and cooling processes are interpreted as thermalization of the ion with an effective heat bath. The thermal interaction of the ion with the cooling laser and the electric field noise has the same characteristics as if the ion is coupled to a real thermal reservoir: thermalization to a finite temperature (the bath temperature) and an exponential temperature evolution with fixed time constant.

## 6.6. Engineering thermal states by exploiting dark resonances

In addition to the temperature measurements presented above, the dark resonances themselves can be used to adjust the temperature. As shown in Sec. 6.2.3, the modified scattering of photons affects the properties of Doppler cooling. Here, we demonstrate how the temperature can be controlled and measured in vicinity of the dark resonance at  $\Delta_0^{\text{DR}}$  corresponding to the  $|D_{3/2}, -3/2\rangle$  state, see Fig. 6.10. Again, we apply the pulsed measurement procedure where the frequency of the 866 nm laser is switched. If  $\Delta_e$  is close to the  $P_{1/2} \leftrightarrow D_{3/2}$  transition and far from any dark resonances during the equilibration time  $t_e$  in step (i), we measure a temperature of  $T_0 = 3.1(4)$  mK (as done



**Figure 6.10.** – Influence of the dark resonance on the temperature of the ion. (a) Measured equilibrium temperatures (blue points) while varying the detuning  $\Delta_e$ . On the low frequency side of the resonance,  $T$  drops below  $T_0$  and we reach 0.7(4) mK (blue shaded area), still above  $T_D$ . On the high frequency side of the resonance,  $T$  rises above  $T_0$  (red shaded area) and even diverges at  $\Delta_e \approx \Delta_0^{\text{DR}} + 2$  MHz. The gray resonance shape in the background serves as orientation, at which point of the resonance feature the measurements have been taken. (b) Influence of the measurement time  $t_m$  on the resulting temperature. The difference of the measured temperatures for  $\Delta_e = \Delta_0^{\text{DR}} + 8.5$  MHz and  $\Delta_e = \Delta_0^{\text{DR}} - 1.2$  MHz (green markers in (a)) has been evaluated as a function of the measurement time  $t_m$ . An exponential fit  $\Delta T = a \exp(t_m/\tau_m)$  reveals a time constant of  $\tau_m = 0.38(7)$  ms.

before). However, if the frequency of the 866 nm laser is close to a dark resonance but red detuned  $\Delta_e < \Delta_0^{\text{DR}}$  during  $t_e$ , we see that the temperature drops by a factor of four and measure 0.7(4) mK at  $\Delta_e = \Delta_0^{\text{DR}} - 1.2$  MHz. In contrast, we observe strong heating effects if  $\Delta_e$  is blue detuned to the dark resonance  $\Delta_e > \Delta_0^{\text{DR}}$ . At  $\Delta_e = \Delta_0^{\text{DR}} + 2$  MHz the ion is excited so much that the dark resonance feature, recorded during step (ii), vanishes within the statistical scattering. We can only give a lower bound of  $T > 80$  mK.

Because different frequencies along the dark resonance lead to different equilibrium temperatures, we investigate experimentally the influence of the measurement duration  $t_m$  in step (ii) on the resulting temperature. Therefore, we vary  $t_m$  between  $2 \mu\text{s}$  and 1 ms. In the latter case,  $t_m$  is sufficiently long to let the thermal state equilibrate to a temperature determined by  $\Delta_m$  during the measurement. For short times of  $t_m$ , however, the temperature is governed by  $\Delta_e$  and not significantly influenced by the measurement. We do not use  $t_m < 2 \mu\text{s}$ , since the internal dynamics need  $\approx 0.5$  ns to reach a steady state of the occupation probabilities [Tol14]. To characterize the influence of  $t_m$ , we have tuned  $\Delta_e$  to two different values at  $\Delta_0^{\text{DR}} - 1.2$  MHz and  $\Delta_0^{\text{DR}} + 8.5$  MHz (green highlights in Fig. 6.10 (a)), corresponding to temperatures of 0.7(4) mK and 3.1(4) mK, respectively. The equilibration process is shown in Fig. 6.10 (b), where the measured temperature difference  $\Delta T$  between both points is plotted as a function of  $t_m$ . An exponential fit of the temperature differences by  $\Delta T(t_m) = a \exp(-t_m/\tau_m)$  reveals a decay time of  $\tau_m = 0.38(7)$  ms. Indeed, for measurement times  $t_m \leq 20 \mu\text{s}$  the modification of the measured temperature of  $\Delta T \leq 0.1$  mK is negligible as compared to the concurrent uncertainties.

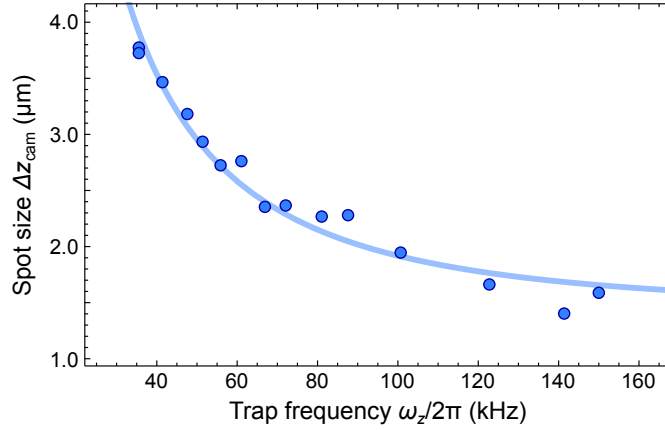


**Figure 6.11.** – Determination of the PSF of the imaging optics by recording the spot size  $\Delta z_{\text{cam}}$  for different values of the trap frequency  $\omega_z$ . This exemplary measurement has been done on the axial degree of freedom. The PSF is the offset for  $\omega_z \rightarrow \infty$  of the fitted function  $\Delta z_{\text{cam}}(\omega_z) = \sqrt{k_B T / (m\omega_z^2) + \Delta z_{\text{PSF}}^2}$ , while the temperature is extracted from its curvature.

## 6.7. Spatial thermometry technique

A different approach to determine the temperature of the trapped ion is an analysis of the spatial spread of the wavefunction of the ion, or, more precisely, of the spatial fluorescence distribution arising from the ion. An ion with higher thermal energy occupies a larger volume inside the harmonic trapping potential. As shown by the group of Hänsch in 2012, an analysis of the increased spot size of the fluorescence distribution of hot ions on camera images can be used to determine their temperature [Knü12]. While the measurement of low temperatures is limited by the spatial resolution of the imaging optics, this technique is well suited for  $T \geq 100$  mK, where the dark-resonances are not resolved anymore. In the classical weak-binding regime,  $k_B T \gg \hbar\omega$ , the root mean square width of the Gaussian probability distribution of a thermal ion at temperature  $T$  is

$$\Delta x_{\text{th}} = \sqrt{\frac{k_B T}{m\omega_x^2}}. \quad (6.25)$$

In order to extract  $\Delta x_{\text{th}}$  from the camera images, we have first to calibrate the resolution of the imaging system, given by its point spread function (PSF) [Knü12]. The PSF is the root mean square width of an image of a point source. Assuming an isotropic broadening, the total width of the recorded fluorescence distribution reads

$$\Delta x_{\text{cam}} = \sqrt{\Delta x_{\text{PSF}}^2 + \Delta x_{\text{th}}^2}. \quad (6.26)$$

To determine  $\Delta x_{\text{PSF}}$  precisely, we make use of the dependance  $\Delta x_{\text{th}} \propto \omega_x^{-1}$  from Eq. (6.25) and measure  $\Delta x_{\text{th}}$  for different values of  $\omega_x$ . Such a measurement is shown in Fig. 6.11, where we assume the laser-cooled ion to have a constant temperature  $T_0$ . The PSF corresponds to the extrapolated spot size  $\Delta x_{\text{cam}}$  for  $\omega_x \rightarrow \infty$ , where the thermal wavefunction of the ion is compressed to a point source. By fitting Eq. (6.25) to the data we find  $\Delta x_{\text{PSF}} = 1.41(9) \mu\text{m}$  and  $T_0 = 3.2(2)$  mK. Within their statistical uncertainties, the resulting temperature  $T_0$  is in accordance with the measured temperature of a laser

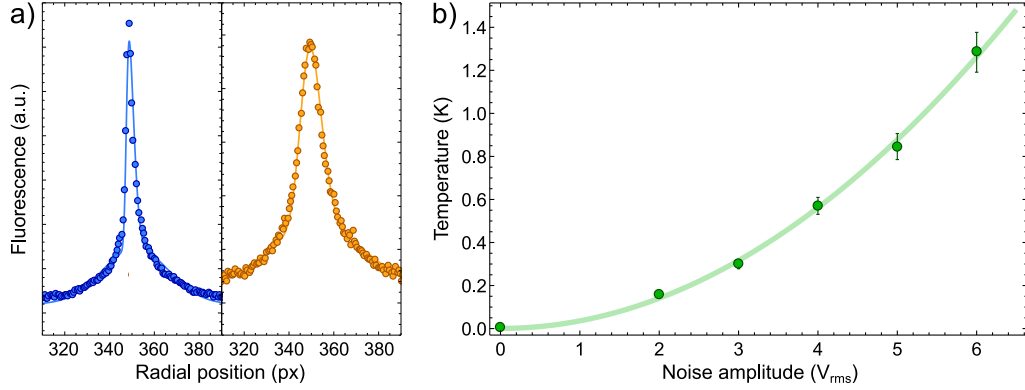


**Figure 6.12.** – Temperature measurement using the spatial thermometry technique. (a) Projection in radial direction of the recorded fluorescence distribution of a cold (blue) and a hot (orange) ion, fitted with Gaussian probability distributions. The resulting temperatures are 4.7 mK and 1.28 K. (b) Evaluation of the measured temperatures as a function of the electric noise amplitude  $\mathcal{N}$ , while the noise has been applied in a pulsed mode. A fit of the function  $T(\mathcal{N}) = a\mathcal{N}^2 + T_0$  demonstrates the accordance of the resulting temperatures with the expected behavior.

cooled ion using the dark-resonance thermometry technique. This comparison serves as a cross check for the validity of both methods.

Knowing the value of  $\Delta x_{\text{PSF}}$  allows us to determine the temperature of the ion directly from the fluorescence distribution on camera images, if  $\Delta x_{\text{cam}} > \Delta x_{\text{PSF}}$ . An evaluation of the temperature of the ion for different amplitudes of the electric noise  $\mathcal{N}$  is shown in Fig. 6.12 and confirms the expected quadratic dependance  $T \propto \mathcal{N}^2$ . Here we have applied the noise in a pulsed mode, in order to cover a larger range of noise amplitudes: we alternate between heating and cooling, whereby we apply heating for 4.1  $\mu\text{s}$  and cooling for 8.2  $\mu\text{s}$ . In this way a thermal equilibrium is reached at some intermediate temperature, which is then measured by spatial thermometry. Later, for the heat engine operation in Sec. 7.4, we will identify the temperature values from Fig. 6.12 as working-point temperatures  $T_w$  of the engine. Note that the technique presented in Fig. 6.11, where the trapping potential is varied, cannot be employed for hot thermal states during electric noise heating. The reason is that a variation of the spatial extent of the probability distribution leads to a modified heating rate due to the quadratic nature of the trapping potential. For more details and an elaborate discussion of systematic uncertainties of the spatial thermometry, see [Knü12].

To summarize, the spatial thermometry technique is easy to use and is evaluated with low effort. It is well suited for hot thermal states and complements seamlessly the temperature range where dark resonance thermometry can be applied. With both techniques at hand, we cover a temperature range from below 1 mK up to 10 K. This coverage will be entirely used when we characterize the temperatures during heat engine operation in Sec. 7.4. However, the spatial thermometry technique relies on a spatially resolved imaging of the fluorescence distribution and therefore the use of a PMT is impossible. This fact limits the time resolution of the temperature measurement to the exposure time of the EMCCD camera and thus to several milliseconds. Therefore, the spatial thermometry technique is appropriate for steady state temperatures and can not be employed for the measurement of fast thermal dynamics. Additionally, the thermal

distribution must exceed considerably the resolution of the imaging system [Nor11]. This concern may be circumvented by using standing waves to probe the spatial extent of the ion [Wal12a], however, involving a high technical effort to obtain laser beams with interferometric stability.

### 6.8. Outlook and applications

In this chapter we have first shown, that by the combination of electric noise and laser cooling, an effective and adjustable heat bath for trapped ions is emulated. We then have adopted the dark resonance thermometry technique for the first time to measure the resulting temperatures of trapped ions. As we will show in Sec. 7.4, only through such a fast and almost non-invasive method we are able to measure and evaluate the thermodynamic cycles of the single-ion heat engine. We have shown that dark resonances in a multi-level electronic system, here in  $^{40}\text{Ca}^+$ , are a versatile tool for controlling and measuring the temperature of a single ion or a small ion crystal. We observe and interpret the modification of the dark resonances and determine the temperature of the ions from a fit of the laser-induced fluorescence data by a model of the expected lineshape. This technique is convenient to use as it only requires the light sources which are used for Doppler cooling and for exciting the ion's fluorescence. Using this type of thermometry, and having characterized the spectral linewidths of the laser sources, we are able to measure temperatures between 0.7 mK and 61 mK.

Beside the application to thermal machines, we see advantages of the dark resonance thermometry for applications with low trap frequencies or large ion crystals, where the quantized energy structure can't be resolved and thus sideband spectroscopy techniques are not applicable. Our method may be well suited for studies of non-linear dynamics in ion crystals, such as structural phase transitions in ion crystals and the formation of defects [Ulm13]. Non-linear couplings may be studied in systems with many ions and in the presence of thermal excitations with two-dimensional spectroscopy [Lem15], in order to detect signatures of a structural phase transition of the ion crystal, as well as resonant energy exchange between vibrational modes. Our method fills the gap between the sideband spectroscopy technique, used for very low temperatures close to the ground state of motion, and classical techniques, such as the Doppler recoiling method, which are well suited for hot thermal states with temperatures above  $10^4$  mK. Its temperature range overlaps with the one of the spatial thermometry, which has been used to crosscheck the validity of both techniques. A combination of both extends the accessible range for steady state temperatures to largely above  $10^3$  mK.

We have demonstrated that a measurement of thermal dynamics can be performed on the timescale of a few microseconds. This opens the door for future measurements of thermal equilibration processes in non-equilibrium situations, such as time-resolved transport of thermal energy through an ion chain or ion crystal [Lin11, Pru11, Ber13].

# 7

## Experimental implementation of the single-atom heat engine

In this chapter we demonstrate experimentally the working principles of the single-ion heat engine. As discussed before, we use a combination of laser cooling and electric field noise to engineer cold and hot reservoirs. By exposing the radial state of motion of the ion alternately to these heat baths, a closed thermodynamic cycle is realized. We show that the work generated by the engine is transferred to the axial mode of motion and is stored in an increasing oscillation amplitude. The ion trap setup allows us to control and to analyze the state of the ion as well as to tune its interaction with the thermal reservoirs precisely. The thermodynamic cycle of the engine is established for various temperature differences of the reservoirs and the corresponding output powers and efficiencies are characterized. We compare both, power and efficiency, with the expected values from an analytical model. The ability not only to generate work, but also to store it and to transfer it to other oscillatory systems is a crucial step towards the implementation of more complex thermodynamic systems.

We first give an overview of the actual experimental setup and parameters in Sec. 7.1 and Sec. 7.2, before we demonstrate the measurement technique to record the ion trajectory with high resolution in space and time in section in Sec. 7.3. Then, in Sec. 7.4, we show how to reconstruct the thermodynamic cycles from the recorded trajectories and the thermal dynamics. This is followed by Sec. 7.5 and an evaluation of the output power derived from the heat engine cycles, as well as directly from the ion trajectories. Sec. 7.6 focuses on the corresponding efficiencies. The experimental results are combined with an analytical model for the expected power and efficiency of the engine, based only on the measured temperatures and trap frequencies. This model is found to be in good agreement with the behavior of the measured values. In section 7.7 we show that we can exclude any other sources of excitation leading to an oscillation of the ion but the conversion from thermal energy difference into mechanical motion. We end this chapter with a short summary of the results in Sec. 7.8.

The experimental realization of the single-ion heat engine and the experimental results are presented in a condensed form in our publication:

**A single-atom heat engine,**

J. Roßnagel, S. Dawkins, K. Tolazzi, O. Abah, E. Lutz, F. Schmidt-Kaler and K. Singer,

Science **352**, 325 (2016).



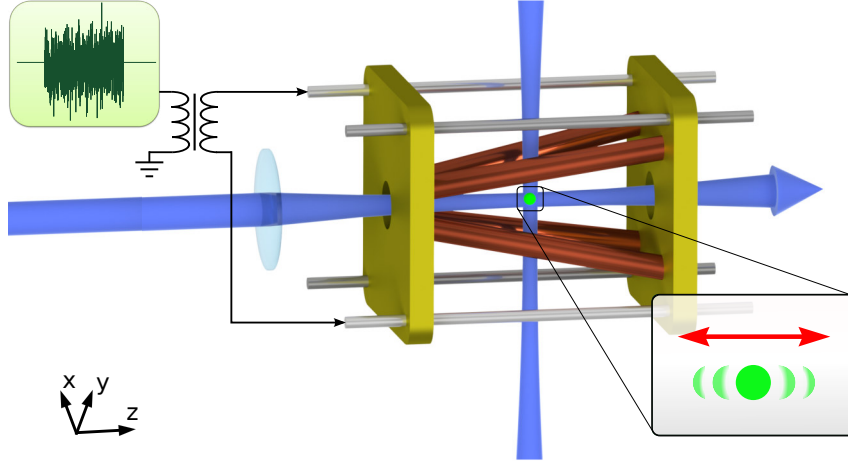


**Figure 7.1.** – Condensed sketch of the setup of the heat-engine experiment, composed of a single trapped ion (green), lasers for cooling, dissipation and observation of the ion (blue), radio-frequency electrodes in funnel geometry (red), end-caps (gold) and outer electrodes (gray). The position of the ion is imaged on an ICCD camera as a function of time, revealing its trajectory (screen). A balun transformer inverts the electric noise signal from the generator, see Sec. 4.1.3. The opposing noise signals are supplied to the outer electrodes, in order to generate electric field noise on the trapping potential without affecting the trap frequencies.

## 7.1. Specific experimental parameters

Before we start to discuss the heat engine experiments we summarize the external parameters for these measurements. The geometry of the trap has been presented in Sec. 4.1. The funnel-electrodes are driven at a symmetrical radio-frequency voltage of 830 V peak-to-peak at  $\Omega_{\text{rf}}/2\pi = 21.41$  MHz. This results in trap frequencies in radial direction of  $\omega_{0x}/2\pi = 447$  kHz and  $\omega_{0y}/2\pi = 450$  kHz, at the axial equilibrium position of the ion  $z = 0$ . The degeneracy of  $\omega_x$  and  $\omega_y$  is lifted, but they are sufficiently close to permit an approximation of cylindrical symmetry with  $r^2 = x^2 + y^2$  and a mean radial trap frequency  $\omega_r$  for the following analytical calculations. The axial trap frequency is kept at  $\omega_z/2\pi = 81.2$  kHz. The axial confinement is low enough to obtain oscillation amplitudes in the range of micrometers due to the heat engine drive, but still high enough to guarantee for stable trapping conditions. The thermal bath interactions are acting on the radial degrees of freedom, as discussed before. The electric noise is fed to the outer electrodes and provides a root mean square amplitude in the range  $(0 \dots 7) V_{\text{rms}}$ . The cooling laser at 397 nm, corresponding to the reservoir interactions, points in radial direction with  $45^\circ$  to both radial components. The beam is collimated with a Gaussian diameter of  $\sigma_r \approx 160 \mu\text{m}$ . The intensity is kept constant at  $I_r = 85 \mu\text{W}$ , while the detuning is stabilized at  $\Delta\omega_r = -55 \text{ MHz} = -2.4 \Gamma$  from the  $S - P$  resonance, where  $\Gamma = 1/(2\pi\tau)$  is the natural linewidth. The pulsed dissipation laser is applied in axial direction, collimated with  $\sigma_z \approx 175 \mu\text{m}$ ,  $I_z = 20 \mu\text{W}$  and  $\Delta\omega_z = \Delta\omega_r$ . It leads to an average damping coefficient of  $\gamma = 480(140) \text{ s}^{-1}$ , determined from a series of step response measurements, as presented in Sec. 5.3. Regarding the repumping laser at 866 nm, we use one single beam which addresses all degrees of freedom and which is stabilized at resonance, saturating the  $D_{3/2} - P_{1/2}$  transition. A condensed sketch of the experimental setup is given in Fig. 7.1, comprising all relevant parts of the experiment.

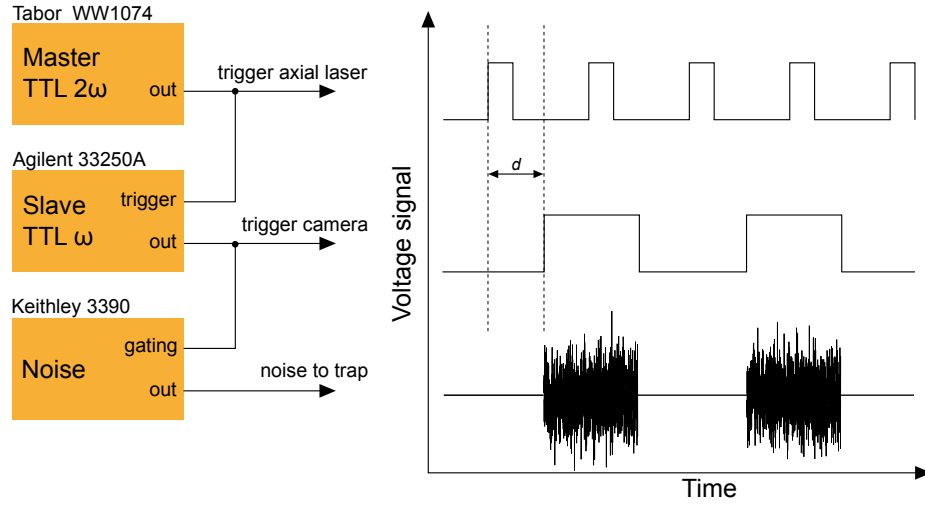


**Figure 7.2.** – TTL circuit and timing of the heat-engine drive consisting of three function generators (orange). The Tabor WW1074 serves as master clock and oscillates at double the desired driving frequency,  $2\omega_z$ . It triggers the axial dissipation laser and the Agilent 33250A, which serves as slave clock. The Agilent generates a TTL pulse on every second trigger pulse, thus at a frequency  $\omega_z$ , and with a variable delay  $d$ . The TTL signal from the Agilent in turn serves as gating for the Keithley 3390, which generates the gated noise signal. The noise pulses are then fed to the inversion circuit and to the trap electrodes.

## 7.2. Electronic control of the experiment

During the heat engine experiments, the TTLs for switching the axial cooling laser and the electric field noise have been controlled by external function generators. We could not use the common electronic control system of the experiment for the following reason: when the control system is switching TTLs at any frequency, there is a current modulation at the same frequency on the common ground line of the TTL control and the DAC device. Due to residual resistances this leads to voltage oscillations in the entire electronic system, and thus on the trap electrodes as well. The voltage modulation is too small to be measured with the available devices, but large enough to excite resonantly coherent oscillations of the ion. Such unintentional oscillations are easy to distinguish from the heat engine drive, since the amplitude does not depend on the strength of the heating and cooling processes and is still visible when the noise generator is not connected to the setup. However, these oscillations conceal the signature of the heat engine drive and thus must be avoided. Therefore, we have set up an independent TTL management by a set of three coupled signal generators, shown in Fig. 7.2, with a power supply decoupled from other devices. By this procedure we avoid to drive the oscillation of the ion by coherent electric field kicks, which is shown and discussed in more detail in Sec. 7.7.

## 7.3. Resolved measurement of the ion's oscillation

In Sec. 2.5 we have shown analytically and numerically that a periodic heating and cooling of the radial mode generates a coherent oscillation along the trap axis, if the drive frequency matches the axial trap frequency. Here we demonstrate this fundamental

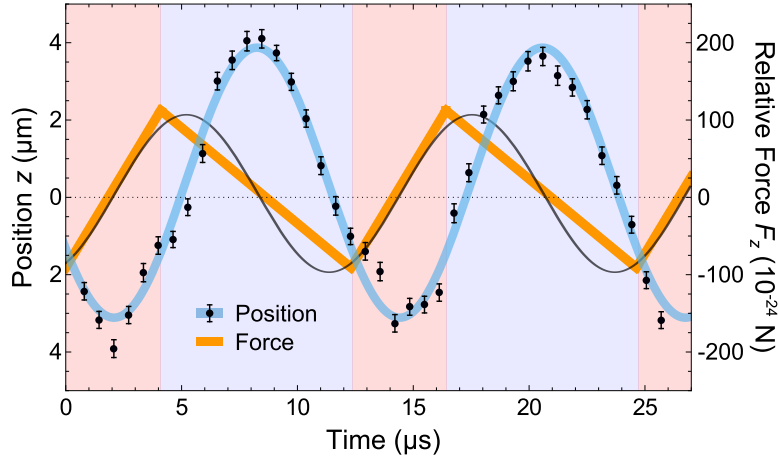


**Figure 7.3.** – Alternating heating and cooling phases (red and blue shaded areas) lead to an oscillation of the ion. The temperature changes induce a periodic driving force  $F_z$  (orange line) according to Eq. (2.21), shown relative to its mean value of  $F_0 = 5.03 \times 10^{-21}$  N which stems from the elevated mean temperature. The precise position  $z$  of the ion (black points) is determined from the average of more than 200 000 camera images at each phase step. The error bars result from the uncertainty of Gaussian fits to the recorded fluorescence images, see Fig. 4.8. The measured positions are described by a sinusoidal fit (blue line). Approximating  $F_z$  by a sinusoidal signal (black line) reveals a relative phase shift of  $88(3)^\circ$ , in accordance with the expected  $\pi/2$  phase shift for a resonantly driven oscillator.

principle of our heat engine experimentally. Therefore we heat and cool the ion alternately and tune the cycle duration precisely to  $t_{\text{cyc}} = 2\pi/\omega_z = 12.32 \mu\text{s}$ . The engine therefore resonantly drives a harmonic oscillation in axial direction. The duration of the heating period is set to  $t_H = 4.1 \mu\text{s}$ , resulting in a duty cycle of  $d_H = t_H/t_{\text{cyc}} = 1/3$ . The cooling period covers the rest of the cycle time,  $t_C = t_{\text{cyc}} - t_H$ . The combination of heating and cooling periods give rise to a closed thermodynamic cycle and leads to a periodic force  $F_z(t) \propto T(t)$  in the axial direction, as derived in Sec. 2.5. The time evolution of the driving force  $F_z(t)$  is shown in Fig. 7.3 and provides a triangular-like waveform, since  $t_H \ll \tau_H$  and  $t_C \ll \tau_C$ , with  $\tau$  being the timescale of the respective thermalization process, see Sec. 6.5.  $F_z(t)$  can be approximated by its first Fourier component, being a sinusoidal signal, which then drives a coherent oscillation of the ion. A measurement of the resulting oscillation of the ion is presented in Fig. 7.3. The measurement of the resolved coherent oscillation demonstrates the transformation of thermal energy into a mechanical motion, and thus manifests the functionality of the fundamental principles of the heat engine system.

The work produced in each cycle is resonantly transferred to the axial degree of freedom and stored in the amplitude of the oscillation. The axial motion thus plays a role similar to the flywheel of a mechanical engine. However, the essentially frictionless nature of the system leads to an ever-increasing oscillation. In order to contain this oscillation, we provide an artificial friction by introducing an additional pulsed dissipation laser in axial direction, as characterized in Sec. 5.3. The relative pulse length  $t_d$  of the dissipation laser is set to  $t_d/t_{\text{cyc}} = 0.1$ . Steady-state operation is reached when the work generated by the engine is balanced by the energy dissipated by the damping. The steady-state oscillation amplitude is analyzed in the following to characterize the output power of the engine.

To resolve phase and amplitude of the oscillation during the heat engine operation we employ the ICCD camera, as described in Fig. 4.8. While the amplitude of the oscillation can be recorded with a normal EMCCD camera, the fast gating and short exposure of the ICCD is mandatory for a detailed reconstruction and analysis of the heat engine cycles. To this goal, the camera takes images of the fluorescence of the ion at different phases of the periodic heat engine drive. The exposure time is set to 700 ns, which is 18 times shorter than the axial oscillation period. The camera is synchronized with the temperature modulation, allowing for the repetitive recording of images at particular phases of the resulting oscillation. More than 200 000 images are integrated at each phase in order to collect enough photons for a reasonable analysis of the ion's position. The fluorescence distribution of the 2-dimensional camera images is projected on the trap axis, and fitting a normal distribution allows to determine the position of the ion precisely. By repeating this procedure at different phases of the driving signal, the oscillation of the ion is reconstructed accurately, revealing the amplitude and phase of the resulting sinusoidal oscillation, see Fig. 7.3. In order to characterize the heat engine properties, those measurements have been done for different noise amplitudes, different relative heating and cooling times and different driving frequencies.

For evaluating the thermodynamic cycles, a precise determination of the relative timing is crucial. By fitting a sinusoidal signal to the measured oscillations we obtain a delay of the ion's trajectory to its expected oscillation, which results from the gating for the heating pulses and the corresponding force. The measured average delay is  $d_f = 1500(1100)$  ns, without showing a systematic dependency on any variation of external parameters. This delay is found to have two major contributions. One is an electronic delay of the noise pulse on the trap electrodes with respect to the gating pulse. It results from charging effects of the low pass filters, the transformers and the bias tees and has been measured to 800(100) ns. The second contribution results from the dynamics of the ion. The electric field noise modifies the velocity of the ion, not its position directly. But the axial force component is sensitive to the position of the ion. Hence, the force rises only with a delay of  $\omega_r/4$  after the onset of the noise, leading to another delay of 560 ns. The delay  $d_f$  has to be respected for the timing of the axial dissipation laser as well as for the following analysis of the heat engine cycles, and is included in the relative timing in Fig. 7.3.

## 7.4. The thermodynamic cycles

### 7.4.1. Measurement of the thermodynamic cycles

Now, we want to reconstruct the thermodynamic cycles from the measured oscillation data. In order to facilitate the evaluation of the cycles in terms of power and efficiency, we here choose to present the mean phonon number  $\langle n_r \rangle = k_B T / \hbar \omega_r$  of the thermal state in radial direction as a function of the corresponding radial trap frequency  $\omega_r$  [Lin03]. The latter can be obtained directly from the measured axial positions  $z(t)$  in conjunction with the calibration measurements of the trap frequency  $\omega_r$  as a function of  $z$ , see Fig. 5.3 and Eq. (5.6). Regarding the small amplitudes of the oscillation  $\omega_r(z)$ , Eq. (2.17) can be approximated linearly, revealing

$$\omega_r(z)/2\pi = (-114(1) \text{ Hz}/\mu\text{m}) \cdot z + 447.9(2) \text{ kHz}, \quad (7.1)$$

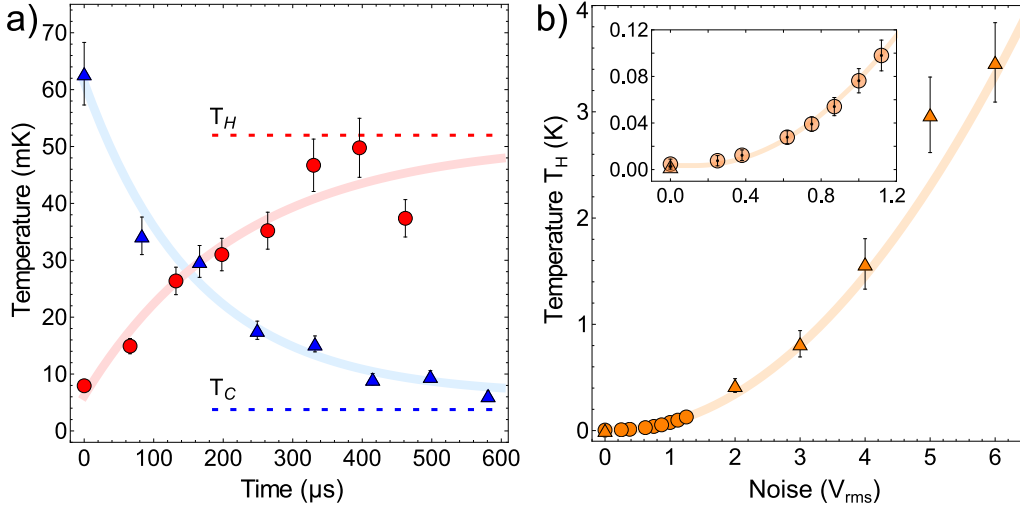


**Figure 7.4.** – Temperature dynamics of the ion in contact with the thermal reservoirs. (a) Thermalization curves, derived from dark-state thermometry of the radial thermal state of the ion when heated to  $T_H$  (red) and cooled to  $T_C$  (blue). Individual errors result from fits to the dark-resonances as well as the uncertainty due to the laser-linewidths, as described in Sec. 6.5. Individual fits reveal thermalization time constants for heating and cooling of  $\tau_H = 189(26) \mu s$  and  $\tau_C = 216(13) \mu s$ , respectively. (b) Dependence of the hot bath temperature  $T_H$  on the root-mean-square of the electric noise applied to the trap electrodes, measured by dark-state thermometry (circles) and spatial thermometry (triangles).

where the positive  $z$ -axis is defined in direction of the wide side of the funnel.

The temperature of the ion at any given moment of the cycle is deduced from the interplay of individually measured heating and cooling rates, determined by dark resonance thermometry, as demonstrated in Sec. 6.5. The measurements of the heating and cooling rates for the heat engine operation are presented in Fig. 7.4 (a). Individual fits to the data reveal thermalization time constants for heating and cooling of  $\tau_H = 189(26) \mu s$  and  $\tau_C = 216(13) \mu s$ , respectively. Both time constants only depend on the parameters of the cooling laser, which are kept constant during the experiments. While the temperature of the cold reservoir  $T_C$  is set by the Doppler-cooling temperature  $T_0$ , the temperature of the hot reservoir  $T_H$  is adjusted by changing the amplitude of the electric field noise. Fig. 7.4 (b) shows the quadratic dependance of  $T_H$  after thermalization as a function of the root mean square amplitude of the electric noise  $\mathcal{N}$  applied to the electrodes, see Eq. (6.11). In order to cover a large range of accessible temperatures for this characterization measurement we combined dark-resonance thermometry (see Sec. 6.4.3) and spatial thermometry (see Sec. 6.7). However, heating the ion continuously with more than  $2 V_{rms}$  noise amplitude leads to high loss rates of the ion. Nevertheless, to characterize the temperature for higher noise amplitudes we apply alternately cooling and heating, as it is done in the heat engine operation. From the measured steady state temperatures we then calculate  $T_H$  using the thermal dynamics from Fig. 7.4 (using Eq. (7.10), which will be derived in the course of this section). This procedure opens an accessible temperature range from 1 mK to 4 K. The fit shown in Fig. 7.4 (b) results in

$$T_H(\mathcal{N}) = 3.4(1) \text{ mK} + 97(5) \text{ mK/V}^2 \cdot \mathcal{N}^2. \quad (7.2)$$

The set of parameters comprising  $\tau_H$ ,  $\tau_C$ ,  $T_H$  and  $T_C$  fully characterizes the thermal dynamics of the heat-engine cycle. We now have to apply the timings for the heating

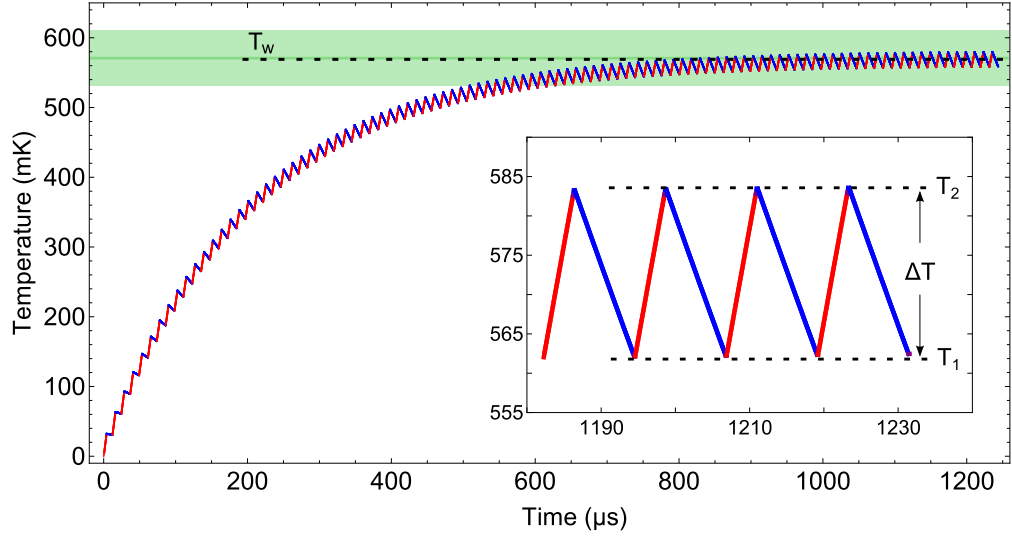


**Figure 7.5.** – Simulated temperature dynamics of the ion as a function of time during heat engine operation using the measured parameters for thermalization from Fig. 7.4. Heating and cooling durations in each cycle are  $t_H = 4.1 \mu\text{s}$  and  $t_C = 8.2 \mu\text{s}$ , respectively. With an electric noise amplitude of  $4 V_{\text{rms}}$ , we determine a working point temperature  $T_w = 568 \text{ mK}$  (black dashed line) and a temperature difference  $\Delta T = T_2 - T_1 = 21.5 \text{ mK}$  (see inset).  $T_w$  is in excellent agreement with the directly measured value  $T_w^{\text{exp}} = 570(40) \text{ mK}$  (green bar), presented in Fig. 6.12.

and cooling period in order to simulate the thermal dynamics of the ion. The duration of one heat engine cycle is defined by the axial trap frequency,  $t_{\text{cyc}} = 2\pi/\omega_z$ . The hot bath interaction time  $t_H$  is given by its duty cycle  $d_H = t_H/t_{\text{cyc}}$ . Since the ion is in permanent bath contact, the cold bath interaction time results to  $t_C = t_{\text{cyc}} - t_H$ .

In Fig. 7.5, we present a simulation of the thermal dynamics  $T(t)$  of the heat engine based on the parameters  $\tau_H$ ,  $\tau_C$ ,  $T_H$  and  $T_C$ , starting with an ion cooled to the laser cooling limit  $T_0$ . In the beginning, the heating process is much more efficient than cooling, due to its steep slope for low temperatures, see Fig. 7.4 (a), and thus the mean temperature increases. With increasing temperature the cooling process becomes more and more effective, until it balances the heating and a steady state is reached, with a mean working-point temperature  $T_w$ . The time evolution of the temperature of the ions radial state of motion in steady-state operation is thus fully characterized by  $T_w$  and the temperature difference  $\Delta T = T_2 - T_1$ , which are the basis for the derivation of the heat engine cycles. In addition to the simulations, the working-point temperatures have been measured directly by spatial thermometry, see Fig. 6.12, and show an excellent agreement with the simulated  $T_w$  (green bar in Fig. 7.5). Note that the heating and cooling processes are much slower than the internal dynamics of the ion and thus can be regarded as quasistatic with negligible losses due to irreversible processes [Aga13].

Here, we want to emphasize the need for resonant switching of the heating and cooling processes. In addition to the fundamental mechanism that the resonant coupling allows to extract the work produced and to store it in a separate mode, it is required to allow for an effective detection of the heat engine operation. For instance, switching a noise amplitude of  $\mathcal{N} = 4 V_{\text{rms}}$  leads to a typical increase of the temperatures from  $T_1 \approx 562 \text{ mK}$  to  $T_2 \approx 584 \text{ mK}$ , as it is the situation in Fig. 7.5. By employing  $F_z(T)$  from

Eq. (2.21) and using the specific geometry of the trap, we calculate a corresponding increase of the force in axial direction to be  $F_z = 2 \times 10^{-22}$  N. Using Newtons law of motion this force leads to a static displacement of  $z = F_z / (m \omega_z^2) = 11$  nm within the given axial trapping potential. Such a small displacement is impossible to detect with our imaging setup. However, driving the cycle resonantly with the axial trap frequency leads to oscillation amplitudes large enough to be observed in our setup, as described above.

The thermodynamic cycle of the engine is obtained by plotting the phonon number  $\langle n_r(t) \rangle = k_B T(t) / \hbar \omega_r$  of the thermal state of the ion in the radial direction as a function of the corresponding trap frequency  $\omega_r(t)$  [Lin03].  $\langle n_r(t) \rangle$  is derived from the measured temperature dynamics and  $\omega_r(t)$  follows from the position of the ion on the camera images. An exemplary cycle is shown in Fig. 7.6, which has been recorded at a noise amplitude of  $4.0 V_{\text{rms}}$ , a cycle period of  $t_{\text{cyc}} = 2\pi / \omega_z = 12.3 \mu\text{s}$  and a heating time of  $t_H = 4.1 \mu\text{s}$ . Thus, the temperature evolution corresponds to the situation in Fig. 7.5 and the axial oscillation to the one in Fig. 7.3. The uncertainties of the phonon numbers for each point of the cycle are obtained by a variation of all relevant input variables within their individual uncertainties, namely  $T_H$ ,  $T_C$ ,  $\tau_H$ ,  $\tau_C$  and  $d_f$ . The resulting changes are separated into a global shift of the center of the cycle, as well as relative changes of the individual points. The error bars in Fig. 7.6 correspond to the relative variations of the cycle points, since only these contribute to an uncertainty of the area of the cycle, and therefore affect the resulting output power and efficiency. The error bars of the relative trap frequencies are obtained in the same way, respecting the uncertainties of the position measurements as well as of the gauge measurement  $\omega_r(z)$ , Eq. (7.1).

#### 7.4.2. Analytical derivation of the thermodynamic cycles

To evaluate different series of thermodynamic cycles in order to characterize the heat engine parameters, it is more convenient to elaborate analytical expressions for the key parameters  $T_w$  and  $\Delta T$ . Therefore we make use of the fact, that in a steady state situation the temperature changes during the heating and cooling processes balance out. More formal, we start from the first law of thermodynamics

$$dU = \delta W + \delta Q \quad (7.3)$$

and assume that there is no residual change in the internal energy after one cycle,  $\int_{\text{cyc}} dU = 0$ . Furthermore we assume that the amount of heat converted into mechanical work is much smaller than the absolute amount of heat absorbed from the hot reservoir  $\delta W \ll \delta Q_H$ . After the evaluation of work and efficiency in Sec. 7.5 and Sec. 7.6, we will see that these assumption are satisfied. We obtain the steady state condition for the heat exchange

$$\delta Q_H + \delta Q_C = 0, \quad (7.4)$$

which can be transferred to temperature changes by using the definition for heat,  $\delta Q = C dT$ , with the heat capacity  $C$ . To transfer Eq. (7.4) to the specific situation in our setup, we use the fact that the heating and cooling processes lead to a variation of the temperature around the same working-point temperature  $T_w$ . Including the different duration of the coupling to the hot and the cold reservoir, we find

$$\Delta T_H + \Delta T_C = \dot{T}_H (\mathcal{T}_H(t) = T_w) \cdot t_H + \dot{T}_C (\mathcal{T}_C(t) = T_w) \cdot t_C = 0, \quad (7.5)$$

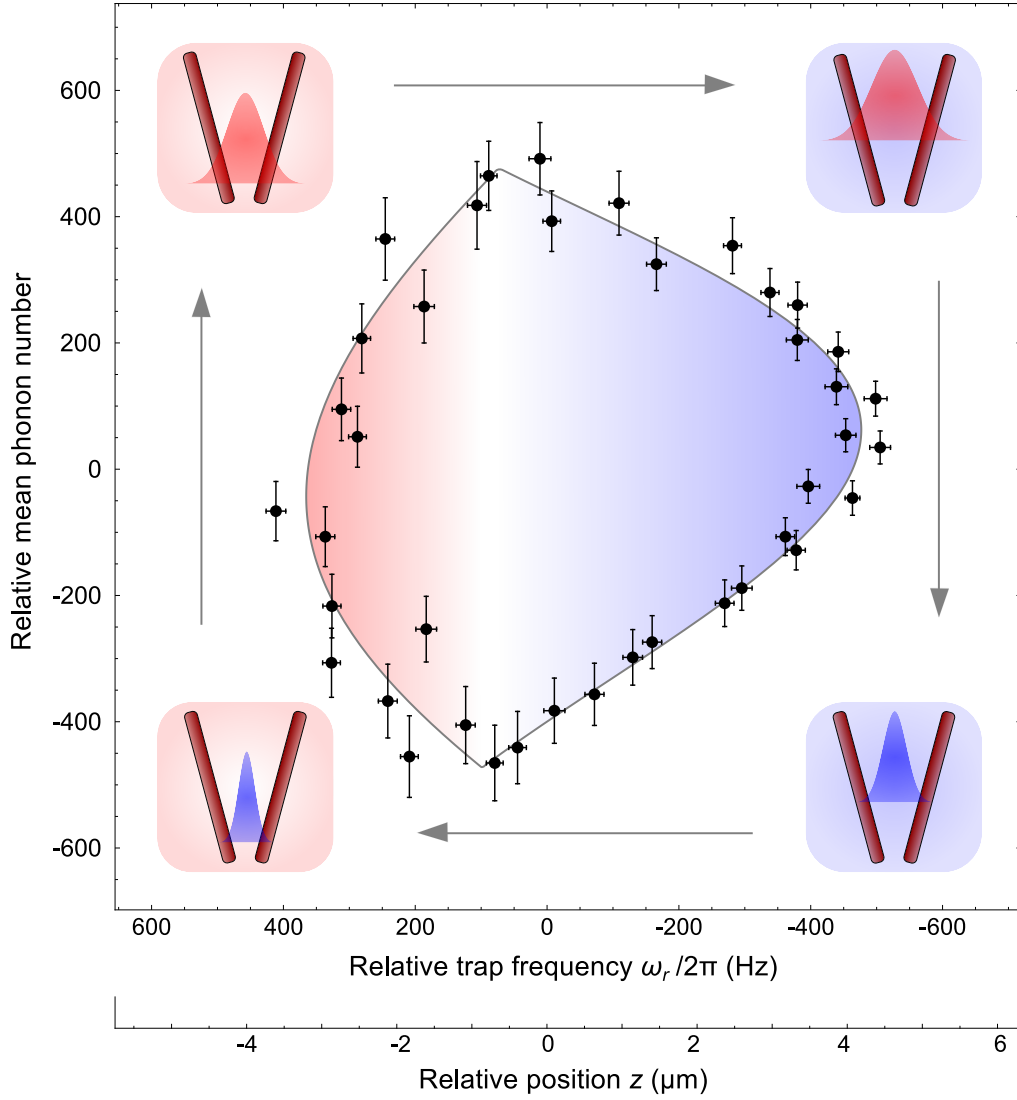


**Figure 7.6.** – Thermodynamic cycle of the engine for one radial direction: the change in the trap frequencies  $\omega_r$  is deduced directly from the measured  $z$ -positions, indicated by the second axis. The temperature  $T$  of the radial state of motion and thus the corresponding mean phonon number  $\langle n_r \rangle$  is determined from separate measurements (see text in Sec. 7.4.1). The values of  $\omega_r$  and  $\langle n_r \rangle$  are given with respect to the center of the cycle at  $\omega_{0r}/2\pi = 447.9(2)$  kHz and  $\langle n_{0r} \rangle = 26160(445)$ . The shaded area enclosed by the cycle reflects the work performed by the engine, where red and blue colors indicate heating and cooling periods, respectively. The gray line is the calculated trajectory of the cycle, see text. The error bars are obtained from a relative shift of the data points with respect to the center of the cycle, under a variation of all relevant parameters within their uncertainties. The four pictograms in the corners illustrate the different strokes of an idealized cycle. They indicate the thermal probability distributions of the ion in between the trap electrodes, while the background colors signify the bath coupling.



where we evaluate the time derivative of the temperature  $\dot{\mathcal{T}}(t)$  at the time  $t$  where  $\mathcal{T}(t) = T_w$ . The underlying assumption  $\dot{\mathcal{T}}(\mathcal{T}(t) = T_w) = \text{const}$  is valid for small temperature changes  $\Delta T \ll T_w$ , which is satisfied for our experimental parameters, as shown in Fig. 7.5. In order to obtain  $\dot{\mathcal{T}}(\mathcal{T}(t) = T_w)$  we express the first derivatives of the heating and cooling dynamics

$$\mathcal{T}_H(t) = T_C + T_H \left[ 1 - \exp\left(-\frac{t}{\tau_H}\right) \right] \quad (7.6)$$

$$\mathcal{T}_C(t) = T_C + T_H \exp\left(-\frac{t}{\tau_C}\right) \quad (7.7)$$

as functions of the time dependent temperature  $\mathcal{T}(t)$  and find

$$\dot{\mathcal{T}}_H(\mathcal{T}_H(t)) = \frac{(T_H + T_C) - \mathcal{T}_H(t)}{\tau_H} \quad (7.8)$$

$$\dot{\mathcal{T}}_C(\mathcal{T}_C(t)) = -\frac{\mathcal{T}_C(t) - T_C}{\tau_C}. \quad (7.9)$$

Including Eqs. (7.8) and (7.9) to Eq. (7.5) we find the analytical expression for the working point temperature

$$T_w = T_C + \frac{T_H}{1 + \frac{\tau_H}{\tau_C} \frac{t_C}{t_H}}. \quad (7.10)$$

In order to obtain the temperature difference  $\Delta T$  we insert Eq. (7.10) in Eqs. (7.8) and (7.9)

$$\Delta T = T_2 - T_1 = \left( T_w + \frac{1}{2} \dot{\mathcal{T}}_H(T_w) \cdot t_H \right) - \left( T_w + \frac{1}{2} \dot{\mathcal{T}}_C(T_w) \cdot t_C \right) = \frac{T_H}{\frac{\tau_H}{t_H} + \frac{\tau_C}{t_C}}, \quad (7.11)$$

where we used the short form  $\dot{\mathcal{T}}(T_w) \equiv \dot{\mathcal{T}}(\mathcal{T}(t) = T_w)$ . The analytic expressions for  $T_w$  and  $\Delta T$  enable us to deduce the phonon numbers  $\langle n_r(t) \rangle$  and to reconstruct the thermodynamic cycles. The cycles now only depend on the temperature of the hot reservoir  $T_H$ , defined by the amplitude of the electric noise  $\mathcal{N}$ , and the duty cycle of the reservoir interactions. All other parameters only depend on the cooling laser and are thus constant. As we will show in the next section, a variation of these two parameters allows to analyze the behavior of the power and the efficiency of the engine.

### 7.4.3. A Stirling-like engine type

The situation for the experimental realization of the single-ion heat engine is different to the one of the simulations presented in Sec. 3.1. There, we have investigated an Otto cycle, where we used independent heating and cooling processes, separated by an isentropic expansion, where the system is completely isolated from any thermal reservoir. This is an idealized situation which could unfortunately not be realized experimentally. To implement an Otto cycle means to switch the radial cooling laser on and off at a rate corresponding to the axial trap frequency. This, however, leads to a periodic modulation of the light force on the ion and hence excites axial oscillations, as shown in Sec. 5.1.1. To avoid light induced oscillations during the heat engine operation, we keep the cooling laser on for the entire experimental sequence. Thus, the ion is in permanent contact with one of the reservoirs, and consequently the dynamics are similar to those of a Stirling engine [Bli12]. The idealized Stirling cycle consists of two isochoric temperature changes

and two isothermal expansion and compression processes, as discussed in Sec. 2.2.2. However, this idealized Stirling cycle is smeared out by the harmonic oscillation of the ion and the fact that a full thermalization with the reservoirs is not reached [Bra15b]. This makes it difficult to distinct between the four individual steps. The same effect arises for thermodynamic cycles of macroscopic engines [Cen15]. However, at this point we want to emphasize that, of course, it is interesting to compare our engine to well-known cycle types, but that such a comparison is rather of an academic nature and not essential to evaluate the parameters of the engine and to prove its functionality.

## 7.5. Output power of the engine

### 7.5.1. Stationary output power

We derive the power output during steady-state operation in three independent ways. We first determine the power  $P_{\text{cyc}} = W_{\text{cyc}}/t_{\text{cyc}}$  by evaluating the work  $W_{\text{cyc}}$  as the area of the cycles,

$$W_{\text{cyc}} = \oint \hbar \langle n_r \rangle d\omega_r. \quad (7.12)$$

This work is computed by a numerical integration of the datapoints  $i$  of the closed polygon according to Green's Theorem [Bra86],

$$W_{\text{cyc}} = \frac{1}{2} \sum_{i=1}^N \left( \omega_r^i \cdot \langle n_r^{i+1} \rangle - \langle n_r^i \rangle \cdot \omega_r^{i+1} \right), \quad (7.13)$$

where  $(\omega_r^{N+1}, \langle n_r^{N+1} \rangle) = (\omega_r^1, \langle n_r^1 \rangle)$ . The resulting  $W_{\text{cyc}}$  corresponds to the work performed in one of the two radial directions. However, since the engine is driven in both radial directions simultaneously, the total power equals to  $P_{\text{cyc}} = 2 W_{\text{cyc}}/t_{\text{cyc}}$ . To assess the performance of the engine, our system has been driven by various temperature differences  $\Delta T$ . As mentioned above,  $\Delta T$  can be tuned either by adjusting the reservoir temperatures via  $\mathcal{N}$ , or by the relative duration of the reservoir interaction, defined by  $d_H$ . We have used both options to vary  $\Delta T$  and have covered a range from 0 mK to 70 mK. The resulting data is shown as orange points in Fig. 7.7 as a function of  $\mathcal{N}$  and  $d_H$ , and reaches up to  $3.4(5) \times 10^{-22}$  J/s.

We alternatively deduce the power directly from the measurement of the axial oscillation amplitudes  $A_z$ , which range up to  $A_z = 15 \mu\text{m}$ . The dissipated power of a damped harmonic oscillator at steady state yields [Dem08]

$$P_{\text{osc}} = \gamma m \omega_z^2 A_z^2, \quad (7.14)$$

with the damping parameter  $\gamma$  according to Sec. 5.3. In a steady state operation the dissipated power equals the energy input by any driving source. Thus,  $P_{\text{osc}}$  corresponds to the power generated by the engine, which is converted into oscillation energy and displayed as gray points in Fig. 7.7 (c).

Both methods,  $P_{\text{cyc}}$  and  $P_{\text{osc}}$ , use the same oscillation data as input variables and lead, in principle, to the same power output of the engine. But, however, they differ fundamentally in their derivation.  $P_{\text{cyc}}$  is based on the thermodynamic parameters of the engine, namely  $\Delta T$ , derived from individual measurements.  $P_{\text{osc}}$ , in contrast, describes the power for any harmonic oscillator, ignoring the origin and the form of the driving

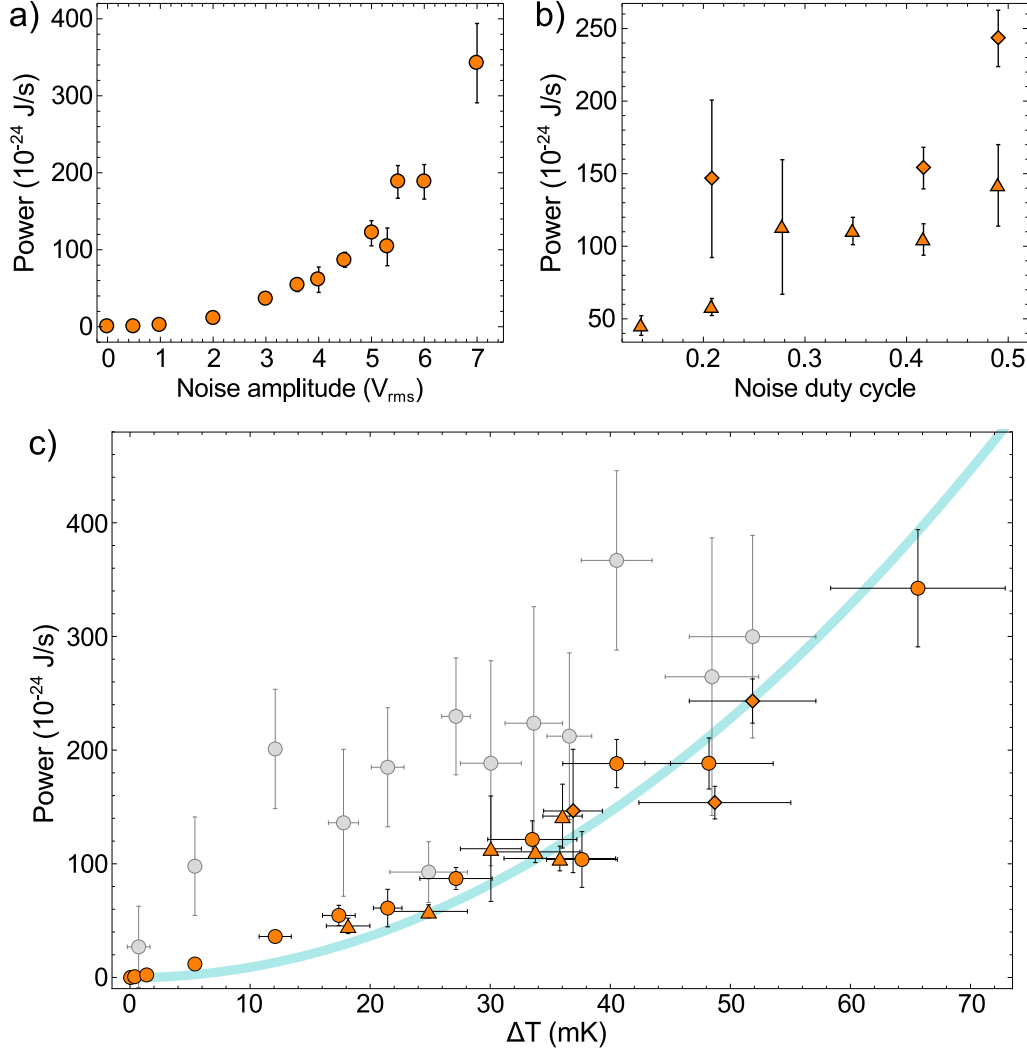


**Figure 7.7.** – Output power of the engine. (a) A variation of the output power is achieved by different electric field noise amplitudes  $N$ . For each point the power is calculated from the area of the corresponding thermodynamic cycles. (b) The power is changed by modifying the duty cycle of the heating period, at constant noise amplitude of  $N = 5 V_{rms}$  (triangles) and  $N = 6 V_{rms}$  (diamonds). The power is again derived from thermodynamic cycles. (c) Combined analysis of the power of the engine as a function of the temperature differences  $\Delta T$ .  $\Delta T$  is calculated from the variation of the electric field noise (see (a), orange circles) and from the duty cycle of the heating periods (see (b), orange triangles and diamonds). These data are consistent with the expected value from analytical calculations (blue line). The values resulting from the measured cycles are complemented by data from a direct analysis of the amplitude of the oscillation (gray).

force. The resulting power values for both methods are consistent with each other and range in the order magnitude of  $10^{-22}$  J/s, depending on  $\Delta T$ . This result shows that the power from a thermodynamic evaluation corresponds to the expected power for a damped harmonic oscillator. It underpins the functionality of the heat engine, or, in other words, that the origin of the oscillation indeed is the temperature variation due to heating and cooling processes.

We further calculate analytically the engines output power to compare this model to the measured values. Therefore, we first compute the expected ion trajectory, assuming the expressions for a driven and weakly damped harmonic oscillator at resonance, see Sec. 5.3. The driving force  $F_z(t)$  is calculated from Eq. (2.21), accounting for the temperature variations of the ion. The triangular-like temperature function  $T(t)$ , shown in Fig. 7.5, leads to a triangular-like driving function  $F_z(t)$ . Since the latter drives a harmonic oscillator resonantly, we need its first harmonic approximation  $F_{\sin}(t)$  to analyze the dynamics of the driven oscillator, see Fig. 7.3. To obtain a harmonic driving signal we calculate the first harmonic component of a discrete Fourier analysis for the periodic temperature function  $T(t)$ ,

$$T_{\text{har}}(t) = \frac{2}{t_{\text{cyc}}} \int_0^{t_{\text{cyc}}} T(t) \cdot \sin\left(\frac{2\pi}{t_{\text{cyc}}}t + \phi\right) dt = \frac{\sin(\pi d)}{\pi^2(d-d^2)} \Delta T \cdot \sin\left(\frac{2\pi}{t_{\text{cyc}}}t + \phi\right). \quad (7.15)$$

To simplify the calculations, we introduce a phase shift of  $\phi = -d\pi$  with respect to the time axis in Fig. 7.3, in order to make sure that the contribution of the other quadrature vanishes.  $T_{\text{har}}(t)$  is now applied to the expression of  $F_z(T)$  from Eq. (2.21) and, neglecting the weak  $z$ -dependence, we obtain

$$F_{\text{har}}(t) \approx \frac{4k_B \sin(\pi d) \tan \theta}{\pi^2(d-d^2)r_0} \Delta T \cdot \sin\left(\frac{2\pi}{t_{\text{cyc}}}t + \phi\right). \quad (7.16)$$

The ion trajectory is deduced from  $F_{\text{har}}(t)$  assuming a driven and weakly damped harmonic oscillator at resonance, Eq. (5.3). Having calculated the expressions for the force and the resulting motion of the ion allows us to compute the analytic expression for the resulting work per cycle,

$$W_{\text{ana}} = \int_{\text{osc}} F_{\text{har}}(t) dz(t) = \int_0^{t_{\text{cyc}}} F_{\text{har}}(t) \frac{dz(t)}{dt} dt, \quad (7.17)$$

where the integration is performed over one cycle period  $t_{\text{cyc}}$ . Thus, for the output power we find

$$P_{\text{ana}} = \frac{W_{\text{ana}}}{t_{\text{cyc}}} = \frac{4k_B^2 \sin^2(\pi d) \tan^2 \theta}{m\pi^4 \gamma (d^2 - d)^2 r_0^2} \Delta T^2 = \left(8.84 \times 10^{-20} \frac{\text{J}}{\text{s K}^2}\right) \cdot \Delta T^2. \quad (7.18)$$

Fig. 7.7 shows that the measured thermodynamic power  $P_{\text{cyc}}$  agrees well with the analytic model  $P_{\text{ana}}$ , which is based only on the temperature variations and the trap geometry, and does not depend on the measured oscillation data. This demonstrates that  $\Delta T$  is expected to cause an oscillation which corresponds to the measured amplitude. Thus, it shows that there is neither an additional loss of oscillation energy nor an additional input of the same.

Regarding the two evaluation methods for the measured data, we observe a significantly higher scattering of the  $P_{\text{osc}}$  data compared to the  $P_{\text{cyc}}$  data. Both results are based on the amplitude  $A_z$  of the measured oscillation. On the one hand, there is the

resulting power from the analysis of the cycles which depends on  $A_z$ , translated to the trap frequency  $\omega_r(z)$ , and on the temperature  $T$ . Thus, statistical scattering of  $A_z$  enters linearly in the resulting power  $P_{\text{cyc}} \propto A_z$ . On the other hand, there is the power deduced from the dynamics of a harmonic oscillator depending quadratically on the amplitude  $P_{\text{osc}} \propto A_z^2$ , see Eq. (7.14), and thus provides a scattering twice as large compared to the data from the cycles. The larger error bars of  $P_{\text{osc}}$  stem from the large uncertainty of the damping coefficient, see Sec. 5.3.

Here, we face the main difficulty during the experiments: due to leakage currents between the radio-frequency electrodes and the end-caps, combined with a finite resistance of the their coating and their electric connection with in total 30 Ohm, we observe fluctuating charges on the end-caps. This leads to a variation of the axial potential and, consequently, of the trap frequency of about  $\pm 200$  Hz on a 10-100 s timescale, also observed as small shifts of the ion along the trap axis. During the experiments we corrected for those frequency variations between the individual runs, but, frequency variations faster than the repetition of experimental runs could not be corrected. As a consequence, this leads to a variation of the measured amplitude due to a mismatch of the driving frequency and the resonance frequency. This amplitude variation is then translated into a variation of the output power of the engine, with a linear dependence for  $P_{\text{cyc}}$ , while  $P_{\text{osc}}$  exhibits a squared dependence.

Additionally, we observe a systematic deviation between  $P_{\text{cyc}}$  and  $P_{\text{osc}}$ . This most likely originates from a systematic error in the calculation of the damping coefficient. However, the deviation of the two data-sets is in the range of their individual error-bars, and hence they are still consistent with each other.

In order to classify the measured power we calculate the corresponding power-to-mass ratio  $\rho$  of the working agent (the single  $\text{Ca}^+$  ion) and compare it to ordinary car engines. The maximum measured power of the single-atom engine,  $P = 3.4 \times 10^{-22}$  W, leads to  $\rho_{\text{sa}} = 5$  kW/kg. Assuming a car engine with 100 kW (136 PS), a total cylinder capacity of 1 l and a density of the gas of 30 kg/m<sup>3</sup> [Gau10], we find  $\rho_{\text{car}} = 3$  MW/kg. Taking account for the fact that the typical temperature difference in a car engine is of the order 100 K instead of 100 mK, both values scale in the same order of magnitude. Even though there is a ratio of  $1 : 10^{24}$  particles. This comparison, of course, is not substantiated for a quantitative evaluation. The result implies, however, that the power of the engine scales approximately as the number of particles in the working medium.

### 7.5.2. Start of the engine

Complementary to the steady state operation, we analyze the start of the engine from rest. Therefore, we initialize the ion in a cold thermal state by laser cooling all degrees of freedom. Then, at  $t = 0$ , we start to apply the heating and cooling pulses as well as the damping laser. The noise amplitude has been set to  $5 V_{\text{rms}}$  and the heating pulses repeat themselves at the resonance frequency  $\omega_d = 81.2$  kHz. At  $t = 0$  the damping force is zero and increases with the ions velocity,  $F_d \propto v$ . Therefore, in the beginning the energy balance is positive and the engine starts to oscillate with an increasing amplitude, until  $F_d$  compensates the driving force and a steady state is reached. To measure this effect, we repeat a sequence of initialization and the start of the engine, and take images of the fluorescence distribution after a fixed delay  $t_s$  with 500  $\mu\text{s}$  exposure time. After integrating 200 images, we evaluate the width of the recorded fluorescence distribution. Fig. 7.8 shows the result for a series of different values of  $t_s$ , revealing the starting

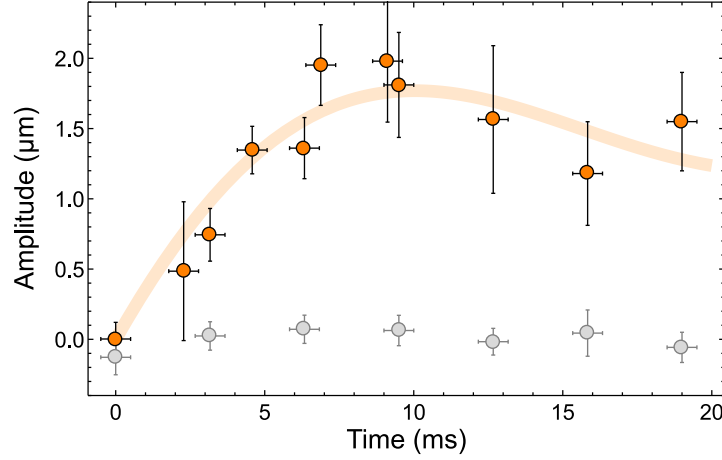


**Figure 7.8.** – Start of the engine from rest. The increasing amplitude of the oscillation is measured as a function of time. Therefore the width of the fluorescence distribution on camera images is evaluated, relative to the initial distribution of an ion at rest (orange points). These data are corrected by the separately measured thermal broadening (gray points), displayed relatively to their mean value. To measure the thermal influence, the engine is driven non-resonantly, leading to an increasing temperature without exciting a coherent oscillation. The fit to the amplitude data follows Eq. (5.8).

behavior of the engine. The functional behavior is similar to the one presented in Sec. 5.3, in the context of the measurements of the damping coefficient, including a beat note between the driving frequency and the resonance frequency. Here, we obtain a damping coefficient of  $\gamma = 140(90) \text{ s}^{-1}$ , using a power of the damping laser of  $10 \mu\text{W}$ . Comparing with the results in Fig. 5.7, this value is in agreement with the characterization of the damping coefficient. Furthermore, the characteristic rise time of  $\tau_s = 7(4) \text{ ms}$  indicates that steady state is reached after approximately 560 engine cycles.

In addition to the coherent oscillation there is a thermal broadening of the probability distribution in the axial degree of freedom, resulting from photon scattering events. In order to separate both effects, we have done the same measurement as above, but with a drive frequency out of resonance at  $\omega_d = 88 \text{ kHz}$ . Thereby, we measure the accompanying heating of the axial degree of freedom, without exciting any relevant coherent oscillation. The data shows that the thermal effect leads to a relative contribution of 0.1 compared to the coherent oscillation amplitude. The data in Fig. 7.8 is corrected by the measured thermal background.

To evaluate the power of the engine, we translate the corrected amplitude  $A(t)$  in an oscillation energy  $E_o(t) = m\omega^2 A(t)^2$ . By calculating the time derivative of the energy,  $dE_o/dt$ , we obtain a value for the output power of the engine from the slope of the increasing energy. Taking the dissipated energy into account,  $dE_d/dt = -2\gamma m v^2$ , the power of the engine results to  $P = 4(2) \times 10^{-23} \text{ J/s}$ . The uncertainty of this measurement is significantly larger than the power values obtained from steady state operation. Although the result here is in the same order of magnitude than the steady state power values, it deviates significantly by 3 standard deviations. We conclude that the measurement of the start of the engine is a concise demonstration of its dynamics, but is not sufficiently precise to analyze the engine characteristics quantitatively.

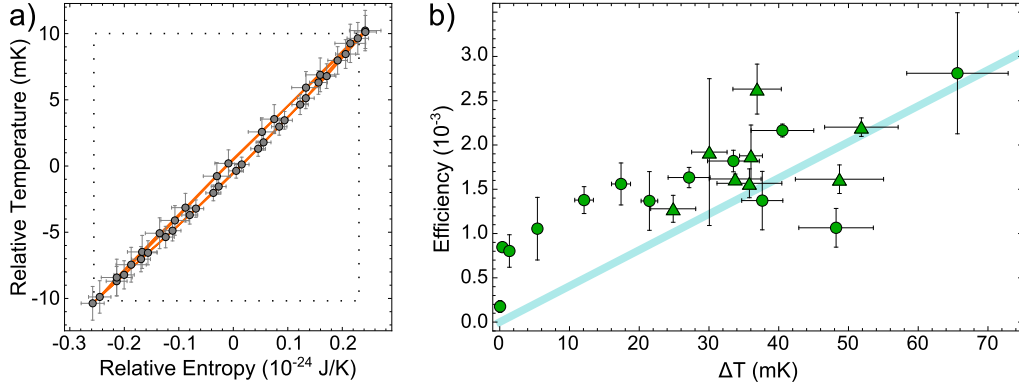


**Figure 7.9.** – Efficiency of the engine. (a) The  $T$ - $S$ -cycle of the heat engine, corresponding to Fig. 7.6, measured as temperature relative to 568 mK versus entropy relative to  $179.6 \times 10^{-24}$  J/K. Both work and efficiency can be derived from integrating this cycle. The square (dotted line) represents the equivalent Carnot cycle for the full range of parameters and shows the case of the theoretical maximum efficiency. (b) Measured efficiency as a function of  $\Delta T$ , by varying the noise amplitude (circles) or the duty cycle (triangles), compared to the result of the analytical calculation.

## 7.6. Efficiency of the engine

We further evaluate the efficiency of the engine,  $\eta = -W_c / Q_H$ , from the measured data by determining the heat absorbed from the hot reservoir,  $Q_H = \int_H T dS$ . Therefore we transform the heat engine cycle from the  $\{n, \omega\}$ -diagram to a temperature-entropy representation. The temperature is obtained directly from the corresponding measurements, as described above, while the entropy  $S$  of a thermal harmonic oscillator is calculated according to [Gem04, Aga13]

$$S = k_B \left[ 1 + \ln \left( \frac{k_B T}{\hbar \omega_r} \right) \right]. \quad (7.19)$$

The resulting thermodynamic cycle  $T(S)$  is shown in Fig. 7.9 (a). As expected, an integration over its area leads to the same output power as we obtained by the integrating over the  $\{n, \omega\}$ -cycle. The  $\{T, S\}$ -cycle has a significant diagonal structure, which originates from the fact that  $S$  depends strongly on  $\omega_r$  as well as on  $T$ . In the  $\{T, S\}$ -coordinates, a comparison with the equivalent Carnot cycle with maximum efficiency is obvious, since the latter shows a rectangular shape [Gem04], which is indicated in Fig. 7.9 (a) by a dotted line. The difference of the measured data to the Carnot cycle reveals a substantial scope for optimization in future experiments. The efficiencies have been calculated for the same measurements as done before for the evaluation of the output power. The resulting values are displayed in Fig. 7.9 (b) and reach up to  $\eta = 0.28\%$ .

In order to obtain an analytic expression for the efficiency,  $\eta_{\text{ana}}$ , we first calculate the heat absorbed by the engine from the analytic expressions for  $T(t)$  and  $\omega_z(t)$ . The former is obtained as above from Fig. 7.5, while the latter is calculated from Eq. (7.1), applying the analytical trajectory  $z_{\text{ana}}(t)$  from Eq. (5.3), using the corresponding driving force  $F_{\text{har}}(t)$ . The heat absorbed from the hot reservoir is given by

$$Q_{\text{ana}}^H = \int_0^{\tau_H} T(t) \frac{dS(t)}{dt} dt, \quad (7.20)$$

where the integration is performed over the heating period and where we neglect vanishing higher order terms. Employing the above analytical approach, we derive the expected behavior of the efficiency to increase linearly with a raising temperature difference  $\Delta T$ . We compute the analytic expression for the efficiency to be

$$\eta_{\text{ana}} = \frac{W_{\text{ana}}}{Q_{\text{ana}}^{\text{in}}} = \frac{4 k_B \sin^2(\pi d) \tan^2 \theta}{m \pi^3 \gamma \omega_z (d^2 - d)^2 r_0^2} \Delta T = (0.041 \text{ K}^{-1}) \cdot \Delta T. \quad (7.21)$$

Fig. 7.9 compares the analytical function  $\eta_{\text{ana}}$  with the measured efficiencies. The expected linear behavior matches qualitatively the resulting data. Nonetheless, due to the fact that there are only 5 to 6 datapoints during the interaction with the hot reservoir, the resulting values for the heat and thus for the efficiency are scattering stronger than their individual errors would suggest. We have decided not to include this effect to the errorbars, which are again deduced from a variation of the individual parameters within their uncertainties. Additionally, we observe that the measured data have a systematic tendency to higher values as compared to the analytical model. This may be explained by the frequency mismatch of the heat engine drive. While a resonator driven at resonance oscillates with a  $\pi/2$  phase shift with respect to the driving signal, its phase shift varies for not well-matched frequencies (see Fig. 5.1). This fact leads to a rotation of the thermodynamic cycle around its center. While the work is unaffected in first approximation, the calculated amount of heat absorbed by the system may decrease. As long as the frequency mismatch is not known precisely, this effect can not be corrected and is reflected in an overestimation of the efficiencies.

A comparison of the measured data with the corresponding efficiency at maximum power, given by the Curzon-Ahlborn formula  $\eta_{\text{CA}} = 1 - \sqrt{T_1/T_2} = 1.9\%$ , reveals that the trap parameters do not correspond to the optimal point [Aba12]. As shown in Sec. 3.2, in principle the ion trap engine is able to achieve the Curzon-Ahlborn condition Eq. 3.17 by adjusting the oscillation amplitude to the temperature differences and vice versa. However, in the realistic experiment we are limited by different aspects, discussed in the following.

First, the amplitude at steady state may be adjusted by tuning the strength of the damping force, but it is hard to adjust for practical reasons. On the one hand, reducing the amplitude below the extent of the thermal distribution of the ion makes it hard to detect. On the other hand, increasing the amplitude leads to higher velocities of the ion and hence requires shorter exposure times of the camera to avoid blurred images. This would increase the duration of the experimental sequences drastically. Furthermore, a larger amplitude requires larger diameters of the laser beams in order to hold the assumption of a uniform intensity distribution over the whole ion trajectory.

Second, regarding the temperature difference we are limited by a certain heating rate through the electric field noise, depending on the trap frequencies, the noise amplitude and the cooling laser. Technically, in our setup,  $\mathcal{N} = 10 \text{ V}_{\text{rms}}$  is the upper limit. However, for  $\mathcal{N} > 7 \text{ V}_{\text{rms}}$  we obtain unstable trapping conditions for the given trap frequencies.

Third, the amplitude and the resulting temperature difference are not decoupled. A stronger heating requires a stronger cooling in axial direction which implies a larger damping force. We summarize that with a high technical effort we may approach the Curzon-Ahlborn efficiency and maximum power output. However, as we have demonstrated the working principle of the engine successfully, a further optimization does not imply new physical findings and thus does not justify the required effort.



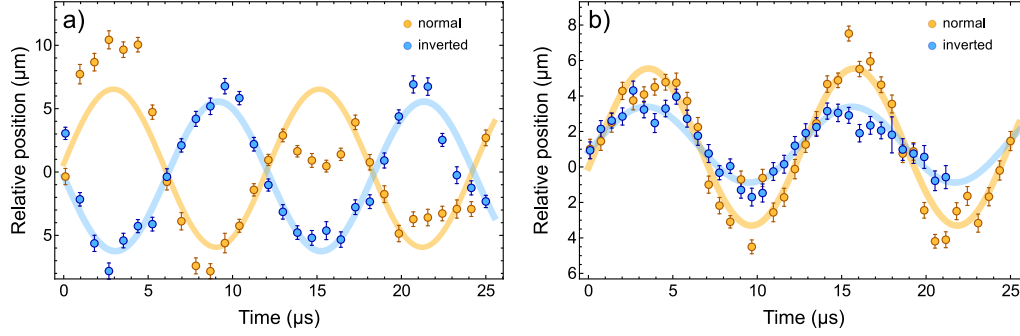


**Figure 7.10.** – Position of the ion as a function of time, as a test for a phase flip under inversion of the signal lines. (a) A coherent oscillation is excited by electric field kicks at the resonance frequency. A inversion of the signal lines leads to a  $180^\circ$  phase flip. (b) The system is now driven in heat engine operation. The resulting oscillation is due to the thermal excitation of the ion and does not undergo any phase flip when the signal lines are inverted.

### 7.7. Exclusion of non-thermal excitation of the ion

In Sec. 7.5.1 we have demonstrated that the temperature variation in combination with the tapered trap geometry is the only origin of the oscillation of the ion. Nonetheless, in this section we want to proof these findings again by a different approach. Therefore, we compare the behavior of the system during the heat-engine operation with the behavior under an artificial excitation of the oscillation. As mentioned above, see Fig. 7.1, the electric noise is fed with inverted sign to two opposing outer electrodes. A pulsed noise signal modulates the temperature of the radial state of the ion, resonant with the axial trap frequency. The heat-engine operation converts the temperature difference into a coherent motion along the trap axis. But, assuming the noise signal has a small constant offset in average, the pulsed signal leads to repetitive radial kicks to the ion, which have constant phase and amplitude. Due to the taper of the trap, the radial field has a contribution in axial direction and its modulation leads to a coherent oscillation of the ion along the trap axis, independent from the heat-engine operation.

In order to exclude this kind of excitation, we apply artificial offset kicks to the ion. We then invert the signal lines of both electrodes and observe that the phase of the resulting oscillation is shifted by  $180^\circ$ . If we apply only the electric noise to the electrodes, a swap of the signal lines does not affect the phase of the oscillation. The ion is heated and its probability distribution is increased, independent of the relative signs of the signals. The result of this comparison is presented in Fig. 7.10. A phase shift of the oscillation under an inversion of the signal lines indicates kicks due to an offset, while its absence shows that a sign-independent energy source, namely the heating process, is responsible for the oscillation. Consequently, Fig. 7.10 demonstrates that under heat-engine operation conditions no additional offset or any other electrical kick contributes to the oscillation of the ion. Thus, we can assign the total oscillatory energy to the heat engine drive and the above evaluation of the engine parameters is justified.

## 7.8. Summary

In this chapter we have demonstrated a first realization of a heat engine whose working agent is reduced to the limit of a single atom. We have shown that, indeed, a single trapped ion is a well suited system to study single-particle thermodynamics. We have driven the ion in a Stirling cycle, whereat the ion converted thermal and undirected excitations into a coherent and directed motion. The versatility of the trapped ion system allowed for the direct measurement of key features of the engine, such as thermodynamic cycles, power output and the corresponding efficiency. These capacities are outstanding characteristics of our system, allowing for a detailed analysis of the engine's behavior. While the efficiency is still low as compared to the Curzon-Ahlborn efficiency, it is interesting to note that the relative output power scales in the same order of magnitude as for macroscopic engines, although there is a difference of some dozen orders of magnitude in the particle number. Thereby we showed that, as expected, the classical framework of thermodynamics can be applied to our single-atom system, while the notion of temperature requires a careful consideration. Our classical device offers a broad platform for future experiments, investigating, for instance, thermal fluctuations of work and heat, machines coupled to non-thermal reservoirs, see Sec. 3.3, nanoscopic refrigerators and quantum heat engines, which will be discussed in Sec. 8.1 and Sec 8.3, respectively.



# 8

## Future perspectives of the single-atom heat engine device

At the current state of the art of nanoscale engines and motors, the development of machines for practical purposes seems to be reserved for molecular devices, which are powered by light or electrochemical processes [Kay07]. Today, they are already produced with high reliability and in large quantities. They are about to be assembled to larger and more complex machines, completing diverse tasks such as transportation, rotation or switching. Even cars on a molecular basis have been developed [Viv09]. However, a future generation of those machines may operate in the quantum regime and on the single-atom basis. Our single-atom engine is a pioneer towards this future generation of single (few) atom devices.

After having presented the successful experimental realization of a single-atom heat engine, we want to focus on the future perspectives of this experiment. Thereby, we will present concrete approaches for the forthcoming investigations, as well as some rough ideas where our findings may lead to.

The naturally following step is the inversion of our engine cycle in order to realize a heat pump, acting as a single-atom refrigerator, which transfers heat between two reservoirs at the expense of work. Two different setups for this device are discussed. Furthermore, the heat engine operation may be refined by implementing an autonomously running engine, where an external switching of the heat baths is not required anymore. However, the trapped ion experiments are predestined for targeting the quantum regime. To this end, we sketch different ideas of how to involve and to exploit quantum features for future heat engine devices with trapped ions. We will end this outlook by a discussion of applications of our setup beyond the purpose of thermodynamics and present our system as a versatile tool for quantum computation.

### 8.1. Single-atom heat pump

In order to drive the ion in a heat pump operation, we essentially have to invert the thermodynamic cycle of the engine [Kos00, Aba16]. A heat pump absorbs heat from a cold reservoir and releases it to a hot reservoir, thereby increasing the temperature difference between both. An external supply of work is required to drive the device, since the heat pump is moving heat against the direction of spontaneous heat flow and thus consumes energy [Lin10b, Kos14b].

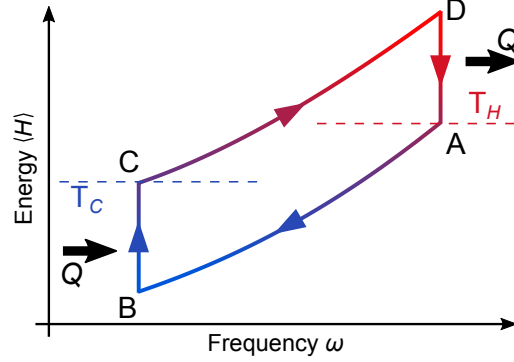


**Figure 8.1.** – Thermodynamic cycle of a heat pump for a harmonic oscillator (HO). The HO starts at A with a hot bath temperature  $T_H$ . Then, the frequency expands adiabatically and thereby the temperature is reduced. At B, the HO temperature  $T$  is below the one of the cold bath,  $T < T_C$ . The HO is now coupled to the cold bath and thermalizes to  $T = T_C$  at C. Next, the frequency is compressed adiabatically, the temperature increases to  $T > T_H$  at D. By thermalizing with the hot bath,  $T = T_H$ , the cycle is closed. As a result of this cycle, the HO absorbs heat from the cold bath and releases it to the hot bath, at the expense of a net work consumption, and therefore acts as a refrigerator.

Putting a nanoscopic heat pump to practical work is of high significance for future applications. Heat production and, in particular, its dissipation is a crucial issue to nano devices, since they provide little heat capacities and are supposed to operate isolated from other systems [Cer09]. In future devices, smallest heat pumps may contribute to the solution of this issue. In the follow we sketch two possible implementations of a heat pump for our single trapped ion system.

### 8.1.1. Single-ion operation

For the single-ion system, the thermodynamic cycle may be inverted directly, maintaining the same working principle as for the heat engine operation. To this end, the ion is driven in a coherent oscillation by an external modulation of the trapping potential, see Sec. 5.1.1. When the ion is oscillating, it is coupled to the hot and to the cold bath at the turning points of its trajectory, but inverted as compared to the heat engine operation. This means coupling to a hot bath when the ion is at the open end of the funnel and coupling to a cold bath when the ion is at the narrow end. As a consequence, the thermodynamic cycle of device is inverted. The ion absorbs work from the oscillation in order to move heat from one side to the other. The resulting decrease of the oscillation amplitude corresponds to the amount of energy consumed for the heat transport. However, the interaction with the heat baths is emulated again, and therefore the baths themselves are not accessible to measurements. In order to make the heat pump acting as a refrigerator, we need to make sure that the virtual reservoir where we extract heat from has a lower temperature than the reservoir where we release the heat to. Therefore, the expansion and compression phases need to provide an energy change which is larger than the thermal energy change during the reservoir interactions. The corresponding thermodynamic cycle is sketched in Fig. 8.1.

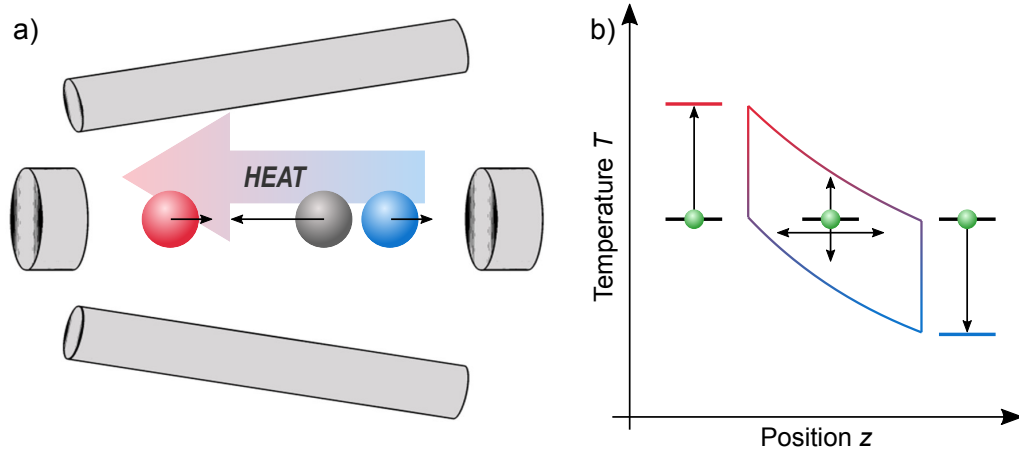


**Figure 8.2.** – Three ion heat pump configuration. (a) The middle ion is performing the thermodynamic cycle as shown in Fig. 8.1, while the outer ions play the role of the heat baths. When driven in the "Egyptian mode", see arrows, the middle ion transfers heat from the ion with low trap frequency (wide end of the tapered potential) to the ion at high trap frequency (narrow end). (b) By the heat pump operation, a temperature gradient is generated in an initially thermalized crystal, only by driving a coherent oscillation of the middle ion.

### 8.1.2. The three-ion heat pump

In order to access the temperatures of the reservoirs directly, a three ion approach is favorable. Here, we assume a three ion Coulomb-crystal in linear configuration along the trap axis, see Fig. 8.2. In this setup, the middle ion represents the heat pump, while the outer ions play the role of reservoirs. We assume all ions to be initialized at the same temperature. Now, we drive the "Egyptian mode" of the crystal, which is the longitudinal mode with highest frequency, where the middle ion moves out of phase with with twice the amplitude then the outer ions, see Fig. 8.2 (a) and [Kau12]. When the middle ion (heat pump) is moving along the trap axis, the trap frequency is changed linearly. Thereby, the effective temperature changes linearly with  $\omega_z$ , according to Eq. (6.2). We initially assume a thermalized crystal at  $T = T_0$ . When the heat pump ion moves from the narrow side of the funnel to the wide side, its state expands adiabatically. When it reaches the reservoir ion, it provides a temperature  $T < T_0$ . Now, the two ions get in thermal contact and (partially) thermalize. Thereby, the outer ion is cooled down and the heat pump ion is heated up. When the heat pump ion moves towards the narrow end of the trap the inverse process occurs: its state is compressed and it reaches the corresponding reservoir ion with  $T > T_0$ . Consequently, this reservoir ion is heated up when thermalizing with the heat pump ion. After some cycles, the heat pump has generated a temperature difference between the two reservoir ions, which have been initially at the same temperature. Note that the interaction between radial modes of the ions is modified by the tapered trapping potential. Introducing artificial dissipation in these modes allows to control the width and the overlap of the resonances, and therefore enables to tune the coupling between the ions when they are close together. A defined thermalization process allows for a conceptual separation between the two reservoir interactions and compression/expansion phases. The final temperature difference between the reservoir ions is proportional to the amplitude of the oscillation of the heat pump ion.

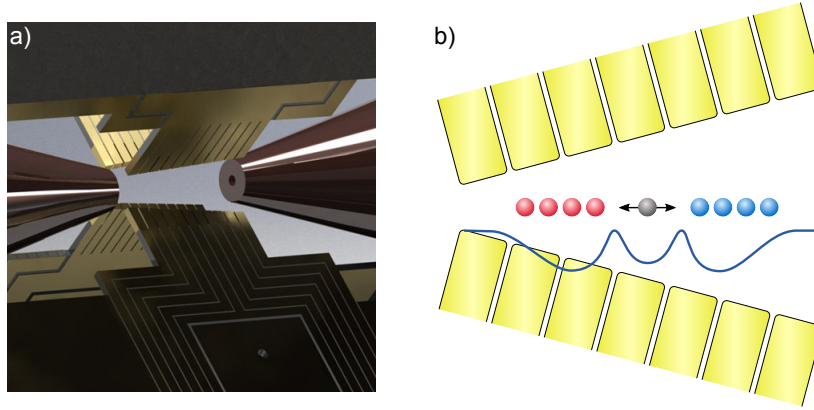


**Figure 8.3.** – Segmented trap design. (a) Model of a funnel-shaped ion trap with segmented electrodes. Based on microfabricated chip traps in X-shape as in [Jac16]. (b) Possible shape of the axial trapping potential (blue) in a segmented trap, in order to separate the cold reservoir (blue ions), the hot reservoir (red ions) and the heat pump (gray ion).

In this configuration, it is beneficial to use a mixed crystal of different atomic species. If the outer ions are much heavier than middle one, the relative amplitude of the middle ion becomes larger and the outer ions may be assumed to remain stationary. Moreover, the ions are resonant to different wavelengths; coupling optically to only one of the ions simplifies the driving of the Egyptian mode drastically [Fel14]. As a consequence of expected amplitudes in the range of  $10\text{ }\mu\text{m}$ , stronger field gradients may be employed to increase the resulting temperature difference, and more sensitive thermometry techniques, such as sideband-spectroscopy, may allow to analyze the temperature difference.

Furthermore, using a trap with segmented electrodes allows for shaping the trapping potential arbitrarily [Wal12b, Rus14]. Then, the heat pump ion and the reservoir ions may be located in individual trapping potentials with individual trap frequencies, see Fig. 8.3. This enables much larger oscillation amplitudes of the pumping ion, and avoids an oscillation of the reservoir ions. In order to increase the heat capacity of the reservoirs, larger ion crystals may be employed.

## 8.2. Autonomous, self-contained engine

One of the most illustrative picture of a self-contained machine is the Feynman ratchet, which extracts work autonomously from an undirected Brownian motion [Rou94, Par02]. Also the famous drinking bird toy is a lively example of a self-contained, cyclic engine process. Autonomous engines are particularly important for future implementations of nanoscopic machines, which may be used for generation of work, energy harvesting or refrigeration [Ton05, Woo16, All16]. They may find applications in nano sensors or nanoscopic electronic devices, where an external switching of reservoir interactions is not feasible.

Our single-ion engine may be operated in a self-driven manner in such a way, that the oscillation of the system is used as feedback control for the bath couplings. This may be achieved a natural way: when strongly focusing the radial cooling beam and pointing it beside the ion but close to it, a strong gradient of the laser intensity is achieved along the trap axis. Now, we can apply a global and continuous heating by electric field noise.

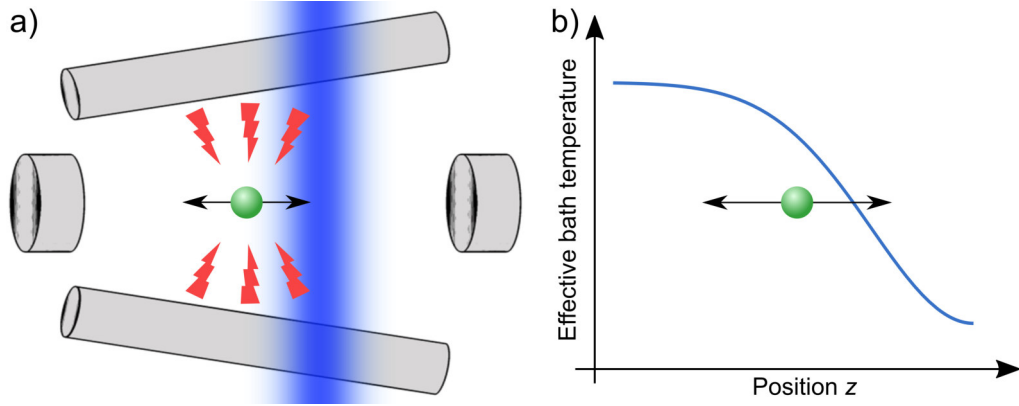


**Figure 8.4.** – Design for an autonomous operation of the single ion heat engine. (a) The cooling laser beam (blue) is pointed slightly beside the rest position of the ion (green), while the ion is heated continuously and globally by electric noise (red flashes). (b) This setup leads to a spatial modulation of the effective temperature of the heat bath the ion is coupled to. As a consequence, an initial oscillation of the ion is amplified in a self-contained manner.

The effective bath temperature is a superposition of the heating and cooling processes, and for constant heating it linearly depends on the laser intensity, see Fig. 8.4. If the ion is oscillating, its trajectory directly leads to a modulation of the heating and cooling processes and the ion is driven in a Stirling-like engine cycle. As a consequence, the heat engine principle amplifies an initial coherent oscillation, while the reservoirs are provided in a continuous manner.

### 8.3. Towards a quantum heat engine

One of the major goals of single particle thermodynamics is to target the quantum regime and to devise engines which are fueled by quantum effects or which generate and amplify quantum states. The idea of a quantum heat engine is discussed extensively since the late 1950s, when Scovil and Schulz-DuBois first showed that a three-level system may act as a heat engine [Sco59], see Sec. 1.5. However, our single-ion system is the first experimentally realized heat engine device, which has the potential to operate in the quantum regime. By doing so, it would permit the study of the performance of small quantum machines [Lin10b, Kos14b] and the exploration of genuine quantum effects in thermodynamics, like quantum coherences [Scu03] and correlations [Dil09]. Note, that in contrast to macroscopic and classical heat engines, on a quantum level the question whether the Curzon-Ahlborn efficiency Eq. (2.9) is a universal bound on the efficiency at maximum power is subject to ongoing discussions [Sch07, Esp09, Wan13a].

Having our system in mind, there are two different approaches to target the quantum regime. On the one hand side, we may retain the working principles as discussed before, but lowering the temperatures of the reservoirs close to the ground state of motion. On the other side, we may not employ motional states but intrinsic quantum states to drive the engine. Both ideas are sketched roughly in the following.



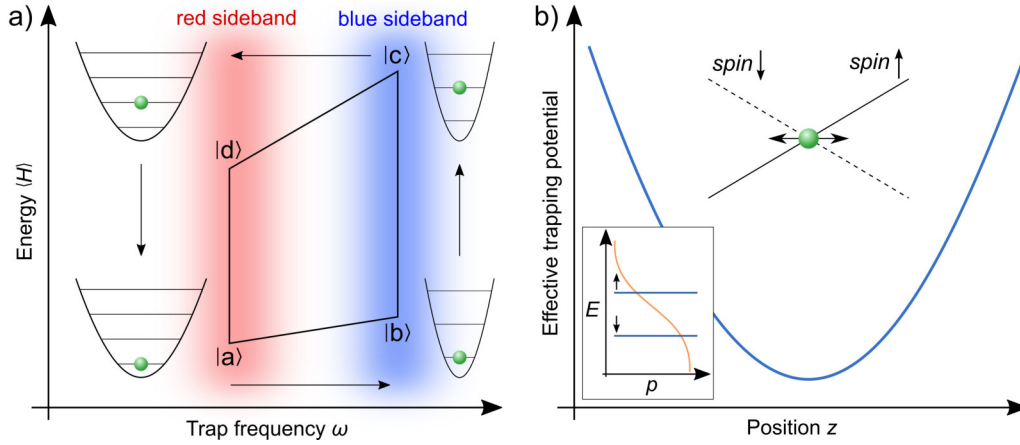


**Figure 8.5.** – Possible approaches to realize a quantum heat engine with a trapped-ion system. (a) The temperature may be lowered in order to approach the ground state of motion, see text. Again, we employ a funnel-shaped trap as before. The cold bath may be at  $\bar{n} = 0$ , the hot bath at, e.g.  $\bar{n} = 1$ . An Otto cycle may be implemented between the stages  $|a\rangle = |\omega_1, \bar{n} = 0\rangle$ ,  $|b\rangle = |\omega_2, 0\rangle$ ,  $|c\rangle = |\omega_2, 1\rangle$  and  $|d\rangle = |\omega_1, 1\rangle$ . (b) Alternatively, the engine may employ the spin of the trapped ion. Therefore, a spin dependent potential (black) is added to the trapping potential (blue), converting a modulation in the occupation probability  $p$  of the spin states in a coherent motion.  $p$  depends on the temperature of spin degree of freedom, see inset.

### 8.3.1. A heat engine at the ground state of motion

At low temperatures,  $k_B T \approx \hbar \omega_r$ , the discreteness of the energy spectrum of the harmonic oscillator plays an important role. Low temperatures may be reached by replacing Doppler cooling by electromagnetically induced transparency cooling or side-band cooling [Lei03], as in the recent verification of the quantum Jarzynski equality [An15]. The ion is then driven again in a thermodynamic cycle, employing a funnel-shaped ion trap and the working principles as before, see Fig. 8.5 (a). In the quantum domain, dark-state thermometry could be replaced by side-band spectroscopy. Therefore, the ion has to be confined in strong trapping fields with trap frequencies high enough to allow for resolved motional sidebands. This allows again for the determination of the thermodynamic cycle of the engine and thus for a precise evaluation of its power and efficiency.

### 8.3.2. The two-level system as heat engine

One of the intrinsic quantum states of an isolated atom is the spin of its electron shell, leading to the fine structure splitting of the individual electron states. The  $^{40}\text{Ca}^+$  ion provides a multiplicity of the ground state of 2, see Sec. 2.7, and may be employed as two-level system. This is a paradigmatic system for analytical investigations and has been analyzed in a variety of theoretical works [Gev92b, Fel00, Scu03, Kie04, Wan13a, Lon15a]. The engine may be driven either by quantum coherent excitations or by conventional thermal excitations. In the latter case, a thermal excitation leads to an increasing population in the higher energy state, according to the Maxwell-Boltzmann distribution. Having a perfectly spin polarized systems with all population in the lower state leads to a minimal entropy and thus to  $T = 0$ . The highest temperature then corresponds to an unpolarized state with probability  $p = 1/2$  for both states. In order to generate work,

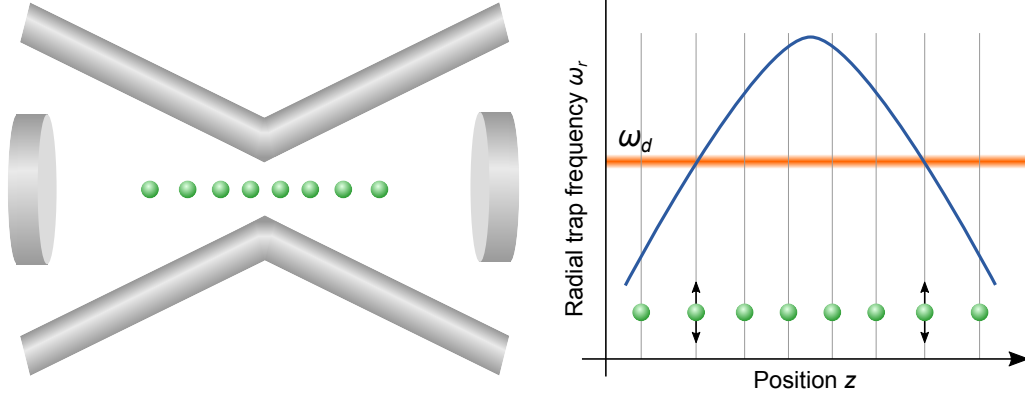


**Figure 8.6.** – Bow-tie configuration of a tapered ion trap for universal quantum computation operations. (a) A linear ion crystal at the node of the bow-tie trap. (b) Expected radial trap frequency  $\omega_r$  along the axis of the modified trap geometry. Ions located symmetrically around the node of the bow-tie are excited by the same external driving frequency  $\omega_d$ . Within the crystal, common modes mediate the excitation between the ions.

a change in the spin state must be translated into motion. This is naturally reached by spin dependent forces, which may be realized by magnetic field gradients [Joh09] or by optically induced ac-Stark shift gradients [Sch16].

Interestingly, occupation inversion in the two level system allows for the investigation of negative temperatures [Bra13b]. This may reveal interesting effects on the dynamics of heat engines, such as an efficiency of unity [Cam16]. However, the notion of negative temperatures and their implications on engines systems is discussed controversially [Hil14]. Nonetheless, bath engineering techniques allow for an dissipative generation of diverse non-thermal quantum states to fuel the engine, employing coherences or quantum correlations.

A converse approach is to employ the heat engine system to drive quantum states [Lev16]. Thereby, the work produced by the engine may be used to increase the energy of a quantum state, such as a Fock state or an entangled state, as long as this state is generated in a distinct degree of freedom and not destroyed by the reservoir interactions [GK14].

## 8.4. The tapered ion trap as a tool for quantum information

Finally, we want to demonstrate the versatility of our novel trap design far beyond the limits of thermodynamic applications. As already outlined in Sec. 5.4, the lifted degeneracy of the radial trap frequencies, in combination with a tunable ion distance and dissipation, promises to be helpful for the investigation of the transport of heat or energy along ion chains.

Furthermore, the concept of a tapered trapping potential may provide a useful tool for scalable quantum information processing. While outstanding quantum computational operations have been performed with trapped ions in the last decade [Häf08, Bla12], a major issue is still the scalability of the system [Mon13]. For universal computation operations, logic quantum gates have to be performed between arbitrary pairs of ions. One of the most promising approaches is the division of larger crystals into smaller subsystems,

where logic gates are performed pairwise within these subsystems [Kie02]. Therefore, reordering of the ion strings becomes necessary and complex shuttling, splitting and swapping operations need to be performed [Wal12b, Rus14, Kau16].

However, using a double tapered trap in bow-tie geometry may facilitate these issues dramatically. Therefore, we combine a funnel trap with a second identical, but inverted trap, such that the potential is symmetric around the center, and a maximum of the trap frequency is obtained in the symmetry plane, see Fig. 8.6. Now, for a linear ion crystal at the center of the trap, always two ions in the left and in the right half of the crystal provide the same trap frequency. Consequently, a common mode of the crystal exists where only these two ions oscillate with a considerable amplitude. Therefore, logic gates between these two ions may be performed deliberately. By moving the crystal around the symmetry point, gates between any two ions may be performed. As a consequence, such a trap design may boost the scalability of quantum computation devices.

# A

## Appendix

### A.1. Treatment of trap electrodes

As electrodes in the chosen trap design, Fig. 4.1, metallic rods are required which provide a small outer diameter below 1 mm and a length of at least 8 mm. From a technical point of view, it is challenging to trim electrodes from solid blocks or to use metal wires such that they are perfectly straight over the length of trap and thus do not lead to distortions of the trapping field. However, these requirements are found to be met by commercial syringe-needles. They are made of hardened stainless steel with an outer diameter of 0.8 mm and provide a high manufacturing quality: They are perfectly straight over a length of several centimeters and have a smooth surface on the micrometer scale. An electron-microscope image of the surface of the syringe-needles is presented in Fig. A.1 (a). However, the needles are produced with a light silicone coating, which is advantageous for medical applications. But, such an insulating surface layer may become electrostatically charged due to stray light from laser beams and thus may disturb the trapping fields, leading to unwanted heating of trapped ions [Bro15]. The effect of the silicone layer can be nicely identified on the electron microscope images Fig. A.1 (a) & (b). We have recorded several images consecutively, exposing to increasing larger sections. On each of the images, the section of the previous images is clearly visible as square structure with different color shading. The electrons from previous images have charged the silicone layer, which then reflects the following electrons differently than the surrounding uncharged surface.

To be used as electrodes, the needles need a special surface treatment. To remove the silicone layer we treated the needles with solvents and with very fine sandpaper. The resulting surface is shown in Fig. A.1 (c), revealing scratches on a micrometer scale, but which are still small as compared to the diameter of the electrodes. However, the charging effect during electron imaging has disappeared.

The needles are inserted in the appropriate holes in the ceramic endcap substrates. On the outer surface, at the wide end side of the funnel, the needles are fixed with small droplets of UHV compatible glue<sup>37</sup>. The electrical connection is made by self-made full metal luster terminals.

---

<sup>37</sup> Deltabond 152, Wakefield-Vette, Inc.

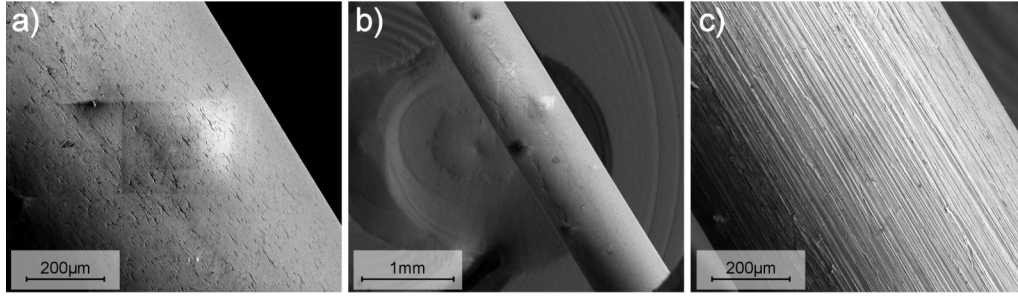


**Figure A.1.** – Electron-microscope images of the syringe needles which are used as rf-electrodes. (a) & (b) Needles before surface treatment. One recognizes the typical surface features of hot rolled steel with a surface flatness on a  $\mu\text{m}$  scale. The rectangular structure on the surfaces in the center of the images results from electron-charging from previous images. These features point out the effect of surface charges on the silicone layer, which repel electrons during subsequent image recording. (c) Needles after treatment. The traces from the sandpaper are clearly visible on a scale of  $10\ \mu\text{m}$ , but the charging effect has disappeared.

## A.2. Processing of PMT pulses

The photomultiplier tube (PMT) is the appropriate device to record the fluorescence of the ion with short exposure times, as long as no spatial resolution is needed. For each photon, the PMT generates a voltage pulse of 5 V at a length of 5 ns. The count rate of the PMT is limited by its dead time of about 100 ns, as a result of the changing process of its internal dynodes. The PMT pulses are counted by a microcontroller (MC) unit, see Sec. 4.1.5. However, the 5 ns pulses are too short to be recognized by the MC. To ensure a reliable pulse counting, the 5 ns pulses are amplified and stretched to 50 ns, still shorter than the dead time of the PMT. Therefore, we have designed an analogue circuit shown in Fig. A.2. The pulse stretcher is based on a two stage transistor amplifier, where the lengthening of the incoming pulses is based on the charging process of the capacitor C1, and thus depends on the ratio of the capacity of C1 to the resistance R2. The modified voltage pulse is fed to the MC. There, it fires an interrupt and thereby increases a counting variable. While the PMT is running continuously, the exposure time is set by gating the MC. The gating is triggered by the FPGA to guarantee precise timing with respect to the laser pulses [Tol14]. The end of the gating pulse fires a second interrupt and the value of the counter is written on the internal memory of the MC. In order to attain a high repetition rate of the measurements, the integration of the PMT-counts can be done directly on the internal memory of the MC with 128 kB. Thereby, we reach a maximum time resolution of  $2\ \mu\text{s}$  and a maximum number of 2000 individual measurements. Subsequently, the memory of MC is read and processed by the experiment control software, and the MC is re-initialized [Tol14].

## A.3. Stroboscopic recording of the ions motion

The ICCD camera allows to acquire images of the fluorescence with exposure times much shorter than the trap frequency. This enables us to resolve a periodic motion of the ion. Therefore, we drive the an oscillation of the ion and trigger the camera phase-locked to the driving signal. An internal delay generator allows to scan the phase of the oscillation where the image is taken. For each phase, a total exposure time of about 100 ms is

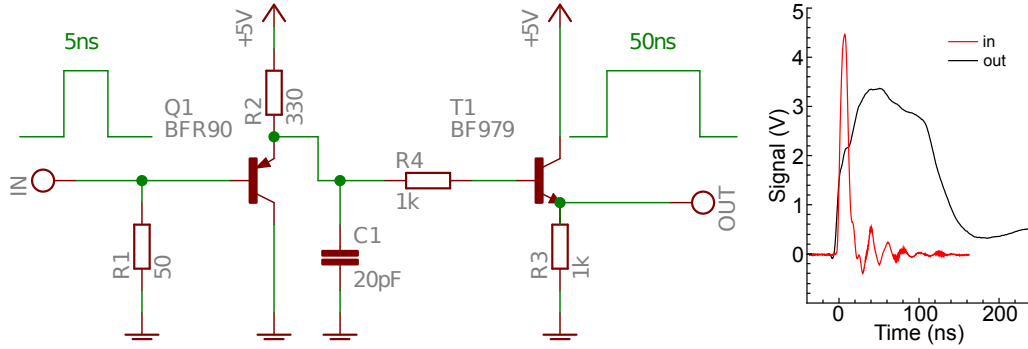


**Figure A.2.** – Circuit diagram for stretching the 5 ns pulses from the PMT to 50 ns pulses, which can be counted by the MC. We use an analogue transistor circuit, where the pulse extension depends on the ratio of the capacity of C1 to the resistance R2. The measured incoming signal from the PMT and the outgoing signal to the MC are shown on the right.

accumulated on the CCD chip, before the chip is read out. A time resolved oscillation is demonstrated by the example of a breathing mode of a two-ion crystal, see Fig. A.3.

#### A.4. Radio-frequency signal generator for AOM driving

To drive the AOM we use a home built radio-frequency (rf) signal generator, which is tunable in power and frequency by external control voltages. The output signal is turned on and off by a TTL signal, which allows us to operate the AOMs as electro-optical shutters and to switch the laser beams on and off. Furthermore, it allows us to adjust the power of laser beams precisely and to tune their frequency within the range of the according AOM. Thereby, the VCO device can be fully integrated into the electronic experiment control system. A simplified block diagram of the circuit is shown in Fig. A.4. The rf-signal is generated in by a VCO<sup>38</sup>, which is controlled either by an external or by an internal control voltage. The external voltages are supplied by our stabilized DAC-device, see Sec. 4.1.2. The internal control voltages are tuned by potentiometers. A

<sup>38</sup>VCO interchangeable, we use POS-100, POS-150 and POS-300, Mini-Circuits.

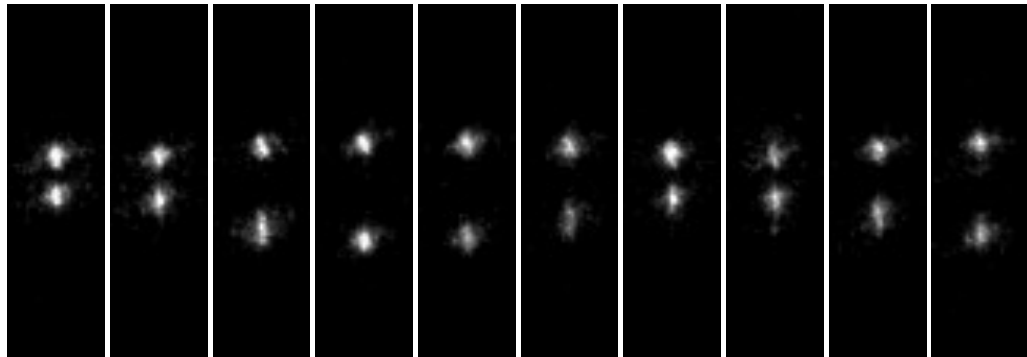


**Figure A.3.** – Stroboscopic record of the breathing mode in axial direction of a two ion crystal at 141 kHz, acquired with the ICCD camera. Each image corresponds to a sum of 200000 exposures of 700 ns. The images are rotated by 90° (axial direction is vertical).

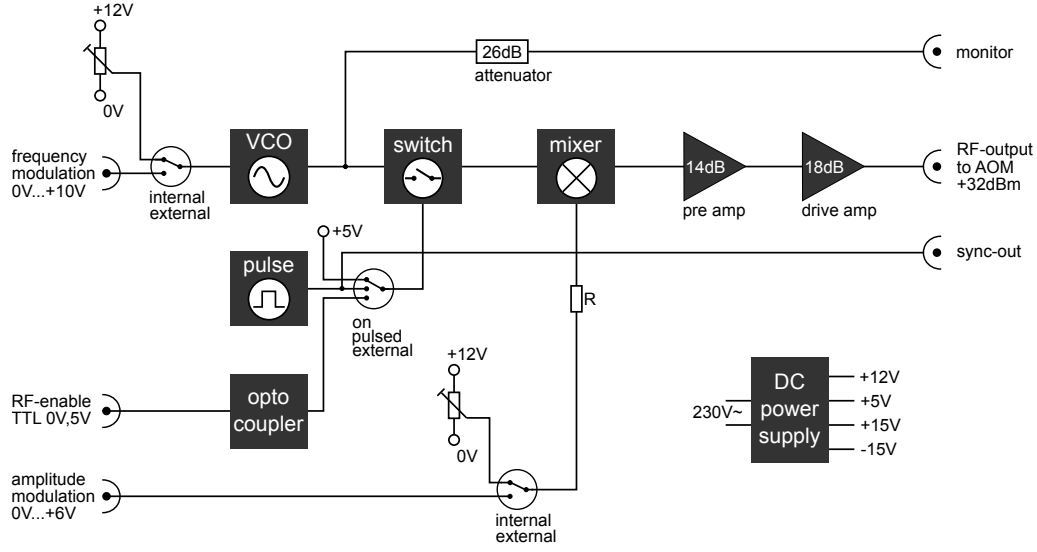


**Figure A.4.** – Block diagram of the controllable rf-signal generator which is used to drive the AOMs. The signal is generated by a VCO. It can be switched and adjusted in power and frequency by external control voltages. The rf-signal is amplified to a maximum level of 32 dBm, which is enough to reach the maximum defraction efficiency of the AOM.

high frequency switch<sup>39</sup> may block the transfer of the rf-signal to the AOM. The switch is either turned steadily on, or controlled by an external TTL signal (decoupled by an opto-coupler and passed via a transistor driving stage), or controlled by an internal rectangular pulse generator<sup>40</sup>. The latter provides a duty cycle of 0.01 and reduces the laser power behind the AOM accordingly. This mode of operation is used for a safe beam adjustment at low optical power. A mixer multiplies the VCO signal by a control voltage, which stems from an external or from the internal voltage source. A two stage amplification (pre-amplifier<sup>41</sup> and high power stage<sup>42</sup>) increases the output power to a maximum level of 32 dBm, which is then fed to the AOM devices. Each VCO module is provided with an separate 12 V and 1 A analogue power supply unit<sup>43</sup>. A monitor signal allows to observe the VCO-frequency during operation. A characterization of the output signal in terms of power and frequency as a function of the corresponding control voltages is shown in Fig. A.5. We further characterized the switching behavior of the AOMs, where we used the rf-enable TTL input of the VCO module. Fig. A.6 reveals a switching of the laser power on a timescale of 50 ns. Each of the AOMs in our setup is supplied by a n individual VCO module.

## A.5. Power stabilization during AOM scans

The controllable VCO-module allows to perform frequency scans by tuning the AOM frequency. As mentioned in Sec. 4.3.3, the internal electronic resonance circuit of the

<sup>39</sup>KSW-2-46+, Mini-Circuits.

<sup>40</sup>LMC555 CMOS Timer, Texas Instruments.

<sup>41</sup>ERA-5XSM+, Mini-Circuits.

<sup>42</sup>1F5500B, RFHIC, not produced anymore. Replaced by RFC1G18H4-24, RFHIC. Needs an upgrade of the supply voltage from 12 V to 24 V.

<sup>43</sup>HA15-0.9-A, CONDOR / SL Power Electronics Corp.

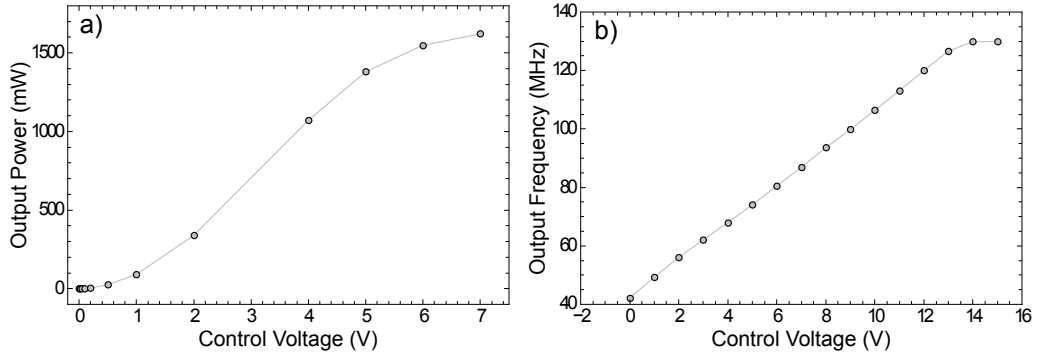


**Figure A.5.** – Characteristics of the VCO module. (a) Power of the rf-output as a function of the AM-control voltage. A voltage between 0 V and 7 V regulates the output power between 0 mW and 1600 mW, which corresponds to a maximum power level of 32 dBm. Measured with a POS-100VCO (Mini-Circuits) at a frequency of 70 MHz. (b) Frequency of the same VCO as a function of the FM-control voltage. The frequency range between 40 MHz to 130 MHz is reached by a control voltage between 0 V and 15 V. Above 10 V, the maximum output power of the VCO drops from 32 dBm to 30 dBm.

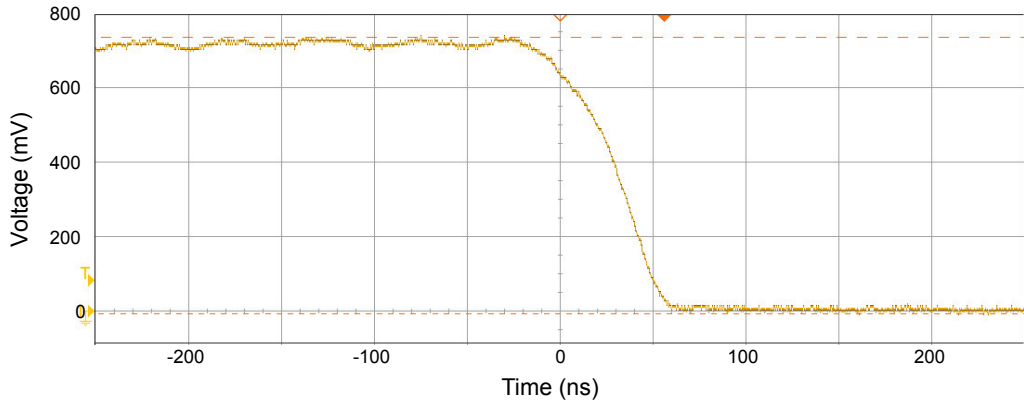


**Figure A.6.** – Step-response of an AOM, operated as electro-optical shutter. The graph shows the laser intensity, measured as a voltage from a photo-diode, as a function of time. After turning off the rf-generator by an external TTL, the intensity of the laser beam decays within 50 ns.

AOMs is strongly frequency dependent. As a consequence, the defraction efficiency of the AOM shows a dependance on the driving frequency, as measured in Fig. A.7 (a). To avoid intensity fluctuations during frequency scans, the beam intensity is first measured on a photo-diode (PD) as a function of the AOM drive frequency. For several grid points of the driving frequency we correct the AOM driving power in order to obtain a constant laser intensity. This results in a look-up table for corrected driving power values. These tables are linearly interpolated and then used for subsequent frequency scans, leading to a relative power stability of better than 99 %.

## A.6. Switching between lasers with two VCOs

In order to switch fast between two driving frequencies of the AOM, we employ two individual VCO-modules. Both signal lines are combined by a rf-power combiner<sup>44</sup> and

<sup>44</sup>ZSC-2-1W+, Mini-Circuits.



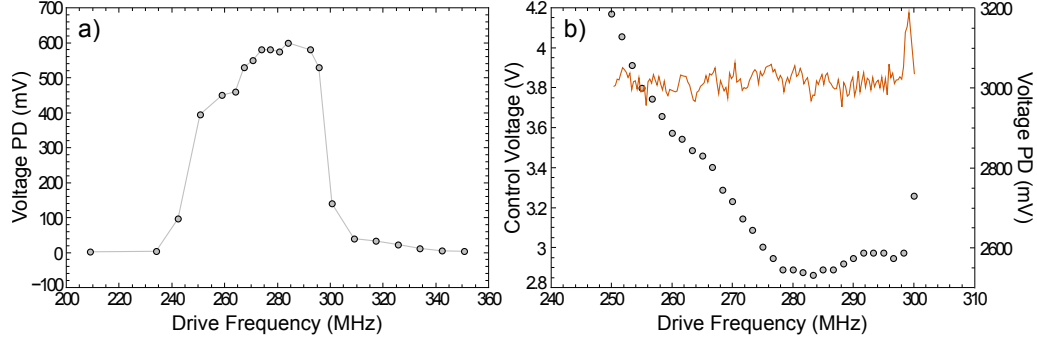


**Figure A.7.** – Frequency dependance of the defraction efficiency of the AOM and its compensation. (a) Optical power of the laser beam on a photo-diode (PD), after having passed the AOM in double pass configuration. Here we characterize the TEF-270-100 AOM from Brimrose. (b) To compensate for the non-uniform power distribution, we adjust the AM-control voltage for each frequency (gray points) in order to reach a defined optical power (here the set point is 3000 mV on the PD). Using the interpolated correction values, the standard deviation of the optical power fluctuations during a scan of 50 MHz, measured as a voltage on a photo-diode (orange line), results to 29 mV. The relative fluctuation is thus  $29/3000 < 0.01$ .

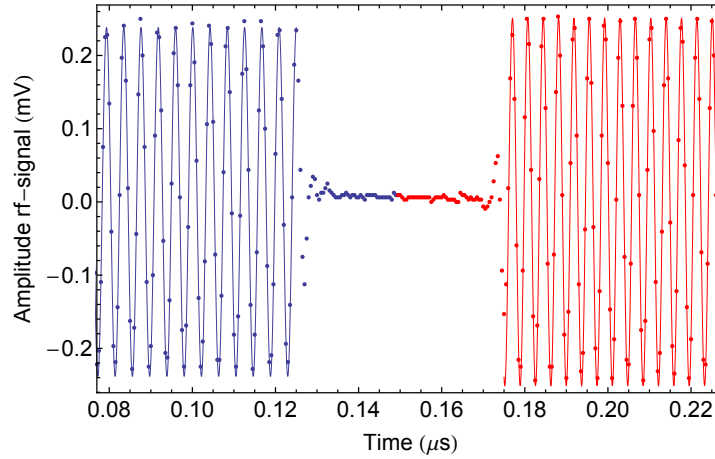


**Figure A.8.** – Switching between two drive frequencies which for the AOM. Measured signal with fitted sine-functions. The frequency is changed from 240 MHz to 270 MHz. In order to avoid any photons with undesired frequencies in the transition regime, we turn off the driving power during the frequency change for 50 ns. This is important for the pulsed temperature measurement process, in order to avoid undesired heating or cooling effects by intermediate frequencies.

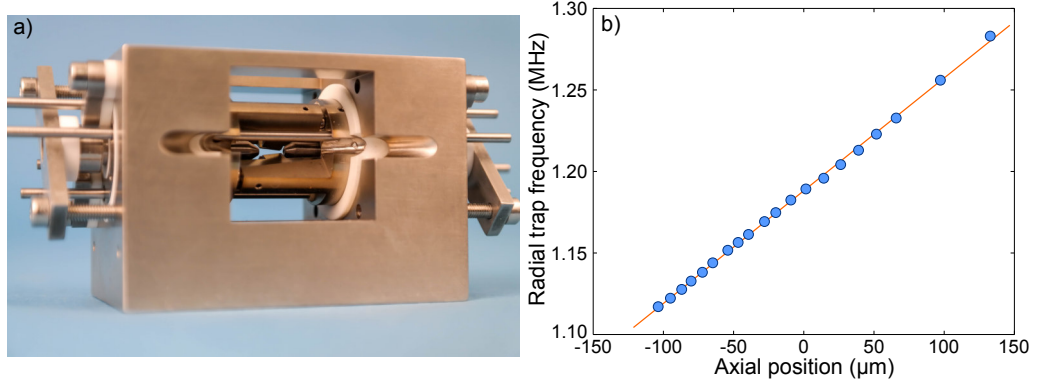


**Figure A.9.** – New design of the funnel-shaped ion trap. (a) Picture of the trap just before being mounted in the vacuum chamber. More details regarding the geometry and the design are presented in Fig. A.10. (b) Measured radial trap frequency as a function of the axial position. Only the lower one of both radial frequencies has been recorded. The degeneracy has been lifted by 5 kHz.

fed to the AOM. The FPGA-controlled TTLs enable the output of one module or the other. This allows us to switch between two driving frequencies within 50 ns, see Fig. A.8. This value is on the same timescale than the decay of the optical signal behind the AOM, Fig. A.6, and much faster than the exposure time during the experiments,  $\tau_{\text{exp}} \leq 5 \mu\text{s}$ . The switching between AOM frequencies is used during the pulsed temperature measurements, see Fig. 6.8, where thermalization processes are resolved.

## A.7. Design of a next generation funnel-shaped ion trap

We have developed a new generation of the funnel shaped ion trap, in order to face the shortcomings of the old trap design, namely the low trap frequencies, the large size of the trap, and a difficult mechanical alignment. We have implemented an X-shaped blade-trap design, whose trapping volume is reduced by a factor of 16 as compared to the rod trap used before. To achieve a high mechanical stability and an optimal alignment of the electrodes, each pair of opposing electrodes is made from one cylindrical block of stainless steel, see Fig. A.9 and Fig. A.10, similar to a fork with two prongs. Both electrode pairs are then put together with an orientation of  $90^\circ$  to each other. The relative alignment in all three dimensions is realized by four balls (diameter 3 mm, grade 10), made of silicon nitride  $\text{Si}_3\text{N}_4$  (low thermal expansion, electrically insulating), which sit in conical ball seats on both sides such that both metal parts are separated by 1 mm. The axis is defined by a common bore in solid metal holder. Concentric ceramic tubes, fitted outside and inside the base cylinder of the electrode pairs ensure a high electric insulation with a wall thickness of 3.5 mm and 2.5 mm. The endcaps consist of stainless steel cylinders, with pointed ends towards the trap volume. They are placed inside the inner ceramic tube, having a mechanical stop to ensure a distance of 0.2 mm between the tips of the endcaps and the trap electrodes. The endcaps provide a concentric bore of 0.8 mm to enable a laser beam to pass along the trap axis. Between the blade electrodes we have placed compensation electrodes, using steel rods with a diameter of 2 mm, insulated within ceramic tubes.

The new trap has a length of 4 mm and a radial distance between the trap axis and the

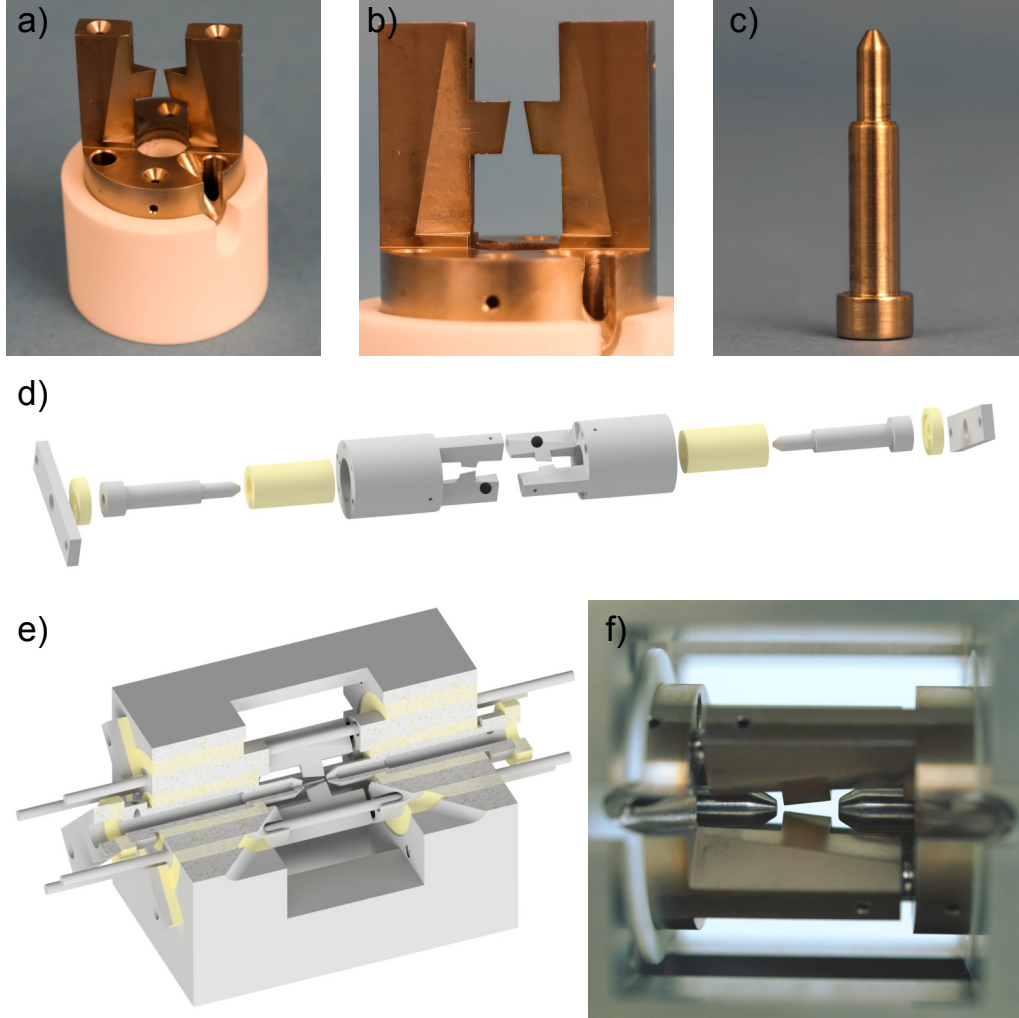


**Figure A.10.** – Composition of the new trap design. (a) One of the two fork-shaped electrode-pairs, with its cylindrical base inside a ceramic insulator tube. Conical ball sits for the  $\text{Al}_2\text{O}_3$  balls are located on top of the fork prongs, as well as on the base. Additionally, a notch for the access of a diagonal laser beam as well as holes for the compensation electrodes can be seen. (b) The trap electrodes protrude from the fork, at the center of the image. The angle of the electrodes provides  $10^\circ$ . The second fork is identical, with an inverted orientation of the tapered electrodes. (c) One of the endcaps, which are designed as elongated conical rods. The edge in the upper part serves as mechanical stop to define a precise position of the endcap. (d) Exploded view of the trap assembly. First the two fork-shaped electrode pairs are fitted with  $90^\circ$  to each other by four silicon nitride balls (black). Then ceramic tubes and the endcaps are inserted, each with a mechanical stop towards the trap volume. From behind, the whole assembly is fixed with a metal clap, screwed to a solid mount. (e) Quarter view of the trap design, including the holder and the compensation electrodes. (f) Trap volume between the funnel shaped rf-electrodes and the endcaps after assembly. Compensation electrodes are removed for a better view of the funnel electrodes.

blade electrodes of 0.5 mm at their narrow ending. The reduced size of the trap, as well as a higher amplitude of the applied rf-voltage, enable for increased trap frequencies, see Fig. A.9 (b). For radial trap frequencies around 1.2 MHz, we measure a gradient of  $\omega_r(z)$  along the trap axis in linear approximation of

$$\omega_r(z)/2\pi = (700(4) \text{ Hz}/\mu\text{m}) \cdot z + 1187.8(3) \text{ kHz}. \quad (1.1)$$

The gradient is about a factor of 7 higher as compared to the old trap design, Eq. (7.1). By the heat engine mechanism, the efficiency of the engine is supposed to increase linearly with  $\partial\omega_r/\partial z$ , allowing for a better performance and a higher output power. But, more important, the higher trap frequencies allow for resolved sideband spectroscopy and sideband cooling. Hence, cooling towards the ground state of motion is possible, which enables for experiments in the quantum regime.

However, the blade-trap design provides an improved shielding of the trap volume against external electric fields. While this fact is beneficial for precision experiments, it makes a heating through electric noise more difficult: increased noise amplitudes by about three orders of magnitude are needed. Alternatively, the ion may be heated using a randomized photon scattering from a spectrally broadened laser beam. To avoid any lock-in effect with the oscillation of the ion, the spectral width of the laser should be larger than the Doppler broadened natural linewidth of the cooling transition of the ion.



# B

## List of publications

The following articles have been published in the course of this thesis, where most parts of the results have been presented:

**A single-atom heat engine,**

J. Roßnagel, S. Dawkins, K.N. Tolazzi, O. Abah, E. Lutz, F. Schmidt-Kaler and K. Singer,  
Science **352**, 325 (2016).

Experimental demonstration of a single-ion heat engine. We drive the ion thermally in a Stirling cycle by coupling it alternately to hot and cold reservoirs. The output power of the engine is used to drive a harmonic oscillation. From direct measurements of the ion dynamics, we are able to determine the thermodynamic cycles and to evaluate the power and efficiency of the engine.

**Fast thermometry for trapped ions using dark resonances,**

J. Roßnagel, K.N. Tolazzi, F. Schmidt-Kaler and K. Singer,  
New J. of Phys. **17**, 045004 (2015).

Demonstration of a method to determine the temperature of trapped ions, which is based on the analysis of the lineshape of dark resonances in the fluorescence spectrum. The method is accurate over a large dynamic range and allows for monitoring fast thermalization processes, as required for analyzing the heat engine performance. Experimental work is supported by a solution of the 8-level optical Bloch equations when including the ions classical motion. Tuning the cooling laser to selected resonance features reveals the capability to control and to adjust the ion's temperature.

**Nanoscale Heat Engine Beyond the Carnot Limit,**

J. Roßnagel, O. Abah, F. Schmidt-Kaler, K. Singer and E. Lutz,  
Phys. Rev. Lett. **112**, 030602 (2014).  
*Editors' Suggestion* and featured in *Physics*.

Investigation of a single-ion heat engine driven by a squeezed thermal reservoir. We show that the efficiency at maximum power increases with the degree of squeezing, surpassing the standard Carnot limit for pure thermal excitations and approaching unity exponentially for large squeezing parameters. We combine an analytical model for harmonic oscillators with realistic numerical simulations of the system.

**Nano-Motor aus einem einzelnen Atom,**

J. Roßnagel, K.N. Tolazzi, O. Abah, E. Lutz, F. Schmidt-Kaler and K. Singer,  
GIT Labor-Fachzeitschrift **6**, 51 (2014).

Characterization measurements of the working principle of the heat engine and of the tapered ion trap (in German).

**Single-ion heat engine at maximum power,**

O. Abah, J. Roßnagel, G. Jacob, S. Deffner, F. Schmidt-Kaler, K. Singer and E. Lutz,  
Phys. Rev. Lett. **109**, 203006 (2012).

Proposal for the single-ion heat-engine concept, containing an analytical framework for the harmonic oscillator model system driven in a thermodynamic Otto cycle. We demonstrate the feasibility of our setup by extensive numerical simulations, showing that the engine is capable to operate at maximum output power with efficiencies of up to 30% under realistic conditions.

Publications not directly related to the selected main topic of this thesis:

**Observation of the Kibble–Zurek scaling law for defect formation in ion crystals,**

S. Ulm, J. Roßnagel, G. Jacob, C. Degünther, S.T. Dawkins, U.G. Poschinger, R. Nigmatullin, A. Retzker, M.B. Plenio, F. Schmidt-Kaler and K. Singer,  
Nat. commun. **4**, 2290 (2013).

**Control of RILIS lasers at IGISOL facilities using a compact atomic beam reference cell,**

T. Kron, R. Ferrer-Garcia, N. Lecesne, V. Sonnenschein, S. Raeder, J. Roßnagel, K. Wendt,  
Hyperfine Interact. **216**, 53 (2013).

**Determination of the first ionization potential of actinium,**

J. Roßnagel, S. Raeder, A. Hakimi, R. Ferrer, N. Trautmann, and K. Wendt,  
Phys. Rev. A **85**, 012525 (2012).

**Performance of a high repetition pulse rate laser system for in-gas-jet laser ionization studies with the Leuven laser ion source @ LISOL,**

R. Ferrer, V.T. Sonnenschein, B. Bastinc, J. Roßnagel *et al.*,  
Nucl. Instr. Meth. Phys. Res. **291**, 29 (2012).

# Bibliography

- [Aba12] O. Abah, J. Roßnagel, G. Jacob, S. Deffner, F. Schmidt-Kaler, K. Singer, and E. Lutz, *Single-Ion Heat Engine at Maximum Power*, Phys. Rev. Lett. **109**, 203006 (2012).
- [Aba14] O. Abah and E. Lutz, *Efficiency of heat engines coupled to nonequilibrium reservoirs*, EPL (Europhysics Letters) **106**, 20001 (2014).
- [Aba15] O. Abah, *Quantum machines at the nanoscale*, Ph.D. thesis, Friedrich-Alexander-Universität Erlangen-Nürnberg (2015).
- [Aba16] O. Abah and E. Lutz, *Optimal performance of a quantum Otto refrigerator*, Europhys. Lett. **113**, 60002 (2016).
- [Aga13] G. S. Agarwal and S. Chaturvedi, *Quantum dynamical framework for Brownian heat engines*, Phys. Rev. E **88**, 012130 (2013).
- [Ale12] A. Alemany, A. Mossa, I. Junier, and F. Ritort, *Experimental free-energy measurements of kinetic molecular states using fluctuation theorems*, Nat. Phys. **8**, 688 (2012).
- [Ali79] R. Alicki, *The quantum open system as a model of the heat engine*, Journal of Physics A: Mathematical and General **12**, L103 (1979).
- [All00] A. Allahverdyan and T. M. Nieuwenhuizen, *Extraction of work from a single thermal bath in the quantum regime*, Phys. Rev. Lett. **85**, 1799 (2000).
- [All16] A. E. Allahverdyan, S. G. Babajanyan, N. H. Martirosyan, and A. V. Melkikh, *Adaptive Heat Engine*, Phys. Rev. Lett. **117**, 030601 (2016).
- [Alo16a] J. Alonso, F. Leupold, Z. Solèr, M. Fadel, M. Marinelli, B. Keitch, V. Negnevitsky, and J. Home, *Generation of large coherent states by bang-bang control of a trapped-ion oscillator*, Nat. Commun. **7** (2016).
- [Alo16b] J. J. Alonso, E. Lutz, and A. Romito, *Thermodynamics of weakly measured quantum systems*, Phys. Rev. Lett. **116**, 080403 (2016).
- [Alz76] G. Alzetta, A. Gozzini, L. Moi, and G. Orriols, *An experimental method for the observation of RF transitions and laser beat resonances in oriented Na vapour*, Il Nuovo Cimento B **36**, 5 (1976).
- [An15] S. An, J.-N. Zhang, M. Um, D. Lv, Y. Lu, J. Zhang, Z.-Q. Yin, H. Quan, and K. Kim, *Experimental test of the quantum Jarzynski equality with a trapped-ion system*, Nat. Phys. **11**, 193 (2015).
- [And84] B. Andresen, P. Salamon, and R. S. Berry, *Thermodynamics in finite time*, Phys. Today **37**, 62 (1984).
- [Ari76] E. Arimondo and G. Orriols, *Nonabsorbing atomic coherences by coherent two-photon transitions in a three-level optical pumping*, Il Nuovo Cimento **17**, 333 (1976).
- [Ari96] E. Arimondo, *V Coherent Population Trapping in Laser Spectroscopy*, Progress in Optics **35**, 257 (1996).
- [Asp88] A. Aspect, E. Arimondo, R. e. a. Kaiser, N. Vansteenkiste, and C. Cohen-Tannoudji, *Laser cooling below the one-photon recoil energy by velocity-selective coherent population trapping*, Phys. Rev. Lett. **61**, 826 (1988).



- [Ast07] R. D. Astumian, *Adiabatic operation of a molecular machine*, Proc. Natl. Acad. Sci. **104**, 19715 (2007).
- [Atk10] P. Atkins, *The laws of thermodynamics: A very short introduction*, Oxford University Press, 2010.
- [Ban08] S. Banerjee and R. Srikanth, *Geometric phase of a qubit interacting with a squeezed-thermal bath*, Eur. Phys. J. D **46**, 335 (2008).
- [Bat14] T. B. Batalhão, A. M. Souza, L. Mazzola, R. Auccaise, R. S. Sarthour, I. S. Oliveira, J. Goold, G. De Chiara, M. Paternostro, and R. M. Serra, *Experimental reconstruction of work distribution and study of fluctuation relations in a closed quantum system*, Phys. Rev. Lett. **113**, 140601 (2014).
- [Ber68] D. Bernoulli, *Hydrodynamics (1738)*, trans. Thomas Carmody and Helmut Kobus, Dover Pub., 1968.
- [Ber98] D. Berkeland, J. Miller, J. Bergquist, W. Itano, and D. Wineland, *Minimization of ion micromotion in a Paul trap*, J. Appl. Phys. **83**, 5025 (1998).
- [Bér12] A. Bérut, A. Arakelyan, A. Petrosyan, S. Ciliberto, R. Dillenschneider, and E. Lutz, *Experimental verification of Landauer's principle linking information and thermodynamics*, Nature **483**, 187 (2012).
- [Ber13] A. Bermudez, M. Bruderer, and M. Plenio, *Controlling and measuring quantum transport of heat in trapped-ion crystals*, Phys. Rev. Lett. **111**, 040601 (2013).
- [Ber14] C. Bergenfeldt, P. Samuelsson, B. Sothmann, C. Flindt, and M. Büttiker, *Hybrid microwave-cavity heat engine*, Phys. Rev. Lett. **112**, 076803 (2014).
- [Bis94] R. A. Bissell, E. Córdova, A. E. Kaifer, and J. F. Stoddart, *A chemically and electrochemically switchable molecular shuttle*, Nature **369**, 133 (1994).
- [Bla86] R. Blatt, P. Zoller, G. Holzmüller, and I. Siemers, *Brownian motion of a parametric oscillator: A model for ion confinement in radio frequency traps*, Z. Phys. D **4**, 121 (1986).
- [Bla01] E. D. Black, *An introduction to Pound–Drever–Hall laser frequency stabilization*, Am. J. of Phys. **69**, 79 (2001).
- [Bla08] R. Blatt and D. Wineland, *Entangled states of trapped atomic ions*, Nature **453**, 1008 (2008).
- [Bla12] R. Blatt and C. Roos, *Quantum simulations with trapped ions*, Nat. Phys. **8**, 277 (2012).
- [Bli12] V. Blickle and C. Bechinger, *Realization of a micrometre-sized stochastic heat engine*, Nat. Phys. **8**, 143 (2012).
- [Bou13] E. Boukobza and H. Ritsch, *Breaking the carnot limit without violating the second law: A thermodynamic analysis of off-resonant quantum light generation*, Phys. Rev. A **87**, 063845 (2013).
- [Bra86] B. Braden, *The surveyor's area formula*, Coll. Math. J. **17**, 326 (1986).
- [Bra13a] J.-P. Brantut, C. Grenier, J. Meineke, D. Stadler, S. Krinner, C. Kollath, T. Esslinger, and A. Georges, *A thermoelectric heat engine with ultracold atoms*, Science **342**, 713 (2013).
- [Bra13b] S. Braun, J. P. Ronzheimer, M. Schreiber, S. S. Hodgman, T. Rom, I. Bloch, and U. Schneider, *Negative absolute temperature for motional degrees of freedom*, Science **339**, 52 (2013).
- [Bra15a] F. Brandão, M. Horodecki, N. Ng, J. Oppenheim, and S. Wehner, *The second laws of quantum thermodynamics*, Proceedings of the National Academy of Sciences **112**, 3275 (2015).
- [Bra15b] K. Brandner, K. Saito, and U. Seifert, *Thermodynamics of micro-and nano-systems driven by periodic temperature variations*, Phys. Rev. X **5**, 031019 (2015).
- [Bre97] G. Breitenbach, S. Schiller, and J. Mlynek, *Measurement of the quantum states of squeezed light*, Nature **387**, 471 (1997).

- 
- [Bro06] W. R. Browne and B. L. Feringa, *Making molecular machines work*, Nature nanotechnology **1**, 25 (2006).
- [Bro12] C. Van den Broeck, N. Kumar, and K. Lindenberg, *Efficiency of isothermal molecular machines at maximum power*, Phys. Rev. Lett. **108**, 210602 (2012).
- [Bro15] M. Brownnutt, M. Kumph, P. Rabl, and R. Blatt, *Ion-trap measurements of electric-field noise near surfaces*, Rev. Mod. Phys. **87**, 1419 (2015).
- [Cal85] H. B. Callen, *Thermodynamics And An Introduction To Thermostatistics*, John Wiley & Sons, 1985.
- [Cam15] M. Campisi, J. Pekola, and R. Fazio, *Nonequilibrium fluctuations in quantum heat engines: theory, example, and possible solid state experiments*, New J. Phys. **17**, 035012 (2015).
- [Cam16] M. Campisi, *Notes on heat engines and negative temperatures*, arXiv:1606.05244 (2016).
- [car] Image source: <http://www.carparts.com/engine.htm>, 08/25/2016.
- [Car24] S. Carnot, *Réflexions sur la puissance motrice du feu et sur les machines propres à développer cette puissance*, Gauthier-Villars, 1824.
- [Cas88] R. Casdorff and R. Blatt, *Ordered structures and statistical properties of ion clouds stored in a Paul trap*, Appl. Phys. B **45**, 175 (1988).
- [Cen15] Y. A. Cengel and M. A. Boles, *Thermodynamics: an engineering approach*, McGraw-Hill Education, 2015, 8th ed.
- [Cer09] G. Cerofolini, *Nanoscale devices*, Springer Berlin Heidelberg, 2009.
- [Cha58] P. Chambadal, *Le choix du cycle thermique dans une usine génératrice nucléaire*, Revue Generale de L'Electricite **67**, 332 (1958).
- [Cir92] J. I. Cirac, R. Blatt, P. Zoller, and W. Phillips, *Laser cooling of trapped ions in a standing wave*, Phys. Rev. A **46**, 2668 (1992).
- [Cir93] J. I. Cirac, A. S. Parkins, R. Blatt, and P. Zoller, *"Dark" squeezed states of the motion of a trapped ion*, Phys. Rev. Lett. **70**, 556 (1993).
- [Cir94a] J. Cirac, L. Garay, R. Blatt, A. Parkins, and P. Zoller, *Laser cooling of trapped ions: The influence of micromotion*, Phys. Rev. A **49**, 421 (1994).
- [Cir94b] J. Cirac, M. Lewenstein, and P. Zoller, *Quantum statistics of a laser cooled ideal gas*, Phys. Rev. Lett. **72**, 2977 (1994).
- [Cla50] R. Clausius, *Über die bewegende Kraft der Wärme und die Gesetze, welche sich daraus für die Wärmelehre selbst ableiten lassen*, Ann. Phys. **155**, 368 (1850).
- [Cla57] R. Clausius, *Über die Art der Bewegung, welche wir Wärme nennen*, Annalen der Physik **176**, 353 (1857).
- [Cla67] R. Clausius, *The mechanical theory of heat: with its applications to the steam-engine and to the physical properties of bodies*, J. van Voorst, 1867.
- [Cle12] B. Cleuren, B. Rutten, and C. Van den Broeck, *Cooling by heating: Refrigeration powered by photons*, Phys. Rev. Lett. **108**, 120603 (2012).
- [Col05] D. Collin, F. Ritort, C. Jarzynski, S. B. Smith, I. Tinoco, and C. Bustamante, *Verification of the Crooks fluctuation theorem and recovery of RNA folding free energies*, Nature **437**, 231 (2005).
- [Cou53] E. Courant, M. S. Livingston, H. Snyder, and J. Blewett, *Origin of the "Strong-Focusing" Principle*, Phys. Rev. Lett. **91**, 202 (1953).
- [Cro99] G. E. Crooks, *Entropy production fluctuation theorem and the nonequilibrium work relation for free energy differences*, Phys. Rev. E **60**, 2721 (1999).

- [CT77] C. Cohen-Tannoudji, *Frontiers in Laser Spectroscopy, Les Houches 1975*, chap. Atoms in Strong Resonant Fields, 5098, North-Holland, 1977.
- [CT11] C. Cohen-Tannoudji and D. Guéry-Odelin, *Advances in atomic physics*, World Scientific, 2011.
- [Cur75] F. L. Curzon and B. Ahlborn, *Efficiency of a Carnot engine at maximum power output*, Am. J. Phys. **43**, 22 (1975).
- [Dec15] A. Dechant, N. Kiesel, and E. Lutz, *All-optical nanomechanical heat engine*, Phys. Rev. Lett. **114**, 183602 (2015).
- [Def13] S. Deffner and E. Lutz, *Thermodynamic length for far-from-equilibrium quantum systems*, Phys. Rev. E **87**, 022143 (2013).
- [Dem08] W. Demtröder, *Experimentalphysik 1*, Springer, 2008.
- [Die89] F. Diedrich, J. Bergquist, W. M. Itano, and D. Wineland, *Laser cooling to the zero-point energy of motion*, Phys. Rev. Lett. **62**, 403 (1989).
- [Die08] S. Diehl, A. Micheli, A. Kantian, B. Kraus, H. Büchler, and P. Zoller, *Quantum states and phases in driven open quantum systems with cold atoms*, Nat. Phys. **4**, 878 (2008).
- [Dil09] R. Dillenschneider and E. Lutz, *Energetics of quantum correlations*, Europhys. Lett.) **88**, 50003 (2009).
- [Din16] L. Dinis, I. Martínez, É. Roldán, J. Parrondo, and R. Rica, *Thermodynamics at the microscale: from effective heating to the Brownian Carnot engine*, J. Stat. Mech. Theor. Exp. **2016**, 054003 (2016).
- [DK14] K. Dr. Kunze, Toptica Photonics AG, private communication (2014).
- [Dod11] V. Dodonov, C. Valverde, L. Souza, and B. Baseia, *Classicalization times of parametrically amplified "Schrödinger cat" states coupled to phase-sensitive reservoirs*, Phys. Lett. A **375**, 3668 (2011).
- [Don05] E. Donley, T. Heavner, F. Levi, M. Tataw, and S. Jefferts, *Double-pass acousto-optic modulator system*, Rev. Sci. Inst. **76**, 063112 (2005).
- [Dor13] K. E. Dorfman, D. V. Voronine, S. Mukamel, and M. O. Scully, *Photosynthetic reaction center as a quantum heat engine*, Proceedings of the National Academy of Sciences **110**, 2746 (2013).
- [Dre86] E. K. Drexler, *Engines of Creation - The Coming Era of Nanotechnology*, Anchor Books, 1986.
- [Dre04] M. Drewsen, A. Mortensen, R. Martinussen, P. Staunum, and J. L. Sørensen, *Nondestructive Identification of Cold and Extremely Localized Single Molecular Ions*, Phys. Rev. Lett. **93**, 243201 (2004).
- [DV95] A. De Vos, *Endoreversible thermoeconomics*, Energy Convers. Manage. **36**, 1 (1995).
- [Ebl11] J. F. Eble, *Versatile operations with calcium and multi-species ion crystals*, Ph.D. thesis, Universität Ulm (2011).
- [Ehr27] P. Ehrenfest, *Bemerkung über die angenäherte Gültigkeit der klassischen Mechanik innerhalb der Quantenmechanik*, Zeitschrift für Physik A **45**, 455 (1927).
- [Eis15] J. Eisert, M. Friesdorf, and C. Gogolin, *Quantum many-body systems out of equilibrium*, Nat. Phys. **11**, 124 (2015).
- [Eps07] R. Epstein, S. Seidelin, D. Leibfried, J. Wesenberg, J. Bollinger, J. Amini, R. Blakestad, J. Britton, J. Home, W. Itano, et al., *Simplified motional heating rate measurements of trapped ions*, Phys. Rev. A **76**, 033411 (2007).
- [Esc03] J. Eschner, G. Morigi, F. Schmidt-Kaler, R. Blatt, et al., *Laser cooling of trapped ions*, J. Opt. Soc. Am. B **20**, 1003 (2003).
- [Esp09] M. Esposito, K. Lindenberg, and C. Van den Broeck, *Universality of Efficiency at Maximum Power*, Phys. Rev. Lett. **102**, 130602 (2009).

- 
- [Esp10] M. Esposito, R. Kawai, K. Lindenberg, and C. Van den Broeck, *Quantum-dot Carnot engine at maximum power*, Phys. Rev. Lett. E **81**, 041106 (2010).
- [Est08] J. Esteve, C. Gross, A. Weller, S. Giovanazzi, and M. Oberthaler, *Squeezing and entanglement in a Bose–Einstein condensate*, Nature **455**, 1216 (2008).
- [Eva93] D. J. Evans, E. Cohen, and G. Morriss, *Probability of second law violations in shearing steady states*, Phys. Rev. Lett. **71**, 2401 (1993).
- [Fau12] T. Faust, J. Rieger, M. J. Seitner, P. Krenn, J. P. Kotthaus, and E. M. Weig, *Nonadiabatic Dynamics of Two Strongly Coupled Nanomechanical Resonator Modes*, Phys. Rev. Lett. **109**, 037205 (2012).
- [Fea88] H. Fearn and M. J. Collett, *Representations of squeezed states with thermal noise*, J. Mod. Opt. **35**, 553 (1988).
- [Fel00] T. Feldmann and R. Kosloff, *Performance of discrete heat engines and heat pumps in finite time*, Phys. Rev. E **61**, 4774 (2000).
- [Fel14] T. Feldker, L. Pelzer, M. Stappel, P. Bachor, R. Steinborn, D. Kolbe, J. Walz, and F. Schmidt-Kaler, *Mode shaping in mixed ion crystals of  $40\text{Ca}^{2+}$  and  $40\text{Ca}^{+}$* , Appl. Phys. B **114**, 11 (2014).
- [Fer16] A. Fernholm, *How molecules became machines*, The Royal Swedish Academy of Sciences, 2016.
- [Fes87] H. Feshbach, *Small systems: when does thermodynamics apply?*, Phys. Today **40**, 9 (1987).
- [Fey60] R. P. Feynman, *There's plenty of room at the bottom*, Engineering and Science **23**, 22 (1960).
- [Fey63] R. P. Feynman and F. L. Vernon, *The theory of a general quantum system interacting with a linear dissipative system*, Ann. Phys. **24**, 118 (1963).
- [Fia12] O. Fialko and D. W. Hallwood, *Isolated Quantum Heat Engine*, Phys. Rev. Lett. **108**, 085303 (2012).
- [Fin01] A. J. Finkelstein, Theodor; Organ, *Air engines : the history, science, and reality of the perfect engine*, Professional Engineering Pub., 2001, [joint ed.] ed.
- [Fle05] M. Fleischhauer, A. Imamoglu, and J. P. Marangos, *Electromagnetically induced transparency: Optics in coherent media*, Rev. Mod. Phys. **77**, 633 (2005).
- [Fli06] T. Fließbach, *Statistische Physik*, German Edition, Spektrum Akademischer Verlag, 2006, 4th ed.
- [Fri15] A. Friedenberger and E. Lutz, *When is a quantum heat engine quantum?*, arXiv:1508.04128 (2015).
- [Gal09] F. Galve and E. Lutz, *Nonequilibrium thermodynamic analysis of squeezing*, Phys. Rev. A **79**, 055804 (2009).
- [Gal14] R. Gallego, A. Riera, and J. Eisert, *Thermal machines beyond the weak coupling regime*, New Journal of Physics **16**, 125009 (2014).
- [Gar15] B. Gardas and S. Deffner, *Thermodynamic universality of quantum Carnot engines*, Phys. Rev. E **92**, 042126 (2015).
- [Gau10] Y. Gauthier, *Einspritzdruck bei modernen PKW-Dieselmotoren*, Springer, 2010.
- [Gem04] J. Gemmer, M. Michel, and G. Mahler, *Quantum thermodynamics: emergence of thermodynamic behavior within composite quantum systems*, Lecture notes in physics 657, Springer Berlin Heidelberg, 2004, 1st ed.
- [Ger05] C. Gerry and P. Knight, *Introductory quantum optics*, Cambridge University Press, 2005.
- [Gev92a] E. Geva and R. Kosloff, *A quantum-mechanical heat engine operating in finite time. A model consisting of spin-1/2 systems as the working fluid*, J. Chem. Phys. **96**, 3054 (1992).

- [Gev92b] E. Geva and R. Kosloff, *A quantum-mechanical heat engine operating in finite time. A model consisting of spin-1/2 systems as the working fluid*, The Journal of chemical physics **96**, 3054 (1992).
- [Gev96] E. Geva and R. Kosloff, *The quantum heat engine and heat pump: An irreversible thermodynamic analysis of the three-level amplifier*, The Journal of chemical physics **104**, 7681 (1996).
- [Gie14] J. Gieseler, R. Quidant, C. Dellago, and L. Novotny, *Dynamic relaxation of a levitated nanoparticle from a non-equilibrium steady state*, arXiv:1404.0411 (2014).
- [GK14] D. Gelbwaser-Klimovsky and G. Kurizki, *Heat-machine control by quantum-state preparation: From quantum engines to refrigerators*, Physical Review E **90**, 022102 (2014).
- [Goo16] J. Goold, M. Huber, A. Riera, L. del Rio, and P. Skrzypczyk, *The role of quantum information in thermodynamics – a topical review*, J. Phys. A **49**, 143001 (2016).
- [Gre06] D. Greenspan, *Numerical Solution of Ordinary Differential Equations: for Classical, Relativistic and Nano Systems*, Wiley-VCH, 2006.
- [Häf08] H. Häffner, C. F. Roos, and R. Blatt, *Quantum computing with trapped ions*, Phys. Rep. **469**, 155 (2008).
- [Hän09] P. Hänggi and F. Marchesoni, *Artificial Brownian motors: Controlling transport on the nanoscale*, Rev. Mod. Phys. **81**, 387 (2009).
- [Has98] T. Hasegawa, D. Tanooka, and T. Shimizu, *Distortion of spectral line profiles of laser-cooled ions in a radio-frequency ion trap*, Phys. Rev. A **58**, 2327 (1998).
- [Haz12] S. Haze, Y. Tateishi, A. Noguchi, K. Toyoda, and S. Urabe, *Observation of phonon hopping in radial vibrational modes of trapped ions*, Phys. Rev. A **85**, 031401 (2012).
- [Hen07] M. J. Henrich, F. Rempp, and G. Mahler, *Quantum thermodynamic Otto machines: A spin-system approach*, Eur. Phys. J. Special Topics **151**, 157 (2007).
- [Her09] M. Herrmann, V. Batteiger, S. Knünz, G. Saathoff, T. Udem, and T. Hänsch, *Frequency Metrology on Single Trapped Ions in the Weak Binding Limit: The  $3s\ 1/2 - 3p\ 3/2$  Transition in  $Mg^{+} 24$* , Phys. Rev. Lett. **102**, 013006 (2009).
- [Het15] M. Hettrich, T. Ruster, H. Kaufmann, C. F. Roos, C. T. Schmiegelow, F. Schmidt-Kaler, and U. G. Poschinger, *Measurement of Dipole Matrix Elements with a Single Trapped Ion*, Phys. Rev. Lett. **115**, 143003 (2015).
- [Hil63] T. L. Hill, *Thermodynamics of small systems*, Courier Corporation, 1963.
- [Hil14] S. Hilbert, P. Hänggi, and J. Dunkel, *Thermodynamic laws in isolated systems*, Phys. Rev. E **90**, 062116 (2014).
- [Hor13] M. Horodecki and J. Oppenheim, *Fundamental limitations for quantum and nanoscale thermodynamics*, Nat. Commun. **4** (2013).
- [Hov13] K. V. Hovhannisyan, M. Perarnau-Llobet, M. Huber, and A. Acín, *Entanglement generation is not necessary for optimal work extraction*, Phys. Rev. Lett. **111**, 240401 (2013).
- [How01] J. Howard et al., *Mechanics of motor proteins and the cytoskeleton*, Sinauer Associates Sunderland, MA, 2001.
- [Hua12] X. L. Huang, T. Wang, and X. X. Yi, *Effects of reservoir squeezing on quantum systems and work extraction*, Phys. Rev. E **86**, 051105 (2012).
- [Hug02] T. Hugel, N. B. Holland, A. Cattani, L. Moroder, M. Seitz, and H. E. Gaub, *Single-molecule optomechanical cycle*, Science **296**, 1103 (2002).
- [Hum02] T. Humphrey, R. Newbury, R. Taylor, and H. Linke, *Reversible quantum Brownian heat engines for electrons*, Phys. Rev. Lett. **89**, 116801 (2002).
- [Ise15] C. Iser and T. L.-Q. G. Pieper, personal communication, Andor iXon 885 data sheet (2015).

- 
- [Jac16] G. Jacob, K. Groot-Berning, S. Wolf, S. Ulm, L. Couturier, S. T. Dawkins, U. G. Poschinger, F. Schmidt-Kaler, and K. Singer, *Transmission Microscopy with Nanometer Resolution Using a Deterministic Single Ion Source*, Phys. Rev. Lett. **117**, 043001 (2016).
- [Jan92] J. Janszky and P. Adam, *Strong squeezing by repeated frequency jumps*, Phys. Rev. A **46**, 6091 (1992).
- [Jar97] C. Jarzynski, *Nonequilibrium equality for free energy differences*, Phys. Rev. Lett. **78**, 2690 (1997).
- [Jar11] C. Jarzynski, *Equalities and inequalities: irreversibility and the second law of thermodynamics at the nanoscale*, Annu. Rev. Condens. Matter Phys. **2**, 329 (2011).
- [Joh09] M. Johanning, A. Braun, N. Timoney, V. Elman, W. Neuhauser, and C. Wunderlich, *Individual addressing of trapped ions and coupling of motional and spin states using rf radiation*, Phys. Rev. Lett. **102**, 073004 (2009).
- [Jül97] F. Jülicher, A. Ajdari, and J. Prost, *Modeling molecular motors*, Rev. Mod. Phys. **69**, 1269 (1997).
- [Kal06] S. A. Kalandarov, Z. Kanokov, G. G. Adamian, and N. V. Antonenko, *Transport coefficients of a quantum system interacting with a squeezed heat bath*, Phys. Rev. E **74**, 011118 (2006).
- [Kar09] R. Karabalin, M. Cross, and M. Roukes, *Nonlinear dynamics and chaos in two coupled nanomechanical resonators*, Phys. Rev. B **79**, 165309 (2009).
- [Kau12] H. Kaufmann, S. Ulm, G. Jacob, U. Poschinger, H. Landa, A. Retzker, M. Plenio, and F. Schmidt-Kaler, *Precise experimental investigation of eigenmodes in a planar ion crystal*, Phys. Rev. Lett. **109**, 263003 (2012).
- [Kau16] H. Kaufmann, T. Ruster, C. T. Schmiegelow, M. A. Luda, V. Kaushal, J. Schulz, D. von Lindenfels, F. Schmidt-Kaler, and U. G. Poschinger, *Fast ion swapping for quantum information processing*, arXiv:1607.03734 (2016).
- [Kay07] E. R. Kay, D. A. Leigh, and F. Zerbetto, *Synthetic molecular motors and mechanical machines*, Angew. Chem. Int. Ed. **46**, 72 (2007).
- [Kha15] S. Khan, M. Kumar, V. Bharti, and V. Natarajan, *Coherent population trapping (CPT) versus electromagnetically induced transparency (EIT)*, arXiv:1503.06956 (2015).
- [Kie02] D. Kielpinski, C. Monroe, and D. J. Wineland, *Architecture for a large-scale ion-trap quantum computer*, Nature **417**, 709 (2002).
- [Kie04] T. D. Kieu, *The second law, Maxwell's demon, and work derivable from quantum heat engines*, Phys. Rev. Lett. **93**, 140403 (2004).
- [Kie15] D. Kienzler, H.-Y. Lo, B. Keitch, L. de Clercq, F. Leupold, F. Lindensefser, M. Marinelli, V. Negnevitsky, and J. Home, *Quantum harmonic oscillator state synthesis by reservoir engineering*, Science **347**, 53 (2015).
- [Kim89] M. S. Kim, F. A. M. de Oliveira, and P. L. Knight, *Properties of squeezed number states and squeezed thermal states*, Phys. Rev. A **40**, 2494 (1989).
- [Knü12] S. Knünz, M. Herrmann, V. Batteiger, G. Saathoff, T. Hänsch, and T. Udem, *Sub-millikelvin spatial thermometry of a single Doppler-cooled ion in a Paul trap*, Phys. Rev. A **85**, 023427 (2012).
- [Kol12] M. Kolar, D. Gelbwaser-Klimovsky, R. Alicki, and G. Kurizki, *Quantum Bath Refrigeration towards Absolute Zero: Challenging the Unattainability Principle*, Phys. Rev. Lett. **109**, 090601 (2012).
- [Kos84] R. Kosloff, *A quantum mechanical open system as a model of a heat engine*, J. Chem. Phys. **80**, 1625 (1984).
- [Kos00] R. Kosloff, E. Geva, and J. M. Gordon, *Quantum refrigerators in quest of the absolute zero*, J. Appl. Phys. **87**, 8093 (2000).

- [Kos13] R. Kosloff, *Quantum thermodynamics: A dynamical viewpoint*, Entropy **15**, 2100 (2013).
- [Kos14a] J. V. Koski, V. F. Maisi, J. P. Pekola, and D. V. Averin, *Experimental realization of a Szilard engine with a single electron*, Proc. Natl. Acad. Sci. **111**, 13786 (2014).
- [Kos14b] R. Kosloff and A. Levy, *Quantum heat engines and refrigerators: Continuous devices*, Annu. Rev. Phys. Chem. **65**, 365 (2014).
- [Kos15] J. Koski, A. Kutvonen, I. Khaymovich, T. Ala-Nissila, and J. Pekola, *On-chip Maxwell's demon as an information-powered refrigerator*, Phys. Rev. Lett. **115**, 260602 (2015).
- [Kou99] N. Koumura, R. W. Zijlstra, R. A. van Delden, N. Harada, and B. L. Feringa, *Light-driven monodirectional molecular rotor*, Nature **401**, 152 (1999).
- [Kra15] A. Kramida, Yu. Ralchenko, J. Reader, and NIST ASD Team, NIST Atomic Spectra Database (ver. 5.3), [Online]. Available: <http://physics.nist.gov/asd> [2016, August 29]. National Institute of Standards and Technology, Gaithersburg, MD. (2015).
- [Kre05] A. Kreuter, C. Becher, G. P. T. Lancaster, A. B. Mundt, C. Russo, H. Häffner, C. Roos, W. Hänsel, F. Schmidt-Kaler, R. Blatt, and M. S. Safronova, *Experimental and theoretical study of the  $3d\ ^2D$ -level lifetimes of  $^{40}\text{Ca}^+$* , Phys. Rev. A **71**, 032504 (2005).
- [Kri16] S. Krishnamurthy, S. Ghosh, D. Chatterji, R. Ganapathy, and A. Sood, *A micrometre-sized heat engine operating between bacterial reservoirs*, Nat. Phys. (2016).
- [Lan61] R. Landauer, *Irreversibility and heat generation in the computing process*, IBM J. Res. Dev. **5**, 183 (1961).
- [Lef87] H. S. Leff, *Thermal efficiency at maximum work output: new results for old heat engines*, Am. J. Phys **55**, 602 (1987).
- [Leg15] B. Leggio, B. Bellomo, and M. Antezza, *Quantum thermal machines with single nonequilibrium environments*, Phys. Rev. A **91**, 012117 (2015).
- [Lei03] D. Leibfried, R. Blatt, C. Monroe, and D. Wineland, *Quantum dynamics of single trapped ions*, Rev. Mod. Phys. **75**, 281 (2003).
- [Lem15] A. Lemmer, C. Cormick, C. T. Schmiegelow, F. Schmidt-Kaler, and M. B. Plenio, *Two-Dimensional Spectroscopy for the Study of Ion Coulomb Crystals*, Phys. Rev. Lett. **114**, 073001 (2015).
- [Lev12a] A. Levy, R. Alicki, and R. Kosloff, *Quantum refrigerators and the third law of thermodynamics*, Phys. Rev. E **85**, 061126 (2012).
- [Lev12b] A. Levy and R. Kosloff, *Quantum Absorption Refrigerator*, Phys. Rev. Lett. **108**, 070604 (2012).
- [Lev16] A. Levy, L. Diósi, and R. Kosloff, *Quantum flywheel*, Phys. Rev. A **93**, 052119 (2016).
- [Lin03] B. Lin and J. Chen, *Performance analysis of an irreversible quantum heat engine working with harmonic oscillators*, Phys. Rev. E **67**, 046105 (2003).
- [Lin10a] Q. Lin, J. Rosenberg, D. Chang, R. Camacho, M. Eichenfield, K. J. Vahala, and O. Painter, *Coherent mixing of mechanical excitations in nano-optomechanical structures*, Nat. Photon. **4**, 236 (2010).
- [Lin10b] N. Linden, S. Popescu, and P. Skrzypczyk, *How Small Can Thermal Machines Be? The Smallest Possible Refrigerator*, Phys. Rev. Lett. **105**, 130401 (2010).
- [Lin11] G.-D. Lin and L. Duan, *Equilibration and temperature distribution in a driven ion chain*, New J. Phys. **13**, 075015 (2011).
- [Lin13] Y. Lin, J. Gaebler, F. Reiter, T. Tan, R. Bowler, A. Sørensen, D. Leibfried, and D. Wineland, *Dissipative production of a maximally entangled steady state of two quantum bits*, Nature **504**, 415 (2013).
- [Lis05] C. Lisowski, M. Knoop, C. Champenois, G. Hagel, M. Vedel, and F. Vedel, *Dark resonances as a probe for the motional state of a single ion*, Appl. Phys. B **81**, 5 (2005).

- 
- [Liv94] A. Livoreil, C. O. Dietrich-Buchecker, and J.-P. Sauvage, *Electrochemically triggered swinging of a [2]-catenate*, J. Am. Chem. Soc. **116**, 9399 (1994).
- [Lo15] H.-Y. Lo, D. Kienzler, L. de Clercq, M. Marinelli, V. Negnevitsky, B. C. Keitch, and J. P. Home, *Spin-motion entanglement and state diagnosis with squeezed oscillator wavepackets*, Nature **521**, 336 (2015).
- [Lon15a] R. Long and W. Liu, *Performance of micro two-level heat devices with prior information*, Phys. Lett. A **379**, 1979 (2015).
- [Lon15b] R. Long and W. Liu, *Performance of quantum Otto refrigerators with squeezing*, Phys. Rev. E **91**, 062137 (2015).
- [Los15] M. Lostaglio, D. Jennings, and T. Rudolph, *Description of quantum coherence in thermodynamic processes requires constraints beyond free energy*, Nat. Commun. **6** (2015).
- [Lüt98] N. Lütkenhaus, J. Cirac, and P. Zoller, *Mimicking a squeezed-bath interaction: Quantum-reservoir engineering with atoms*, Phys. Rev. A **57**, 548 (1998).
- [Mac59] W. Macalpine and R. Schildknecht, *Coaxial resonators with helical inner conductor*, Proc. IRE **47**, 2099 (1959).
- [Mar93a] P. Marian and T. A. Marian, *Squeezed states with thermal noise. I. Photon-number statistics*, Phys. Rev. A **47**, 4474 (1993).
- [Mar93b] P. Marian and T. A. Marian, *Squeezed states with thermal noise. II. Damping and photon counting*, Phys. Rev. A **47**, 4487 (1993).
- [Mar12] A. Mari and J. Eisert, *Cooling by Heating: Very Hot Thermal Light Can Significantly Cool Quantum Systems*, Phys. Rev. Lett. **108**, 120602 (2012).
- [Mar15] I. A. Martínez, É. Roldán, L. Dinis, D. Petrov, and R. A. Rica, *Adiabatic processes realized with a trapped Brownian particle*, Phys. Rev. Lett. **114**, 120601 (2015).
- [Mar16] I. A. Martínez, É. Roldán, L. Dinis, D. Petrov, J. M. Parrondo, and R. A. Rica, *Brownian carnot engine*, Nat. Phys. **12**, 67 (2016).
- [Max71] J. C. Maxwell, *Theory of Heat*, Dover Publications Inc., 1871.
- [Mee96] D. M. Meekhof, C. Monroe, B. E. King, W. M. Itano, and D. J. Wineland, *Generation of nonclassical motional states of a trapped atom*, Phys. Rev. Lett. **76**, 1796 (1996).
- [Met99] H. J. Metcalf and P. van der Straten, *Laser cooling and trapping*, Springer New-York Inc., 1999.
- [Mil03] P. W. Milonni, *Photon steam engines*, Physics World **16**, 22 (2003).
- [Mil14] J. Millen, T. Deesuwana, P. Barker, J. Anders, et al., *Nanoscale temperature measurements using non-equilibrium Brownian dynamics of a levitated nanosphere*, Nat. Nano. **9**, 425 (2014).
- [Mil16] J. Millen and A. Xuereb, *Perspective on quantum thermodynamics*, New J. Phys. **18**, 011002 (2016).
- [Mon13] C. Monroe and J. Kim, *Scaling the ion trap quantum processor*, Science **339**, 1164 (2013).
- [Mur12] K. W. Murch, U. Vool, D. Zhou, S. J. Weber, S. M. Girvin, and I. Siddiqi, *Cavity-Assisted Quantum Bath Engineering*, Phys. Rev. Lett. **109**, 183602 (2012).
- [Mya00] C. J. Myatt, B. E. King, Q. A. Turchette, C. A. Sackett, D. Kielpinski, W. M. Itano, C. Monroe, and D. J. Wineland, *Decoherence of quantum superpositions through coupling to engineered reservoirs*, Nature **403**, 269 (2000).
- [Nag83] W. Nagourney, G. Janik, and H. Dehmelt, *Linewidth of single laser-cooled  $^{24}\text{Mg}^+$  ion in radiofrequency trap*, Proc. Natl. Acad. Sci. **80**, 643 (1983).
- [Näg98] H. Nägerl, D. Leibfried, F. Schmidt-Kaler, J. Eschner, and R. Blatt, *Coherent excitation of normal modes in a string of  $\text{Ca}^+$  ions*, Opt. Express **3**, 89 (1998).



- [Nal13] P. Nalbach and M. Thorwart, *Enhanced quantum efficiency of light-harvesting in a biomolecular quantum "steam engine"*, Proc. Natl. Acad. Sci. **110**, 2693 (2013).
- [Ner69] W. Nernst, *The new heat theorem: Its foundations in theory and experiment*, Dover Publications, 1969.
- [Nor11] B. G. Norton, E. Streed, M. Petasiunas, A. Jechow, and D. Kielpinski, *Millikelvin spatial thermometry of trapped ions*, New J. Phys. **13**, 113022 (2011).
- [Nov58] I. I. Novikov, *The efficiency of atomic power stations*, J. Nucl. Energy **7**, 125 (1958).
- [Obe99] H. Oberst, *Resonance fluorescence of single barium ions*, Master's thesis, Leopold-Franzens-Universität Innsbruck (1999).
- [O'C10] A. D. O'Connell, M. Hofheinz, M. Ansmann, R. C. Bialczak, M. Lenander, E. Lucero, M. Neeley, D. Sank, H. Wang, M. Weides, et al., *Quantum ground state and single-phonon control of a mechanical resonator*, Nature **464**, 697 (2010).
- [Oka80] K. Okada, K. Hashimoto, T. Shibata, and Y. Nagaki, *Novel method for high resolution measurement of laser output spectrum*, Electron. Lett. **16**, 630 (1980).
- [Orz01] C. Orzel, A. Tuchman, M. Fenselau, M. Yasuda, and M. Kasevich, *Squeezed states in a Bose-Einstein condensate*, Science **291**, 2386 (2001).
- [OV91] J. Oz-Vogt, A. Mann, and M. Revzen, *Thermal coherent states and thermal squeezed states*, J. Mod. Opt. **38**, 2339 (1991).
- [Par99] A. Parmeggiani, F. Jülicher, A. Ajdari, and J. Prost, *Energy transduction of isothermal ratchets: Generic aspects and specific examples close to and far from equilibrium*, Phys. Rev. E **60**, 2127 (1999).
- [Par02] J. Parrondo and B. J. de Cisneros, *Energetics of Brownian motors: a review*, Appl. Phys. A **75**, 179 (2002).
- [Par15] J. M. Parrondo, J. M. Horowitz, and T. Sagawa, *Thermodynamics of information*, Nature Phys. **11**, 131 (2015).
- [Pau90] W. Paul, *Electromagnetic traps for charged and neutral particles (Nobel lecture)*, Rev. Mod. Phys. **62**, 531 (1990).
- [Pek15] J. P. Pekola, *Towards quantum thermodynamics in electronic circuits*, Nat. Phys. **11**, 118 (2015).
- [Pet12] T. Peters, B. Wittrock, F. Blatt, T. Halfmann, and L. P. Yatsenko, *Thermometry of ultracold atoms by electromagnetically induced transparency*, Phys. Rev. A **85**, 063416 (2012).
- [Pet16] J. Peterson, R. Sarthour, A. Souza, I. Oliveira, J. Goold, K. Modi, D. Soares-Pinto, and L. Céleri, *Experimental demonstration of information to energy conversion in a quantum system at the Landauer limit*, Proc. R. Soc. A **472**, 20150813 (2016).
- [Pie07] S. Pielawa, G. Morigi, D. Vitali, and L. Davidovich, *Generation of Einstein-Podolsky-Rosen-entangled radiation through an atomic reservoir*, Phys. Rev. Lett. **98**, 240401 (2007).
- [Pos14] U. G. Poschinger, private communication (2014).
- [Poy96] J. F. Poyatos, J. I. Cirac, and P. Zoller, *Quantum Reservoir Engineering with Laser Cooled Trapped Ions*, Phys. Rev. Lett. **77**, 4728 (1996).
- [Poz02] C. Pozrikidis, *A practical guide to boundary element methods with the software library BEM-LIB*, CRC Press, 2002.
- [Pru11] T. Pruttivarasin, M. Ramm, I. Talukdar, A. Kreuter, and H. Häffner, *Trapped ions in optical lattices for probing oscillator chain models*, New J. Phys. **13**, 075012 (2011).
- [Pyk13] K. Pyka, J. Keller, H. Partner, R. Nigmatullin, T. Burgermeister, D. Meier, K. Kuhlmann, A. Retzker, M. Plenio, W. Zurek, et al., *Topological defect formation and spontaneous symmetry breaking in ion Coulomb crystals*, Nat. Commun. **4**, 2091 (2013).

- 
- [Qua07] H. T. Quan, Y.-x. Liu, C. P. Sun, and F. Nori, *Quantum thermodynamic cycles and quantum heat engines*, Phys. Rev. E **76**, 031105 (2007).
- [Rab04] P. Rabl, A. Shnirman, and P. Zoller, *Generation of squeezed states of nanomechanical resonators by reservoir engineering*, Phys. Rev. B **70**, 205304 (2004).
- [Rae10] S. Raeder, *Spurenanalyse von Aktiniden in der Umwelt mittels Resonanzionisations-Massenspektrometrie*, Ph.D. thesis, Johannes Gutenberg-Universität Mainz (2010).
- [Rai11] M. G. Raizen, *Demons, entropy and the quest for absolute zero*, Sci. Am. **304**, 54 (2011).
- [Ram13] M. Ramm, T. Pruttivarasin, M. Kokish, I. Talukdar, and H. Häffner, *Precision measurement method for branching fractions of excited  $P\ 1/2$  states applied to  $\text{Ca}^+ 40$* , Phys. Rev. Lett. **111**, 023004 (2013).
- [Ram14] M. Ramm, T. Pruttivarasin, and H. Häffner, *Energy transport in trapped ion chains*, New J. Phys. **16**, 063062 (2014).
- [Rei02a] P. Reimann, *Brownian motors: noisy transport far from equilibrium*, Phys. Rep. **361**, 57 (2002).
- [Rei02b] D. Reiß, K. Abich, W. Neuhauser, C. Wunderlich, and P. Toschek, *Raman cooling and heating of two trapped  $\text{Ba}^+$  ions*, Phys. Rev. A **65**, 053401 (2002).
- [Rey92] O. Reynolds, *Memoir of James Prescott Joule*, Manchester Literary and Philosophical Society, 1892.
- [Rez06] Y. Rezek and R. Kosloff, *Irreversible performance of a quantum harmonic heat engine*, New J. Phys. **8**, 83 (2006).
- [Rez09] Y. Rezek, P. Salamon, K. H. Hoffmann, and R. Kosloff, *The quantum refrigerator: The quest for absolute zero*, Europhys. Lett. **85**, 30008 (2009).
- [Roo00] C. Roos, D. Leibfried, A. Mundt, F. Schmidt-Kaler, J. Eschner, and R. Blatt, *Experimental demonstration of ground state laser cooling with electromagnetically induced transparency*, Phys. Rev. Lett. **85**, 5547 (2000).
- [Ros10] W. Rosen, *The most powerful idea in the world: A story of steam, industry, and invention*, Univ. of Chicago Pr., 2010.
- [Roß16] J. Roßnagel, S. T. Dawkins, K. N. Tolazzi, O. Abah, E. Lutz, F. Schmidt-Kaler, and K. Singer, *A single-atom heat engine*, Science **352**, 325 (2016).
- [Rou94] J. Rousselet, L. Salome, A. Ajdari, J. Prost, et al., *Directional motion of Brownian particles induced by a periodic asymmetric potential*, Nature **370**, 446 (1994).
- [Rus14] T. Ruster, C. Warschburger, H. Kaufmann, C. T. Schmiegelow, A. Walther, M. Hettrich, A. Pfister, V. Kaushal, F. Schmidt-Kaler, and U. G. Poschinger, *Experimental realization of fast ion separation in segmented Paul traps*, Phys. Rev. A **90**, 033410 (2014).
- [Sar11] A. Sarlette, J.-M. Raimond, M. Brune, and P. Rouchon, *Stabilization of nonclassical states of the radiation field in a cavity by reservoir engineering*, Phys. Rev. Lett. **107**, 010402 (2011).
- [Sch95] M. Schubert, I. Siemers, R. Blatt, W. Neuhauser, and P. Toschek, *Transient internal dynamics of a multilevel ion*, Phys. Rev. A **52**, 2994 (1995).
- [Sch01] W. P. Schleich, *Quantum optics in phase space*, Wiley-VCH, 2001.
- [Sch07] T. Schmiedl and U. Seifert, *Efficiency at maximum power: An analytically solvable model for stochastic heat engines*, Europhys. Lett. **81**, 20003 (2007).
- [Sch09] S. A. Schulz, *Scalable Microchip Ion Traps for Quantum Computation*, Ph.D. thesis, Universität Ulm (2009).
- [Sch16] C. T. Schmiegelow, H. Kaufmann, T. Ruster, J. Schulz, V. Kaushal, M. Hettrich, F. Schmidt-Kaler, and U. G. Poschinger, *Phase-Stable Free-Space Optical Lattices for Trapped Ions*, Phys. Rev. Lett. **116**, 033002 (2016).

- [Sco59] H. E. D. Scovil and E. O. Schulz-DuBois, *Three-level masers as heat engines*, Phys. Rev. Lett. **2**, 262 (1959).
- [Scu97] M. O. Scully and M. S. Zubairy, *Quantum optics*, Cambridge University Press, 1997.
- [Scu03] M. O. Scully, M. S. Zubairy, G. S. Agarwal, and H. Walther, *Extracting work from a single heat bath via vanishing quantum coherence*, Science **299**, 862 (2003).
- [Scu10] M. O. Scully, *Quantum Photocell: Using Quantum Coherence to Reduce Radiative Recombination and Increase Efficiency*, Phys. Rev. Lett. **104**, 207701 (2010).
- [Sei11] U. Seifert, *Efficiency of autonomous soft nanomachines at maximum power*, Phys. Rev. Lett. **106**, 020601 (2011).
- [Sei12] U. Seifert, *Stochastic thermodynamics, fluctuation theorems and molecular machines*, Rep. Prog. Phys. **75**, 126001 (2012).
- [Sha13a] E. Shahmoon and G. Kurizki, *Engineering a thermal squeezed reservoir by energy-level modulation*, Phys. Rev. A **87**, 013841 (2013).
- [Sha13b] S. Shankar, M. Hatridge, Z. Leghtas, K. Sliwa, A. Narla, U. Vool, S. M. Girvin, L. Frunzio, M. Mirrahimi, and M. H. Devoret, *Autonomously stabilized entanglement between two superconducting quantum bits*, Nature **504**, 419 (2013).
- [Sin02] K. Singer, S. Jochim, M. Mudrich, A. Mosk, and M. Weidemüller, *Low-cost mechanical shutter for light beams*, Rev. Sci. Instr. **73**, 4402 (2002).
- [Sin10] K. Singer, U. Poschinger, M. Murphy, P. Ivanov, F. Ziesel, T. Calarco, and F. Schmidt-Kaler, *Colloquium: Trapped ions as quantum bits: Essential numerical tools*, Rev. Mod. Phys. **82**, 2609 (2010).
- [Siv12] J. Sivers, L. Simkins, S. Weidt, and W. Hensinger, *On the application of radio frequency voltages to ion traps via helical resonators*, Appl. Phys. B **107**, 921 (2012).
- [Slu85] R. E. Slusher, L. W. Hollberg, B. Yurke, J. C. Mertz, and J. F. Valley, *Observation of Squeezed States Generated by Four-Wave Mixing in an Optical Cavity*, Phys. Rev. Lett. **55**, 2409 (1985).
- [Sre94] M. Srednicki, *Chaos and quantum thermalization*, Phys. Rev. E **50**, 888 (1994).
- [Ste86a] S. Stenholm, *The semiclassical theory of laser cooling*, Rev. Mod. Phys. **58**, 699 (1986).
- [Ste86b] S. Stenholm, *The semiclassical theory of laser cooling*, Rev. Mod. Phys. **58**, 699 (1986).
- [Ste11] P. Steeneken, K. Le Phan, M. Goossens, G. Koops, G. Brom, C. Van der Avoort, and J. Van Beek, *Piezoresistive heat engine and refrigerator*, Nat. Phys. **7**, 354 (2011).
- [Szi29] L. Szilard, *Über die Entropieverminderung in einem thermodynamischen System bei Eingriffen intelligenter Wesen*, Zeitschrift für Physik **53**, 840 (1929).
- [Tan74] N. Taniguchi et al., *On the basic concept of nanotechnology*, in: Proc. Intl. Conf. Prod. Eng. Tokyo, Part II, 18–23, 1974.
- [Tei89] M. C. Teich and B. E. A. Saleh, *TUTORIAL: Squeezed state of light*, Quantum Optics **1**, 153 (1989).
- [Thi15] H. Thierschmann, R. Sánchez, B. Sothmann, F. Arnold, C. Heyn, W. Hansen, H. Buhmann, and L. W. Molenkamp, *Three-terminal energy harvester with coupled quantum dots*, Nat. Nano. **10**, 854 (2015).
- [Tho08] J. J. Thorn, E. A. Schoene, T. Li, and D. A. Steck, *Experimental realization of an optical one-way barrier for neutral atoms*, Phys. Rev. Lett. **100**, 240407 (2008).
- [Tol14] K. N. Tolazzi, *Dunkelresonanzthermometrie für eine Einzel-Ionen Wärmekraftmaschine*, Master's thesis, Johannes Gutenberg-Universität Mainz (2014).
- [Tom12] A. Tomadin, S. Diehl, M. D. Lukin, P. Rabl, and P. Zoller, *Reservoir engineering and dynamical phase transitions in optomechanical arrays*, Phys. Rev. A **86**, 033821 (2012).

- 
- [Ton05] F. Tonner and G. Mahler, *Autonomous quantum thermodynamic machines*, Phys. Rev. E **72**, 066118 (2005).
- [Tor13] E. Torrontegui and R. Kosloff, *Quest for absolute zero in the presence of external noise*, Phys. Rev. E **88**, 032103 (2013).
- [Toy10] S. Toyabe, T. Okamoto, T. Watanabe-Nakayama, H. Taketani, S. Kudo, and E. Muneyuki, *Nonequilibrium Energetics of a Single F<sub>1</sub>-ATPase Molecule*, Phys. Rev. Lett. **104**, 198103 (2010).
- [Toy11] S. Toyabe, T. Watanabe-Nakayama, T. Okamoto, S. Kudo, and E. Muneyuki, *Thermodynamic efficiency and mechanochemical coupling of F<sub>1</sub>-ATPase*, Proc. Natl. Acad. Sci. **108**, 17951 (2011).
- [Toy13] K. Toyoda, Y. Matsuno, A. Noguchi, S. Haze, and S. Urabe, *Experimental realization of a quantum phase transition of polaritonic excitations*, Phys. Rev. Lett. **111**, 160501 (2013).
- [Tur00a] Q. Turchette, B. King, D. Leibfried, D. Meekhof, C. Myatt, M. Rowe, C. Sackett, C. Wood, W. Itano, C. Monroe, et al., *Heating of trapped ions from the quantum ground state*, Phys. Rev. A **61**, 063418 (2000).
- [Tur00b] Q. Turchette, C. Myatt, B. King, C. Sackett, D. Kielpinski, W. Itano, C. Monroe, and D. Wineland, *Decoherence and decay of motional quantum states of a trapped atom coupled to engineered reservoirs*, Phys. Rev. Lett. A **62**, 053807 (2000).
- [Uhl30] G. E. Uhlenbeck and L. S. Ornstein, *On the theory of the Brownian motion*, Phys. Rev. Lett. **36**, 823 (1930).
- [Ulm13] S. Ulm, J. Roßnagel, G. Jacob, C. Degünther, S. Dawkins, U. Poschinger, R. Nigmatullin, A. Retzker, M. Plenio, F. Schmidt-Kaler, et al., *Observation of the Kibble–Zurek scaling law for defect formation in ion crystals*, Nat. Commun. **4**, 2290 (2013).
- [Vah09] K. Vahala, M. Herrmann, S. Knünz, V. Batteiger, G. Saathoff, T. W. Hänsch, and T. Udem, *A phonon laser*, Nat. Phys. **5**, 682 (2009).
- [Ver67] L. Verlet, *Computer "Experiments" on Classical Fluids. I. Thermodynamical Properties of Lennard-Jones Molecules*, Phys. Rev. **159**, 98 (1967).
- [Ver09] F. Verstraete, M. M. Wolf, and J. I. Cirac, *Quantum computation and quantum-state engineering driven by dissipation*, Nat. Phys. **5**, 633 (2009).
- [Ver14a] G. Verley, M. Esposito, T. Willaert, and C. Van den Broeck, *The unlikely Carnot efficiency*, Nat. Commun. **5** (2014).
- [Ver14b] G. Verley, T. Willaert, C. Van den Broeck, and M. Esposito, *Universal theory of efficiency fluctuations*, Phys. Rev. E **90**, 052145 (2014).
- [Vid16] M. D. Vidrighin, O. Dahlsten, M. Barbieri, M. Kim, V. Vedral, and I. A. Walmsley, *Photonic Maxwell's demon*, Phys. Rev. Lett. **116**, 050401 (2016).
- [Vin15] S. Vinjanampathy and J. Anders, *Quantum thermodynamics*, arXiv:1508.06099 (2015).
- [Viv09] G. Vives and J. M. Tour, *Synthesis of single-molecule nanocars*, Acc. Chem. Res. **42**, 473 (2009).
- [Vol26] M. Volmer and A. Weber, *Tröpfchenbildung in Dämpfen*, Z. Phys. Chem. **119**, 227 (1926).
- [Wal12a] A. Walther, U. Poschinger, K. Singer, and F. Schmidt-Kaler, *Precision measurements in ion traps using slowly moving standing waves*, Appl. Phys. B **107**, 1061 (2012).
- [Wal12b] A. Walther, F. Ziesel, T. Ruster, S. T. Dawkins, K. Ott, M. Hettrich, K. Singer, F. Schmidt-Kaler, and U. Poschinger, *Controlling Fast Transport of Cold Trapped Ions*, Phys. Rev. Lett. **109**, 080501 (2012).
- [Wan93] B.-G. Wang and J.-X. Zhu, *Wigner functions for coherent and squeezed states with thermal noise*, J. Mod. Opt. **40**, 1917 (1993).

- [Wan02] G. Wang, E. M. Sevick, E. Mittag, D. J. Searles, and D. J. Evans, *Experimental demonstration of violations of the second law of thermodynamics for small systems and short time scales*, Phys. Rev. Lett. **89**, 050601 (2002).
- [Wan13a] R. Wang, J. Wang, J. He, and Y. Ma, *Efficiency at maximum power of a heat engine working with a two-level atomic system*, Phys. Rev. E **87**, 042119 (2013).
- [Wan13b] Y.-D. Wang and A. A. Clerk, *Reservoir-Engineered Entanglement in Optomechanical Systems*, Phys. Rev. Lett. **110**, 253601 (2013).
- [Wer66] H. Wergeland and D. ter Haar, *Elements of Thermodynamics*, Addison-Wesley Reading, 1966.
- [Wes07] J. Wesenberg, R. Epstein, D. Leibfried, R. Blakestad, J. Britton, J. Home, W. Itano, J. Jost, E. Knill, C. Langer, et al., *Fluorescence during Doppler cooling of a single trapped atom*, Phys. Rev. A **76**, 053416 (2007).
- [Wha03] S. Whalen, M. Thompson, D. Bahr, C. Richards, and R. Richards, *Design, fabrication and testing of the P 3 micro heat engine*, Sens. Actuators A: Phys. **104**, 290 (2003).
- [Woo14] M. Woolley and A. Clerk, *Two-mode squeezed states in cavity optomechanics via engineering of a single reservoir*, Phys. Rev. A **89**, 063805 (2014).
- [Woo15] M. P. Woods, N. Ng, and S. Wehner, *The maximum efficiency of nano heat engines depends on more than temperature*, arXiv:1506.02322 (2015).
- [Woo16] M. P. Woods, R. Silva, and J. Oppenheim, *Autonomous quantum machines and finite sized clocks*, arXiv:1607.04591 (2016).
- [Yur88] B. Yurke, P. G. Kaminsky, R. E. Miller, E. A. Whittaker, A. D. Smith, A. H. Silver, and R. W. Simon, *Observation of 4.2-K equilibrium-noise squeezing via a Josephson-parametric amplifier*, Phys. Rev. Lett. **60**, 764 (1988).
- [Yvo55] J. Yvon, *Proceedings of the International Conference on Peaceful Uses of Atomic Energy*, United Nations Pub., 1955.
- [Zen95] H. Zeng and F. Lin, *Coherent squeezed states of motion in an ion trap generated with Raman-driven sideband transitions*, Phys. Rev. A **52**, 809 (1995).
- [Zha14a] K. Zhang, F. Bariani, and P. Meystre, *Quantum optomechanical heat engine*, Phys. Rev. Lett. **112**, 150602 (2014).
- [Zha14b] X. Zhang, X. Huang, and X. Yi, *Quantum Otto heat engine with a non-Markovian reservoir*, J. Phys. A **47**, 455002 (2014).
- [Zie12] F. Ziesel, *Quantum State Manipulation and Dynamics in Micro Ion Traps*, Ph.D. thesis, Universität Ulm (2012).

## Acknowledgments

Im Verlauf dieser Arbeit haben viele Menschen maßgeblich zu deren Erfolg beigetragen. Mein Dank gilt insbesondere meinem Betreuer Prof. Dr. Ferdinand Schmidt-Kaler und meinem Gruppenleiter Prof. Dr. Kilian Singer, die mir Vertrauen geschenkt und viel Freiheit bei der Durchführung meiner Projekte eingeräumt haben. Beide haben mich durch zahlreiche und intensive Diskussionen unterstützt, sodass ich stets von ihrem Wissen und ihren Erfahrungen profitieren konnte. Mein besonderer Dank gilt auch Prof. Dr. Eric Lutz, der mir mit viel Geduld die theoretischen Hintergründe erläutert und neue Denkanstöße gegeben hat.

Nicolas Tolazzi, dessen Diplomarbeit ich betreuen durfte, war mit viel Leidenschaft, Enthusiasmus und seinem technischen Wissen maßgeblich an der erfolgreichen Durchführung der Experimente beteiligt. Sam Dawkins hat sich mit Begeisterung und Raffinesse an der analytischen Auswertung der Messdaten beteiligt. Die Fit-Routine zur Anpassung komplexer Spektren wurde von Uli Poschinger programmiert. Meine Büro- und Laborkollegen Karin Groot-Bering, Stefan Ulm und Georg Jacob, dessen visionärer Erfindungsgeist dieses Forschungsprojekt erst möglich gemacht hat, haben stets für ein angenehmes Arbeitsklima gesorgt und mich bei allen kleineren und größeren Schwierigkeiten unterstützt. Ich danke allen für die tatkräftige Mitarbeit an meinem Forschungsprojekt. Außerdem danke ich der gesamten Arbeitsgruppe QUANTUM für die produktive Atmosphäre und die unterhaltsamen Diskussionen während der Essens- und Kaffeepausen, während der zahlreiche kreative Ideen entstanden sind. Das gesamte Arbeitsumfeld am Institut hat mir eine sehr schöne Zeit beschert und stets dazu beigetragen, dass ich mich mit Freude der wissenschaftlichen Forschung widmen konnte.

Außerdem danke ich Heinz Lenk, der mich in die Kunst der analogen Signalverarbeitung eingewiesen hat. Der gesamten mechanischen Werkstatt danke ich für ihre ausgezeichnete Arbeit. Christine Best und Elvira Stuck-Kerth danke ich für die Unterstützung in allen bürokratischen Angelegenheiten.

Zuletzt, dafür von ganzem Herzen, danke ich meiner Frau Susanne, die für mich in schwierigen Zeiten eine wichtige Stütze war, und die immer versucht hat, die Hintergründe meiner Experimente zu verstehen.



# Curriculum Vitae

## PERSÖNLICHE DATEN

Name	<b>Johannes Roßnagel</b>
Geboren am	27.08.1984 in Heidelberg
Nationalität	deutsch
Familienstand	Verheiratet, 1 Kind

## HOCHSCHULSTUDIUM

Seit 01/2012	<b>Promotion in Physik</b> Johannes Gutenberg-Universität Mainz Titel der Arbeit: <i>A single atom heat engine</i> bei Prof. Dr. Ferdinand Schmidt-Kaler
10/2005 – 08/2011	<b>Diplomstudium Physik</b> Johannes Gutenberg-Universität Mainz <b>Diplomarbeit</b> Titel der Arbeit: <i>Aufbau einer Atomstrahl-Massenspektrometer-Apparatur zur resonanten Laserionisation</i> bei Prof. Dr. Klaus Wendt <b>Vordiplom:</b> Albert-Ludwigs-Universität Freiburg
08/2007 – 06/2008	<b>Auslandsstudium, Angewandte Physik</b> Université de Limoges, Frankreich <b>Abschluss:</b> Bachelor of Science ( <i>Licence de science</i> )

## SCHULE UND ZIVILDIENT

08/2004 – 07/2005	<b>Anderer Dienst im Ausland,</b> Anneville-sur-Scie, Frankreich Wohneinrichtung für Menschen mit geistiger Behinderung
05/2004	<b>Abitur</b> Kurfürst-Friedrich-Gymnasium, Heidelberg